INVESTIGATION OF MICROSTRUCTURE EFFECTS ON HARDNESS AND OXIDATION RESISTANCE OF NEW GENERATION CERAMIC COATINGS

by

MINGHUI ZHANG

Presented to the Faculty of the Graduate School of
The University of Texas at Arlington in Partial Fulfillment
of the Requirements
for the Degree of

DOCTOR OF PHILOSOPHY

THE UNIVERSITY OF TEXAS AT ARLINGTON

August 2017

ACKNOWLEDGEMENTS

I would like to express my sincere appreciation to all who helped and supported me in any respect during the completion of my research. First of all, I would like to graciously thank Dr. Efstathios I. Meletis, who advised this work. Without his guidance and support, I would not be able to complete my doctoral program. I would also like to express my sincere gratitude to Dr. Jiechao Jiang for guiding me in the field of materials characterization and electron microscopy. His dedication to research inspired me and his care and encouragement enable the completion of this work. I would also like to thank my committee members, Dr. Aswath, Dr. Yum and Dr. Luo for their precious time and suggestions.

I would like to thank Dr. Jaroslav Vlcek's Research Group from University of West Bohemian for providing the high quality coatings for my mechanism study. I would like to thank my SANEL labmates and all coworkers involved in this work. Special thanks to Dr. Jie He for training me on electron microscopy, Randall Kelton for his suggestions on oxidation diffusion analysis, Dr. Jessica Mooney, Dr. Yishu Wang and Anna Zaman for their assistance with the magnetron sputtering system. I would like to acknowledge my friends, Zi Wei, Huandi Gu, Yi Shen and Hsiaochien Wu for their help, encouragement and friendship.

I would like to express my appreciation to Jennifer Standlee and Beth Robinson who were really patient and helpful in dealing with my courses enrollment, scholarship application and all kinds of problems.

Finally, I would like to thank my lovely parents and parents-in-law for their unconditional love and support. I'm so lucky to meet my husband Po-Cheng Lu during my Ph.D. studies. With his love, support, encouragement and accompany, I am able to overcome all the difficulties I faced during these years.

This work is supported by the National Science Foundation under Award NSF/CMMI 1335502.

August 2, 2017

ABSTRACT

INVESTIGATION OF MICROSTRUCTURE EFFECTS ON HARDNESS AND OXIDATION RESISTANCE OF NEW GENERATION CERAMIC COATINGS

Minghui Zhang, Ph.D.

THE University of Texas at Arlington, 2017

Supervising Professor: Efstathios I. Meletis

This work was motivated by the demand for a new generation of materials capable for harsh environment applications, and focused on developing a better understanding of the effects of elemental composition and microstructure on the mechanical and thermal properties of coatings. The knowledge gained from this work can be used to design protective coatings with tailored properties for harsh environment applications in the future. High resolution transmission electron microscopy (HRTEM) and electron diffraction have been mainly employed in the microstructure studies of the new generation ceramics, with the assistance of other materials characterization techniques, such as x-ray diffraction (XRD), x-ray photoelectron spectroscopy (XPS), atomic force microscopy (AFM) and nano-indentation measurements.

Ceramic coatings studied in this work have been divided into two groups: 1) Transition metal based nanocomposite coatings with enhanced hardness, 2) Amorphous coatings with high oxidation resistance. In the first group, the microstructure effects and hardness enhancement mechanism of Zr-B-C-N, Hf-B-Si-C and Hf-Si-N coatings are discussed. The hardness enhancement is based on the design of nanostructure and the control of grain size during the formation of coatings. The formation of amorphous boundaries with proper thickness between crystalline structures and the well aligned

crystallographic orientation were found to result in the increasing of hardness and decreasing of compressive stress of coatings. In the second group, a mechanism of extraordinary high oxidation resistance is established for the Si-B-C-N and Hf-B-Si-C-N coatings by studying the microstructure evolution as a function of being exposed to high temperatures. The results showed that the oxidation resistance enhancement of coatings was based on the suppression of crystallization. The oxidation resistance increases with increasing thermal stability of amorphous structure. Amorphous coatings containing phases can react with oxygen will hinder the ingress of oxygen and prevent further oxidation by forming barrier layers.

Two new nanostructures can result in the hardness enhancement have been discovered: 1) Grains composed of sub nano-domains with same orientation separated by semicoherent monolayer boundaries observed from the $Zr_{41}B_{30}C_8N_{20}$ coating; 2) The columnar structures which grow on multilayers, consisting a bundle of small subdomains separated by thin boundaries observed from the Hf-Si-N coating deposited with 15% nitrogen in the gas mixture. Further studies of amorphous coatings with outstanding oxidation resistance indicated that the barrier layers consisting of grains dispersed in amorphous matrix can provide good protection for substrate against oxidation. A compromise between the oxidation resistance and hardness can be reached if nanocomposite coatings are composed of small amount of nanograins embedded in amorphous matrix.

Table of Contents

List of Figures

List of Tables

Chapter 1

INTRODCTION

1.1 Research Motivation

Human history is tied to the development and use of materials, and the searching for the right materials to fulfill human needs has never stopped. The development of technology is based on the use and application of a great variety of materials, not only natural materials, but also the physically mixing and chemically synthesized materials. With the continually development of technology, materials that can endure harsh environment have attracted significant attention. In all the materials that can be used in extreme environment, special attention has been applied to ceramic coatings based on the nitrides, borides and carbides of transition metals. This kind of ceramic coatings exhibit exceptional combination of outstanding oxidation, wear resistance, high hardness, high electrical conductivity and high thermal stability [1-4]. Pioneer work have shown that enhanced hardness can be achieved based on nanostructures formed under different conditions. The addition of one or more selected elements into the based material to form the amorphous Si_3N_4 phase surrounding nanoscale crystalline transition metal nitride grains is a very effective way to produce hard ceramic coatings, such as the addition of Si into the transition metal nitride T_mN (T_m= Ti, Zr, Hf, V, Nb, Ta, etc) [1]. Oxidation resistance at high temperatures can be achieved by nanocomposite coatings containing > 50 vol. % of silicon nitride with amorphous structure since the high thermal stability is ensured by the amorphous silicon nitride against crystallization [2-5].

As is well known that materials' physical properties are determined by the microstructure, getting a clear understanding of the microstructure and how the microstructure affects coatings' properties is very imperative. Previous reports regarding these coatings were focusing on the fabrication methods, composition and properties. However, very few detailed microstructure studies relevant to the coatings had been reported. With a good understanding of the effects of fabrication parameters on microstructure of coatings, preferred nanoscale multi-components, including certain nanocrystalline and amorphous phases can be controlled to produce novel coatings with tailored properties. This work is

very essential to develop new multifunctional coating materials which can be used as hard protective coatings with high oxidation resistance.

1.2 Research Objectives

Nanostructured multifunctional coatings have shown great potential in coating industry. However, at high temperature and oxidative environment, many hard coatings will deteriorate very quickly due to the thermal instability and chemical degradation. Therefore, producing coatings exhibiting enhanced mechanical properties and good thermal stability at high temperature is a great challenge.

The overall objective of the present research is to develop a better understanding of the effects of the elemental composition, phase composition and microstructure on the mechanical and thermal properties of the coatings which can be applied to design protective coatings with tailored properties for harsh environment applications in the future. The coatings used for mechanism studies were fabricated by magnetron sputtering which has been proved to be an effective technique to produce coatings with high purity and refined microstructure. The specific objectives of this research are as follows:

1. To explore the effects of elemental composition (especially Si and N) and microstructure on the enhanced hardness of the transition metal based nanocomposite coatings:
    a) To study the microstructural evolution and its effects on the properties of Zr-B-C-N coatings as a function of nitrogen content.
    b) To develop an understanding of the effects of silicon content on the microstructure and properties of Hf-B-Si-C coatings, especially the amount of silicon needed to reduce the residual stress while maintaining high hardness and good electrical conductivity.
    c) To study the microstructure change as a function of nitrogen content in Hf-Si-N coatings and the effects of microstructure on the mechanical property of the coatings.
2. To investigate the mechanisms of high oxidation resistance based on microstructure:
    a) Obtain a better understanding of the microstructure evolution in the Si-B-C-N coatings at high temperatures and explore the mechanism of extraordinary high oxidation resistance.

b) To understand the behavior of oxidation resistance of Hf-B-Si-C-N coating under high temperature (Produced by incorporating N into Hf-B-Si-C coatings in view of the important role of N in ultrahigh thermal stability of Si-B-C-N coatings) by studying its microstructure evolution as a function of its exposure to high temperatures.

3. Based on the knowledge gained from above systems, developing an overall understanding for designing new protective coating systems with desirable properties.

1.3 Dissertation Overview

This dissertation consists of seven chapters. The following part is an outline and brief summary of each chapter included in this dissertation.

Chapter 1, Introduction: This chapter introduces the research motivation and objectives. It provides a brief introduction to the current situation and the necessity of mechanism studies for designing new protective nanocomposite coatings in the future.

Chapter 2, Literature Review: This chapter gives background information about development of ceramic coatings. The manufacturing process, outstanding properties and growth mechanisms of nanocomposite coatings, which represent the new generation of materials, are discussed. Transition metal based nanocomposites which appear to be very promising for various applications are mentioned too.

Chapter 3, Nanocomposite Coatings Synthesis and Characterization: This chapter describes the detailed magnetron sputtering parameters used to fabricate different nanocomposite coatings. In addition, the characterization techniques used to analyze and study the coatings including X-ray diffraction (XRD), X-ray photoelectron spectroscopy (XPS), high resolution transmission electron microscopy (HRTEM), atomic force microscopy (AFM), nano-indentation and optical 3D surface profilometer are explained in detail.

Chapter 4. This chapter presents the results and discussion about the effects of elemental composition and microstructure on transition metal based nanocomposite coatings with enhanced hardness. This chapter is divided into three subchapters. Chapter 4.1 discusses the effects of nitrogen content on the microstructure evolution and hardness of Zr-B-C-N coatings. Chapter 4.2 discusses the effects of

silicon content on the microstructure evolution, development of residual stresses and oxidation resistance of Hf-B-Si-C coatings. Chapter 4.3 discusses the effects of the nitrogen content on the microstructure and enhanced hardness of Hf-Si-N coatings.

Chapter 5. This chapter presents the results of mechanism study and discussion of nanocomposite coatings exhibiting high oxidation resistance. Chapter 5.1 focuses on the microstructure analysis and discussion of the possible mechanism for the high temperature oxidation resistance of the Si-B-C-N coatings. Chapter 5.3 focuses on understanding the high temperature oxidation resistance behavior of the transition metal based Hf-B-Si-B-N coatings by studying the microstructure evolution as a function of being exposed to high temperatures.

Chapter 6. This chapter summarizes all coating systems that have been studied in this work. The knowledge gained from the microstructure study regarding both the mechanical and oxidation behavior of the nanocomposite coatings and trends revealed are summarized.

Chapter 7, Conclusions: Presents the major conclusions and the direction of future work.

Chapter 2

LITERATURE REVIEW

2.1 Development of Hard Ceramic Coatings

The ever increasing demands have led to the search for new materials with continuously improved properties. It has been found that after surface engineered, such as coated or surface treated, materials can perform very efficiently even under certain extreme working conditions. Coating can be explained as a cover that is applied to the surface of a substrate. The purpose of applying the coatings may be decorative, functional (such as improves the quality and durability of the product), or both. Ceramic coatings have continually developed for many years, and the most commonly used ceramic coatings are hard ceramic coatings prepared by physical vapor deposition (PVD) techniques.

The development of hard PVD ceramic coatings can be divided into four generations: 1) The first generation of hard PVD ceramic coatings are some metal nitride coatings such, as TiN, CrN and ZrN. These coatings can be used for decorative purposes due to their attractive appearance. For example, the TiN exhibits metallic gold color and the ZrN appears as light gold color. These coatings have been exploited commercially and widely used in industrial applications since the middle of the 1980's for cutting applications. A large improvement in the lifetime of a cutting tool (2 to 10 times compared with uncoated tools with the same cutting parameters) or a drilling tool (often more than 10 times) after being coated with hard material (e.g. TiN) has been reported [6]. However, oxidation resistance of these coatings is not sufficient enough for high operating temperature applications, such as high speed machining and high temperature wear protection. 2) For the second generation of hard PVD ceramic coatings, the properties of ceramic coatings are improved by adding other elements (Al, Cr, Y or C) into certain metal nitrides: such as TiAlN and TiCrN. Compared to pure TiN coatings, the TiAlN coatings exhibit improved hardness due to microstructure changes and solid solution hardening. The improved oxidation resistance of the TiAlN coatings is due to the formation of the stable aluminum oxide layer which prevents further oxidation and the ability of age hardening is due to the spinodal decomposition of TiAlN into TiN and cubic AlN. The TiAlN coatings may also exhibit high wear resistance and good

thermal stability [7-11]. 3) The hardness and oxidation resistance are further improved by the third generation of hard PVD ceramic coatings by the formation of multilayers and superlattices. Although single-layer coatings have already been used in many area of engineering, there are an increasing number of applications where the properties of single layer material are not sufficient. Multilayer structure is produced by alternating layers of two suitable materials which can lead to improvements in performance, such as enhanced hardness, improved resistance against wear, corrosion and oxidation, etc. [6, 12]. Multilayer coatings become superlattices when the period of alternating layers is several nanometers thick. Superlattice coatings of materials with similar structures tend to present columnar structure through the whole coating. The coating which combined TiN/NbN is one of the first examples of super lattice coatings [13, 14]. 4) Nanocomposite coatings are considered as a new generation of materials, and also be concerned in priority area of modern science and technology. Nanocomposite coatings are composed at least two separated phase with nanocrystalline and/or amorphous structure or their combination. The basic idea for designing nanocomposite coatings is based on the thermodynamically driven segregation in binary (ternary, quaternary) systems [15-17].

2.2 Nanocomposite Coatings

Nowadays, nanostructured multifunctional coatings have attracted considerable attention due to their outstanding properties compared to the traditional binary or ternary coatings, which also leads to a much wider potential applications in electronic devices, advanced biomaterials and especially with the application in extreme environments. Compared to the conventional materials that are composed of large grains (>100 nm), nanocomposite coatings compose tiny grains (<100 nm) surrounded by boundary regions. Due to the structure differences, the nanocomposite coatings exhibit enhanced, combination of desirable properties or even completely novel properties and functional capabilities [1, 4-5, 17-18]. The main feature of nanocomposite coatings is the enhanced hardness, and it is vitally important to improve the thermally stability of hard nanocomposite coatings and simultaneously ensure a good protection against oxidation from external atmosphere.

2.2.1 Enhanced Hardness of Nanocomposite Coatings

Hardness is defined as material's ability to resist permanent shape change when a compressive force is applied. One of the main features of the nanocomposite coatings is the enhanced hardness.

The nanocrystalline/amorphous composite materials can reach the hardness more than twice larger than its hard component. According to the hardness, the nanocomposite coatings can be divided into three groups: 1) Hard coatings (Hardness below 40 GPa); 2) Superhard coatings (Hardness from 40 GPa to 80 GPa); 3) Ultrahard coatings (Hardness larger than 80 GPa).

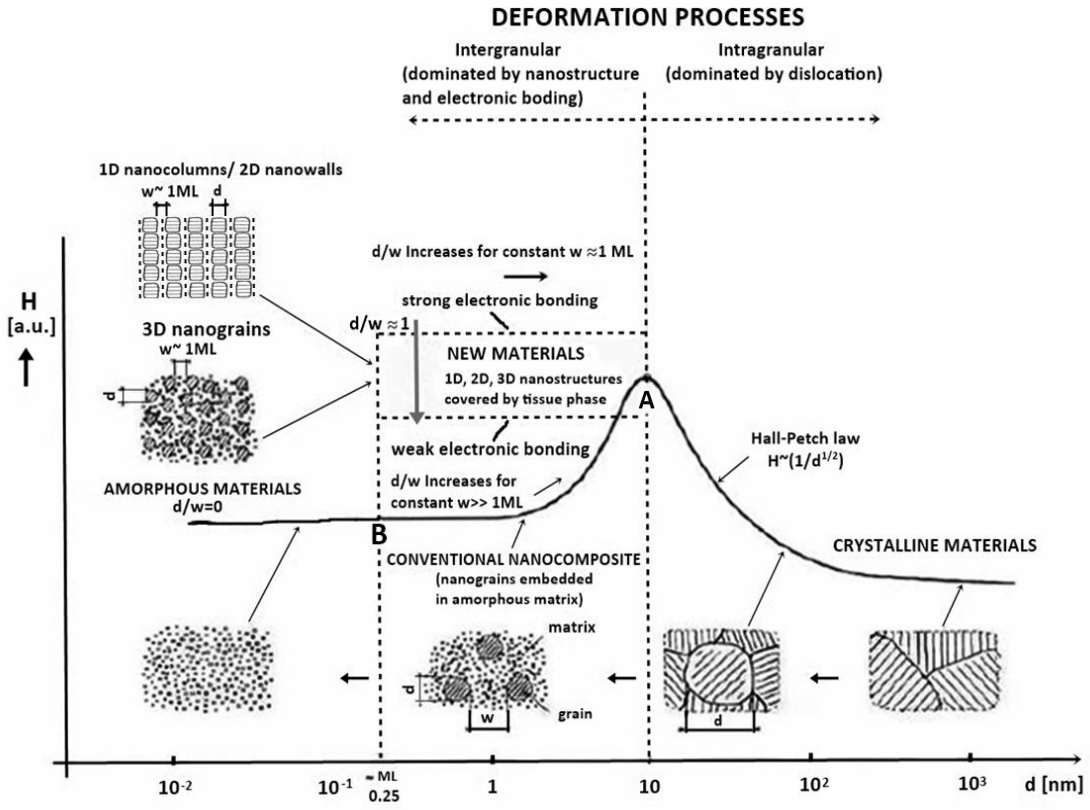

Fig. 2.1. Schematic illustration of evolution of coating hardness as a function of the grain size d Ref. [18].

There are some main factors that cause the hardness enhancement: 1) The plastic deformation due to dislocations; 2) the nanostructure of materials; 3) the cohesive forces acting between atoms; and 4) the compression macrostress σ [$\sigma=\sigma_{th}+\sigma_i$; σ_{th} is the thermal stress, σ_i is the intrinsic stress] generated in the coating during its growth. In real experiments, it is very difficult to select the best combination of deposition conditions because hardness of the coatings is usually affected by two or more factors. A high compressive macrostress σ can detach the coating from the substrate. Therefore, the macrostress σ is undesirable and it is very necessary to try to produce stress-free coatings by controlling the coating deposition process. It has been demonstrated that the macrostress σ can be reduced by a combination of the substrate heating (Ts/Tm), the bombardment of growing coatings by

ions and fast atoms (Ep), and also doping with different elements to the coatings. However, doping elements will not only reduce the macrostress, but also change the structure, phase composition and physical properties of the coating. When the compressive macrostress of coatings is low enough (<1 GPa), the hardness enhancement of the coatings will be mainly depend on the nanostructure.

Fig. 2.1 shows the hardness of coatings as a function of the grain size d. This figure shows that the hardness enhancement of the coatings strongly depends on the grain size, and there is a critical value of the grain size dc ≈10 nm at which the maximum hardness of the coating is achieved. According to the Hall- Petch law $H\sim(1/d^{1/2})$, the hardness of the coatings increases with the decrease of grain size for single phase materials until the grain size reduces to 10 nm. For the coatings composed of grains with the size larger than 10 nm, the deformation process is dominated by the dislocation induced plastic deformation. Dislocations will be nucleated inside grains during the deformation, however, dislocations will not be propagated at grain boundaries. Therefore, with the decreasing of grain size, there are more grain boundaries to stop dislocations. At the point when grain size is around 10 nm, the hardness of the coatings reaches maximum. If the grain size further decreases to less than 10 nm, dislocations are not generated since the grain size d is smaller than the length of dislocation. The deformation process transits from the intragranular processes to the intergranular processes which is dominated by the coating's nanostructure.

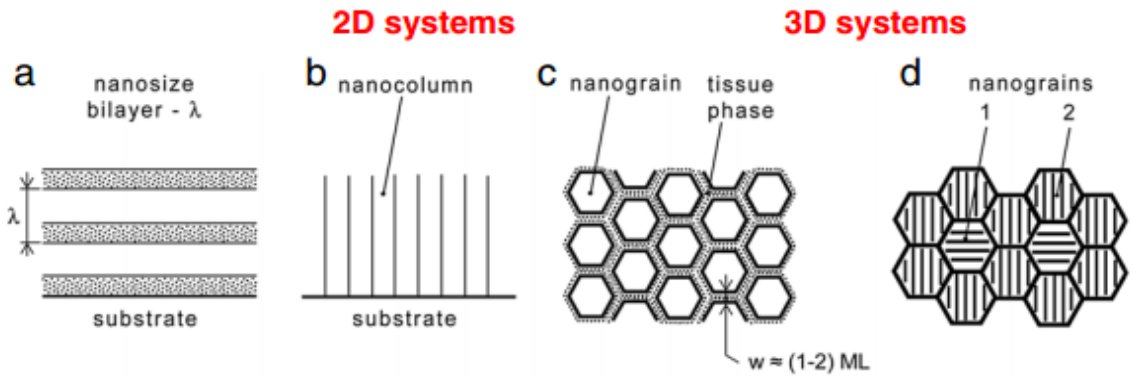

Fig. 2.2. Schematic illustration of different nanostructure of nanocomposite coating with enhanced hardness: (a) nanosize bilayers; (b) columnar nanostructure; (c) nanograins surrounded by tissue phase; and (d) mixture of nanograins Ref. [1, 4, 5].

There are three important factors that will influence the hardness based on the nanostructure: 1) The size and the shape of grains; 2) The amount of the phase surrounding the nanograins; 3) The chemical and electronic bonding between atoms of neighboring grains [4-5，17-18].

The relationship between the coatings' microstructure and hardness has been investigated by using the sputtered coatings with low compressive macrostress. Until now, at least four types of nanostructures that will result in the hardness enhancement of nanocomposite coatings are found, as shown in Fig. 2.2: (1) Nanocomposite composed of multi bilayers with the period size λ: The coatings with nanoscale multilayers are usually constituted by two transition metal nitrides with controlled individual layer thickness around several nanometers. This kind of coatings also can be named as "superlattice" coatings, and has been demonstrated to exhibit high hardness and high wear resistance [13-14, 19-21]. (2) Nanocomposites with nanocolumnar structures composed of the grains assembled in nanocolumns. Hard coatings with TiB_2 and TiN column structures have been reported [22, 23]; (3) Nanocomposites composed of globular structure with nanograins surrounded by very thin tissue phase (thickness is around 1 to 2 monolayer), such as coatings composed of crystalline TiN nanograins surrounded by an amorphous silicon-nitride matrix [24, 25]. Veprek suggests that the hardness enhancement of this kind of structure is due to the spinodal decomposition occurring during the phase separation in the nc-TiN/ Si_3N_4 system; (4) Nanocomposite with the compact globular structure comprising mixture of nanograins with different crystallographic orientations and different phases [26].

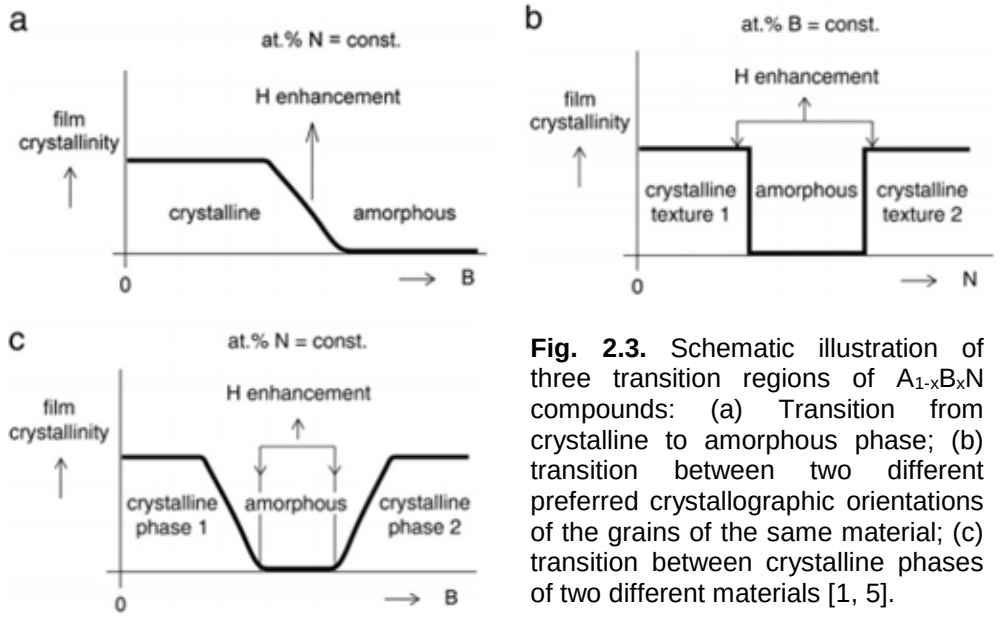

Fig. 2.3. Schematic illustration of three transition regions of $A_{1-x}B_xN$ compounds: (a) Transition from crystalline to amorphous phase; (b) transition between two different preferred crystallographic orientations of the grains of the same material; (c) transition between crystalline phases of two different materials [1, 5].

The coatings with enhanced hardness are always related to the existence of transitions from the crystalline to the amorphous regions. The nanocrystalline coatings of various nanostructures are

formed under different conditions in the transition regions where their structures are essentially changed. There are three transition regions of $A_{1-x}B_xN$ compounds: (1) The transition from a crystalline to amorphous phase; (2) the transition between two crystallographic orientations of the grains of the same material; (3) the transition between two crystalline phases of different materials.

As demonstrated in Fig. 2.3, each element can reach an optimal composition around the transition region at which the nanocrystalline /amorphous or nanocrystalline /nanocrystalline nanocomposite coatings can be formed. It has been proven that there are two very effective ways to produce nanocomposite coatings with enhanced hardness: (1) adding one or more selected elements into a base material. For example, the addition of Si in the nitride transition metals, such as Ti, Zr, Hf, V, Nb, Ta, and so on; (2) nanocrystallization from the amorphous phase [4-5, 18].

2.2.2 High-Temperature Oxidation Resistance of Nanocomposite Coatings

Oxidation resistance is one of the most attractive properties of hard nanocomposite coatings. A considerable effort has been made on the development of hard nanocomposite coatings with high oxidation resistance. These coatings are used in many applications, such as 1) cutting tools for high-speed cutting [27]; 2) turbine blades; 3) some special protection parts (wing, leading edges, nose-tip, etc.) of rockets, high speed aircrafts and space vehicles [28].

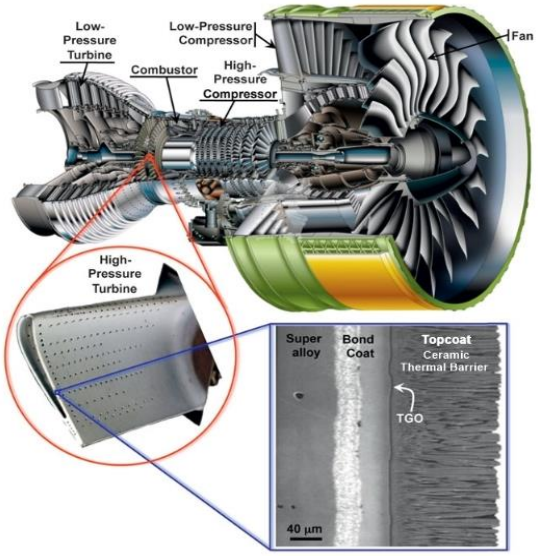

Fig. 2.4. Cutaway view of Engine Alliance GP7200 aircraft engine and photo of turbine blade with thermal-barrier coating [29].

Hypersonic vehicles are invented for high speed travel. During travel, leading edges of vehicles including the nose and tail are going to be exposed to intense and severe thermal environment above 2000 K. Most of the materials will degrades rapidly at this severe condition, therefore, the use of thermal barrier coating is crucial. Thermal barrier coatings are materials with very high melting temperatures, very low thermal conductivity and high specific heat capacity. They have the ability to perform under extreme thermal environments [29, 30]. Much higher quality demands is driving the research and development of thermal barrier coatings all over the world. The improvement of core power and efficiency of gas turbine engines is relying on high temperature thermal barrier coatings. Fig. 2.4 shows a cross-section view of Engine Alliance GP7200 aircraft engine with turbine blade with ceramic coating acts as the thermal barrier coatings. The substrate is the single crystal alloy, and the top layer is the nanocomposite coating.

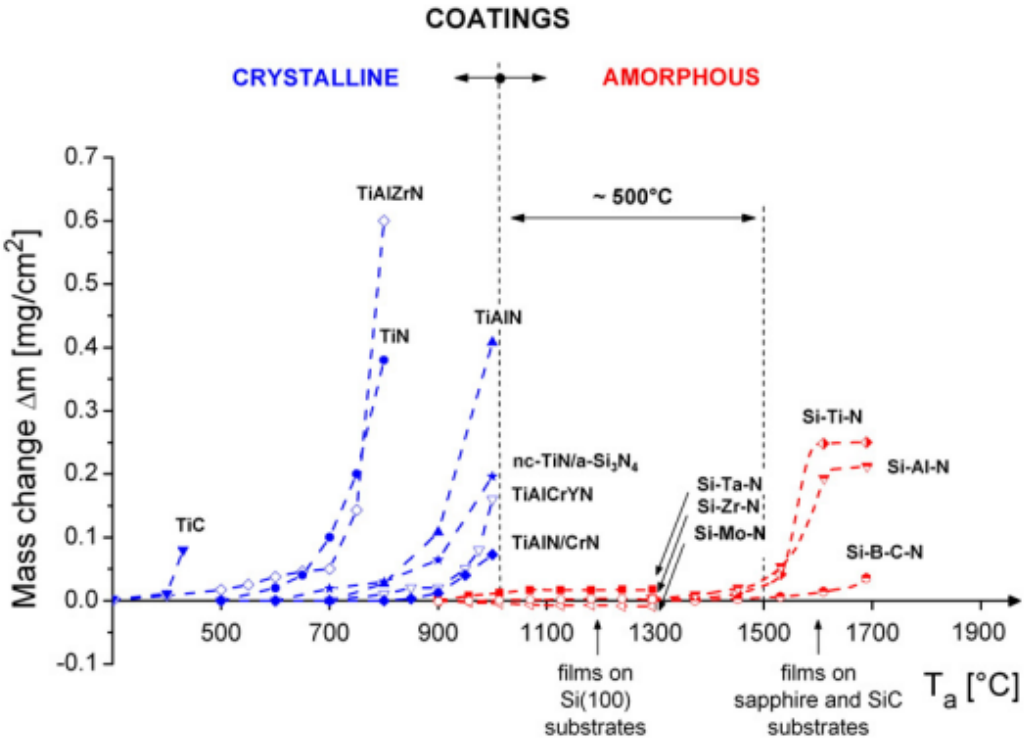

Fig. 2.5. Oxidation resistance of selected hard coatings, and characterized by the mass increase △m as a function of annealing temperature T. [1, 18, 31].

Fig. 2.5 shows a comparison of the high temperature oxidation resistance of many types of hard coatings. The temperature at which the mass change of the coatings sharply increases represents the maximum temperature that the coatings can withstand. This figure clearly shows that the oxidation

resistance of hard coatings not only depends on their elemental composition, but also strongly depends on their structure. The maximum oxidation resistant temperature of crystalline/ nanocrystalline coatings such as crystalline TiC, TiN and TiAlZrN coatings is below 1000 °C which is relatively low compared to the amorphous coatings.

The crystalline coatings are composed of many grains and therefore there is always a direct contact between the external atmosphere at the coating surface and the substrate surface through the grain boundaries. This phenomenon will obviously decrease the oxidation resistance of the bulk coating. On the contrary, the observed oxidation resistance of amorphous coatings is very high at temperatures exceeding 1000 °C. Without grains, there will be no direct contact between the external environments with the substrate through boundaries. Therefore, the reactions between the external atmosphere and the substrate are eliminated, as summarized in Fig. 2.6. The research of Si_3N_4/MeN_x has already shown that the amorphous Si_3N_4/MeN_x coatings can exhibit excellent thermal stability over 1000 °C if they have correctly designed structure [31, 32].

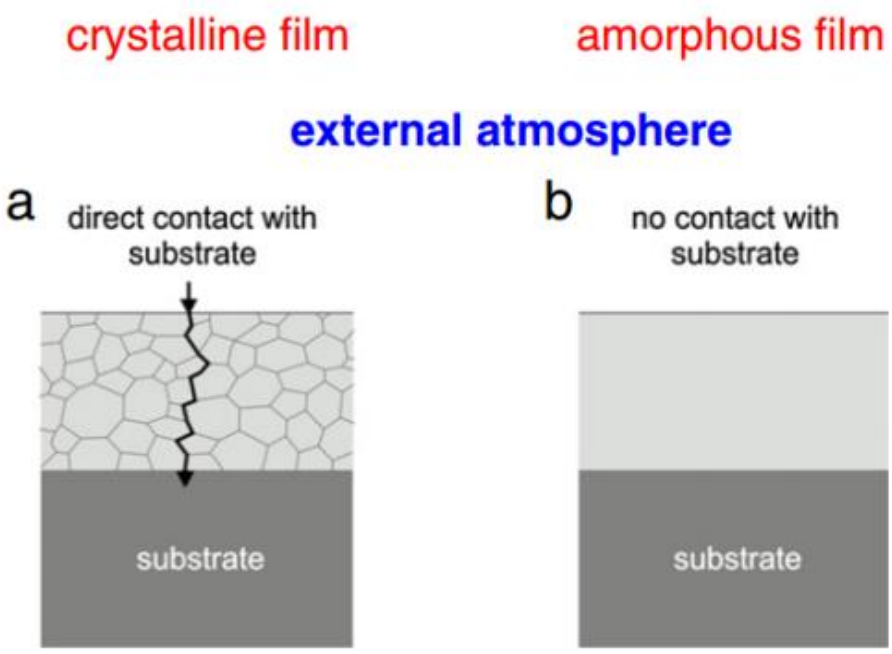

Fig. 2.6. Principle of the oxidation resistance enhancement of hard nanocomposite coatings (adapted from Ref. [32]).

It has been demonstrated that the high temperature oxidation of amorphous coatings is mainly determined by two factors: 1) Crystallization of the material; 2) Diffusion of elements from the substrate

to coating which will stimulate the crystallization of coating and reduce crystallization temperature. Therefore, oxidation resistance enhancement of the coating is based on the suppression of coating's crystallization. Based on current demanding for the materials with new applications, developing new hard coatings which will be thermal stable over the temperature 1000 °C is very necessary. The efficient way to produce hard coating with high temperature oxidation resistance is to produce coatings with proper designed amorphous structure, and try to avoid the diffusion of elements from the substrate into the coatings.

2.2.3 Transition Metal Based Nanocomposites

Transition metal based ceramics (carbides, borides, and nitrides) have been given special attention due to several unique properties, such as high melting point and hardness, high thermal and electrical conductivity, good chemical stability and exceptional oxidation resistance. This combination of unique properties makes these materials potential candidates for a variety of high temperature applications [33].

Titanium, zirconium and hafnium are from the same elemental group IV and very similar to each other, both structurally and chemically. So it is not surprising that the nitrides, borides and carbides of Ti, Zr and Hf may exhibit similar properties. Titanium has been extensively investigated and used in industry. At 1960's, TiC coatings (the earliest tribological coatings) have been developed [34]. During the middle of 1980's, TiN coatings, the so called first generation hard PVD ceramic coatings, have been exploited commercially [6]. Since then, TiC and TiN coatings have being used by the industry, however, significant efforts have been made to improve the performance of the coatings to fulfill the needs for various applications. TiCN coatings are developed to combine the good properties of TiN coatings and TiC coatings. Compared to TiN, TiCN coatings present a much higher hardness, good thermal properties and reduced coefficient of friction which leads to an improvement in overall utility as tribological coating [34]. Further improvements are made by incorporation of aluminum in TiN to form TiAlN coatings, which exhibit higher hardness, better oxidation resistance and thermal stability compared to TiN, TiC and TiCN. Therefore, TiAIN coatings are more suitable for machining and metal forming tools for wear resistance applications [8-11]. Other improvements have also been made to develop coatings for extreme environments application, such as transition metal nitrides, multilayer

composites and nanocomposites. Transition metal based nanocomposite coatings can be used to combine nanoscale multicomponents including amorphous or nanocrystalline phases selected from various transition metal based nitrides, borides, carbides and silicides. These coatings can achieve combined good properties which are difficult to obtain from conventional coatings. The Ti-B-C-N exhibits a combination of desirable properties through a nanostructure design of different ternary systems. The literatures show that the Ti-B-C-N coatings may compose of many phases, such as TiB_2, TiN, c-BN, h-BN, Ti_2N, TiC, and so on [35-39].

Compared to ceramics which are based on the nitrides and borides of titanium, investigation of ceramics which based on zirconium is very limited. This is due to the higher price of zirconium compared to titanium. However, it has been reported that ZrN coatings exhibit higher oxidation resistance, higher corrosion resistance and lower electrical resistivity compared to TiN coatings with comparable mechanical properties. Moreover, ZrN coatings can be used in some areas where the implementation of TiN has proven unsuccessful [40-45]. The ZrB_2-based nanocomposite is recognized earlier as relatively oxidation resistant non-oxide refractory compound due to low density and lower price. Compared to TiB_2 materials, ZrB_2 materials are reported to exhibit higher oxidation resistance. In addition, hard Zr-B-C and Zr-B-C-N coatings with high erosion and thermal shock resistance and good adhesion to substrates have already been reported [46, 47]. A few papers have reported Zr-B-C-N coatings prepared by chemical vapor deposition [46-48], and the first physical vapor deposition high-quality Zr-B-C-N coatings with low compressive stress, high electrical conductivity and high oxidation resistance are fabricated by Vlček's research group [49].

Over the past decades, HfB_2-based ceramics have attracted less attention probably due to their higher density and cost [50-52]. However, compared to TiB_2-based and ZrB_2-based materials, HfB_2-based materials exhibit higher density which enables maneuverability during re-entry and higher oxidation resistance which is more adaptable in high temperature oxidizing environment [50, 53]. Moreover, much higher thermal conductivity of HfB_2 compared to ZrB_2 is also reported [54]. High thermal conductivity offers a lot of advantages for high temperature applications, such as enhanced thermal radiation and improved thermal shock resistance. When combined with SiC, the ZrB_2-SiC and HfB_2-SiC composites are indeed excellent refractories exhibiting higher flexural strength, superior

oxidation resistance [50, 55-56]. When ZrB_2/HfB_2 is exposed to air at elevated temperatures, ZrO_2/HfO_2 and B_2O_3 are formed. SiO_2 formed from the SiC oxidation at temperatures above 1100 °C, and SiO_2 together with the B_2O_3 can form protective borosilicate glass providing more efficient oxidation protection than B_2O_3[57-65]. Recently, a series of hard multifunctional Hf-B-Si-C quaternary coatings were fabricated using pulsed magnetron sputtering by Vlček's research group [66]. However, after modeling the oxidation behavior of these composite materials under the simulated hypersonic vehicle application environments, the protective borosilicate glass starts to fail when operating temperature is above 1723 °C (the melting point of SiO_2) [67-69]. Studies have been conducted on incorporating some additional phases into the HfB_2-SiC composites to further improve the oxidation resistance [64 70-72]. Based on the knowledge gained from Si-B-C-N and Hf-B-Si-C systems, a hard and optically transparent amorphous Hf-B-Si-C-N coating is designed, showing high-temperature oxidation behavior in air up to 1700 °C [73].

2.3 Ultra-High Temperature Ceramics

Ultra-High Temperature Ceramics (UHTCs) belong to a family of refractory ceramics that displays a unique combination of properties. High melting temperature (usually higher than 2000 °C) is a major criterion, but not the only one.

Table 2.1. Ceramics with melting point above 3000 °C [74-75].

Materials	Crystal Structure	Melting Point (°C)	Density(g/mL)
TiB_2	Hexagonal	3225	4.52
ZrB_2	Hexagonal	3247	6.10
NbB_2	Hexagonal	3036	6.97
HfB_2	Hexagonal	3380	11.19
TaB_2	Hexagonal	3037	12.54
TiC	Cubic	3067	4.94
ZrC	Cubic	3445	6.56
NbC	Cubic	3610	7.82
HfC	Cubic	3928	12.76
TaC	Cubic	3997	14.50

Several properties should be considered in the materials selection process for real engineering applications: 1) High melting point; 2) Good oxidation behavior; 3) Strength, thermal conductivity, corrosion and shock resistance at elevated temperatures. Besides the extremely high melting point, UHTCs should exhibit high hardness, outstanding oxidation and corrosion resistance, good thermal shock resistance, good chemical and thermal stability at elevated temperatures.

Since early 1960s, the investigation of those kinds of coating materials has been intrigued due to the demand for a new class of materials with superior properties to be used in hypersonic flight vehicles that can withstand extreme environments. Current increasing interest in UHTCs is due to their exceptional combination of extremely high thermos-chemical and thermos-mechanical properties which is very important for potential applications at high temperatures and high oxidizing environments. The UHTCs can be used in high performance aerospace vehicles and systems including missiles and other defense applications, such as high altitude, space flight and high velocity air breathing engines. Typical applications for UHTCs are rocket nozzles, nose cones, thin leading edges of wings, stabilizers on hypersonic missiles and so on[76]. There are a lot of materials with high melting points, including SiC, refractory metals, a variety of oxides, nitrides, borides and carbides of transition metals and their composites. Only a few materials can be classified as UHTCs, and most of them are ceramics and composites containing borides, carbides, or nitrides of transition metals, such as titanium, zirconium, hafnium and tantalum [75, 77].

UHTCs usually need to be exposed to extremely high temperatures at which chemical reactions including oxidation reaction will occur rapidly. These reactions will limit the function of the materials much more than the thermos-mechanical performance. Coating is a commonly used approach to prevent oxidation. However, due to the extremely high operating temperature, the melting point of most oxide and silicate coatings is often exceeded. Under this condition, the development of nanocomposite materials containing phases that can form surface layers to hinder the ingress of oxygen and prevent further oxidation process is needed [76]. Current increasing interest in materials based on the nitrides and diborides of transition metals such as TiB_2, ZrB_2 and HfB_2-based composite is related to their exceptional combination of outstanding oxidation and wear resistance, high hardness, high electrical conductivity and high thermal stability which make it potential candidates for extreme environment

applications [78-81]. When combined with SiC, the TiB_2, ZrB_2, and HfB_2-based composites exhibit excellent refractories, high oxidation resistance and higher flexural strength [50, 55-56]. The excellent refractory behavior that makes UHTCs attractive also makes the materials difficult to manufacture. Usually very high temperature processing is required to densify the materials to fulfill the certain specific shape. Many manufacturing processes to fabricate UHTCs have been reported and typical processes include: 1) Pressureless sintering; 2) Hot pressing or hot isostatic pressing; 3) Spark plasma sintering; 4) Reaction sintering; 5) Plasma or vapor deposition techniques [82-87]. The manufacturing process of transition metal based nanocomposite will be introduced in Chapter 2.4.

2.4 Manufacturing Processes of Coatings

Fabrication of nanocomposite coatings with high utility properties including mechanical properties, thermal properties and other good properties simultaneously is one of the most concerning issues of surface engineering development. Chemical vapor deposition (CVD) and PVD are the most commonly used methods to fabricate nanocomposite coatings. CVD is one of the most promising methods to fabricate nanocomposite coatings since it shows some advantages, such as high deposition rate, uniform deposition for complicated geometries and also doesn't require very high vacuum. However, in large scale fabrication of thin coatings, CVD has some disadvantages which make it difficult to be implemented. The first concern of the CVD method is that most CVD precursors and byproducts are highly toxic. Second, CVD method needs to deposit at elevated temperatures which will result in the substrate distortion and mechanical instabilities in the deposited coatings [88, 89].

For the past decades, nanocomposite coatings produced by PVD technique have attracted research attention due to their combination of good properties, such as extremely high hardness, excellent high temperature oxidation resistance, good corrosion resistance, abrasion and erosion resistance [31-32, 90-94]. As summarized in Table 2.2, PVD can be divided into four main groups including thermal evaporation, arc vapor deposition, ion implantation and sputtering deposition. All forms of physical vapor deposition are following three basic steps in coating formation: 1) Materials to be deposited must be in a vapor phase; 2) The vapor species must be transported to the substrate; 3) Nucleation and growth of coating on the substrate. At present, significant effort has been devoted to the fabrication of nanocomposite coatings using magnetron sputtering while some other methods, such as

thermal evaporation, ion beam deposition and ion implantation, are also used by some researchers [89, 95].

Table 2.2. Typical preparation methods for nanocomposite coatings [89].

Group	Sub-group	Methods
Physical vapor deposition (PVD)	Thermal evaporation (TE)	Pulsed laser deposition (PLD)
		Electron beam deposition (EB-PVD)
	Sputter deposition	Magnetron sputtering
		Ion beam sputtering
	Arc vapor deposition	Vacuum arc deposition
		Filtered arc deposition
	Ion implantation	Ion beam deposition (IBD)
Chemical vapor deposition (CVD)		Plasma enhanced CVD (PECVD)
		Plasma assistant CVD (PACVD)
		Electron cyclotron resonance CVD (ECR-CVD)

The primary advantages of the magnetron sputtering includes low operation temperature requirement, high deposition rates, producing high- purity coatings, good adhesion of coatings and substrates, ease of sputtering any metal, alloy and compound, ease in adjusting experimental deposition parameters, easily scalable for the industrial applications and so on. Magnetron sputtering has been proved to be an alternative method to produce high quality coatings with refined microstructure, and there are numerous literature reporting the coatings fabricated with magnetron sputtering exhibit the specific properties of hard, low friction, wear-resistance, corrosion resistance, thermal resistance, optical properties, electrical properties and so on [96]. Magnetron sputtering is an ideal technique for the fabrication of multifunctional composite materials since it allows complex

chemical composition coatings to be achieved and enables the better control of coatings' structure growth which determines the high mechanical and thermal properties [94-98].

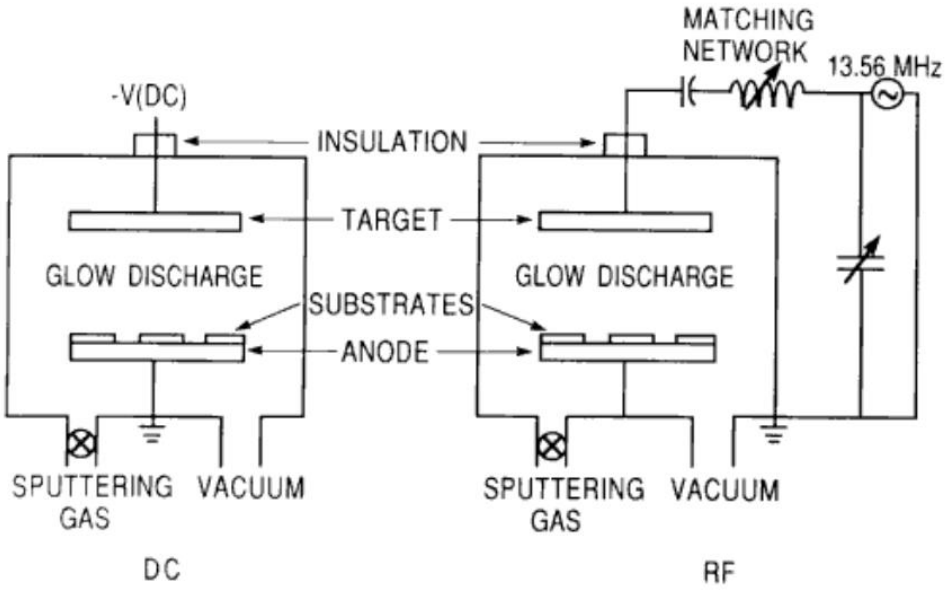

Fig. 2.7. Schematics of simplified sputtering systems: (a) DC, (b) RF [97].

Sputtering can be defined as the ejection of surface atoms or particles from a target material and subsequently deposit them onto a substrate by energetic ion bombardment. The target and substrate faces each other and act as electrodes. An inert gas (Usually Argon gas) with certain pressure is introduced into the system as the medium to initiate and also maintain a discharge. When an electric field is introduced or a DC voltage is applied on the electrodes, a discharge will be initiated and maintained between the two electrodes. Free electrons present in the sputtering chamber will be accelerated by the electric field and gain enough energy to ionize the Ar atoms eventually. Ionized Ar^+ will then hit the target material and ejection of target atoms will occur. The mixture of target atoms, ions, molecules, secondary electrons and photons will pass through the discharge towards to the substrate surface and grow as thin coating (coating). Usually, in order to improve the deposition rate and deposition quality, a magnetic field will be applied at the cathode to catch electrons to increase the chance of collision between electrons and Ar atom. Direct current (DC) sputtering and Radio frequency (RF) sputtering are two of the most common methods used in sputtering. The power used in DC sputtering is direct current and it keeps the target at a constant potential, while the power used in RF

sputtering is alternating current and it keeps the target potential varying. DC sputtering can only be used for the conductive materials sputtering, however, the RF sputtering can be used for all kinds of materials, especially good for the insulating materials. Figure 2.7 shows the simplified construction of sputtering systems with DC and RF power supply [95, 97].

According to specific needs of coatings, some deposition parameters will affect the composition and microstructure of the coating. Basic deposition parameters includes power applied to the target, power applied to the substrate, working pressure, flow rate of the sputtering gases, substrate temperature, substrate rotation and the distance between target and substrate.

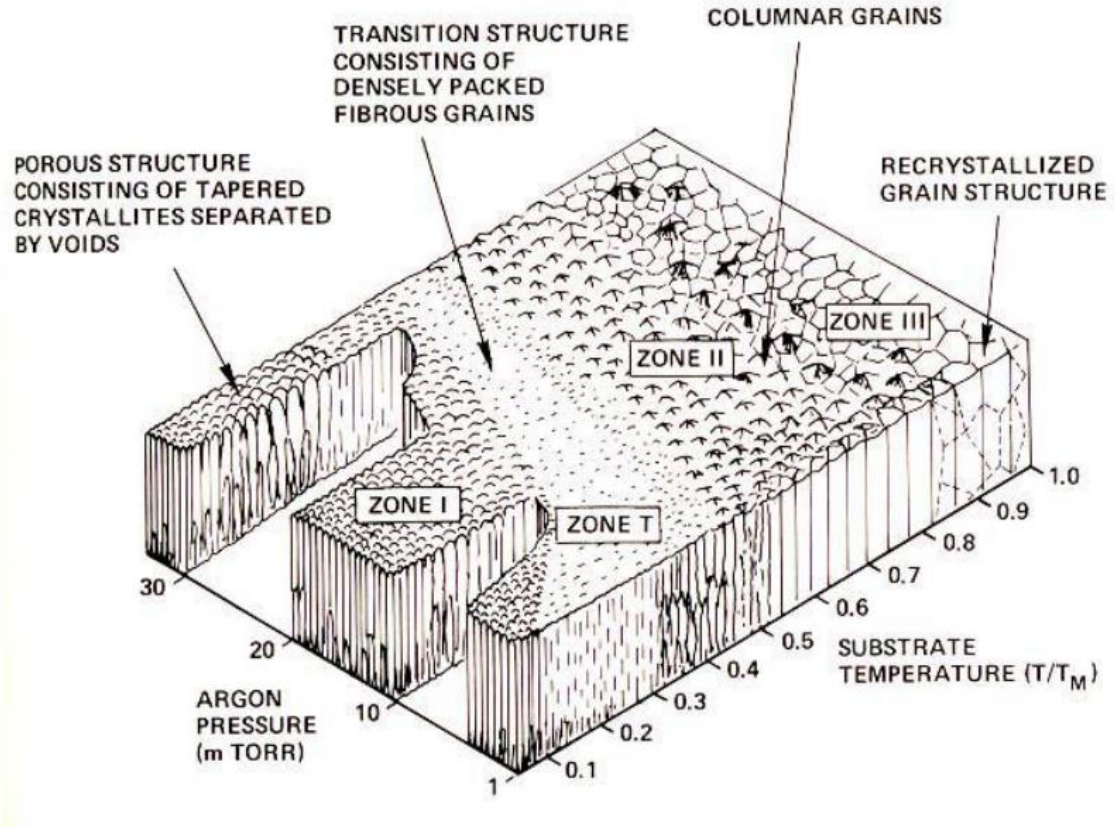

Fig. 2.8. Thornton's Model describing effect of deposition conditions on the coatings' structure and morphology [99-102].

As shown in Figure 2.8, a Model related to deposition conditions and coating morphology is built by Thornton. During the deposition, the coating growth steps can be summarized as the following process: (1) The condensation and nucleation of the atoms on the surface; (2) Nuclei growth; (3)

Interface formation; (4) Nucleation and reaction with previous deposited material and coating growth; (5) Post-deposition modification. These processes lead to the development of “Structure Zone Model”. The deposition of atoms includes three procedures: (1) Atomic shadowing during transport; (2) surface diffusion; (3) bulk diffusion. Since all of these procedures are affected by energy, the formation of coatings will be related to the ratio of substrate temperature to the melting temperature (T/Tm) and the energy of the deposited atoms during the deposition. Besides the substrate temperature, the working pressure during the deposition also has significant effects on the structure of the coatings. The structure zone model describes four growth zones as Zone 1, Zone T, Zone 2, and Zone 3. They are classified by different growth mechanisms controlled by the ratio of substrate temperature to the melting temperature (T/Tm) and the working pressure during the deposition [99-102].

It has been found that spinodal transformation plays a very important role in the formation of special nanostructure during the investigation in nanocomposite coatings. In the case of nanocomposite coating of nc-TiN/ a-Si_3N_4, spinodal decomposition determines the formation of nanocrystalline TiN structure surrounded by amorphous Si_3N_4 phase. Spinodal decomposition is affected by two conditions: 1) Temperature: appropriate temperature makes it possible to complete the segregation of nanocrystalline and amorphous phases via controlling the diffusion; 2) Pressure during deposition [103]. During the deposition, power applied to the target can be altered to control the deposition rate. Target may consist of single element or compounds, and several targets can be sputtered at the same time or sequentially to obtain an alloy coating or a coating with composition altered layers. The bias applied to the substrate will increase the chance of ions striking on the substrate during the deposition. Therefore, microstructure will be refined and surface roughness of coatings can be reduced [95].

Chapter 3

COATINGS SYNTHESIS AND CHARACTERIZATION

The fabrication conditions of each coating will be described in detail in this chapter. Representative coatings from different coating systems are selected to be further studied to get insight into the relationship between the microstructure-processing-properties. The microstructures of the coatings are characterized in details using x-ray diffraction, x-ray photoelectron spectroscopy, atomic force microscopy, nano-indentation, high-resolution transmission electron microscopy, as described in the following sections.

3.1 Coatings Synthesis

All the coatings used in this research were fabricated by magnetron sputtering which has been demonstrated as an ideal technique for the fabrication of multifunctional composite materials. This is a collaborative research to design and develop a new class of protective coatings. The Zr-B-C-N, Hf-B-Si-C, Si-B-C-N and Hf-B-Si-C-N coatings used for theoretical study were fabricated using a Balzers BAS 450 sputtering system (as shown in Fig. 3.1) by our research collaborator Professor Vlček's research group at the University of West Bohemia, Plzen, Czech Republic. The Hf-Si-N coatings were fabricated using home-made hybrid plasma assisted sputtering system in our Surface and Nano Engineering Lab at UT Arlington. The details of the deposition parameters for each coating system are introduced below.

3.1.1 Zr-B-C-N Coatings

The Zr-B-C-N coatings were fabricated in a Balzers BAS 450 PM sputtering system (Fig.3.1) with a planar rectangular unbalanced magnetron and a modified stationary circular substrate holder (80 mm in diameter). The Zr-B-C-N coatings were deposited on p-type Si (100) or glass substrates using pulsed magnetron co-sputtering of zirconium, boron and carbon from a single B_4C-Zr target (127 × 254 mm^2) in the nitrogen-argon gas mixtures. The single B_4C-Zr target was prepared using a B_4C plate (thickness 6 mm) overlapped by Zr stripes covering 45% of the target erosion area. A pulsed dc power supply (Rübig MP120) operating at an average target power of 500 W with a repetition frequency of pulses of 10 kHz and a fixed 85% duty cycle was used to drive the magnetron. During the deposition, the voltage pulse duration of 85 μs was used since it was sufficiently short to avoid the micro arcing at the

nonconductive layer found on the target during deposition. The base pressure was 3×10^{-3} Pa, and the total pressure of argon–nitrogen gas mixtures was 0.5 Pa with a constant gas flow rate about 25 sccm. The nitrogen fraction in the gas mixtures varied for different coating deposition. During the deposition, the substrate temperature was adjusted to 450 °C by an IR heater on the substrates at a floating potential in order to improve the crystallinity of the coatings. The target to substrate distance was 100 mm.

The composition of coatings was determined by the Rutherford backscattering spectrometry and elastic recoil detection methods using a Van de Graaff generator with a linear electrostatic accelerator. Four coatings deposited with different nitrogen percentage were selected to be studied in this work. The four coatings have the composition of $Zr_{61}B_{27}C_6N_3$, $Zr_{41}B_{30}C_8N_{20}$, $Zr_{26}B_{26}C_5N_{42}$ and $Zr_{24}B_{19}C_6N_{49}$ (without 1–2 at.% of H and <1 at.% of O and Ar) which were prepared with the N_2 fraction of 0%, 5%, 10% and 15% in an N_2/Ar gas mixture, respectively [49].

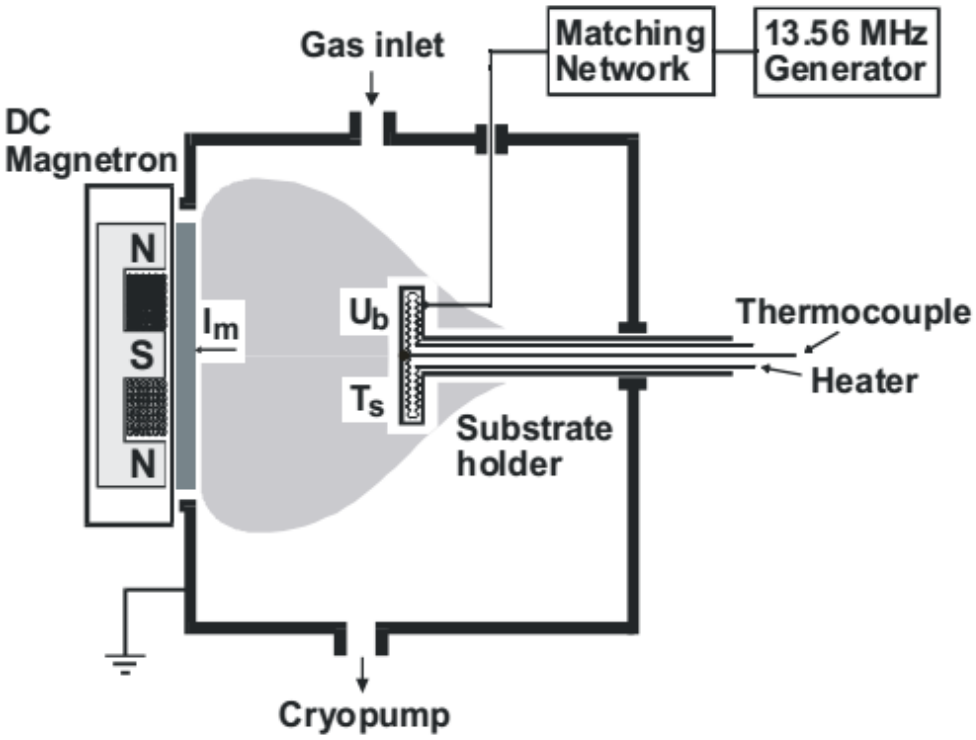

Fig. 3.1. Schematic illustration of the Balzers BAS 450PM sputtering system used for the depositions of Zr-B-C-N, Hf-B-Si-C, Si-B-C-N and Hf-B-Si-C-N coatings [104].

3.1.2 Hf-B-Si-C Coatings

The Hf–B–Si–C coatings were fabricated in a Balzers BAS 450 PM sputtering system (Fig.3.1) with a planar rectangular unbalanced magnetron and a stationary circular substrate holder (80 mm in diameter). The Hf-B-Si-C coatings were deposited on p-type Si (100) substrates using pulse magnetron co-sputtering of Hf, B, Si and C from a single target (127 × 254 mm^2) in pure Ar gas. The single B_4C-Hf-Si target was prepared using a B_4C plate overlapped by Hf stripes with a fixed 15% Hf fraction and Si stripes with a varying fraction in the target erosion area. The stripes were positioned on the target in order to achieve maximum homogeneity of the deposited coatings. A pulsed dc power supply (Rübig MP120) operating at an average target power of 500 W with a repetition frequency of pulses of 10 kHz and a fixed 85% duty cycle was used to drive the magnetron. During the deposition, the substrates were at a floating potential and adjusted to 450 °C by an infrared heater in order to reduce the possible generation of internal stresses and improve the crystallinity of the coatings. The base pressure was 3 × 10^{-3} Pa and the argon pressure was 0.5 Pa with a constant gas flow rate of approximately 25 sccm. The target to substrate distance was 100 mm.

The elemental composition of coatings was determined by the Rutherford backscattering spectrometry and elastic recoil detection methods using a Van de Graaff generator with a linear electrostatic accelerator. Four coatings deposited with different Si fraction in the target erosion area were selected to do the microstructure analysis. The four coatings have the composition of $Hf_{27}B_{57}C_8$, $Hf_{23}B_{55}Si_2C_{11}$, $Hf_{22}B_{54}Si_9C_9$ and $Hf_{21}B_{28}Si_{35}C_7$ which were prepared with the silicon fraction of 0%, 1%, 7.5% and 30% in the target erosion area, respectively [66].

3.1.3 Hf-Si-N Coatings

HfSiN coatings were fabricated using the home-made hybrid plasma assisted magnetron sputtering system in our SaNEL. Fig. 3.2 shows the schematic diagram of the magnetron system including power supplies, pumps, valves, heater, chiller, gas line and the power control system. In center, the stainless steel sputtering chamber has a cylindrical shape. The inner diameter of the sputtering chamber is 47 cm, and the height of the cylinder is 50 cm. Fig. 3.3 shows the actual PVD reactive magnetron sputtering system in SaNEL.

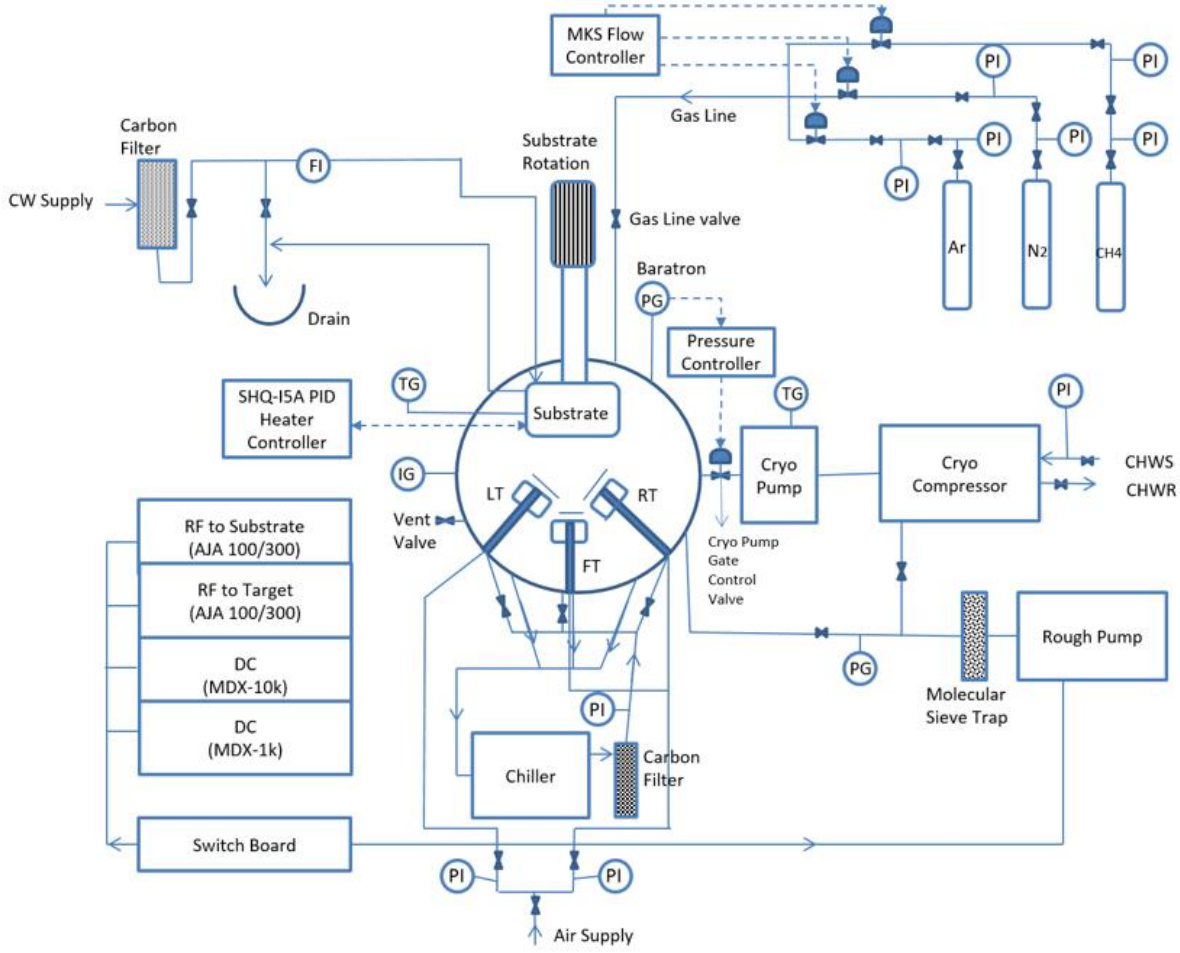

Fig. 3.2. Schematic diagram of the home-made hybrid plasma assisted sputtering system.

There are three magnetron guns (each with 2 inch diameter target) placed at the bottom of the chamber. The magnetron guns can support targets with thickness of 1/8 inch, 3/8 inch and ¼ inch". The front gun has a high magnetic source, and the left and right guns are equipped with low magnetic sources. All the magnetron guns are placed with 30° inclination to the center of the substrate holder center. Each magnetron gun can be easily connected to DC or RF power supply depends on the specific needs. The targets and substrate holder have a face to face arrangement serving as two electrodes, and the distance between targets and substrate is adjustable between 100 mm to 150 mm, as shown in Fig. 3.4.

Fig. 3.3. The hybrid plasma assisted magnetron sputtering system in the Surface and Nano Engineering Lab (SaNEL).

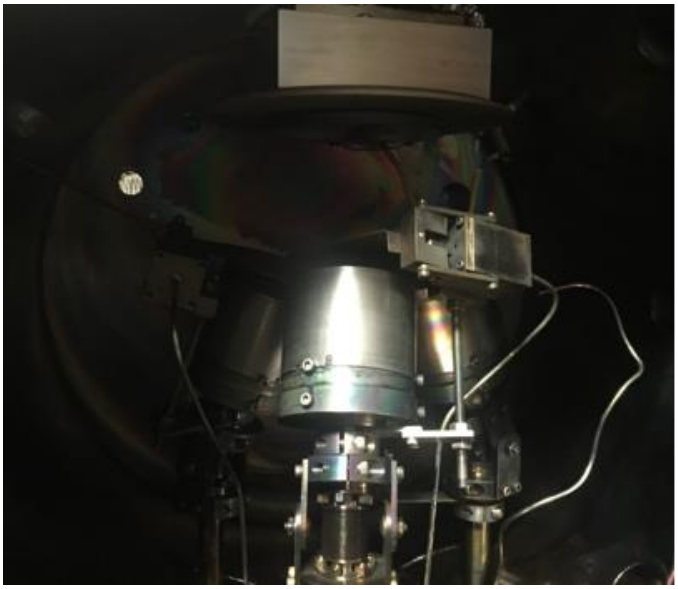

Fig. 3.4. Schematic diagram of the inner structure of the sputtering chamber.

The substrate holder is a 10 cm diameter-round shape plate where the substrate can be loaded. The substrate holder has the capability of heating and rotation. In order to acquire homogenous coating, the substrate holder should be rotated at certain speed during sputtering, especially when the heater is on. The substrate heating is controlled by an AJA SHQ-15 temperature controller and the maximum setting temperature is 900 °C.

The sputtering system should be pumped under 20 mTorr using the mechanical pump (Pressure of the lines between mechanical pump and cryo pump is measured by a pressure gauge). After pumping down the chamber with the mechanical pump to the pressure around 10 mTorr, a cryo pump from the backside and cryo compressor (cooled by a chilled water supply) are used to achieve high vacuum with a base pressure around 10^{-7} Torr (this pressure is measured using an ion gauge and displayed on a digital panel). Argon gas (99.99% purity) which acts as the medium to start and maintain plasma should be introduced to the chamber during the deposition. After reaching an appropriate base pressure, single gas Ar or a mixture of the Ar and reactive gasses such as N_2, O_2 and CH_4 can be flowed into the chamber. The precise pressure in the chamber during the deposition is controlled by an automatic gate valve which is connected with MKS 146C PID controller.

The HfSiN coatings were deposited on p-type Si (100) substrates using reactive magnetron sputtering co-sputtering of Hf and Si from two single targets in a mixed argon and nitrogen atmosphere. The Hf target (2" Dia x 0.250" Thick, purity of 99.9%) was placed on the front magnetron gun and the Si target (2" Dia x 0.250" Thick, purity of 99.999%) was placed on the left magnetron gun. 100 W DC power was applied to the Hf target and 60 W RF power was applied to the Si target. The chamber was pumped down to a base pressure (in the range of 10^{-7} Torr) before deposition and the working pressure was maintained at 5 mTorr during the deposition process with a total constant gas flow rate of 20 sccm. In order to obtain the desired nanocrystalline structure, 500 °C was selected as the deposition temperature based on the literature review and preliminary experiments. The substrate temperature was maintained at 500 °C during the deposition by a substrate heater which was carefully calibrated using an external thermocouple before depositions. Substrate rotation was applied during the deposition process to ensure the substrate was homogenously heated up by the heater and uniformly deposited from the two magnetron guns. In order to increase the density and reduce the surface roughness of the coating, a 100 V negative bias was applied on the substrate during the deposition. The distance between the substrate and the target was set to 100 mm to ensure sufficient plasma density at the substrate. Both the Hf and Si target, as well as the substrate were cleaned for 2 mins with the Ar plasma before starting the deposition to remove surface oxide and other impurities. The coatings

were deposited for 1 h. The coatings studied in this work were prepared with varied N_2 fraction range from 5% to 20% (2.5% in step) in the N_2/Ar gas mixture (purity of N_2, Ar > 99.999%).

3.1.4 Si-B-C-N Coatings

The Si-B-C-N coatings were fabricated in a Balzers BAS 450 PM sputtering system (Fig.3.1) with a planar rectangular unbalanced magnetron and a modified stationary circular substrate holder (125 mm in diameter). The Si-B-C-N coatings were deposited on 6H-SiC (0001) substrates using pulsed dc magnetron co-sputtering of silicon, boron and carbon from a single B_4C-Si target (127 × 254 mm^2) in a 50%Ar+ 50% N_2 gas mixtures. The single B_4C-Si target was prepared using a B_4C plate (thickness of 6 mm) overlapped by p-type Si stripes with fixed 25% B_4C + 75% Si fractions in the target erosion area. A pulsed dc power supply (Rübig MP120) operating at a repetition frequency of pulses of 10 kHz, an average target power of 500 W with a voltage pulse duration of 85um, a fixed 85% duty cycle was used to drive the magnetron. The voltage pulse duration of 85 μs is short enough to avoid the micro arcing at the nonconductive layer found on the target during deposition. The base pressure was 3×10^{-3} Pa. The total pressure of argon–nitrogen gas mixtures was 0.5 Pa with a constant gas flow rate about 25 sccm. During the deposition, substrate temperature was adjusted to 350 °C by an Ohmic heater on the substrates at a floating potential. The distance from target to substrate was 100 mm.

The as-deposited coating has a composition of $Si_{30–32}B_{10–12}C_{2–4}N_{49–51}$ and low contamination level (H + O + Ar < 4 at.%) as determined by Rutherford backscattering spectrometry and elastic recoil detection methods using a Van de Graaff generator with a linear electrostatic accelerator. The annealing of the coatings was carried out using a symmetrical high-resolution Setaram thermogravimetric system TAG 2400 in a helium atmosphere (flow rate of 1 liter/hour) from room temperature to 1400 °C (a limit for thermal stability of the SiC substrate in inert gases) and in pure air from room temperature to 1700 °C at the same flow rate (a limit imposed by thermogravimetric analysis in oxidative atmospheres). The samples were heated at a rate of 10 °C/min, and then, cooled down at 30 °C/min (with no dwell time at the highest temperature). Three coatings were chosen to be studied in this work: as-deposited coating, coating annealed to 1400 °C in He and coating annealed to 1700 °C in air [105, 106].

3.1.5 Hf-B-Si-C-N Coatings

The Hf-B-Si-C-N coating selected for the high- temperature oxidation resistance study was deposited utilizing a Balzers BAS 450PM sputtering system (Fig.3.1). The coating was deposited on polished and ultrasonically pre-cleaned single-crystalline Si (100) and SiC substrates using reactive magnetron so-sputtering of Hf, B, Si and C from a single B_4C-Hf-Si target in an Ar-N gas mixture. The single B_4C-Hf-Si target (127 × 254 mm^2) was prepared using a B_4C plate (6 mm thick) overlapped by p-type Si and Hf stripes with fixed 65% B_4C+ 15% Hf+20% Si fractions in the target erosion area. A pulsed dc power supply operating at a repetition frequency of 10 kHz with an average target power of 500 W and a fixed 85 us negative-voltage pulse length was used to drive the magnetron. During the reactive sputtering of the coatings, the voltage pulse duration of 85 us is short enough to avoid micro-arcing at the non-conductive layer formed on the B_4C-Hf-Si target. The base pressure before the deposition was 3×10^{-3} Pa. During the deposition, the total pressure of argon-nitrogen gas mixtures was 0.5 Pa with the nitrogen fraction in the mixture of 20%. The target to substrate distance was 100 nm and the substrate temperature was maintained at 450 °C. In order to reduce the ion-induced internal stresses in the coating to improve the application potential of the coatings, the substrates were held at a floating potential.

The as-deposited coating studied in this work has a composition of $Hf_7B_{23}Si_{17}C_4N_{45}$ and low contamination level (H + O + Ar < 4 at.%) as determined by Rutherford backscattering spectrometry (RBS) and elastic recoil detection methods (ERD) using a Van de Graaff generator with a linear electrostatic accelerator. The thickness of the coating was 1.4um as measured by profilometry (Dektak 8 Stylus Profiler, Veeco).

The annealing of the coatings was performed using a symmetrical high resolution Setaram TAG 2400 system in synthetic atmospheric air (flow rate of 1 liter/hour) from room temperature up to 1500 °C. The coatings were heated at a rate of 10 °C /min, and cooled down at a rate of 30 °C/min, respectively. Six coatings were studied in this work: the as –deposited $Hf_7B_{23}Si_{17}C_4N_{45}$ coating, the coatings on Si substrates annealed in air up to 1100 °C, 1200 °C, 1300 °C, and the coatings on SiC substrates up to 1400 °C, 1500 °C [73].

3.2 Characterization of Coatings

Complementary characterization techniques were carried out to systematically study the microstructure of the nanocomposite coatings. X-ray diffraction analysis provided the information of phase composition, crystallographic structure of the coatings. X-ray photoelectron spectroscopy investigated the elemental composition, chemical state and electronic state of the elements at the top surface of the coatings. Atomic force microscopy was used to observe the surface morphology in 3D dimensions and optical profilometer acquired the stress accumulated during the deposition. High resolution transmission electron microscopy was used to do detailed analysis regarding to the phases formation, structure exhibition which correspond and supply the x-ray diffraction analysis. The mechanical properties of the coatings can be measured using the Nano-indentation instrument. A better understanding on the microstructure and growth mechanism of the coating systems was acquired from these studies.

3.2.1 X-Ray Diffraction

The crystal structure and phase formation of the coatings were studied using Bruker D8 Advance X-ray diffractometer. A Cu Kα with the wavelength of 1.54 Å was used as the radiation source. The acceleration voltage and filament current were set at 40 kV and 40 mA, respectively. Different scan types, such as θ-2θ scan, rocking curve scan, and detector scan were performed to identify the crystal structure and phase.

The θ-2θ scan was the most commonly used scan type in this research. In this scan type, the sample stage remains stable, and tube and detector moves at the same time, the angle between tube and sample stage and the angle between detector and sample stage are always equal to θ. We did phase analysis, composition analysis and grain size analysis from this kind of scan. The Scherrer's equation was used to examine the crystalline size.

$$\tau = \frac{K\lambda}{\beta cos\theta}$$

In this formula, τ represents the grain size, K is a dimensionless shape factor(0.8-1.2), λ is the wavelength of the X-Ray, β represents the full width at half maximum (FWHM) of the peak, measured along the specific direction normal to the lattice plane given by the 2θ peak position, and θ is the Bragg angle of the diffraction peak.

The rocking curve measurements provide the information of the texture structure and crystalline quality of the coatings. During this scan, the 2θ angle is fixed while tube is moving around a θ position. In this way, the rocking curve scan can determine whether a coating with specific orientation is perfectly aligned.

In the detector scan, the angle of the tube (incident x-ray beam) is fixed at a small angle while the detector (diffracted x-ray beam) is moving. The conventional θ-2θ scans detect only the lattice planes aligned parallel to the coating surface. However, the detector scans can detect lattice planes in all directions.

3.2.2 X-ray Photoelectron Spectroscopy

XPS is also known as the electron spectroscopy for chemical analysis, and it is a quantitative spectroscopic technique which can measure elemental composition, chemical state and electronic state of the elements that exit in a material. The measurement can only take place at very top surface of the material, usually from the top 1 to 10 nm. In this research, the elemental composition and chemical state of elements near the coating surface were investigated by a Perkin-Elmer Phi 560 ESCA/SAM system equipped with non-monochromated Al K_a excitation source. The Al K_a excitation was characteristic unresolved $K_{a1,2}$ and has an energy of 1253.6 eV. Usually the coatings were pre-clean treated by using Ar^+ sputtering for 5 mins before the XPS survey collection. The spectra of the coatings were calibrated by the C 1s peak at a binding energy of 284.5 eV. Survey scans were usually conducted in the 0-1200 eV range in 0.5 eV step or in the 0-600 eV range in 0.2 eV steps.

3.2.3 Atomic Force Microscopy

AFM is a very high-resolution type of scanning probe microscopy with resolution on the order of fractions of a nanometer, which is more than 1000 times better than the optical microscopy. The AFM provides high resolution 3D dimensions measurement of the material surface by using cantilever with a sharp tip scans the sample surface. In this research, the surface roughness and morphology of the

coatings were measured by a Park systems' XE 70 AFM. Both contact mode and non-contact mode were used.

3.2.4 High-Resolution Transmission Electron Microscopy

A JEOL 1200 EX conventional TEM with a point resolution of 0.34 nm and operated at 120 KV was used to record selected area electron diffraction patterns (SAED) for larger angle sample tilt and low magnification bright field and dark field images record. The Hitachi H-9500 high resolution transmission electron microscopy with a point resolution of 0.18 nm and operated at high voltage 300 kV was used a lot to recording high magnification image, SAED and also EDS analysis. Gatan Digital Micrograph software installed with Hitachi H-9500 HRTEM was used for as-taken images process, such as d-spacing measurement, selected area electron diffraction pattern analysis, and Fast Fourier Transformation (FFT) image acquirement. Diamond Crystal and Molecular Structure Visualization was used for building the structure models. EMS simulation software was used for structure simulation to check the feasibility of the structure models by comparing the experimental TEM image and simulated TEM image. Some imaging analysis soft wares were also used to help analyzing TEM and HRTEM images.

There were two sample preparation techniques used in this research: Cross-section and plan-view, depending on the need of observation. The cross-section samples were prepared to observe the interface area between coating and substrate which is very easy to judge whether the coating is bonding well with the substrate. The crystal structure nucleation, growth, defects, size and preferred orientation were observed from the cross-section TEM. The plan-view TEM samples were prepared to get more two-dimensional structure such as the details information of the grain boundaries, domain structures and also the top view of some column structure which can provide more supply information for the cross-section TEM. The sample preparation procedure for TEM is very critical since the TEM samples need to be thin enough to allow the electron beam penetrate itself without too much attenuation. After the final preparation step, the sample should provide a thin and uniform area for observation under electron beam. Normally, the TEM sample preparation procedure including mechanical grinding, polishing, dimpling and Ar-ion milling. The detailed procedures for the preparation of cross-section and plan-view sample are described as the following:

a) Cross-section TEM Sample Preparation

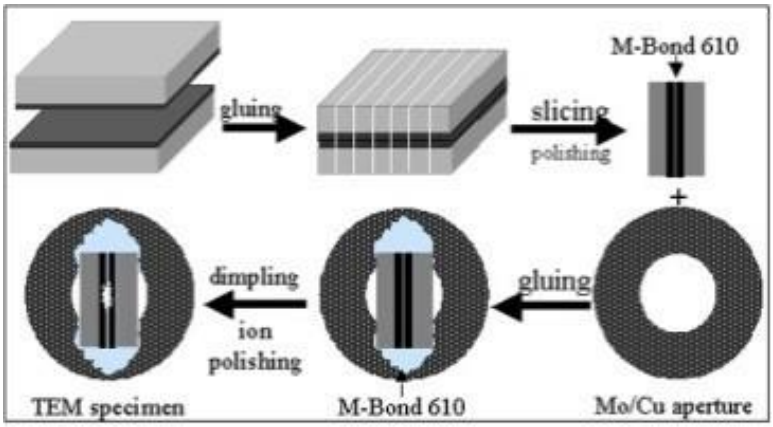

Fig. 3.5. Schematic illustration showing procedures for cross-section TEM sample preparation.

Fig. 3.5 is a schematic illustration of cross-section TEM sample preparation procedure. The steps for preparing a cross-section TEM sample are:

1. Cut two rectangular slices with the size of length~ 3 mm and width ~ 1 mm from the sample along a specific direction using diamond saw;

2. Clean the two sample slices under light microscope thoroughly in acetone and then ethanol;

3. Glue the two as-cut slides with the coating side face to face by using proper amount of M-bond 610 adhesive;

4. Precisely polishing one cross section side of the sample with Disc Grinder on diamond lapping coatings sequentially from the roughness 30 μm, 3 μm to 0.5 μm. Check under the light microscope, a very flat and mirror like fine surface should be reached;

5. Mount the grinded side on a 3 mm Cu/Mo ring with M-bond 610 adhesive, and then grind the second sample side using 1000 grit sand paper to gradually reduce the thickness of the sample to around 60um.

6. Place the sample on a dimple grinder and polish the sample using copper wheel with diamond paste first, and then use a fiber wheel with alumina paste to finer the surface. At the end of this step, the thickness of the sample thin area should be around 10-20 um;

7. Put sample into the Ar-ion mill Gatan model 691 precise ion polishing system (PIPS), use two Ar^+ ion guns to reduce the sample thickness from both top and bottom at the same time, until there is a hole cut to the coating interface. The edge area of the hole could be thin enough for TEM investigation.

b) Plan-view TEM Sample Preparation

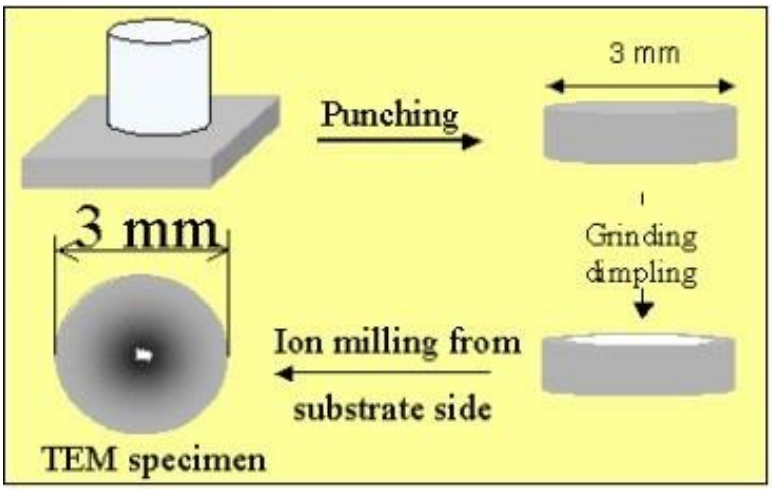

Fig. 3.6. Schematic illustration showing procedures for plan-view TEM sample preparation.

Fig. 3.6 is a schematic illustration of plan-view TEM sample preparation procedure. The steps for preparing a plan-view TEM sample are:

1. Cut a square size sample piece with the size about 3×3 mm using the diamond saw.

2. Clean the sample slice under light microscope thoroughly in acetone and then ethanol;

3. Glue the sample piece on a 3 mm diameter Cu/Mo ring with the coating side facing down using M-bond 610 adhesive.

4. Polish the backside of the sample using a 1000 grit sand paper until the sample thickness is around 60 um.

5. Place the sample on a dimple grinder and polish the sample using copper wheel with diamond paste first, and then use a fiber wheel with alumina paste to finer the surface. At the end of this step, the thickness of the sample thin area should be around 10 - 20 um;

6. Put sample into the Ar-ion mill Gatan model 691 precise ion polishing system (PIPS), use two Ar^+ ion guns to reduce the sample thickness from top, until there is a tiny hole in the center. The edge area of the hole could be thin enough for TEM investigation.

3.2.5 Optical Profilometry

A Veeco NT-9100 Optical Surface Profilometer with 5X objective was used to roughly measurement of coating thickness for the deposition rate calculation by measuring the step height between the coating and the substrate. The accurate thickness measurement was obtained in the cross-section HRTEM sample observation. The optical profilometer was also used to determine the residual stress present in coatings since the curvature of Si wafer (substrate) will be different between pre and after the coating deposition. The residual stress present in the coating can be calculated by the Stoney's Equation:

$$\sigma = \frac{E_s h_s^{\,2}}{6(1-\nu_s)h}\left(\frac{1}{R}-\frac{1}{R_0}\right)$$

E_s, h_s, and vs are the Young's modulus, thickness, and Poisson's Ratio of the Si wafer used as substrate, respectively, h is the thickness of the coating, and R and R_0 are the curvature measured from the Si wafer pre and after the coating deposition.

3.2.6 Nano-indentation

A Hysitron Ubi 1 Nanomechanical Test Instrument was used to investigate the mechanical properties including the hardness and Young's Modulus of coatings. Two kinds of tips including the three-sided pyramid Berkovich diamond tip and Cube Corner tip were used in the measurements depending on the thickness of the samples. The samples were mounted on the magnetic disks using crystal bond rather than the carbon tape to avoid the impacts from the soft carbon tape. In order to avoid the impacts from the substrate, the indentation depth should be performed less than 10% of the total depth of the coatings. Cube corner tip was used for coatings which were relative thin (below 400 nm) and Berkovich tip was used for the coatings were thick enough. The measurement of the Berkovich tip are not very accurate for the contact depth less than 60 nm (Coatings' thickness less than 600 nm), however, the cube corner tip can be very good for thinner sample measurement (Even coatings less

than 200 nm thick). There were two control modes used during the nano-indentation measurements: Load control and displacement control. Displacement control was selected for the sample with thickness less than 1 um, otherwise, the load control was selected. The area function of the tips was calibrated using a fused quartz standard sample. During the test, a loading and unloading time of 5 s, and an indenting time of 2 s were used. The average hardness and Young's modulus were determined by at least sixteen indents in a 4 ×4 array with point to point distance of 10 μm.

Chapter 4

MICROSTRUCTURE EFFECTS ON COATINGS' HARDNESS

4.1 Introduction

Nanostructured multicomponent coatings of transition metal-based carbonitrides have been found to have a much wider industry-specific applications due to their outstanding properties compared to the conventionally used binary or ternary hard coatings. These coatings can combine nanoscale multicomponents including amorphous or nanocrystalline phases selected from various transition metal based nitrides, borides, carbides and silicides [107]. As mentioned in Chapter 2, transition metal based borides (ZrB_2, HfB_2, TaB_2), carbides (TiC, ZrC, HfC), and nitrides (ZrN, HfN, TaN) and their composites are commonly referred as ultra-high temperature ceramics which are very important for potential applications at high temperatures and highly oxidizing environment.

Transition metal carbonitrides Ti-C-N and Zr-C-N with high hardness and improved wear performance are potential candidates of effective protective layers in biomedical applications [108-109]. The Ti-B-C-N coating system consist of numerous phases of TiB_2, TiN, c-BN, h-BN, Ti_2N and TiC and exhibit combine good properties of different binary and ternary systems by a nanostructure design [35-39]. ZrN coatings exhibit higher corrosion resistance [44], lower electrical resistivity [45] and comparable mechanical properties [110-112] compared to TiN coatings and ZrB_2 materials show a higher oxidation resistance than TiB_2 materials [59]. Therefore, the Zr-based carbonitride coatings have been developed [107, 113]. Multifunctional Zr-B-C and Zr-B-C-N coatings with high hardness, improved corrosion resistance, high erosion and thermal shock resistance, and good adhesion to substrates have also been reported [51, 52]. A few papers reported Zr-B-C-N coatings prepared by chemical vapor deposition [46-48], and the first physical vapor deposition high-quality Zr-B-C-N coatings with low compressive stress, high electrical conductivity and high hardness have been fabricated by Vlček's research group [49]. Compared to ZrB_2-based materials, HfB_2-based materials exhibit higher density which enables maneuverability during re-entry and higher oxidation resistance which more adaptable in high temperature oxidizing environment [50, 53]. HfB_2-based materials also exhibit higher thermal conductivity which offers a lot of advantages for high temperature applications, such as enhanced

thermal radiation and improved thermal shock resistance [54]. When combined with SiC, the ZrB_2-SiC and HfB_2-SiC composites are indeed excellent refractories exhibiting higher flexural strength, superior oxidation resistance [50, 55-56]. Various fabrication techniques have been investigated in order to optimize the processing procedures and performances of TiB_2-SiC, ZrB_2-SiC and HfB_2-SiC ceramics. Very recently, Hf-B-Si-C coatings with different silicon content which exhibit high hardness, high electrical conductivity and very smooth defect-free surfaces have been fabricated using magnetron sputtering. The silicon content has been found to have significant effect on the hardness and oxidation resistance of the Hf-B-Si-C coatings [66].

A profound knowledge regarding to the relationship between microstructure and hardness is necessary to produce coatings with desired mechanical properties. Transition metal based Zr-B-C-N, Hf-B-Si-C and Hf-Si-N coating systems with enhanced hardness were investigated.

4.2 Zr-B-C-N Coatings

Very few fabrication techniques have been used to prepare Zr-B-C-N materials from the literature. Early Zr-B-C-N coating was prepared using DC-pulse plasma-assisted chemical vapor deposition (PACVD) and thermal characteristics were studied [52, 53]. Recently, nanostructured multifunctional Zr-B-C-N coatings with good properties that can be used as hard protective coatings have been fabricated by pulsed reactive magnetron co-sputtering deposition [54]. These Zr-B-C-N coatings were deposited using a single B_4C-Zr target (15% or 45% Zr fraction in the target erosion area) in N_2-Ar gas mixture (Ranging from 0% to 50%). These are high-quality, defect-free coatings with low surface roughness and good attachment to the substrate. The hard $Zr_{41}B_{30}C_8N_{20}$ coatings with high electrical conductivity, low compressive stress, and high oxidation resistance in air up to 550 °C were achieved using the B_4C-Zr target with 45% Zr fraction in the target erosion area and in a 5% N_2+ 95% Ar gas mixture [54]. Tremendous change in hardness and oxidation resistance has been found in these coatings by slightly changing the N content in the coating. In this part, characterization work was carried out with the Zr-B-C-N coatings prepared using the B_4C-Zr target with 45% Zr fraction in the target erosion area. The coatings were deposited in four different nitrogen-argon gas mixture (0% N_2 + 100% Ar, 5% N_2 + 95% Ar, 10% N_2 + 90% Ar, 15% N_2 + 85% Ar). The microstructures of the Zr-B-C-N coatings were studied using both cross-section and plan-view high resolution transmission electron microscopy. The

motivation for this research was to explore the mechanism of Zr-B-C-N coatings' high hardness and get a better understanding about the effect of microstructure on the extraordinary properties of the coatings.

The Zr-B-C-N coatings were provided by our research collaboration Professor Vlcek's group at the University of West Bohemian, Plzen, Czech Republic. The fabrication details of the Zr-B-C-N coatings have been described in Chapter 3.1.1. Four representative Zr-B-C-N coatings deposited in different gas mixture were selected to study the effect of the N content on the microstructure and properties of the coatings. The following table shows the detailed information of coatings.

Table 4.2.1. Received Zr-B-C-N coatings composition and hardness.

Composition（at%）	Gas mixture composition	Hardness (GPa)
$Zr_{61}B_{27}C_6N_3$	0%N_2, 100%Ar	13.5
$Zr_{41}B_{30}C_8N_{20}$	5%N_2, 95%Ar	36.4
$Zr_{26}B_{26}C_6N_{42}$	10%N_2, 90%Ar	17.2
$Zr_{24}B_{19}C_6N_{49}$	15%N_2, 85%Ar	14.8

4.2.1 Nano-indentation Measurements

Nano-indentation tests were conducted to study the effect of the N content on the coatings' hardness and Young's modulus. A Berkovich diamond tip was used in the tests, and a fused quartz (hardness of 9.25 GPa, modulus of 69.6 GPa) was used as the standard sample to calibrate the apparatus. The indention curves were obtained by plotting the applied force vs the tip displacement. An indenting force of 4000 μN and a three-segment loading function were used for tests of all of the four Zr-B-C-N coatings. To minimize the experimental error, the average hardness and modulus values were determined by performing 4×4 array indents with 10 μm ×10 μm distance for each coating.

Fig. 4.2.1 (e) shows typical force vs. displacement curves for the four Zr-B-C-N coatings. The mean hardness for the $Zr_{61}B_{27}C_6N_3$, $Zr_{41}B_{30}C_8N_{20}$, $Zr_{26}B_{26}C_6N_{42}$ and $Zr_{24}B_{19}C_6N_{49}$ coatings was 13.5, 36.4, 17.2 and 14.8 GPa, respectively. The mean modulus for the $Zr_{61}B_{27}C_6N_3$, $Zr_{41}B_{30}C_8N_{20}$, $Zr_{26}B_{26}C_6N_{42}$ and $Zr_{24}B_{19}C_6N_{49}$ coatings was 175.1, 316.8, 197.3 and 167.1 GPa, respectively. Figs. 4.2.1(a) - (b) show the images of the indentations on the coatings $Zr_{61}B_{27}C_6N_3$, $Zr_{41}B_{30}C_8N_{20}$,

$Zr_{26}B_{26}C_6N_{42}$ and $Zr_{24}B_{19}C_6N_{49}$, respectively. With the decreasing of the coating hardness, the indentation area on the coating increases. The coating deposited with 5% N_2 exhibits a tremendous high hardness about 36.4 GPa and high Young's modulus 316.8 GPa compared to the other coatings. This result indicates that there must be a something special in the microstructure of the coating deposited with 5% N_2, more attentions were paid on the $Zr_{41}B_{30}C_8N_{20}$ coating which deposited with 5% N_2 in the following microstructure analysis.

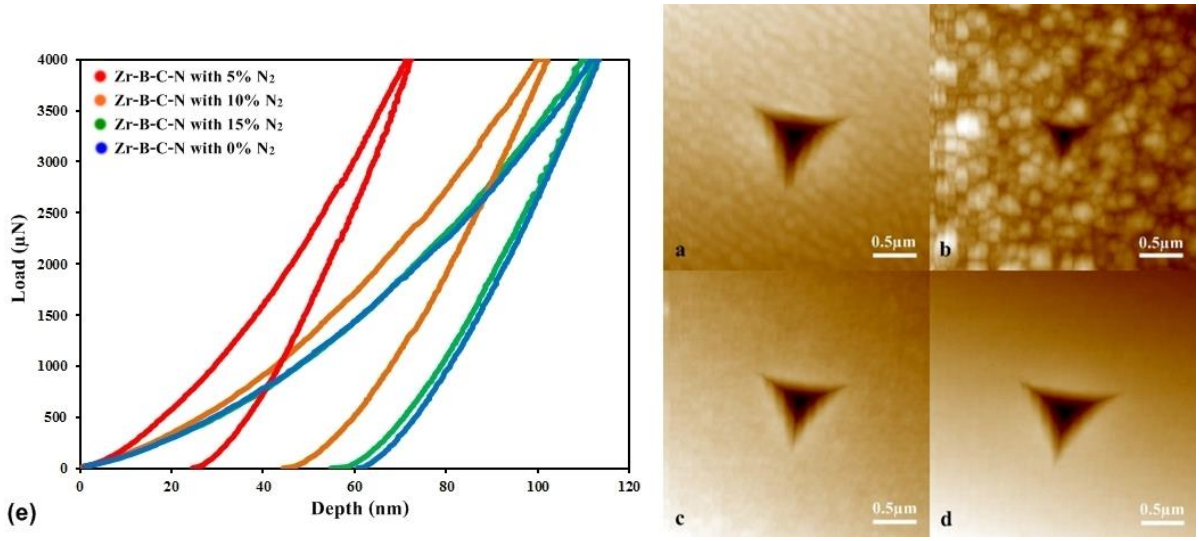

Fig. 4.2.1. (a)-(d) Images of indentation area on the coating of $Zr_{61}B_{27}C_6N_3$, $Zr_{41}B_{30}C_8N_{20}$, $Zr_{26}B_{26}C_5N_{42}$ and $Zr_{24}B_{19}C_6N_{49}$, respectively. (e) Force vs. displacement curves for the coatings.

4.2.2 XRD Studies

We have reexamined the crystal structure of the coatings using XRD before conducting systematic TEM studies. Fig. 4.2.2 shows XRD spectra of the $Zr_{61}B_{27}C_6N_3$, $Zr_{41}B_{30}C_8N_{20}$, $Zr_{26}B_{26}C_6N_{42}$ and $Zr_{24}B_{19}C_6N_{49}$ coatings deposited with the nitrogen fraction of 0%, 5%, 10% and 15% in the Ar/N_2 gas mixture, respectively. The XRD spectrum of the $Zr_{61}B_{27}C_6N_3$ coating shows only one broad intense peak at a 2θ-angle position of 33.30°, corresponding to the lattice spacing 2.69 Å. Since the measure lattice constant of this coating is around 4.66 Å which is between the lattice constant of ZrN (4.60 Å) and recently calculated lattice constant of metastable ZrB (4.90 Å) [83,84]. Taking into account the overall elemental composition of the coating (only small amount of N compared to the amount of Zr and B) and the characteristics of possible phase, this peak can be identified as a metastable B-rich Zr(B,C,N) solid solution. The presence of impurities (C, N) with smaller atom size gives a reasonable

explanation of the formation of such a metastable solid solution with relative lower lattice parameter compared with ZrB.

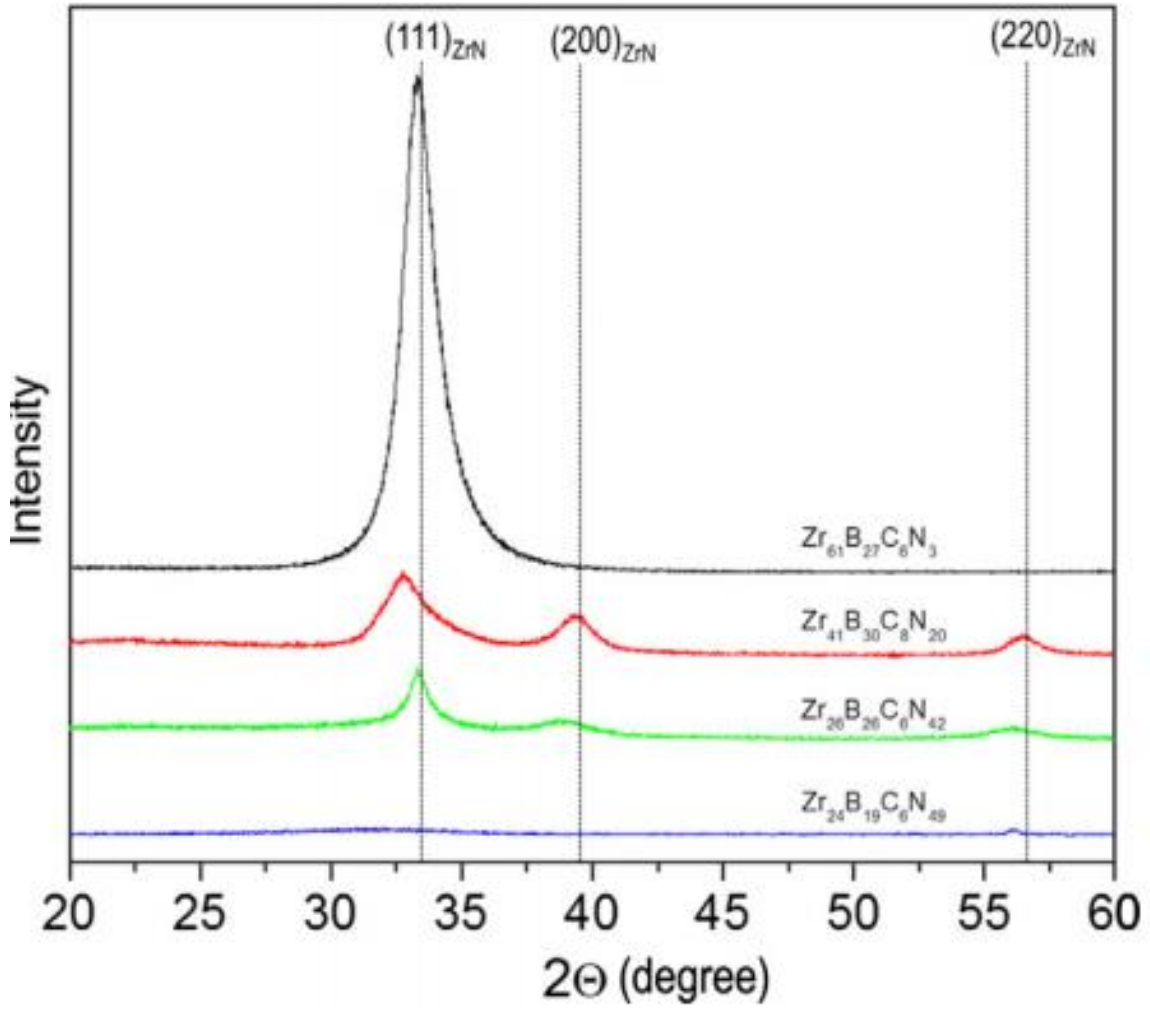

Fig. 4.2.2. XRD patterns of the coatings: $Zr_{61}B_{27}C_6N_3$, $Zr_{41}B_{30}C_8N_{20}$, $Zr_{26}B_{26}C_5N_{42}$ and $Zr_{24}B_{19}C_6N_{49}$.

The XRD spectrum of the $Zr_{41}B_{30}C_8N_{20}$ coating deposited with nitrogen fraction of 5% in the gas mixture exhibits peaks at 2θ position angle of 32.76°, 38.97° and 56.01°, corresponding to the lattice spacing of 2.73 Å, 2.31 Å and 1.64 Å, respectively. Considering the possible phases, ZrN (4.60 Å), ZrB (4.90 Å) and Zr(B,C,N) are fcc structures with similar lattice parameters, these three peaks can be considered as the (111), (200) and (220) diffractions. For the (200) and (220) diffraction peaks, the calculated lattice constant is 4.62 Å, which is 0.65% larger than the lattice constant of ZrN (4.60 Å). The slightly shift to the lower angle can be attributed to the Zr(B,C,N) phase with larger lattice parameter. It is noticed that the calculated lattice constant of (111) diffraction is 4.73 Å, which is 2.83% larger than

that of ZrN. Compared with the diffraction peak of (200) and (220), the shift of (111) diffraction is relative large, however, no orientation preference was found in this coating. This indicates that the large shift of (111) diffraction peak may be contributed to other microstructure characteristics.

The XRD spectrum of the $Zr_{26}B_{26}C_6N_{42}$ coating exhibits three peaks at 2θ angle position of 33.36°, 38.72° and 56.04°, corresponding to the lattice spacing of 2.68 Å, 2.32 Å and 1.64 Å, which can be identified as the (111), (200) and (220) diffractions. The calculated lattice constant of this coating is about 4.64 Å, which is 0.87% larger than that of ZrN. Based on the previous discussion, since both ZrN and Zr(B,C,N) are fcc phases with similar lattice parameters, it is very difficult to distinguish the exact phase in the coating. This coating may be composed of ZrN and Zr(B,C,N), and the larger lattice parameter cab be attributed to contributions from the Zr(B,C,N) phase.

In the XRD spectrum of the $Zr_{24}B_{19}C_6N_{49}$ coating, no sharp peaks were detected. This indicates the formation of the amorphous-like or very short-range ordering structure in this coating.

4.2.3 XPS Studies

Fig. 4.2.3(a) shows general XPS survey spectra of the $Zr_{61}B_{27}C_6N_3$, $Zr_{41}B_{30}C_8N_{20}$, $Zr_{26}B_{26}C_6N_{42}$ and $Zr_{24}B_{19}C_6N_{49}$ coatings deposited with the nitrogen fraction of 0%, 5%, 10% and 15% in the argon–nitrogen gas mixture, respectively. The spectra of the four coatings exhibit mainly the presence of Zr, B, N, C, O and Ar (Ar, O and some of the C are from contaminations). It clearly shows that the intensity of the N 1s peak increases with the increase of the nitrogen fraction in the argon-nitrogen mixture.

Fig. 4.2.3(b) shows the high-resolution XPS spectra of the N1s peak of the Zr-B-C-N coatings with different N content. The binding energy for the N 1s peak in the spectrum is 397.0 eV for the $Zr_{41}B_{30}C_8N_{20}$ coating and 396.5 eV for the $Zr_{26}B_{26}C_6N_{42}$ and $Zr_{24}B_{19}C_6N_{49}$ coatings. This indicates that the N1s peak shifts to lower binding energy position with the increase of the nitrogen fraction in the argon–nitrogen gas mixture. The element quantification analysis of the $Zr_{41}B_{30}C_8N_{20}$ coating shows that the Zr content in the coating of is enough to bond with all the nitrogen in the coating to form ZrN. This is consistent with the XRD analysis which shows the main present phase in the $Zr_{41}B_{30}C_8N_{20}$ coating is ZrN. This result is also in agreement with the literature report of binding energy for N1s peak is 397.1 eV [109], and the binding energy for N1s peak of the over-stoichiometric metastable phases ZrN_2 will shift to a lower binding energy also has been reported. For the $Zr_{26}B_{26}C_6N_{42}$ and $Zr_{24}B_{19}C_6N_{49}$ coatings

deposited in the gas mixture with nitrogen percentage of 10% and 15%, the content of N is much higher than Zr, therefore, the excess nitrogen may contribute to the formation of the over-stoichiometric zirconium nitride and amorphous structure in the coatings which results in the reduction in the binding energy of N 1s.

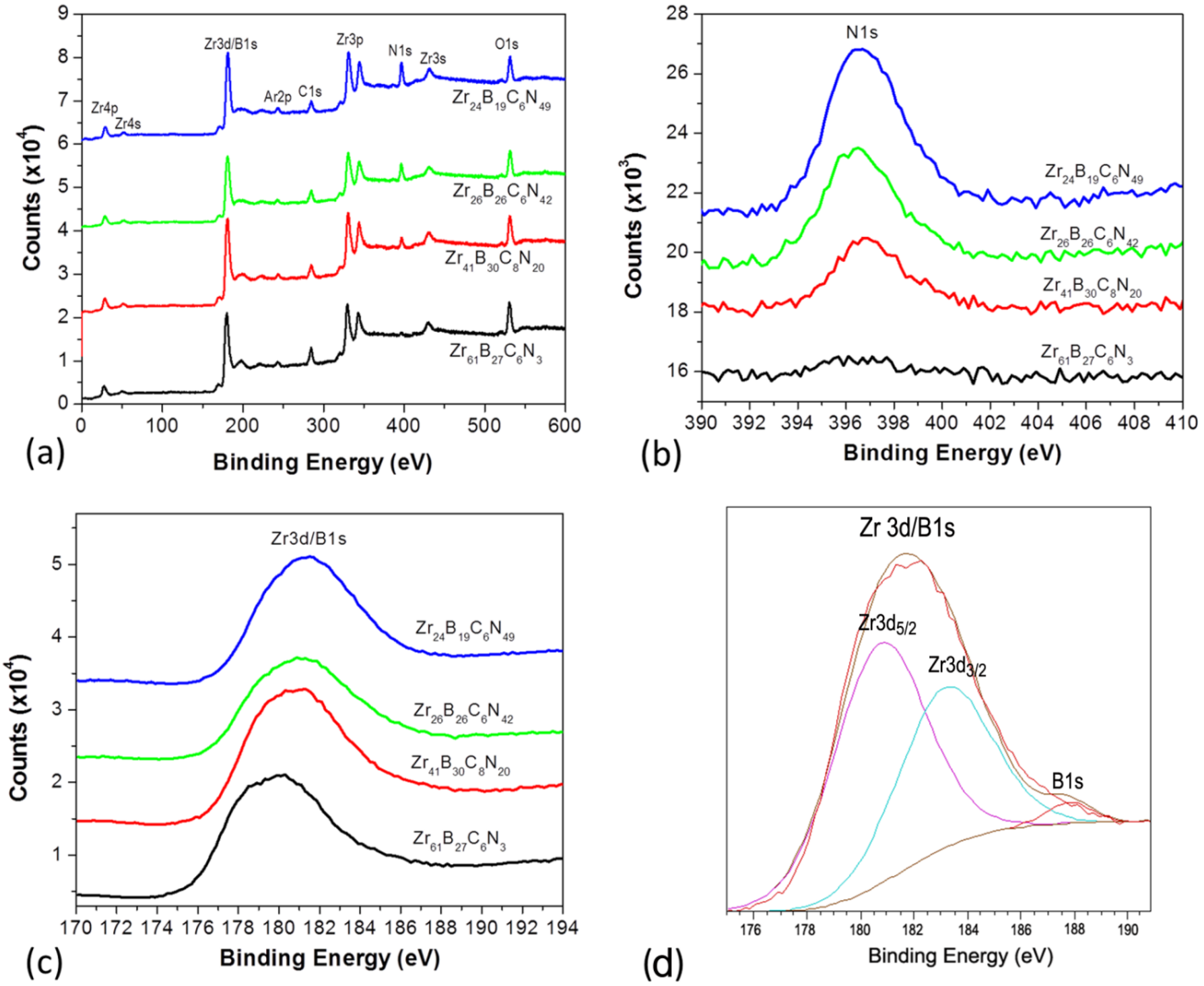

Fig. 4.2.3. (a) XPS survey spectra; (b) High resolution XPS spectra of peak N1s; (c) Zr 3d/B1s of the $Zr_{61}B_{27}C_6N_3$, $Zr_{41}B_{30}C_8N_{20}$, $Zr_{26}B_{26}C_6N_{42}$ and $Zr_{24}B_{19}C_6N_{49}$ coating; (d) Deconvolution of the Zr 3d/B1s peak of the $Zr_{41}B_{30}C_8N_{20}$ coating.

Fig. 4.2.3(c) shows the high-resolution XPS spectra of the peaks with the binding energy around 180 - 182 eV of the four coatings. Those peaks can be de-convoluted as the peaks Zr3d5/2 (binding energy from 179.0 to 181.0 eV), Zr3d3/2 (binding energy from 181.0 to 184.0 eV) and the B1s (binding energy is about 187.8 eV) which is overshadowed by the Zr peaks due to the lower resolution because

of the non-monochromated Al Kα excitation source. For example, Fig. 5.2.3(d) shows the deconvolution of such a peak for the $Zr_{41}B_{30}C_8N_{20}$ coating which can be de-convoluted into three components Zr3d5/2, Zr3d3/2 and B1s at a binding energy of 180.7 eV, 183.1 eV and 187.8 eV, respectively.

Fig. 4.2.3 (d) shows that the Zr3d5/2 and Zr3d3/2 components are dominated over the B1s component. It can be observed from Fig. 4.2.3(c) that the peak being convoluted from Zr3d5/2, Zr3d3/2 and B1s components shifts to the high binding energy with increasing the nitrogen fraction in the argon–nitrogen gas mixture. Therefore, it can be concluded that Zr 3d peak shift to the high binding energy with the increase of the nitrogen content in the coating, similar to the result observed in the ZrN layers deposited by reactive magnetron sputtering [109].

4.2.4 TEM Studies

The detail nanostructure of the coatings was further studied using both cross-section and plan-view TEM. Fig. 4.2.4 shows a typical cross-section TEM image of the $Zr_{61}B_{27}C_6N_3$ coating. It shows a very flat Zr-B-C-N coating surface, uniform coating and a sharp interface between coating and Si substrate. The cross-section TEM images of the other three coatings $Zr_{41}B_{30}C_8N_{20}$, $Zr_{26}B_{26}C_6N_{42}$ and $Zr_{24}B_{19}C_6N_{49}$ deposited with the nitrogen fraction of 5%, 10% and 15% in the Ar/N_2 gas mixture show similar characteristic to that in Fig. 4.2.4. The thickness of the coatings obtained from the measurement of the cross-section TEM images is about 3.4 μm, 3.9 μm, 4.0 μm and 2.0 μm for the $Zr_{61}B_{27}C_6N_3$, $Zr_{41}B_{30}C_8N_{20}$, $Zr_{26}B_{26}C_6N_{42}$ and $Zr_{24}B_{19}C_6N_{49}$ coating, respectively.

Fig. 4.2.5 is a bright-field TEM image of a cross-section $Zr_{61}B_{27}C_6N_3$ coating which presents a columnar structure (dark contrast) in the coating. The lateral size of the columnar structures varies from about 20 nm to 60 nm. The inserted SAED pattern in the Fig. 4.2.5 was taken from an interface area covering both the $Zr_{61}B_{27}C_6N_3$ coating and Si substrate. The very sharp spots are diffraction spots from the [110] zone of Si substrate, while the diffused arcs are diffractions from the $Zr_{61}B_{27}C_6N_3$ coating indicating the formation of nanocrystalline structure in the coating. The diffused arcs are located on diffraction rings with different lattice spacing. Specifically, diffraction arcs 1, 2, 3, 4 and 5 are located on the diffraction rings with a lattice spacing of 2.71 Å, 2.35 Å, 1.66 Å, 1.41 Å and 1.34 Å, respectively. These diffraction rings can be identified as the (111), (200), (220), (311) and (222) diffractions of a face-centered-cubic structure with a lattice constant of 4.70 Å. The inhomogeneous intensity distribution of

the diffused diffraction arcs indicates that the nanocrystalline in the coating are strongly orientation preferred. This result is consistent with the XRD analysis which identified the lattice constant of the metastable B rich Zr(B,C,N) solid solution is around 4.66 Å. The small difference of the lattice spacing measured from the XRD and the SAED may due to the strain was relaxed during the preparation of tiny TEM sample.

Fig. 4.2.4. Cross-section TEM image of the $Zr_{61}B_{27}C_6N_3$ coating.

Fig. 4.2.6(d) is an enlarged diffraction pattern taking from the interface of the $Zr_{61}B_{27}C_6N_3$ coating and substrate. Further studies show that the diffused arcs in first two inner diffraction rings are nearly located in the positions of the diffraction spots in two [110] zone diffraction patterns of the fcc Zr(B,C,N) overlap together. As illustrated in Fig. 4.2.6(a), it is a simulated diffraction pattern of fcc Zr(B,C,N) from $[1\bar{1}0]$ Zone axis. For the same $[1\bar{1}0]$ Zone axis, if we see the diffraction pattern from the botteom view, the indexed diffraction will be the same as the Fig. 4.2.6(b). Considering the diffraction in Fig. 4.2.6 (a) as diffraction A and the diffraction in Fig. 4.2.6 (b) as the diffraction B. If we overlap the transmission beam of these two diffraction patterns together, we will find that $(111)^A$ and $(111)^B$, $(\bar{1}\,\bar{1}\,\bar{1})^A$ and $(\bar{1}\,\bar{1}\,\bar{1})^B$ overlapped together. The $(11\,\bar{1})^A$ and $(002)^B$, $(00\bar{2})^A$ and $(\bar{1}\,\bar{1}\,1)^B$, $(\bar{1}\,\bar{1}\,1)^A$ and $(00\bar{2})^B$, $(002)^A$ and $(11\,\bar{1})^B$ are located very near to each other. That is why the real diffraction pattern shows very strong intensity at position of the $(111)^A$ / $(111)^B$, $(\bar{1}\,\bar{1}\,\bar{1})^A$ / $(\bar{1}\,\bar{1}\,\bar{1})^B$, and the others show diffused arcs. The

simulated overlapped two diffraction sets with the same zone axis in Fig. 4.2.6(c) gives a good explanation of the diffraction pattern in Fig. 4.2.6(d). The $(111)^A/(111)^B$ spots are in coincident with the (002) spot of the Si in the [110] zone diffraction pattern which indicates that the (111) planes of the face centered cubic Zr(B,C,N) crystalline are nearly parallel to the coating surface.

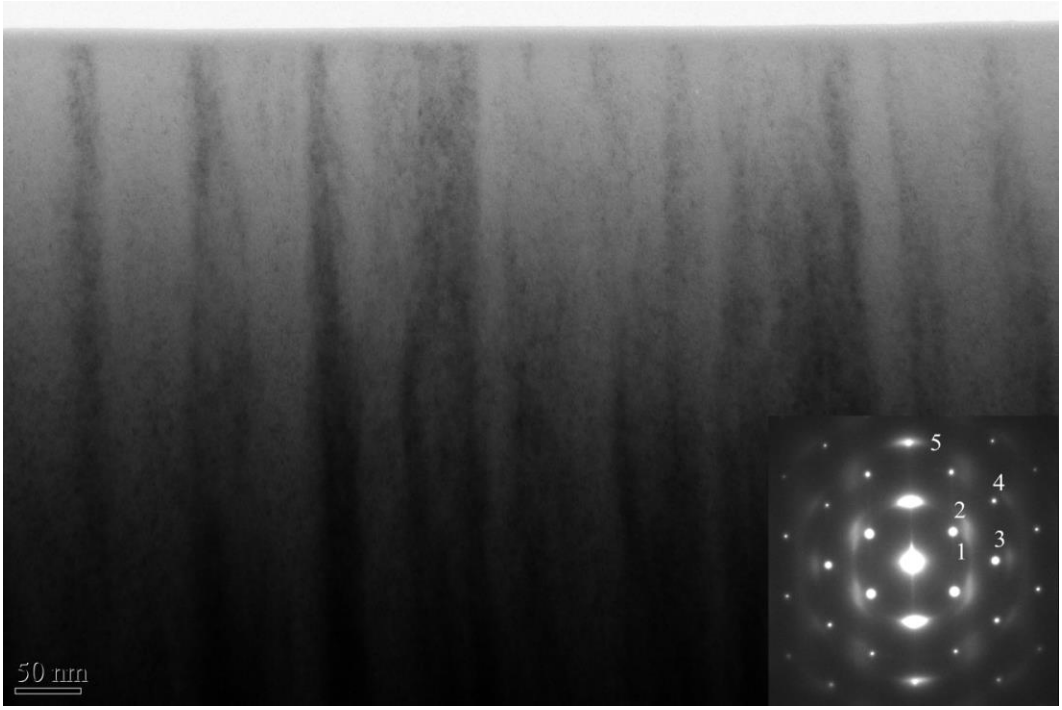

Fig. 4.2.5. Cross-section bright field TEM image of the $Zr_{61}B_{27}C_6N_3$ coating with inserted SAED taking from the interface of coating and substrate.

Figs. 4.2.7 (a) and (b) show bright field and dark field TEM image taking from the same sample area. The dark field image is obtained using the objective aperture selected the diffraction spot (111) from the electron diffraction which means the white contrast regions from the dark field image represent the crystalline exhibits (111) plane. The white contrast almost dominates the dark-field image indicating that the $Zr_{61}B_{27}C_6N_3$ coating exhibits strong (111) preferred orientation.

Fig. 4.2.8 is a bright-field plan-view TEM image showing the morphology and distribution of the cross-section view of the columnar structures in $Zr_{61}B_{27}C_6N_3$ coating. The dark regions correspond to the columnar structures (dark contrast) shown in 4.2.7(a) and the white regions correspond to the boundary structures between the columnar structures. The inserted SAED pattern taking from the coating exhibits a diffraction ring pattern. The diffraction ring 1, 2 and 3 has a lattice spacing of 2.71 Å, 1.66 Å and 1.41 Å, which can be identified as the (111), (220) and (311) diffraction of face centered

cubic Zr(B,C,N). The inhomogeneous intensity distribution of the diffraction rings further confirms the formation of a texture structure in the $Zr_{61}B_{27}C_6N_3$ coating.

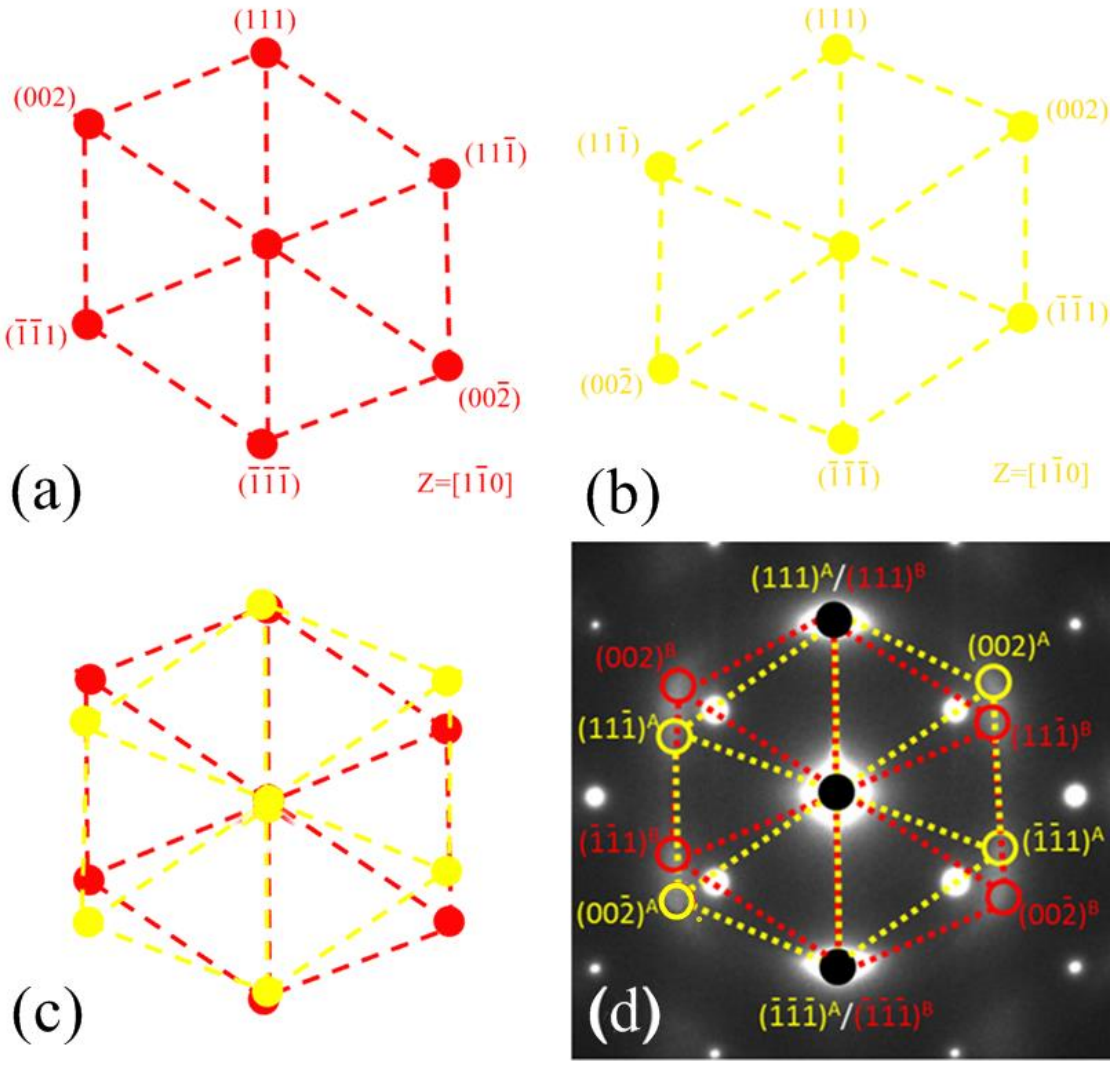

Fig. 4.2.6. Schematic illustration shows (a) inner diffraction pattern from $[1\bar{1}0]$ Zone see from the top; (2) inner diffraction pattern from $[1\bar{1}0]$ Zone see from the bottom; (c) simulation of two diffraction patterns from the same zone axis overlap together; (d) The enlarged diffraction pattern taking from the interface of coating and substrate which in good consistence with (c).

Fig. 4.2.9 (a) is a HRTEM image taken from a dark region in Fig. 4.2.8 shows many lattice fringes, and most of them are almost oriented in the same orientation. Those aligned lattice fringes exhibit the d spacing of 2.71 Å, and can be identified as (111) plane of Zr(B,C,N). Fig. 4.2.9(b) is a HRTEM image taken from a bright region in Fig. 4.2.8 exhibits mainly an amorphous-like structure**.** Very small

nanocrystalline with a small size of several nanometers can be occasionally observed. The excess Zr in the coating probably bond together with C and N to form the amorphous structure.

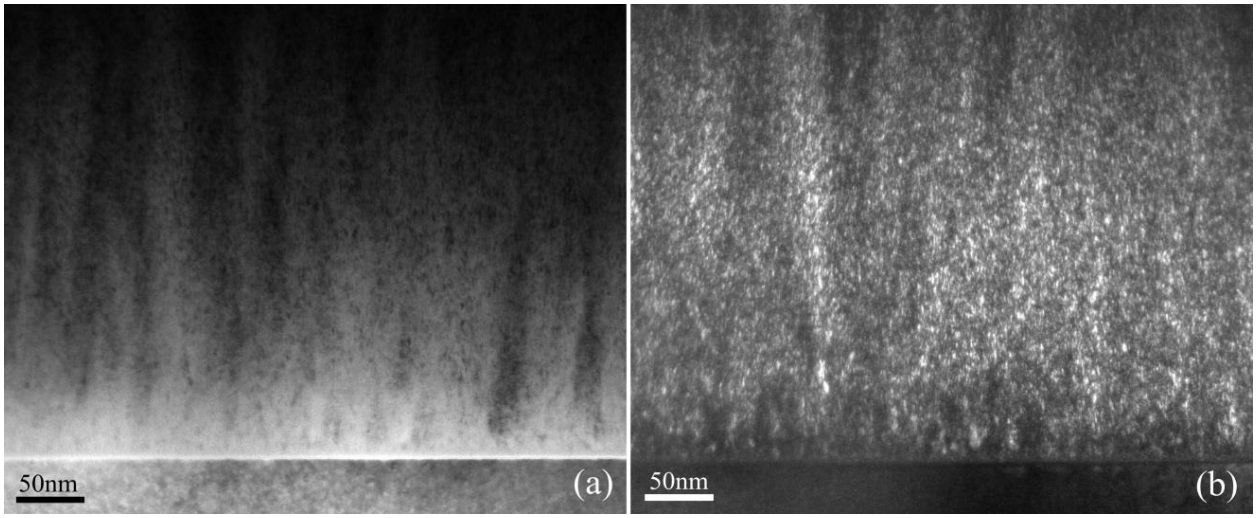

Fig. 4.2.7. (a) Cross-section bright field TEM image (b) dark filed TEM image of the $Zr_{61}B_{27}C_6N_3$ coating taking from the same area.

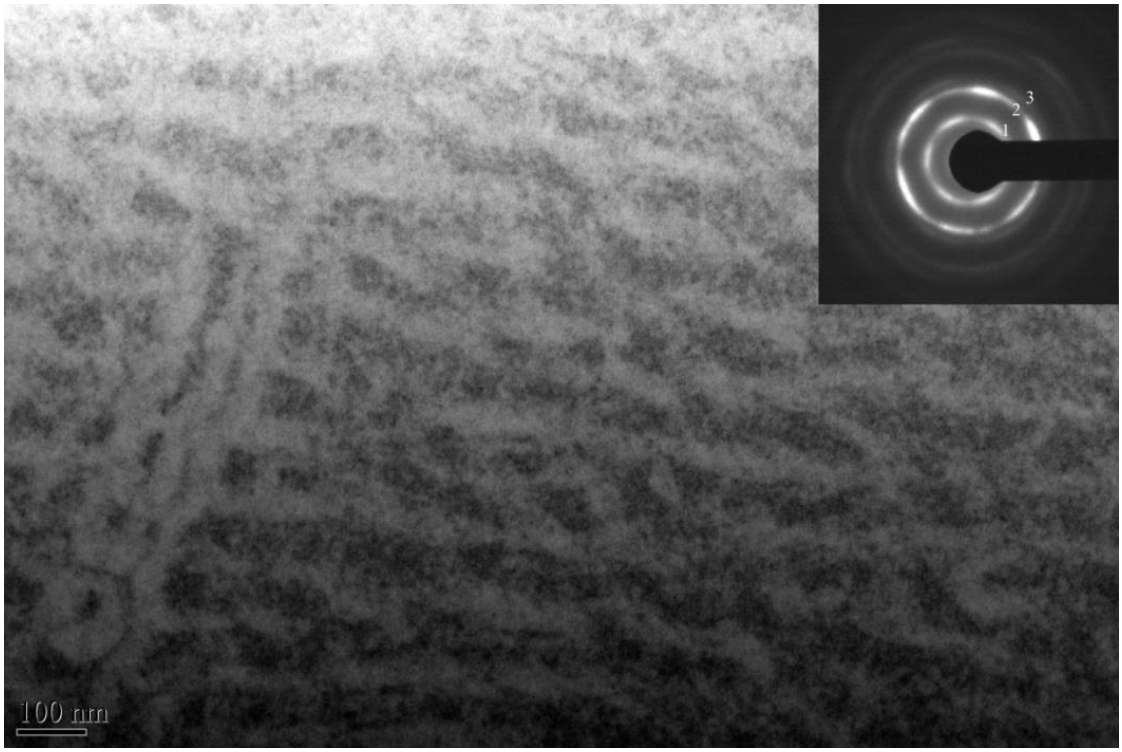

Fig. 4.2.8. Plan-view bright field TEM image of the $Zr_{61}B_{27}C_6N_3$ coating with inserted SAED taking from the coating.

Fig. 4.2.9(c) shows a HRTEM image of the coating taken from a cross-section TEM foil. It can be clearly seen that the (111) lattice fringes of fcc Zr(B,C,N) are nearly parallel to the coating surface. This

result indicates that the nano columnar structures are basically composed of nanocrystalline with their (111) planes being well-aligned to the coating growth direction, while the boundaries between the columnar structures more likely possess an amorphous structure. Fig. 4.2.9(d) is a HRTEM image of the interface between the $Zr_{61}B_{27}C_6N_3$ coating and Si substrate. An atomically sharp interface is observed indicating the coating is very well attached to the Si substrate.

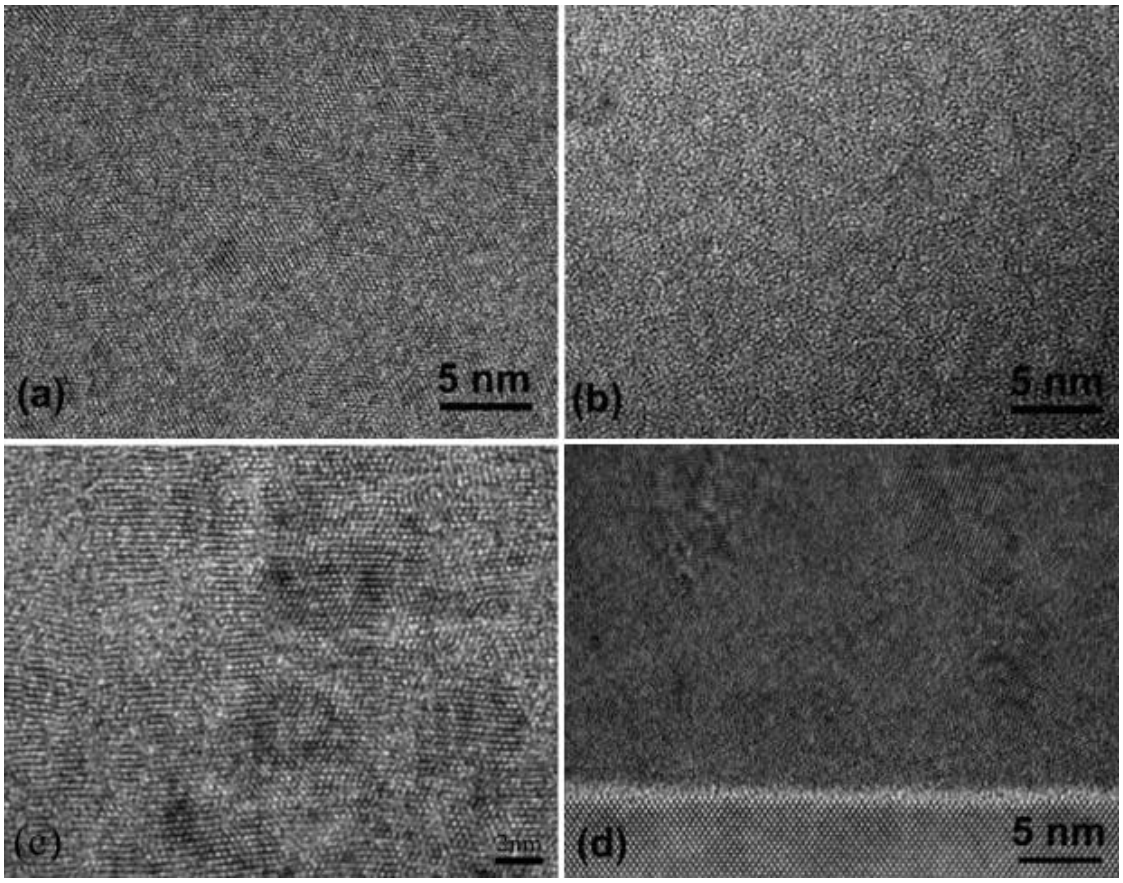

Fig. 4.2.9. (a) and (b) HRTEM image of the dark and bright regions in Fig. 4.2.8. (c) HRTEM image of the $Zr_{61}B_{27}C_6N_3$ coating taken from a cross-section TEM foil. (d) HRTEM image of the interface between $Zr_{61}B_{27}C_6N_3$ coating and Si substrate.

Fig. 4.2.10 (a) is a bright-field cross-section TEM image of the $Zr_{26}B_{26}C_6N_{42}$ coating deposited with 10% nitrogen fraction in the Ar/N_2 gas mixture. It shows the presence of nano-needle like structures. The typical length of the nano-needles is about ~30 nm and width is about 2 to 3 nm. The inserted SAED shows that the nano-needles in the coating exhibits fcc structure. The amorphous structure in this coating has increased a lot compared with the $Zr_{61}B_{27}C_6N_3$ coating. Fig. 4.2.10 (b) is a bright-field plan-view TEM image and SAED pattern of the $Zr_{26}B_{26}C_6N_{42}$ coating. The morphology of the

particles shows the cross-section of the nano-needles. The nano-needles in this coating have nearly a uniform lateral size of about 2 nm in diameter. The SAED pattern taken from the plan-view TEM foil shows the similar characteristic with the SAED from the cross-section TEM foil which indicates randomly oriented nano-crystalline formed in the coating. Fig. 4.2.10(c) is a HRTEM image taken from the area covering both the $Zr_{26}B_{26}C_6N_{42}$ coating and Si substrate showing the interface regions. The white layer between the coating and the Si substrate can be identified as SiO_2 layer. It can be seen that the $Zr_{26}B_{26}C_6N_{42}$ coating exhibits an intimate interface with the substrate and is very well attached to the substrate. Fig. 4.2.10(d) is a plan-view HRTEM image from the same coating further confirms that the nano-crystalline with a size about 2 nm embedded in an amorphous structure.

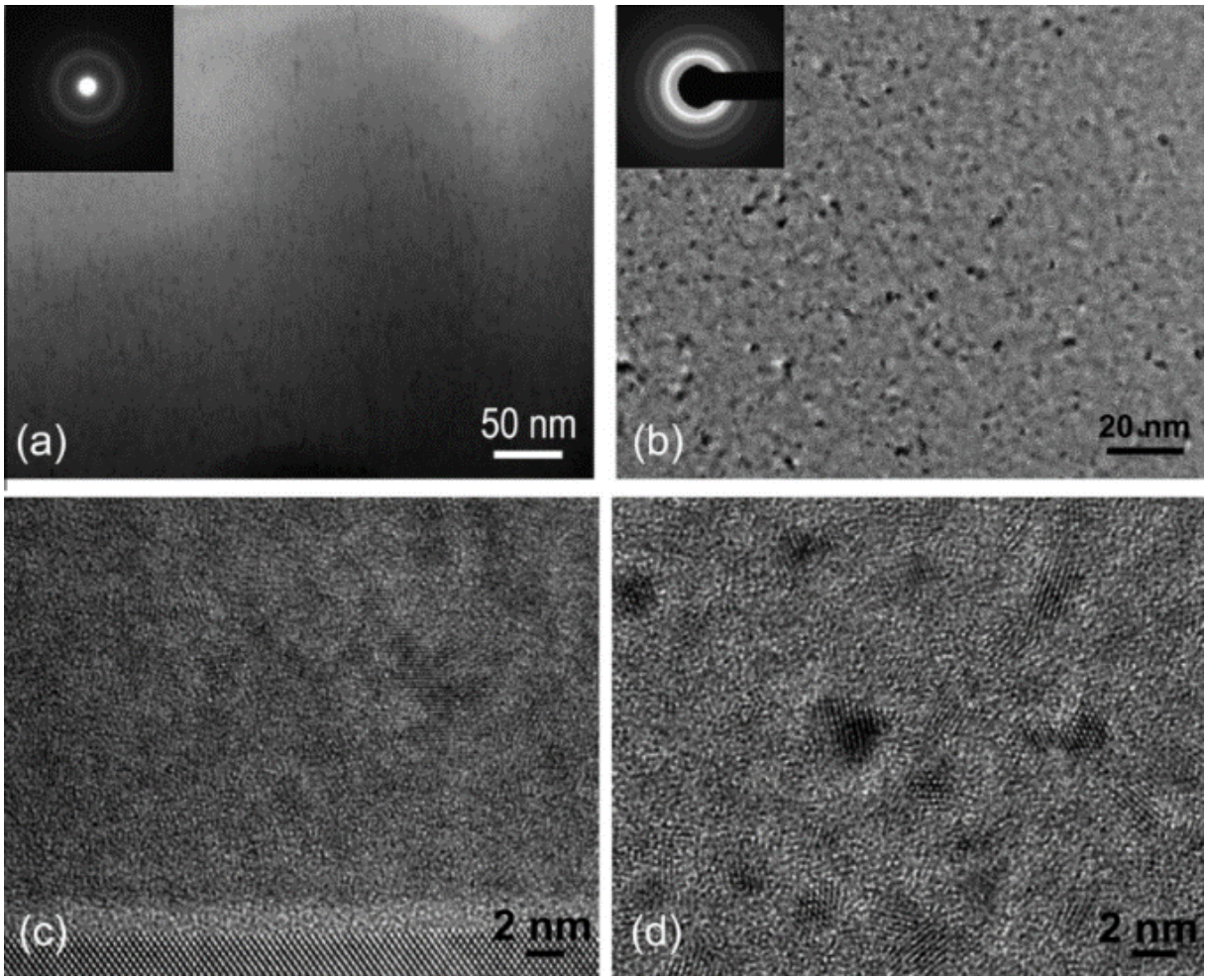

Fig. 4.2.10. (a) Cross-section and (b) plan-view TEM image and SAED pattern (inset) of the $Zr_{26}B_{26}C_5N_{42}$ coating. (c) Cross-section and (d) plan-view HRTEM image of the $Zr_{26}B_{26}C_5N_{42}$ coating.

Fig. 4.2.11 is a HRTEM image taken from the area covering both the $Zr_{24}B_{19}C_6N_{49}$ coating deposited with 15% N_2 and Si substrate showing the interface regions. It shows the $Zr_{24}B_{19}C_6N_{49}$ coating exhibits an amorphous like structure. Nano clusters with the size of a couple of nanometers were occasionally observed, and the SAED shows diffused diffraction rings also confirm the amorphous like structure formed in the coating.

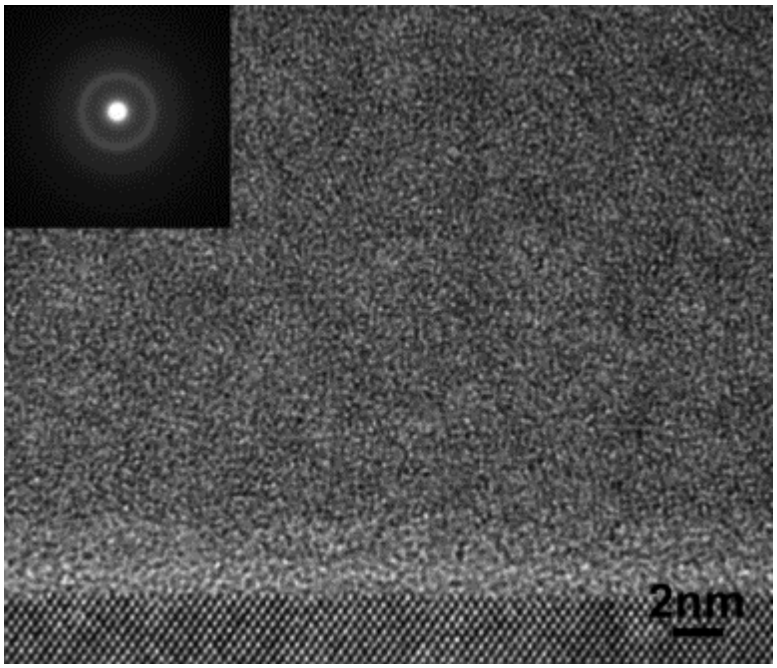

Fig. 4.2.11. Cross-section HR TEM image and SAED pattern (inset) of the $Zr_{24}B_{19}C_6N_{49}$ coating.

Fig. 4.2.12(a) is a bright-field cross-section TEM image of the $Zr_{41}B_{30}C_8N_{20}$ coating deposited with 5% nitrogen fraction in the gas mixture showing the presence of nano-needle like structures. The nano-needles are oriented along the coating growth direction and the length is up to 100 nm. The lateral size of the nano-needles is about 10 - 20 nm. Fig. 4.2.12(b) presents the SAED pattern of the coating showing a typical diffraction ring pattern indicates the nanocrystals in this coating are randomly oriented. The lattice spacing of the inner five rings 1, 2, 3, 4 and 5 is about 2.71 Å, 2.32 Å, 1.63 Å, 1.43 Å and 1.34 Å, respectively, demonstrating the formation of an fcc structure in the $Zr_{41}B_{30}C_8N_{20}$ coating. The lattice parameter calculated from the (111) plane is 4.70 Å while the lattice parameter from all the other diffraction planes is 4.64 Å. This result is consistent with the XRD analysis of the $Zr_{41}B_{30}C_8N_{20}$ coating. This result indicates that there should be two fcc phases presented in this coating, one is B-rich

Zr(B,C,N) solid solution and the other is ZrN phase. All the diffractions should be attributed to the contribution from both phases, but there is an additional contribution presents in the (111) diffraction.

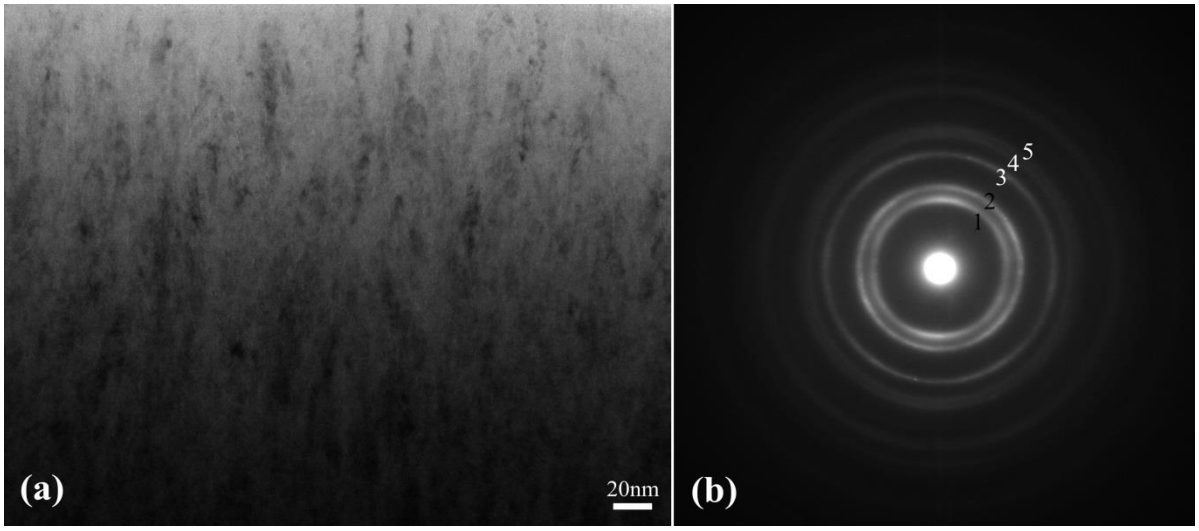

Fig. 4.2.12. (a) Bright-field TEM image and (b) SAED pattern of the $Zr_{41}B_{30}C_8N_{20}$ coating taking from a cross-section TEM foil.

Fig. 4.2.13 (a) is a bright-field plan-view TEM image of the $Zr_{41}B_{30}C_8N_{20}$ coating. Grain structures separated by discrete boundary segments with a size of ~20 - 30 nm are observed. The discrete boundary segments have been identified as amorphous structure by the HRTEM. Fig. 4.2.13(b) shows the SAED patterns taken from the plan-view TEM foils of the $Zr_{41}B_{30}C_8N_{20}$ coating presenting the same characteristics as that taken from the cross-section TEM foil further confirms the randomly oriented nanocrystals formed in this coating.

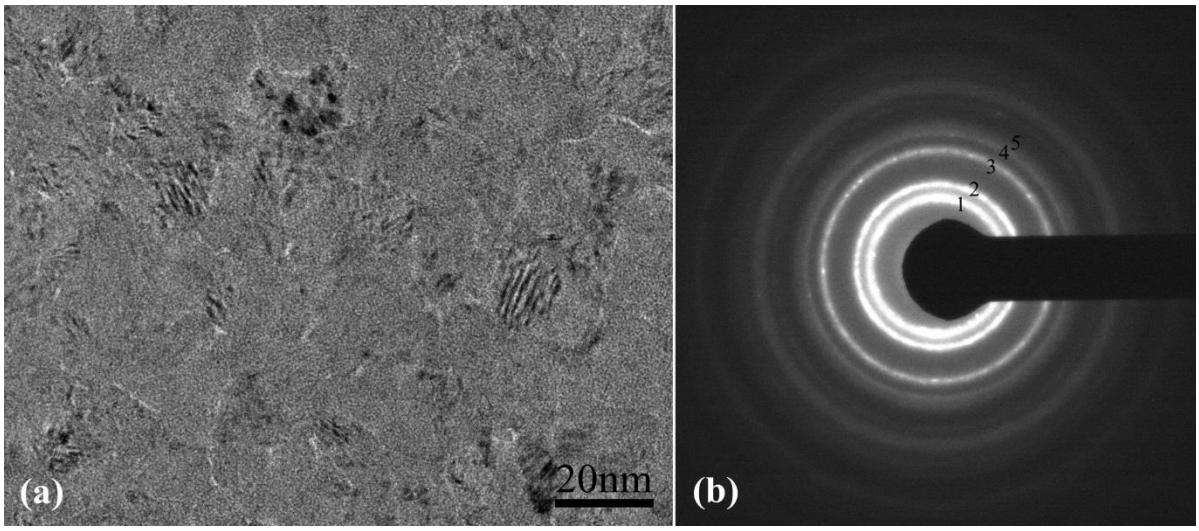

Fig. 4.2.13. (a) Bright-field TEM image and (b) SAED pattern of the $Zr_{41}B_{30}C_8N_{20}$ coating taking from a plan-view TEM foil.

Fig. 4.2.14 (a) is a cross-section HRTEM image of the $Zr_{41}B_{30}C_8N_{20}$ coating exhibiting the presence of two nano-needles structure (P & Q). The inset FFT was obtained from the nano-needle P shows that this nano-needle has a single crystal structure. Similarly, the nano-needle Q is also found to have a single crystal structure but with different crystal orientation form P. The nano-needle structures in the coating have a length of ~40 nm and a width of ~10 nm. Fig. 4.2.14 (b) is a plan-view HRTEM image of the $Zr_{41}B_{30}C_8N_{20}$ coating showing the atomic-structure of a nano-needle cross-section (region X). It can be observed that the nano-needles are composed of the same oriented sub nano-domains (with a size of ~1- 2 nm) separated by a monolayer interface/boundary, such as shown in the region X. In addition, it can be found that the lattice fringes in region Y are separated by a brighter fringe in every several fringes (2, 3 or more). No grains with an amorphous structure have been found in this coating.

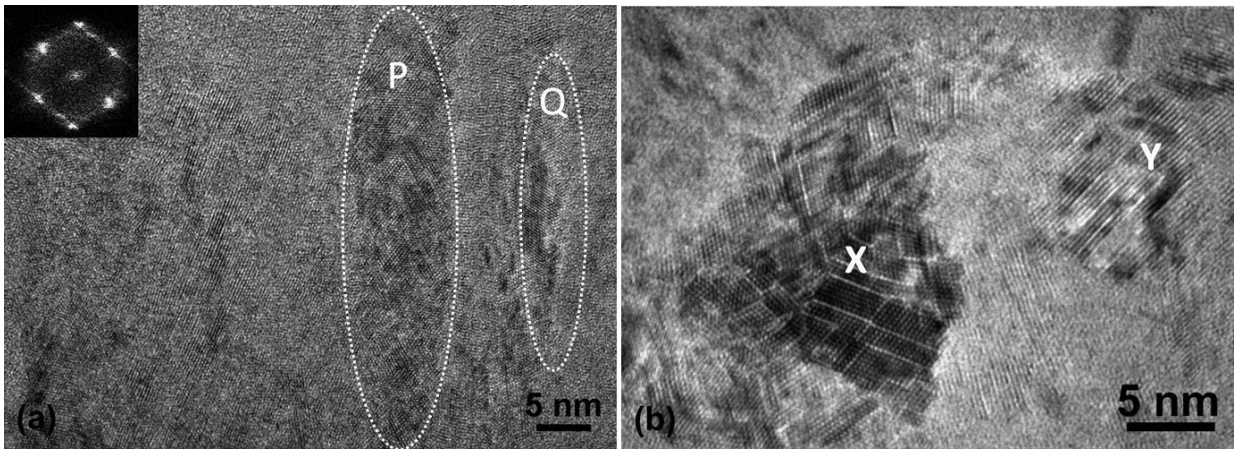

Fig. 4.2.14. (a) Cross-section HRTEM image and FFT (inserted) (b) Plan-view HRTEM image of the $Zr_{41}B_{30}C_8N_{20}$ coating.

It can be concluded that the nano needles in the $Zr_{41}B_{30}C_8N_{20}$ coating are likely possess a single crystal fcc structure with a lattice constant of ~4.70 Å and various orientations. The fcc structure in this coating can be considered as either a Zr(B,N) solid solution structure, or a mixture of ZrN and ZrN(B). The nano needles are randomly oriented in the coating. The nano-needle structures that composed of same oriented sub nano-domains that are separated by a monolayer interface only exist in the $Zr_{41}B_{30}C_8N_{20}$ coatings which exhibit significantly enhanced hardness and modulus compared to the other coatings without such nanostructures.

In another words, the formation of such unique nanostructures plays a critical role in the high hardness and modulus of the $Zr_{41}B_{30}C_8N_{20}$ coating. Such nano-domains are joined semi-coherently at

the interface. Understanding the atomic structure of such semi-coherent monolayer interface/boundary becomes extremely important for a better understanding the outstanding mechanical behavior of the coatings. We have conducted HRTEM imaging in combination with structure modeling and HRTEM image simulation to study the monolayer interface structure.

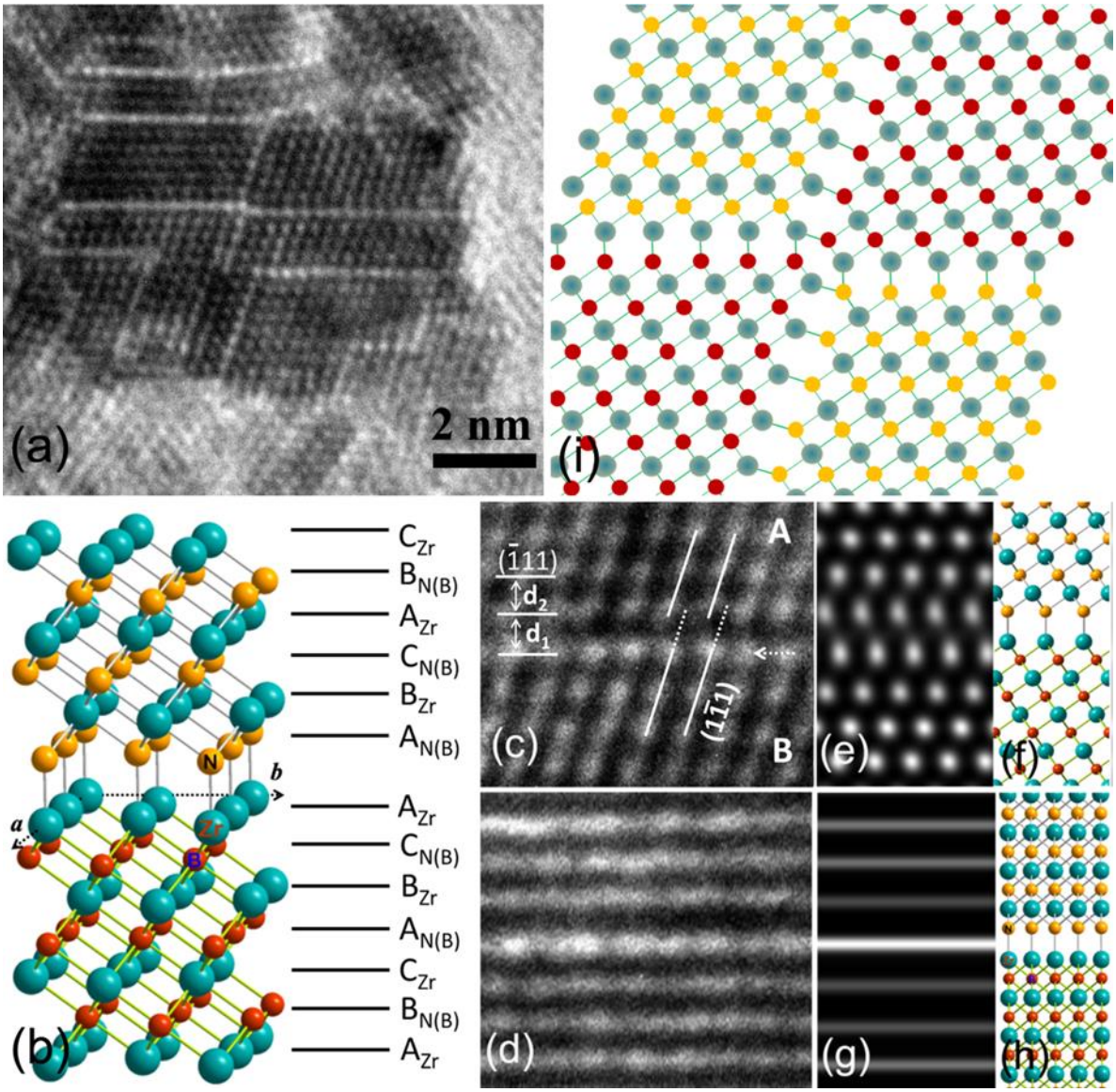

Fig. 4.2.15. (a) A zoom-in HRTEM image of a cross-section nano-needle structure in the $Zr_{41}B_{30}C_8N_{20}$ coating. (b) Atomic structural model for the monolayer interface. (c) and (d) HRTEM of a monolayer interface viewed along different directions. (f) & (h) Projection of the structural model along the ***a*** and ***b*** direction, respectively. (e) and (g) simulated HRTEM image of the structural model calculated with the electron beam parallel to the direction ***a*** and ***b,*** respectively; (e) was calculated using a defocus of 5 nm and a thickness of 5.8 nm, while (g) using a defocus of 15 nm and a thickness of 6 nm. (i) Schematic illustration of the atomic arrangement at the intersection of the four monolayer interfaces.

Fig. 4.2.15 (a) shows the zoom-in HRTEM image of a cross-section nano-needle structure in the $Zr_{41}B_{30}C_8N_{20}$ coating. This image was taken with the electron beam parallel to the [110] of the Zr(B,N) structure. The grain is composed of several nano-domains separated by semi-coherent monolayer interfaces appearing as a line composed of brighter lattice dots. Systematic studies of the HRTEM images show that the monolayer interfaces have the characteristics similar to that of the typical anti-phase boundaries (APBs). However, beside the monolayer interface, the $(1\bar{1}1)$ lattice planes in one domain (such as domain **A**) are shifted with those in the other domain (such as domain **B**) by ~30% of the corresponding lattice spacing along the interface rather than 50% displacement in the typical APBs, as shown in Fig. 4.2.15(c). Furthermore, for the lattice fringes that parallel to the interface such as $(\bar{1}11)$, the lattice spacing between the first lattice fringe next the monolayer interface and the interface (i.e., d_1) is about 13% larger than that of the rest lattice fringes, such as d_2. Taking the expanded ZrN monolayers surrounding the sub nano domains and the number of the atomic layers in each domain into account, the lattice parameter was calculated to be expanded about 3%. This result is consistent with the shift of the (111) peak to a lower angle in the XRD spectrum of this coating.

Based on the former result, an atomic structural model for the monolayer interface was built, as schematically illustrated in Fig. 4.2.15(b). Zr (B,N) is a fcc structure and can be considered as sequential packing of the three close packed layers (A, B and C) along the [111] direction in the order of $A_{Zr}B_{N(B)}C_{Zr}A_{N(B)}B_{Zr}C_{N(B)}A_{Zr}B_{N(B)}C_{Zr}A_{N(B)}B_{Zr}$…., where A_{Zr}, B_{Zr} and C_{Zr} represent the close packed layers of Zr; $A_{N(B)}$, $B_{N(B)}$ and $C_{N(B)}$ represent the close packed layers of N and B. Assuming that if during the packing process of the close-packed layers, two layers, such as, $B_{N(B)}$ and C_{Zr} between A_{Zr} and $A_{N(B)}$ were removed, a monolayer interface Zr-N(B) will be introduced. The Zr-N(B) bond length at the interface is equal to that in the bulk fcc Zr (B,N), *i.e.,* 2.28 Å. It should be noted that it is possible that the nano-domains beside the monolayer interface have different compositions: with the domain on one side having a ZrB structure and that on the other side having ZrN, as shown in Fig. 4.2.15(b). We have employed the HRTEM image simulation to check the feasibility of this structural model. Fig. 4.2.15(e) is a simulated HRTEM image of the structural model shown in Fig. 4.2.15(b) calculated using a defocus of 5 nm and a thickness of 5.8 nm, with the electron beam parallel to the direction ***a***, whose projection is

shown in Fig. 4.2.15(f). A very good match can be found between the simulated image and the experimental HRTEM image.

Grains with the lattice images similar to those of grain Y shown in Fig. 4.2.14(b) were also frequently observed during plan-view HRTEM studies of the $Zr_{41}B_{30}C_8N_{20}$ coating. A zoom-in of such a HRTEM image is also shown in Fig. 4.2.15(d), in which the lattice fringes **p** and ***q*** are brighter than the rest of lattice fringes. The lattice fringes in Fig. 4.2.15(d) correspond to the (111) planes of the fcc. Zr (B,N) and the brighter fringes correspond to the monolayer interfaces. Fig. 4.2.15(d) can be considered as a HRTEM image of the structure shown in Fig. 4.2.15(c) obtained with the electron beam parallel to its horizontal direction in the image plane. Fig. 4.2.15(g) is a simulated HRTEM image of the structural model (shown in Fig. 4.2.15(b)) calculated using a defocus of 15 nm and a thickness of 6.0 nm, with the electron beam parallel to the direction ***b***, whose projection is shown in Fig. 4.2.15(h). A very good match can be seen between the simulated image and the experimental HRTEM image. We have also observed that several monolayer interfaces, usually four, intersect at one point forming a line defect as shown in Fig. 4.2.15(a). The atomic arrangement of such a monolayer interface intersection structure is schematically illustrated in Fig. 4.2.15(j).

The $Zr_{61}B_{27}C_6N_3$ coating deposited with 0% nitrogen fraction in the argon–nitrogen gas mixture has a nanocomposite structure composed of crystalline columnar structures with a lateral size of ~20 - 60 nm surrounded by an amorphous material. The columnar structures have an fcc structure with a lattice constant of 4.65 Å which can be regarded as the ZrB structure based on the stoichiometric composition of the coating. The excess Zr together with C and N forms the amorphous structure. Among the four Zr-B-C-N coatings investigated in the present study, $Zr_{61}B_{27}C_6N_3$ coating with large columnar structure surrounded by amorphous phase exhibits lowest hardness. The large amount of amorphous structure should contribute to the relative low hardness.

The $Zr_{26}B_{26}C_6N_{42}$ coating deposited with 10% nitrogen fraction in the argon–nitrogen gas mixture is composed of refined crystalline ZrN nano-needle structures (~2 nm) embedded in an amorphous structure. Sizeable amount of amorphous structure was formed in this coating and the amorphous can be regarded as the Zr-B-C-N structure. It has been aware that the lattice constants of Zr(B,C,N) and ZrN are very close and it is possible that the crystalline nano-needles can possess the Zr(B,C,N)

structure. However, such a possibility can be ruled out after considering the following factors: (1) ZrN is an equilibrium phase and Zr(B,C,N) is a metastable phase; (2) It was reported the Zr $3d_{5/2}$ and Zr $3d_{3/2}$ in ZrB_2 exhibits lower binding energy than those in ZrN. Our XPS studies showed that Zr 3d in the $Zr_{26}B_{26}C_6N_{42}$ has a higher binding energy than that $Zr_{41}B_{30}C_8N_{20}$ coating.

The $Zr_{24}B_{19}C_6N_{49}$ coating deposited with 15% nitrogen fraction in the argon–nitrogen gas mixture has an amorphous-like structure. This coating possesses further reduced hardness and modulus compared to the $Zr_{26}B_{26}C_6N_{42}$ coating.

The $Zr_{41}B_{30}C_8N_{20}$ coating deposited with 5% nitrogen fraction in the argon–nitrogen gas mixture exhibits the highest hardness and modulus among the four coatings. This coating is composed of crystalline nano-needles in which a unique structure of nano-domain structures (~2 nm) separated by semi-coherent monolayer interfaces was formed. No amorphous grain structures were observed in this coating. It is quite possible that introducing nitrogen into the coating by increasing the nitrogen fraction in the argon–nitrogen gas mixture, part of the Zr will form ZrN fcc structure and part of the Zr will continue to preserve the B-rich Zr(B,C,N) structure. The two structures ZrB and Zr(B,C,N) will be formed as nano-domains and joined together semi-coherently via Zr-N monolayer interfaces. The formation of such a unique nanostructure in the $Zr_{41}B_{30}C_8N_{20}$ coating could play a critical role in the significant enhancement of its hardness and modulus.

4.2.5 Summary

In this study, pulsed reactive magnetron sputtering was used to deposit the ZrBCN coatings in N_2/Ar gas mixture with different N_2 fraction 0%, 5%, 10% and 15%, respectively at a 45% Zr faction in the target erosion area. The coatings were investigated by XPS, XRD, HRTEM and nano-indentation. The $Zr_{41}B_{30}C_8N_{20}$ coating deposit with 5% N_2 possesses the highest hardness and Young's modulus among the four coatings. This coating consists of fcc nano-needle structures with length about 40 nm and width about 10 nm. The nano needle structures composed ZrN and Zr(B,N) nano-domains that semi-coherently joined by the Zr-N monolayer interfaces. This unique structure plays a very important role in the hardness enhancement of the coating. The change in structures of the coating can be achieved by changing the N/Zr ratio by adjusting the N_2 fraction in the gas mxiture results in a

significant enhancement of coating's properties. The introduce amount of amorphous structure should be well controlled in order to achieve enhanced hardness in the coating.

4.3 Hf-B-Si-C Coatings

In this part, the Hf-B-Si-C coatings prepared using the target of a B_4C plate with a fixed 15% Hf fraction and four different Si fraction (0%, 1%, 7.5%, 30%) in the target erosion were characterized. A detailed microstructure analysis of the Hf-B-Si-C coatings was carried out using HRTEM and selected–area electron diffraction. In addition, the coatings were also characterized using XRD, XPS and nano-indentation measurements. The motivation for this research was to get a better understanding about microstructure evolution as a function of the silicon content in the Hf-B-Si-C coatings.

The Hf-B-Si-C coatings were provided by our research collaboration Professor Vlcek's group at the University of West Bohemian, Plzen, Czech Republic. The fabrication details of the Hf-B-Si-C coatings have been described in Chapter 3.1.2. Four representative Hf-B-Si-C coatings prepared with the Si fraction of 0%, 1%, 7.5% and 30% in the target erosion area were selected to study the effect of the Si content on the microstructure and properties of the coatings. The elemental composition of the coatings was determined by the Rutherford backscattering spectrometry and the elastic recoil detection methods. The following table shows the detailed information of coatings.

Table 4.3.1. Received Hf-B-Si-C coatings composition and hardness

Composition（at%）	Si%	Hardness (GPa)
$Hf_{27}B_{57}C_{8}$	0%	37.1
$Hf_{23}B_{55}Si_{2}C_{11}$	1%	34.1
$Hf_{22}B_{54}Si_{9}C_{9}$	7.5%	30.9
$Hf_{21}B_{28}Si_{35}C_{7}$	30%	16

4.3.1 Mechanical Properties and Residual Stress Measurements

The nano-indentation test was conducted to study the effect of the Si content on the coatings' hardness and Young's modulus. A Berkovich diamond tip was used in the tests, and a fused quartz (hardness of 9.25 GPa, modulus of 69.6 GPa) was used as the standard sample to calibrate the apparatus. The indention curves were obtained by plotting the applied force vs the tip displacement. An

indenting force of 10000 μN and a three-segment loading function were used for tests of all of the four Hf-B-Si-C coatings. To minimize the experimental error, the average hardness and modulus values were determined by performing 4×4 array indents with 10 μm ×10 μm distance for each coating.

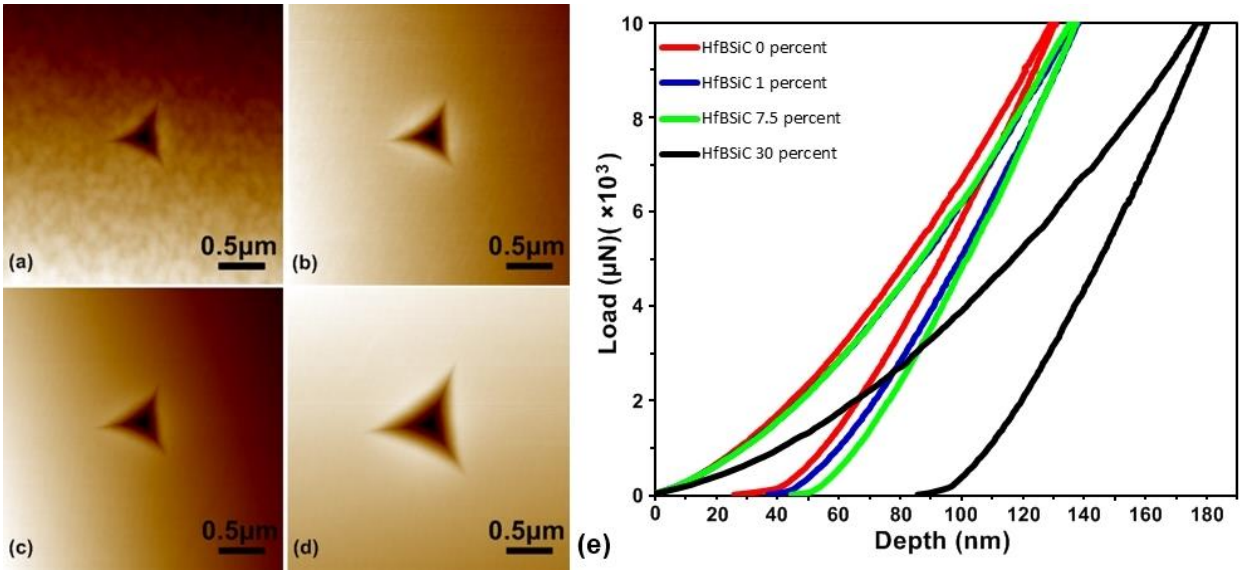

Fig. 4.3.1. (a)-(d) Images of indentation area on the coating of $Hf_{27}B_{57}C_8$, $Hf_{23}B_{55}Si_2C_{11}$, $Hf_{22}B_{54}$ Si_9C_9 and $Hf_{21}B_{28}$ $Si_{35}C_7$, respectively. (e) Force vs. displacement curves for the coatings.

Fig. 4.3.1 (e) shows typical force vs. displacement curves for the four Hf-B-Si-C coatings. The mean hardness for the $Hf_{27}B_{57}C_8$, $Hf_{23}B_{55}Si_2C_{11}$, $Hf_{22}B_{54}$ Si_9C_9 and $Hf_{21}B_{28}$ $Si_{35}C_7$ coatings was 37.1, 34.1, 30.9 and 16.1 GPa, respectively. The mean modulus for the $Hf_{27}B_{57}C_8$, $Hf_{23}B_{55}Si_2C_{11}$, $Hf_{22}B_{54}$ Si_9C_9 and $Hf_{21}B_{28}$ $Si_{35}C_7$ coatings was 243.6, 233.2, 221.3 and 173.8 GPa, respectively. Figs. 4.3.1(a) - (b) show the images of the indentations on the coatings $Hf_{27}B_{57}C_8$, $Hf_{23}B_{55}Si_2C_{11}$, $Hf_{22}B_{54}$ Si_9C_9 and $Hf_{21}B_{28}$ $Si_{35}C_7$, respectively.

Optical profilometer was used to determine the residual stress present in the Hf-B-Si-C coatings. Fig. 4.3.2 presents the hardness and residual stress of the Hf-B-Si-C coatings deposited with different silicon percentage in the target erosion area. It can be clearly seen that the Si-free coating $Hf_{27}B_{57}C_8$ exhibits the highest hardness of 37.1 GPa and highest compressive stress of 4.9 GPa. Slight incorporation of Si (2 at%) into the coating results in a significant decrease in the compressive stress from 4.9 GPa to 1.8 GPa while there is only a slight decrease in hardness from 37.1 GPa to 34.1 GPa.

Further increasing of silicon content in the coatings results in further gradually decreases in the residual stress.

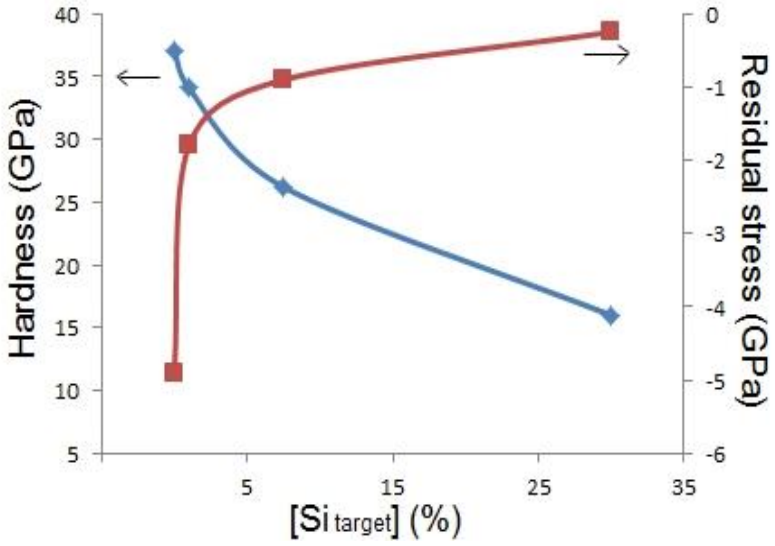

Fig. 4.3.2. Hardness and residual stress of the $Hf_{27}B_{57}C_8$, $Hf_{23}B_{55}Si_2C_{11}$, $Hf_{22}B_{54}$ Si_9C_9 and $Hf_{21}B_{28}$ $Si_{35}C_7$ coatings.

4.3.2 XPS Studies

Fig. 4.3.3 (a) shows the general XPS survey spectra of the $Hf_{27}B_{57}C_8$, $Hf_{23}B_{55}Si_2C_{11}$, $Hf_{22}B_{54}Si_9C_9$ and $Hf_{21}B_{28}Si_{35}C_7$ coatings deposited with 0%, 1%, 7.5% and 30% Si in the target erosion area. The spectra exhibit mainly the presence of Hf, B, Si, C, and O (O and some of the C are from the contamination). The results clearly show that the intensity of both Si2p and Si2s peaks increases with the increase of the Si fraction in the target erosion area.

Fig. 4.3.3 (b) presents the high resolution spectra of the Si 2p peaks of all four Hf-B-Si-C coatings. The Si2p peak for the $Hf_{23}B_{55}Si_2C_{11}$ coating is very weak due to the small amount of silicon presents in the coating, and the binding energy of the Si 2p is around 101.7 eV. The binding energy of the Si 2p is about 101 eV for the , $Hf_{22}B_{54}Si_9C_9$ and is about 100.5 eV for the $Hf_{21}B_{28}Si_{35}C_7$ coating indicates that the Si 2p peak shifts slightly to a lower binding energy with the increase of the silicon content. The Si 2p peaks for both the $Hf_{22}B_{54}Si_9C_9$ and $Hf_{21}B_{28}Si_{35}C_7$ coatings can be de-convoluted into two components with a binding energy of 101.7 eV and 99.5 eV which can be identified as the Si 2p peak of Si-B and hafnium silicide, respectively. This result indicate that increasing the silicon content in the coating

results in the increase of the hafnium silicide and accordingly result in the Si 2p peak shifting to lower binding energy position.

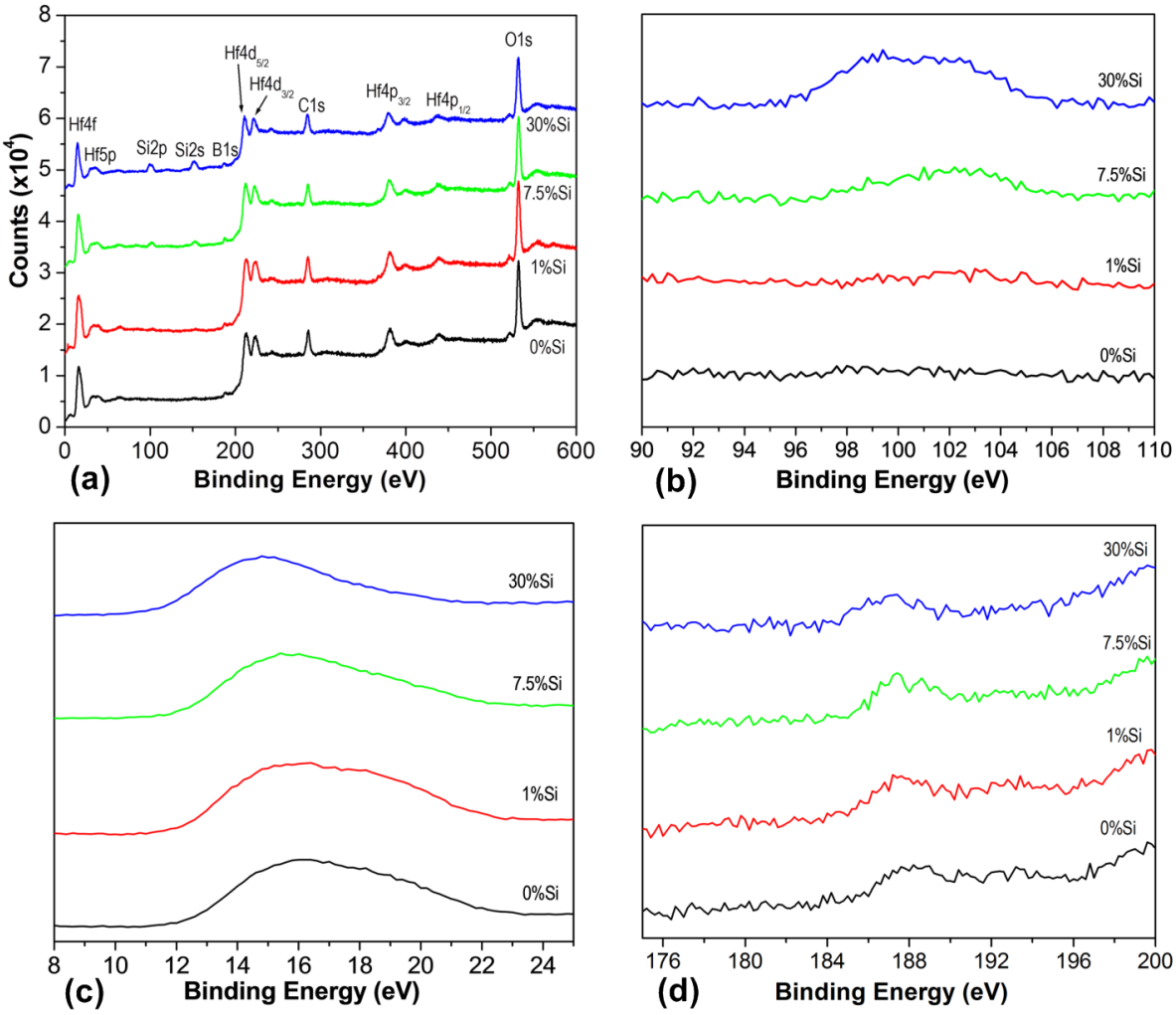

Fig. 4.3.3. XPS survey spectra (a) and high resolution XPS spectra of peak Si2p (b) Hf4f (c) and B1s of the Hf-B-Si-C coating with [Si $_{target}$] = 0%, 1%, 7.5% and 30%.

Fig. 4.3.3 (c) shows the high-resolution XPS spectra of the Hf 4f peak of all four Hf-Si-B-C coatings presenting a binding energy of 16.4 eV, 16.0 eV, 15.5 eV and 14.5 eV for the $Hf_{27}B_{57}C_8$, $Hf_{23}B_{55}Si_2C_{11}$, $Hf_{22}B_{54}Si_9C_9$ and $Hf_{21}B_{28}Si_{35}C_7$ coating, respectively. The binding energy of Hf 4f peak for the $Hf_{27}B_{57}C_8$ is very close to that for HfB_2 (16.3 eV) reported in the literature [114]. The Hf4f peaks for the $Hf_{23}B_{55}Si_2C_{11}$, $Hf_{22}B_{54}Si_9C_9$ and $Hf_{21}B_{28}Si_{35}C_7$ coatings can be de-convoluted into two components with binding energy of 16.4 eV and 14.6 eV, respectively. The latter one is closely equal to the binding energy of Hf 4f for hafnium silicide [115]. It clearly shows that increasing the Si content in the coatings

produce more component of hafnium silicide and accordingly results in the peak shifts to lower binding energy position.

Fig. 4.3.3 (d) shows the high-resolution XPS spectra of the B1s peak of all four Hf-Si-B-C coatings. The B1s peak for the $Hf_{27}B_{57}C_8$ coating can be de-convoluted into two components with binding energy of 188.1 eV and 186.6 eV, which attributed to the B1s peak of Hf-B in HfB_2 [114] and that of B-C [117], respectively. The de-convolution of the B1s peak for the $Hf_{23}B_{55}Si_2C_{11}$, $Hf_{22}B_{54}Si_9C_9$ and $Hf_{21}B_{28}Si_{35}C_7$ coatings exhibit one more component with binding energy of 186.9 eV in addition to the components Hf-B and B-C. The binding energy of this new component is close to that for B1s in B-Si around 186.8-187.5 eV [115]. The intensity of the component B-Si increases with the silicon content in Hf-B-Si-C coatings indicating the increase of the amount of Si-B bonds and results in the observed lower shift of the peak.

4.3.3 XRD Studies

We examined the crystal structure of the coatings using the XRD before conducting systematical TEM analysis. Fig. 4.3.4(a) shows the XRD spectra of the Hf-B-Si-C coatings deposited at varying Si fraction in the target erosion area [Si_{target}] = 0, 1, 7.5, 30%. The spectrum of the Si free $Hf_{27}B_{57}C_8$ coating shows three diffraction peaks at 2θ position of 25.28°, 41.95° and 51.98°, corresponding to the lattice spacing of 3.52 Å, 2.151 Å and 1.758 Å. Considering the elemental composition of the coatings, those peaks can be identified as the (001), (101) and (002) of the hexagonal HfB_2 crystal structure with a lattice constant of a=3.14 Å and c=3.52 Å. All the three peaks were shifted a little to lower angles caused by the residual stress in the coating. It should be noted that the (100) diffraction of HfB2 is not present in this XRD spectrum. The XRD spectrum of the $Hf_{23}B_{55}Si_2C_{11}$coating with increased Si fraction to 1% exhibits two peaks at 2θ position of 25.44°, 52.25°, which can be identified as the (001) and (002) of the hexagonal HfB_2 structure. Compared to the Si free coating, the intensity of the (001) and (002) peaks was significantly increased, but the (101) peak disappears. This result indicates that this coating exhibits a strong preferential orientation with only the (001) of HfB_2 parallel to the coating surface.

By further increasing of the Si fraction to 7.5%, the spectrum of the $Hf_{22}B_{54}Si_9C_9$ coating shows four broad and weak peaks that can be identified as the (001), (100), (101) and (002) of HfB_2 indicating the formation of a randomly oriented nanocrystalline structure in the coating. The XRD spectrum of the

$Hf_{21}B_{28}Si_{35}C_7$ coating presents three barely seen broad and weak peaks that can be identified as the (001), (100) and (101) of HfB_2 indicating the formation of a nearly amorphous like or very short range ordered structure.

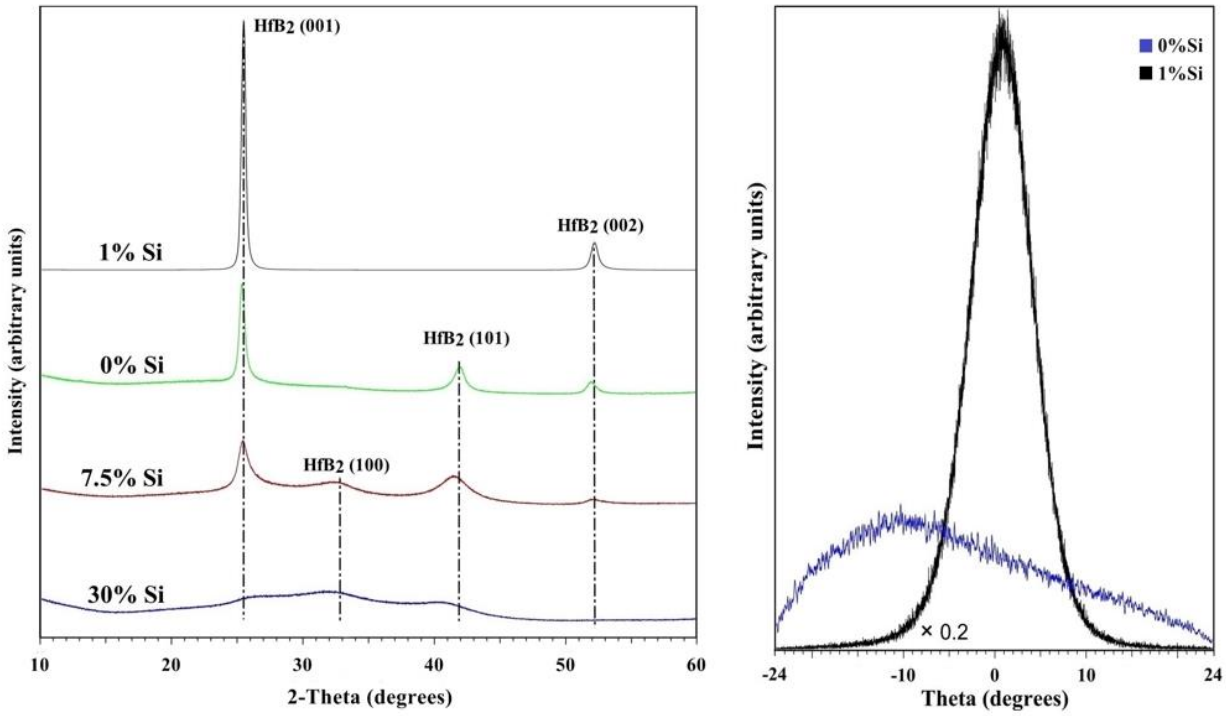

Fig. 4.3.4. (a) XRD spectra of the Hf-B-Si-C coatings $Hf_{27}B_{57}C_8$, $Hf_{23}B_{55}Si_2C_{11}$, $Hf_{22}B_{54}Si_9C_9$ and $Hf_{21}B_{28}Si_{35}C_7$ with $[Si_{target}]$= 0%, 1%, 7.5% and 30%. (b) Rocking curves of the (002) peak of the Hf-B-Si-C coatings with $[Si_{target}]$= 0% and1%.

4.3.4 HRTE studies

In order to further study the effect of the Si content on the microstructure and the properties of the Hf-B-Si-C coatings, we systematically studied the microstructures of the coatings using TEM. The coating thickness measured using cross-section TEM is about 1.1 µm, 1.0 µm, 1.4 µm and 1.5 µm for the Hf-B-Si-C coatings with 0%, 1%, 7.5% and 30% Si in the target erosion area, respectively.

Fig. 4.3.5(a) is a cross-section bright field TEM image of the Si-free $Hf_{27}B_{57}C_8$ coating showing the presence of nano-needle like structures. The nano-needles have a lateral size of ~5 -10 nm and a length of ~50 - 60 nm. The long axis of the nano-needles is several degrees away from the normal direction of the coating. Fig. 4.3.5(b) is a typical SAED pattern taken from an area in the coating (away

from the interface between coating and silicon substrate) exhibiting a clean and well-defined array of diffraction spots. This SAED was taken with the incident electron beam parallel to the [1 1 0]-Si. The diffraction spots on the x-y direction are periodically distributed and can be indexed as (00l) (l = 1, 2, . .) of HfB_2 structure. The diffraction spots along the A–B direction are quasi-periodically arranged. The first three spots close to the center beam correspond to the (100), (110) and (200) of HfB_2. Fig. 4.3.5(c) is a dark-field TEM image obtained using the (001) spot in Fig. 4.3.5(b). The brightness areas dominate the image contrast indicating that the HfB_2 structures of the bright nano-needles possess the same orientation are well aligned along a single direction.

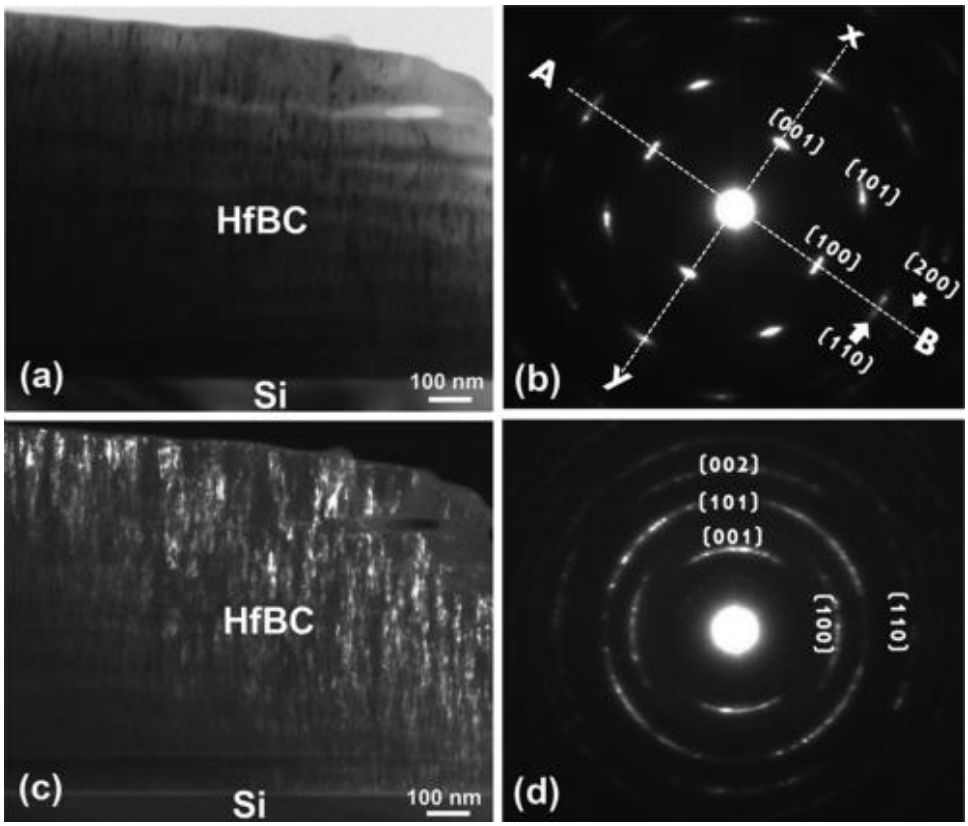

Fig. 4.3.5. (a) Bright field TEM image and (b) SAED pattern from the area away from the interface in a cross-section TEM foil of the $Hf_{27}B_{57}C_8$ coating, (c) dark-field image of the (001) diffraction(b). (d) SAED pattern from a different area of the $Hf_{27}B_{57}C_8$ coating.

However, the strong texture suggested by the SAED in Fig. 4.3.5 (b) is not reflected in the θ-2θ XRD of the $Hf_{27}B_{57}C_8$ coating shown in Fig. 4.3.4 (a). TEM studies were carried on additional cross section TEM foils from other areas. The SAED pattern taken from the $Hf_{27}B_{57}C_8$ coating in a newly prepared cross-section TEM foil is shown in Fig. 4.3.5 (d). It presents arc diffractions that match very

well with the θ-2θ XRD pattern of the coating shown in Fig. 4.3.4 (a). It should be noted that the XRD pattern presents the overall structure of the coating and in certain cases may not able to capture diffractions if a strongly textured structure is inappropriately oriented for diffraction. Thus, these observations show that both random and textured regions exist in this coating.

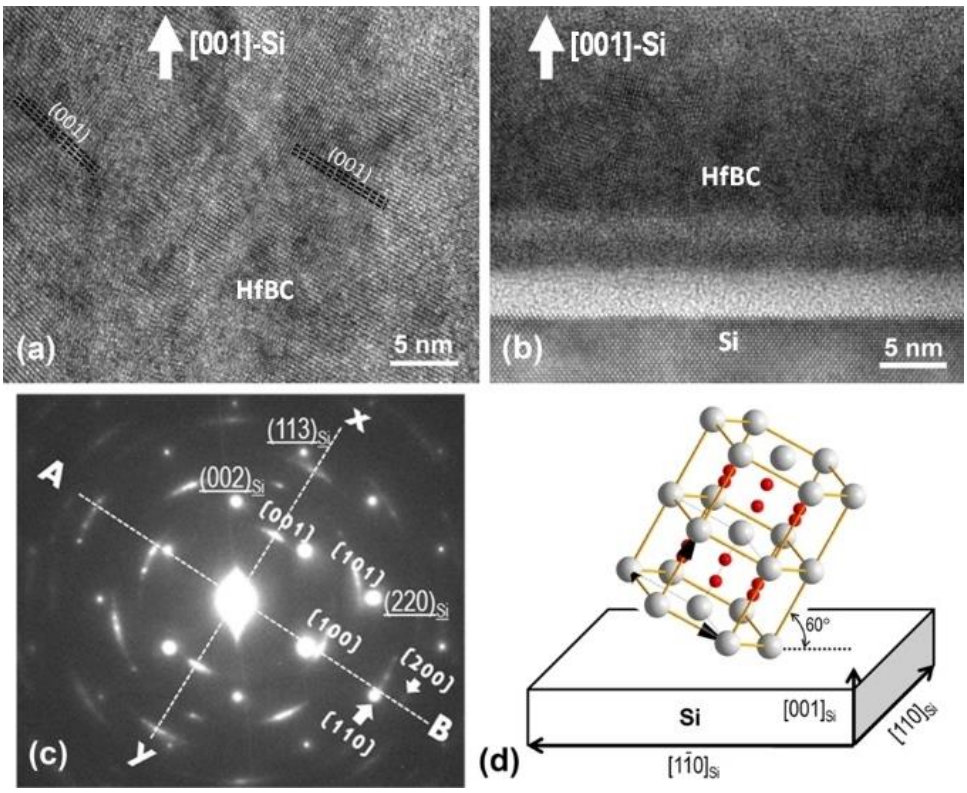

Fig. 4.3.6. (a) HRTEM image of the $Hf_{27}B_{57}C_8$ coating. (b) HRTEM image and (c) SAED pattern of the interface between the $Hf_{27}B_{57}C_8$ coating and Si. (d) Schematic illustration the orientation relationship between the HfB_2 of the majority phase in the coating and the Si substrate.

Fig. 4.3.6(a) is a HRTEM image of an area in the $Hf_{27}B_{57}C_8$ coating away from the coating/substrate interface, taken from a cross-section TEM foil showing the atomic structure of the nano-needles. The marked lattice fringes have a lattice spacing of 3.46 Å can be identified as the (0 0 1) HfB_2. These (0 0 1) lattice fringes are oriented with an angle about 30° away from the coating surface. Fig. 4.3.6 (b) is a HRTEM image of the interface between the coating and substrate taken from the same cross-section TEM foil. It can be observed that the coating is very well attached to the Si substrate via an amorphous layer. The grain structure in the coating region near the interface shows much smaller size compared to that in Fig. 4.3.6(a), indicating that there are more boundary defects in

this area. Fig. 4.3.6(c) is a SAED pattern from the coating/Si interface region taken using the same direction Fig. 4.3.5(b), using the incident electron beam parallel to the [1 1 0]-Si. It shows an overlap diffraction pattern of the Si-[1 1 0] zone and the coating. Compared to the well-defined diffraction spots in Fig. 4.3.5(b), the diffraction spots of the coating in Fig. 4.3.6(c) appear as diffraction arc. This also indicates that nanostructures in the coating near the interface have shorter range ordering than those in the areas away from the interface. It is noted that the [0 0 1] direction of HfB_2 is nearly aligned to the [1 1 3]-Si. In other words, the [0 0 1] direction of HfB_2 which consists the majority of the nano-needles in the coating, is oriented with an angle of 30° with respect to the coating growth direction. Fig. 4.3.6(d) schematically illustrates the orientation relationship between the HfB_2 of the majority phase in the coating and the Si substrate.

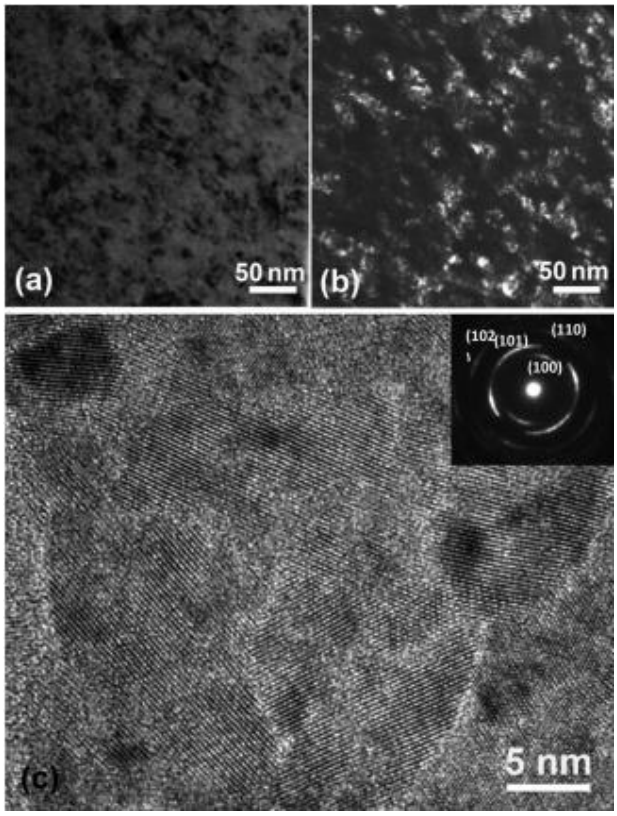

Fig. 4.3.7. (a) Bright-field, (b) dark-field TEM image obtained using the HfB_2-(100) reflection in the SAED pattern (inset in (c)) and (c) HRTEM image of the coating in a plan-view TEM foil of the $Hf_{27}B_{57}C_8$ coating.

Fig. 4.3.7 (a) is a bright field TEM image taken from a plan-view TEM foil of the $Hf_{27}B_{57}C_8$ coating showing the cross-section structure of the nano-needles in Figs. 4.3.5 (a) and (c). Grain structures have a size from 10 to 30 nm, and no visible boundaries between the grains were found. The SAED pattern from the plan-view sample also shows the formation of a strong texture. Diffractions with indices (0 0 l) (l = 1, 2, 3, . .) were also absent in this SAED pattern. Fig. 4.3.7 (b) is a dark-field image obtained using diffraction (1 0 0) in the SAED pattern. The portion of the bright contrast area is less than 50% over the entire image, indicating that the percentage of the structures possessing the (100) orientation in the Si free $Hf_{27}B_{57}C_8$ coating is less than 50%. Fig. 4.3.7 (c) is a HRTEM image taken from an area in Fig. 4.3.7 (a) presenting grains with a size of 5 - 25 nm. Most grains are interconnected

with their adjacent grains directly without the presence of amorphous boundaries. Very few amorphous boundaries were formed between the grains. The crystallographic orientations of the grains are quite different and no common orientation can be found among them.

The crystallographic orientation of HfB_2 in the $Hf_{27}B_{57}C_8$ coating varies with regions. We also conducted rocking curve scan of the (002)-HfB_2 reflection of the $Hf_{27}B_{57}C_8$ coating by tilting the specimen around a horizontal axis ±24° to study the orientation variation with respect to the coating surface over a large area in Fig. 4.3.4 (b). A broad and symmetrical peak was observed over a tilt angle range (−24°, 24°) indicating the formation of orientation preferred structures. The highly orientation preferred structure with the (0 0 1) HfB_2 tilted away from the coating surface by 30°, as observed by TEM, is not able to be detected using θ-2θ XRD and rocking curve due to the limit of permitted angle tilt.

Fig. 4.3.8(a) shows a bright field TEM image of the $Hf_{23}B_{55}Si_2C_{11}$ coating. Island-like dark grain structures together with fine structures assembled by white dots were observed. Fig. 4.3.8 (b) shows the SAED pattern taken from a plan-view TEM foil presenting discontinued diffraction rings indicating the formation of a strong textured structure in the coating. The first three diffraction arcs close to the center spot can be identified as the (1 0 0), (1 0 1) and (1 1 0) of hexagonal HfB_2. It can be observed that the diffractions with indices (0 0 l) (l = 1, 2, . .) were invisible in this SAED pattern. Fig. 4.3.8(c) is a dark-field image taken using the diffraction arc (1 0 0) in Fig. 4.3.8(b). Over 50% of the area in the image is showing bright contrast indicating that structures in those areas possess nearly the same crystallographic orientation. Furthermore, fine structures of white nano-domains separated by dark boundaries were formed within the white regions. Fig. 4.3.8(d) is a HRTEM image taken from a white region in Fig. 4.3.8(c) showing nanocrystalline domain structures separated by amorphous boundaries. The nano-domains have a typical size of about 5 nm and the boundaries have a typical thickness less than 1 nm. Nearly all of the nano-domains in Fig. 4.3.8(d) exhibit hexagonal lattice patterns whose orientation is either closely aligned or rotated by a small angle with respect to each other.

Fig. 4.3.9(a) is a cross-section bright field TEM image of the $Hf_{23}B_{55}Si_2C_{11}$ coating. Nano-needle structures with a length of ~20 – 30 nm and a width about 5 nm were formed in the coating. The long axis of the nano-needles is aligned with the growth direction of the coating. Fig. 4.3.9(b) is a typical SAED pattern taken from an area in the $Hf_{23}B_{55}Si_2C_{11}$ coating (away from the coating/Si interface)

exhibiting a clean and well-defined array of diffraction spots, quite similar to a single crystal diffraction pattern. The diffraction spots on the vertical direction are periodically distributed and can be indexed as (0 0 l) (l = 1, 2, . .) of HfB_2 structure. The (0 0 1) spots in Fig. 4.3.9(b) produce a lattice spacing of 3.45 Å. The diffraction spots along the horizontal direction in Fig. 4.3.9(b) are “quasi-periodically” arranged. The first three spots close to the center beam have a lattice spacing of 2.71 Å, 2.14 Å and 1.57 Å that can be indexed as the (1 0 0), (1 1 0) and (2 0 0) of HfB_2, respectively.

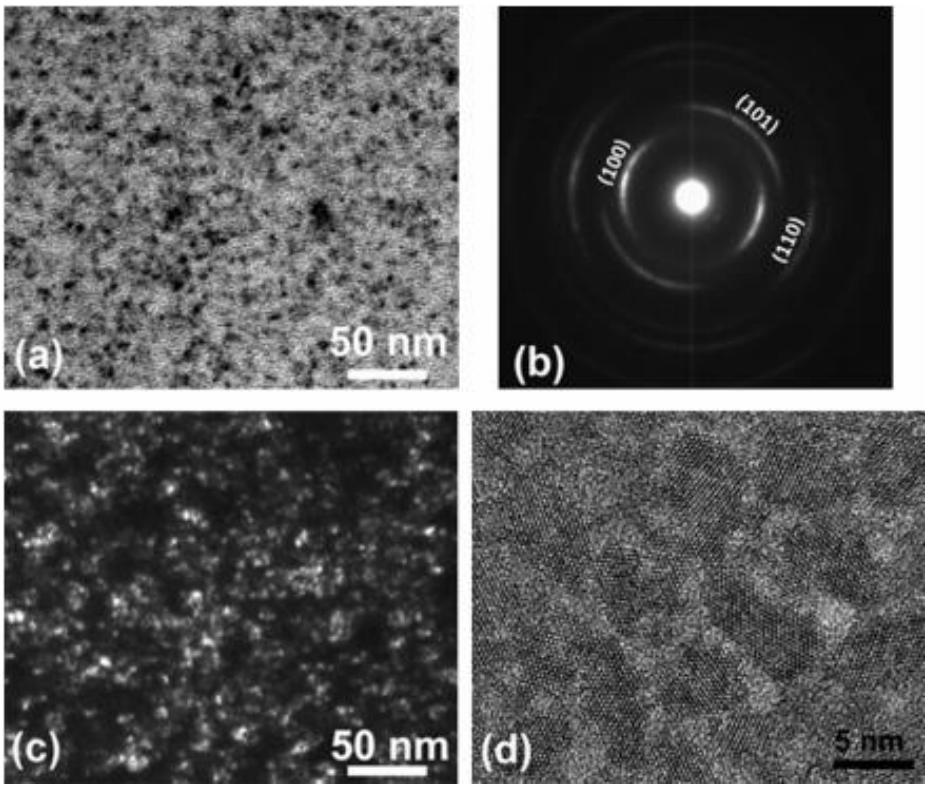

Fig. 4.3.8. (a) Bright field TEM image (b) SAED pattern (c) dark field image obtained using the HfB_2 (100) diffraction in (b). (d) HRTEM image taken from a plan-view TEM foil of the $Hf_{23}B_{55}Si_2C_{11}$ coating.

Fig. 4.3.9(c) is a dark-field TEM image obtained using the (001) diffraction spot in Fig. 4.3.9(b) showing white/dark linear fine structures with their long axis parallel to the [001] direction of HfB_2 and the coating growth direction. The linear white nano-domains have a thickness of ~1 – 2 nm. SAED in Fig. 4.3.9(b) was taken with the incident electron beam parallel to the [110] direction of Si. We have tilted the cross-sectional TEM foil of the $Hf_{23}B_{55}Si_2C_{11}$ coating in the microscope using a double tilt holder by ±30° starting from the [110]-Si. No difference on the SAED patterns of the coating was observed by tilting the TEM foil. In addition, SAED patterns taken from the other areas in the coating

show the same pattern as that in Fig. 4.3.9(b) attesting to the coating uniformity. The SAED pattern of the $Hf_{23}B_{55}Si_2C_{11}$ coating taken from the cross-section TEM foil agrees with its XRD pattern, Fig. 4.3.4(a). The previous XRD and plan-view TEM studies of the $Hf_{23}B_{55}Si_2C_{11}$ coating suggest that the (001) of the hexagonal HfB2 nano-domains is parallel to the coating surface. The arrangement of diffraction spots of the coating in the three-dimensional (3D) space can be schematically illustrated in Fig. 4.3.9(d).

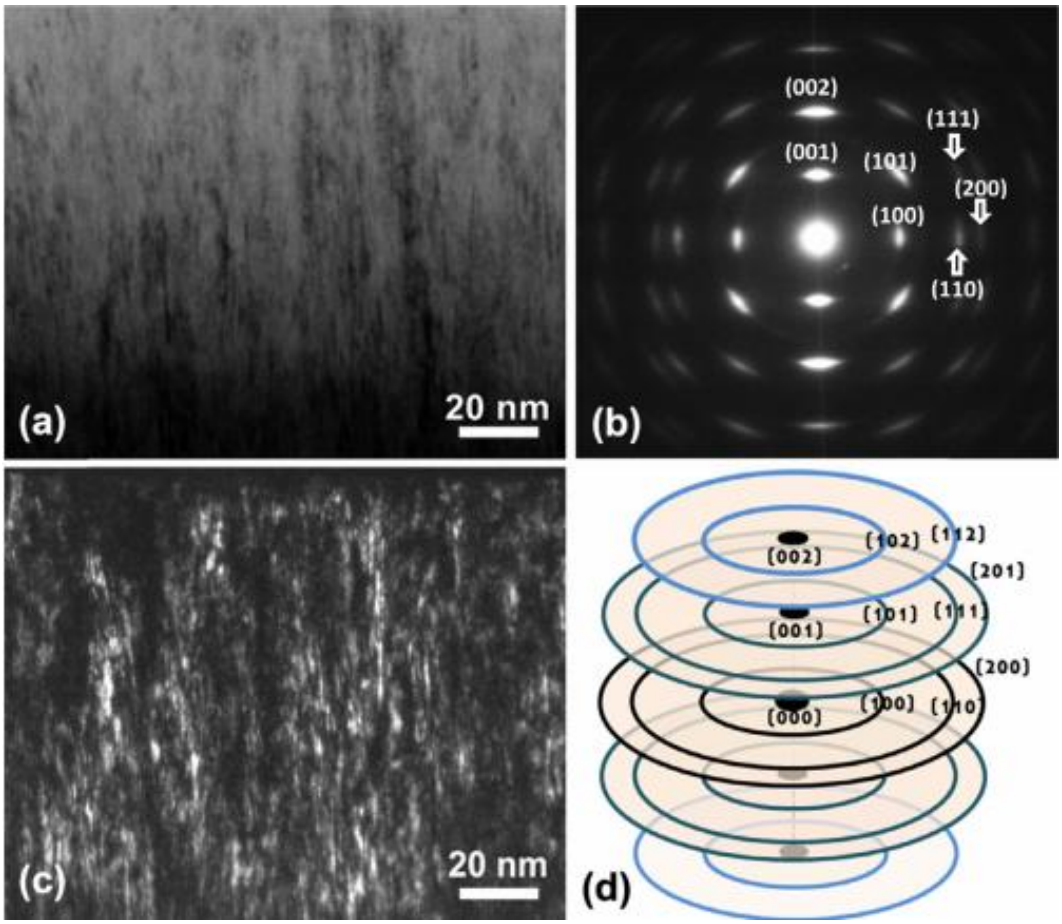

Fig. 4.3.9. (a) Bright field TEM image (b) SAED pattern (c) dark field image of the HfB_2 (001) diffraction in (b) of the $Hf_{23}B_{55}Si_2C_{11}$ coating in a cross-section TEM foil. (d) Schematic illustration of 3D diffraction pattern of this coating.

We have conducted rocking curve scan of the (002) reflection of the $Hf_{23}B_{55}Si_2C_{11}$ coating (Fig. 4.3.4(b)) over a large angle range to investigate the orientation variation of the (001)-HfB_2 with respect to the coating surface over a large area. A strong sharp peak with a Full-Width-Half-Maximum (FWHM) of 10° is obtained. This indicates that the (001) of HfB_2 of the local structures (i.e., nano-needles) is

basically parallel to coating surface with a miss orientation up to a few degrees. The arrangement of the HfB_2 structure within the nano-domains in the $Hf_{23}B_{55}Si_2C_{11}$ coating can be illustrated in Fig. 4.3.10.

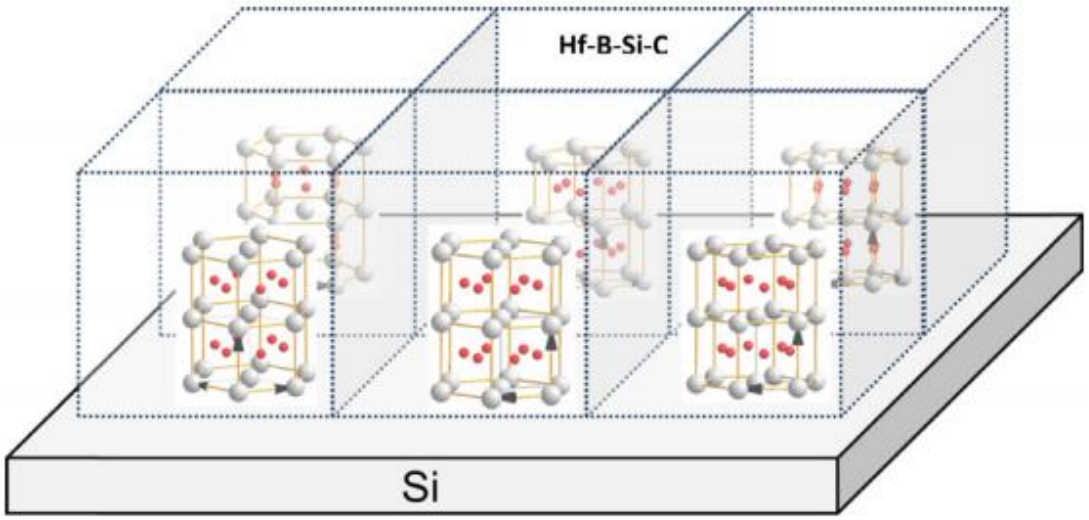

Fig. 4.3.10. Illustration of HfB_2 structure arrangement within the nano-domains in the $Hf_{23}B_{55}Si_2C_{11}$ coating.

Fig. 4.3.11(a) is a HRTEM image taken from an area away from the coating/substrate interface in a cross-section TEM foil of the $Hf_{23}B_{55}Si_2C_{11}$ coating. The nano-needle or linear structures with a width of ~1 - 3 nm are clearly seen. The nano-needles have a single crystal structure with their (001)-HfB_2 parallel to the coating surface. It is also frequently observed that the lattice images in the adjacent nano-needle domains are shifted with respect to each other at the boundary regions along the growth direction. Fig. 4.3.11(b) is a HRTEM image showing the coating/Si substrate interface region in a cross-section TEM foil of the $Hf_{23}B_{55}Si_2C_{11}$ coating, taken with the incident electron beam parallel to the [11 0]-Si. The inset SAED pattern shows an overlap diffraction pattern of the Si-[110] zone and of the $Hf_{23}B_{55}Si_2C_{11}$ coating. Compared to the well-defined diffraction spots in Fig. 4.3.9(b), the diffraction spots of the coating in the inset in Fig. 4.3.11(b) appear as diffraction arcs. This indicates that the nanostructures in the coating near the interface region are smaller, less defined with shorter range ordering than those in the areas away from the interface. HRTEM image of region near the interface shows nano-crystals with only sub-nanometer scale. This more than likely is due to the fact that the coating nucleates on the amorphous SiO_2 layer present on the Si substrate.

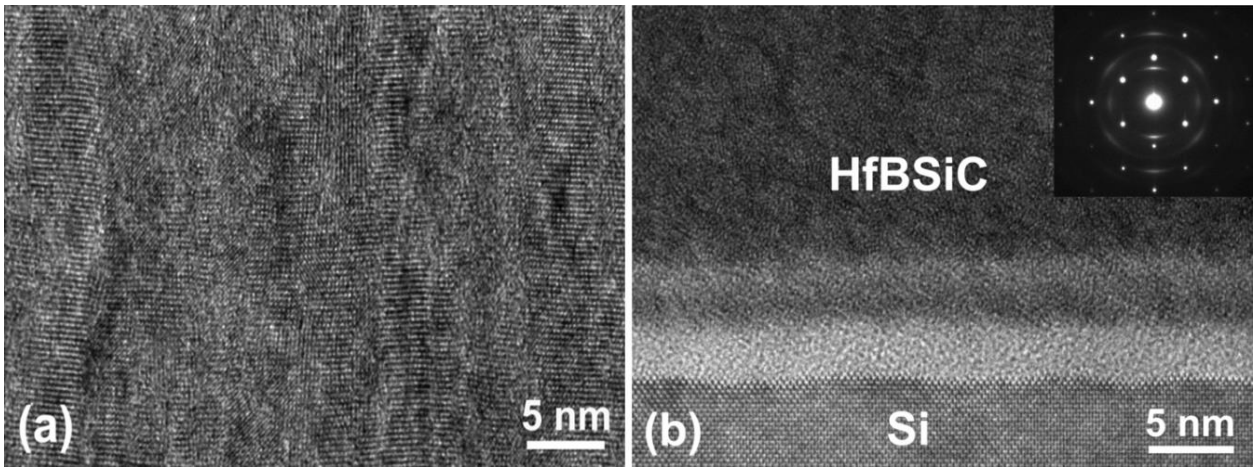

Fig. 4.3.11. (a) HRTEM image of the coating and (b) HRTEM images and the EDP of the interface of the $Hf_{23}B_{55}Si_2C_{11}$ coating taken from a cross-section TEM foil.

Fig. 4.3.12(a) is a plan-view TEM image of the $Hf_{22}B_{54}Si_9C_9$ coating. This coating exhibits an inhomogeneous morphology with the presence of visible nanoparticles. The SAED pattern of the coating (inset in Fig. 4.3.12(a, c)) shows sharp diffraction rings indicating the formation of long range order structures in this coating, and this agrees well with the XRD results. In addition to the diffraction rings (1 0 0), (1 0 1) and (1 0 2)/(1 1 1) of hexagonal HfB_2 (1, 2, 3) observed in Fig. 4.3.13(c), additional diffraction rings are present. They are marked by 4, 5 and 6 with a lattice spacing of ~3.5 Å, 1.7 Å and 1.6 Å which can be identified as the (0 0 1), (0 0 2) and (1 1 0) of HfB_2. Fig. 4.3.12(b) is a plan-view HRTEM image of the $Hf_{22}B_{54}Si_9C_9$ coating. Nanocrystals with a typical size ~2 - 3 nm can be observed. Fig. 4.3.12(c) is a cross-section TEM image of the $Hf_{22}B_{54}Si_9C_9$ coating showing the presence of needle structures (~2 – 5 nm wide). The SAED patterns of the coating taken from this cross-section TEM foil are the same as those taken from the plan-view TEM foil (inset in Fig. 4.3.12(a, c)) indicating that the nanocrystals in the coating are randomly oriented. The SAED pattern matches very well with the XRD pattern shown in Fig. 4.3.4(a). Fig. 4.3.12(d) is a HRTEM image taken from an area in Fig. 4.3.12(c). It shows that each nano-needle structure in this coating is a single crystal structure rather than multi grain structure.

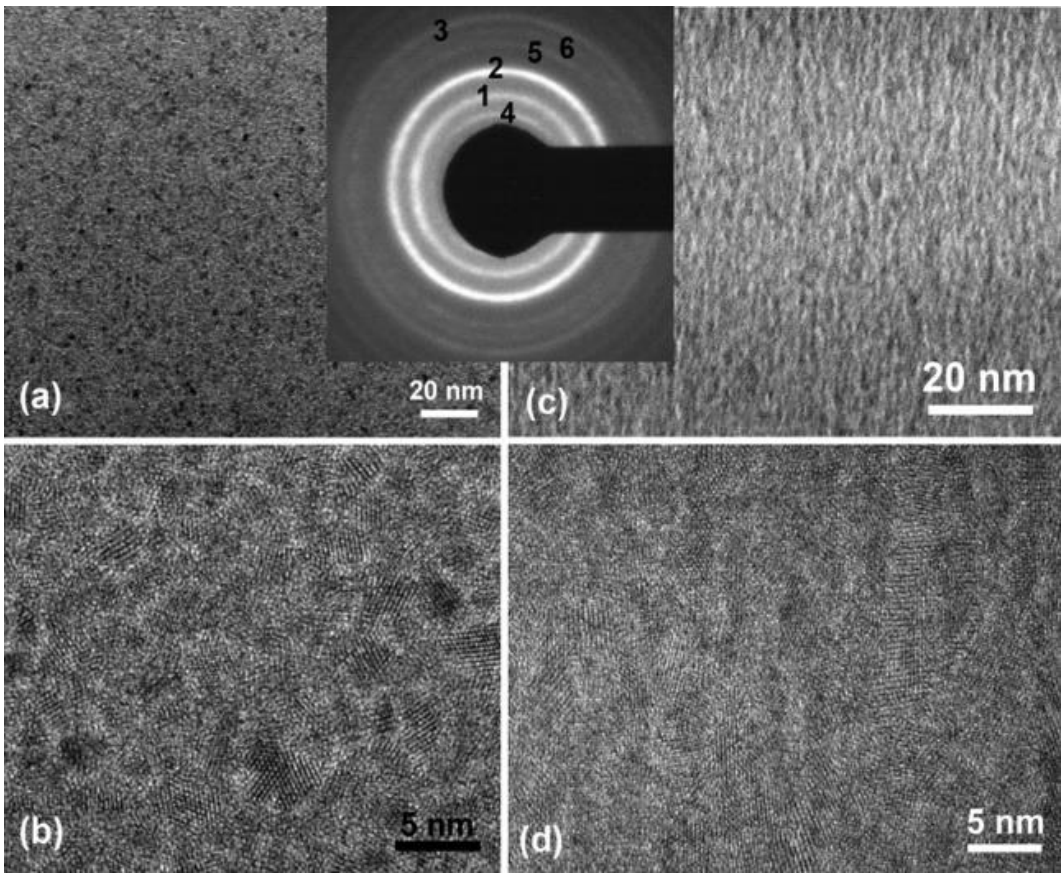

Fig. 4.3.12. (a) TEM and (b) HRTEM image from a plan-view TEM foil of the $Hf_{22}B_{54}Si_9C_9$ coating. (c) TEM and (d) HRTEM image from a cross-section TEM foil of the $Hf_{22}B_{54}Si_9C_9$ coating. The SAED pattern is taken from the plan-view TEM foil.

Fig. 4.3.13(a) is a cross-section TEM image of the same $Hf_{21}B_{28}Si_{35}C_7$ coating showing a rather amorphous structure with the presence of fine needle structures. The needles are typically ~10 nm long and ~2 nm wide with their long axis oriented along the coating growth direction. Fig. 4.3.13(b) is a HRTEM image taken from an area in Fig. 4.3.13(a). It can be seen that each nano-needle is not a single crystal structure. Instead, it is composed of several smaller nano-crystalline domains as evidenced by the presence of the fine lattice fringes in the image. Fig. 4.3.13(c) is a plan-view TEM image of the $Hf_{21}B_{28}Si_{35}C_7$ coating presenting a homogeneous morphology. The inset SAED pattern of the coating shows the presence of diffused rings. The measured lattice spacing of the ring 1, 2 and 3 is about 2.7 Å, 2.2 Å and 1.4 Å which can be identified as the (1 0 0), (1 0 1) and (1 0 2)/(1 1 1) of the hexagonal HfB_2, respectively. Fig. 4.3.13(d) is a plan-view HRTEM image of the $Hf_{21}B_{28}Si_{35}C_7$ coating. Nanocrystals with a size ~1 – 2 nm surrounded by an amorphous structure were observed. So, the

$Hf_{21}B_{28}Si_{35}C_7$ coating consists of a nanocomposite structure of HfB_2 nanocrystalline embedded in an amorphous matrix.

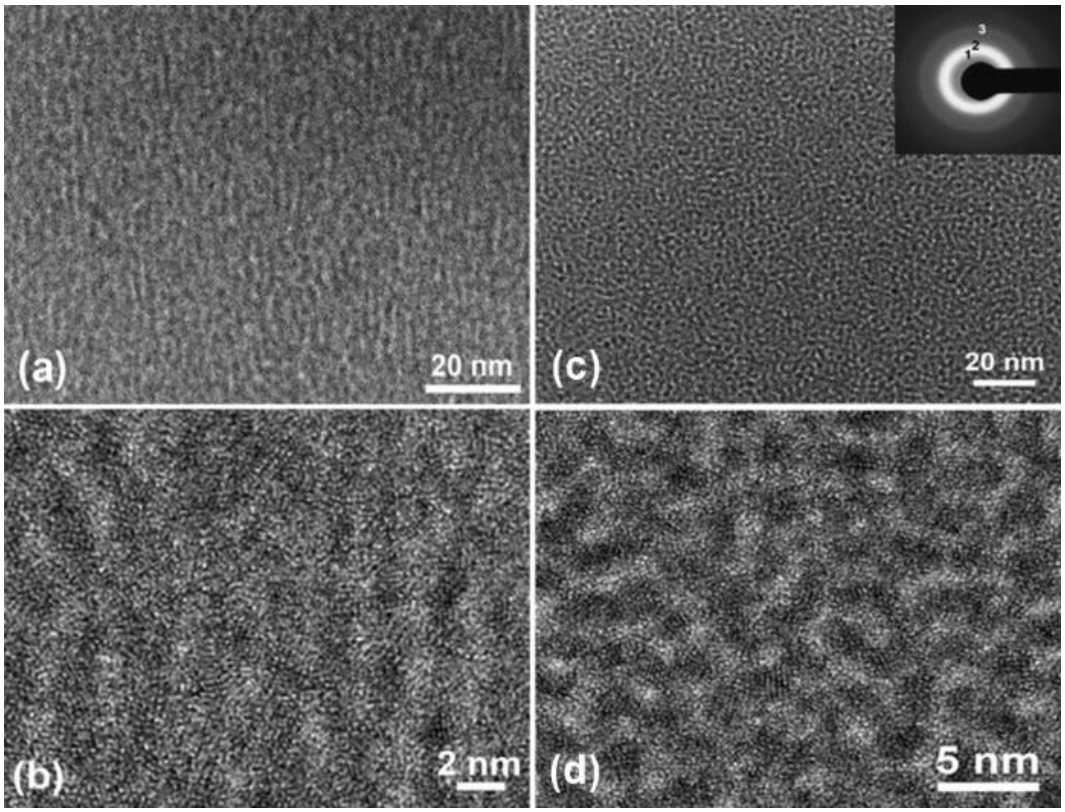

Fig. 4.3.13. (a) TEM and (b) HRTEM image showing the fine lattice fringes from a cross-section TEM foil of the $Hf_{21}B_{28}Si_{35}C_7$ coating. (c) TEM and SAED (d) HRTEM image from a plan-view TEM foil of the $Hf_{21}B_{28}Si_{35}C_7$ coating.

4.3.5 Effect of Si Content on the Microstructure of Hf-B-Si-C Coatings

The observed microstructures of the Hf-B-Si-C coatings with different Si content provide a good insight for understanding the relationship between microstructure and the coating properties. The Si free $Hf_{27}B_{57}C_8$ coating consists of HfB_2 nano-columnar structures with a length of about 50 - 60 nm and a width of ~ 5 - 10 nm. Most of the nano-columnar structures connected directly without the formation of amorphous boundaries. The nano-columnar structures have a single crystal structure of HfB_2 whose orientation is highly preferred with the (001) tilted $\sim 30^\circ$ away from the coating surface. The composition of the coating can be expressed using the following decomposition:

$$Hf_{27}B_{57}C_8 \Rightarrow Hf_{27}B_{54} + B_3C_8 \Rightarrow 27 \times (HfB_2) + B_3C_8$$

The B_3C_8 can either dissolve into HfB_2 forming a solid solution or exist in the boundaries. However, both the C content in the HfB_2 grains and the volume fraction of the B_3C_8 boundaries are very small. This hypothesis is consistent with the XPS results that the binding energy of Hf4f and B1s of this coating is very close to the value reported in HfB_2 coating [114]. Such a coating microstructure induces a high hardness of 37 GPa and a high compressive stress of 4.9 GPa. Slight incorporation of Si (2 at%) significantly changes the microstructure of the coating by: (i) realigning the textured HfB_2 nanocolumnar structures with the (001) parallel to the coating surface in the $Hf_{23}B_{55}Si_2C_{11}$ coating; (ii) reducing the nano-needle structure size to a length of ~20 – 30 nm and a width of ~5 nm; and (iii) forming a layer of ~1 nm amorphous structure in the boundaries between nano-needle structures. A quite significant boundary and grain thickness ratio is shown in the range from 1/10 to1/5. The composition of the $Hf_{23}B_{55}Si_2C_{11}$ coating can be expressed using the following decomposition:

$$Hf_{23}B_{55}Si_2C_{11} \Rightarrow Hf_{23}B_{46} + B_9Si_2C_8 \Rightarrow 23 \times (HfB_2) + B_9Si_2C_8$$

We speculate that $B_9Si_2C_8$ forms an amorphous structure in the boundaries. The ratio between the atoms in the boundaries and HfB_2 nanocrystals is 19:69 ≈ 1:3.63. The XPS results of the $Hf_{23}B_{55}Si_2C_{11}$ coating show that the binding energy of Hf 4f is slightly lower than that in HfB_2 [114] but higher than that in $HfSi_2$ [115], and the binding energy of B 1s is slightly lower than that in HfB_2 [114] but slightly higher than that for B in Si [116]. This downwards shift of the BE of Hf 4f and B1s is likely due to formation of Si Hf and Si B bonds in the boundaries. The $Hf_{23}B_{55}Si_2C_{11}$ coating with such a microstructure possesses a similar high hardness but with over 60% reduced compressive stress compared to the Si-free coating. Regarding the crystalline part of the coating, the stress relaxation may be explained by the realignment of the crystallographic orientation of the nanocolumns, and by the fact that the Si incorporation decreases the size of the nanocolumns. Thus, interstitials implanted into the nanocolumns (either directly implanted Ar atoms, or also knock on implanted B and C atoms), which are probably responsible for the high compressive stress in the Si-free Hf–B–C coating, can more easily diffuse to the amorphous boundary regions. Further increase in the Si content in the $Hf_{22}B_{54}Si_9C_9$ coating causes the nano-needle structures in the coating to be diminished in size. Each nano-needle is composed of multi nanocrystals instead of a single crystal structure. Those nanocrystals are distributed with their crystalline orientation randomly oriented and no more texture structure was formed in the

coating. Reducing the grain size will substantially increase the volume fraction of the boundaries in the coating. Considering the decomposition of the coating composition $Hf_{22}B_{54}Si_9C_9$ can be expressed by

$$Hf_{22}B_{54}Si_9C_9 \Rightarrow Hf_{22}B_{44} + B_{10}Si_9C_9 \Rightarrow 22 \times (HfB_2) + B_{10}Si_9C_9$$

The $B_{10}Si_9C_9$ forms the disordered structure in boundaries. Then, the ratio between the atoms in the boundaries and HfB_2 nanocrystals is 28:66 ≈ 1:2.36. The boundary fraction increase is accomplished by the increase of the Si content in the coating. Higher Si content in the coating results in more Si-Hf and Si-B bonds in the coating which produce further downwards shift of the BE of Hf 4f and B1s, as observed in the XPS spectra. Increasing the fraction of the Si-rich boundary structure can be considered as a major driving force for the reduction of the compressive stress in the coating and the improvement of high oxidation resistance at elevated temperatures. The coating with high Si content, $Hf_{21}B_{28}Si_{35}C_7$ has a nanocomposite structure of HfB_2 nanocrystalline (1 – 2 nm) embedded in an amorphous matrix. It can be seen that the volume fraction of the amorphous region is higher than that of the nanocrystalline. Considering a similar decomposition can be expressed as

$$Hf_{21}B_{28}Si_{35}C_7 \Rightarrow Hf_{14}B_{28} + B_7Si_{35}C_7 \Rightarrow 14 \times (HfB_2) + B_7Si_{35}C_7$$

The $B_7Si_{35}C_7$ Forms amorphous structure, the ratio between the atoms in the amorphous structure and HfB_2 nanocrystals is 49:42 ≈ 1.17:1. The BE of the Hf 4f, Si 2p and B1s in this coating is about 14.5 eV, 100.5 eV and 187.5 eV, respectively. The BE of Hf 4f and B1s in this coating is very close to that in $HfSi_2$ (14.65 eV in [115]) and that for B in Si (186.8-187.5 eV in [116]), respectively. It is more than likely that Si in the coating is located in the amorphous structure. The $Hf_{21}B_{28}Si_{35}C_7$ with a dominant amorphous structure also demonstrates improved oxidation resistance showing almost no mass change after annealing up to 800 °C.

4.3.6 Summary

In summary, four Hf-B-Si-C coatings with composition of $Hf_{27}B_{57}C_8$, $Hf_{23}B_{55}Si_2C_{11}$, $Hf_{22}B_{54}Si_9C_9$ and $Hf_{21}B_{28}Si_{35}C_7$ were deposited by pulsed magnetron sputtering. The Si-free $Hf_{27}B_{57}C_8$ coating possessed high hardness and high compressive stress, and consisted of hexagonal HfB_2 nano-columnar structures with a length of about 50 - 60 nm and a width of ~5 - 10 nm. The nano-columnar structures exhibit HfB_2 single crystal structure and show a preferred orientation with the (001) tilted ~30° away from the coating surface. No amorphous boundaries were formed between the nano-columnar

structures. Incorporation of 2% Si in the $Hf_{23}B_{55}Si_2C_{11}$ coating results in the refinement of the nano-columnar structures that showed a length of ~20 - 30 nm and a width of <5 nm, surrounded by ~1 nm thick amorphous boundaries. All the nano-columnar structures are uniquely oriented with (001) parallel to the coating surface. Realignment of the crystallographic orientation of the nano-columnar structures and formation of thin amorphous boundaries result in a 60% reduction of the compressive stress while maintaining a high hardness and improving the oxidation resistance. The $Hf_{22}B_{54}Si_9C_9$ coating consists of refined nano-needle structures (~2 - 3 nm wide) being composed of randomly oriented multi nanocrystals instead of a single crystal structure, while the $Hf_{21}B_{28}Si_{35}C_7$ coating consists of a nanocomposite structure of HfB_2 nanocrystalline (1 - 2 nm) embedded in an amorphous matrix. These results indicate that the incorporation of Si into the coating results in microstructural refinement and eventual formation of an amorphous structure. Increasing the Si content results in increasing the volume fraction of the amorphous boundaries, refining the microstructure as well as modifying the orientation of the HfB_2 crystal structures, which significantly reduce the compressive stress and improve the oxidation resistance of the coatings at elevated temperatures.

4.4 Hf-Si-N Coatings

Hafnium nitride is the most refractory material with superior hardness compared to other carbides and nitrides at higher temperatures, and exhibits a melting point of 3305 °C. Besides, the stoichiometric HfN is the most stable compound among the transition metal nitrides at higher temperatures. Therefore, HfN is an excellent coating material for high temperature applications [118-120]. Incorporation a third element to form the transition metal based ternary system [(Ti, X) N, where X= B, C. Si, Al, etc.] has already been approved to be a promising method for improving the hardness and oxidation resistance. These coatings have shown enhanced hardness by adjusting the crystalline size based on the Hall-Petch law and improved oxidation resistance with the formation of amorphous phase surrounding the crystallites [121-123]. Compared to the work has been done on Ti-Si-N and Zr-Si-N ternary systems, little is known about the Hf-Si-N.

In this part, Hf-Si-N coatings were deposited on silicon substrates using reactive magnetron sputtering with single Hf and Si targets. The fabrication details of the Hf-Si-N coatings have been

described in Chapter 3.1.3. XRD, XPS and HRTEM were applied to study the composition effect on the microstructure evolution and mechanical properties of the Hf-Si-N coatings.

4.4.1 XPS Studies

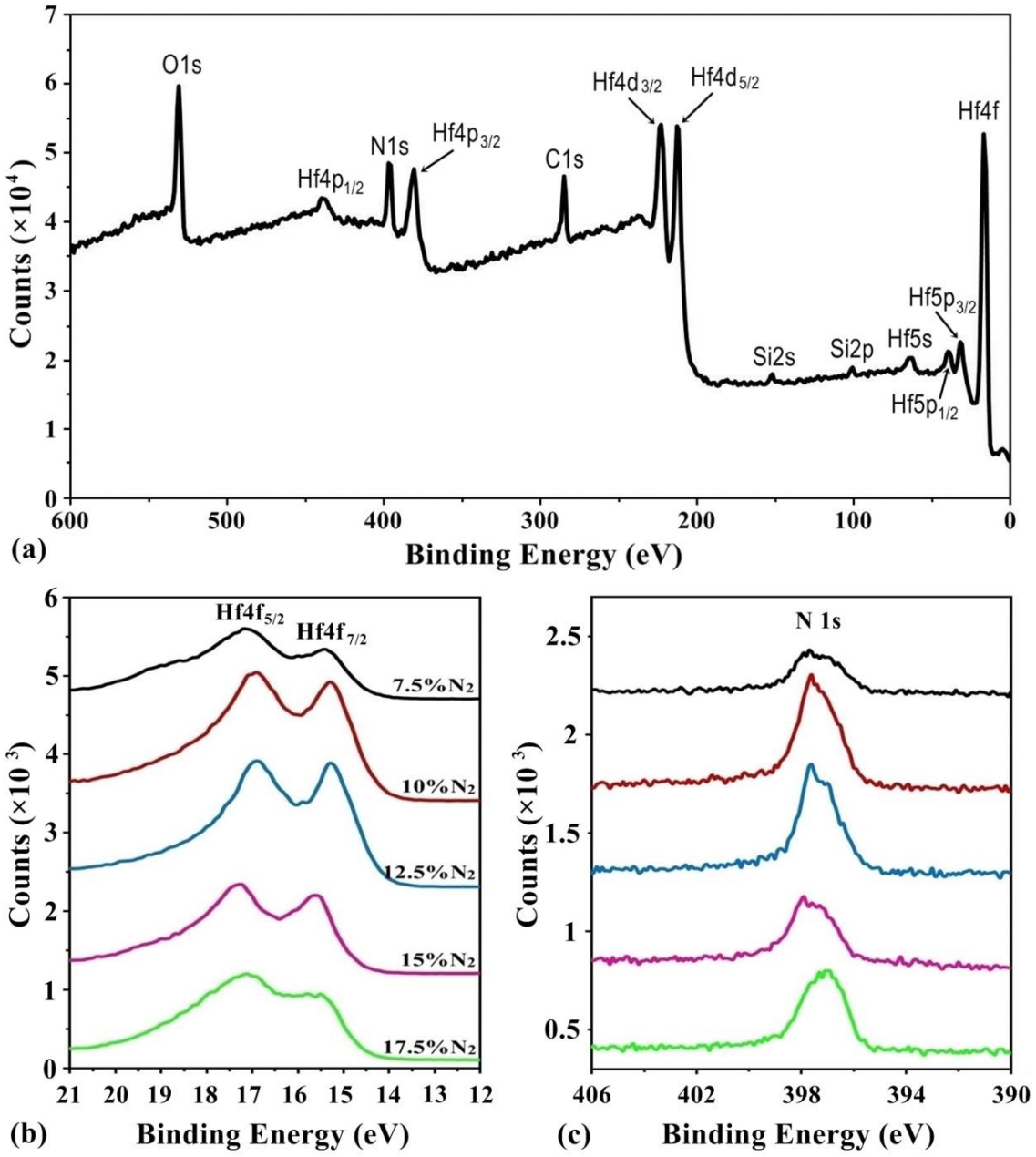

Fig. 4.4.1. (a) General XPS survey spectrum of Hf-Si-N coating deposited with 17.5%N (F5) in the Ar/N_2 gas mixture and high resolution XPS spectra of peak (b) Hf4f and (c) N1s of the Hf-Si-N coatings with nitrogen fraction of 7.5% (F1), 10% (F2), 12.5% (F3), 15% (F4) and 17.5% (F5) in the N_2/Ar gas mixture during the deposition.

Fig. 4.4.1 (a) presents the XPS survey spectrum of the Hf-Si-N coating deposited with 17.5% nitrogen (F5) in the Ar/N_2 gas mixture. This spectrum is selected to represent the spectra of all coatings since they exhibit mainly the presence of Hf, Si, N, C and O. The presence of oxygen may be attributed to the oxygen impurities that remain on the walls of sputtering chamber and oxidation of the coatings surface in air (most of the C is also from contamination). With the increase of nitrogen fraction in the Ar/N_2 gas mixture during the deposition, both the content of nitrogen and silicon increase, but the content of Hf decrease [content figure not shown here]. This result indicates that the deposition rate of both hafnium and silicon target are highly influenced by the fraction of nitrogen in the sputtering atmosphere. When the nitrogen flow rate was low, the hafnium was deposited at a very high rate which may produce a not stoichiometric nitride phase with Hf metal phase. At the same time, very small amount of silicon is detected in the coating because the plasma of silicon from the RF power was too weak compared to hafnium produced by DC power during the deposition which may result in silicon atoms were stroke away from the deposition path. As the nitrogen fraction was increased, the deposition rate of hafnium decreased due to a very common phenomenon during the reactive sputtering “target poisoning effect”. The “target poisoning effect” means the compound coating is not only form on the substrate, but also on the sputtering target. The deposition rate of silicon increased due to two main factors: 1) The silicon target controlled by RF power can avoid the target poisoning effect; 2) The hindering factor produced by hafnium plasma was reduced along with the decrease in deposition rate of hafnium.

Fig. 4.4.1(b) shows the evolution of the high resolution Hf4f peaks of the Hf-Si-N coatings with the increasing of N fraction in the Ar/N_2 gas mixture. The theoretical metallic Hf exhibits doublet peak $Hf4f_{5/2}$ at around 16 eV and $Hf4f_{7/2}$ at around 14.3 eV with a difference of ~1.7 eV. With the introduction of nitrogen into the gas mixture, broad bands at higher binding energies associated with the formation of hafnium nitride are observed. This broad band has its $Hf4f_{7/2}$ range from 15.3 eV to 15.6 eV, indicating the compositional differences in the coating formed [124-125]. Fig. 4.4.1(c) shows the evolution of the high resolution N1s peaks of the Hf-Si-N coatings with the increasing of N fraction in the Ar/N_2 gas mixture. With the increasing of nitrogen fraction, the N1s peak shifts to lower binding energy [126].

4.4.2 XRD Studies

Crystal structure and preferred orientation of Hf-Si-N coatings were analyzed using XRD before conducting systematic microstructure studies by TEM. Fig. 4.4.2 present the XRD patterns for all five Hf-Si-N coatings produced in different nitrogen fraction from 7.5% to 17.5% in the gas atmosphere.

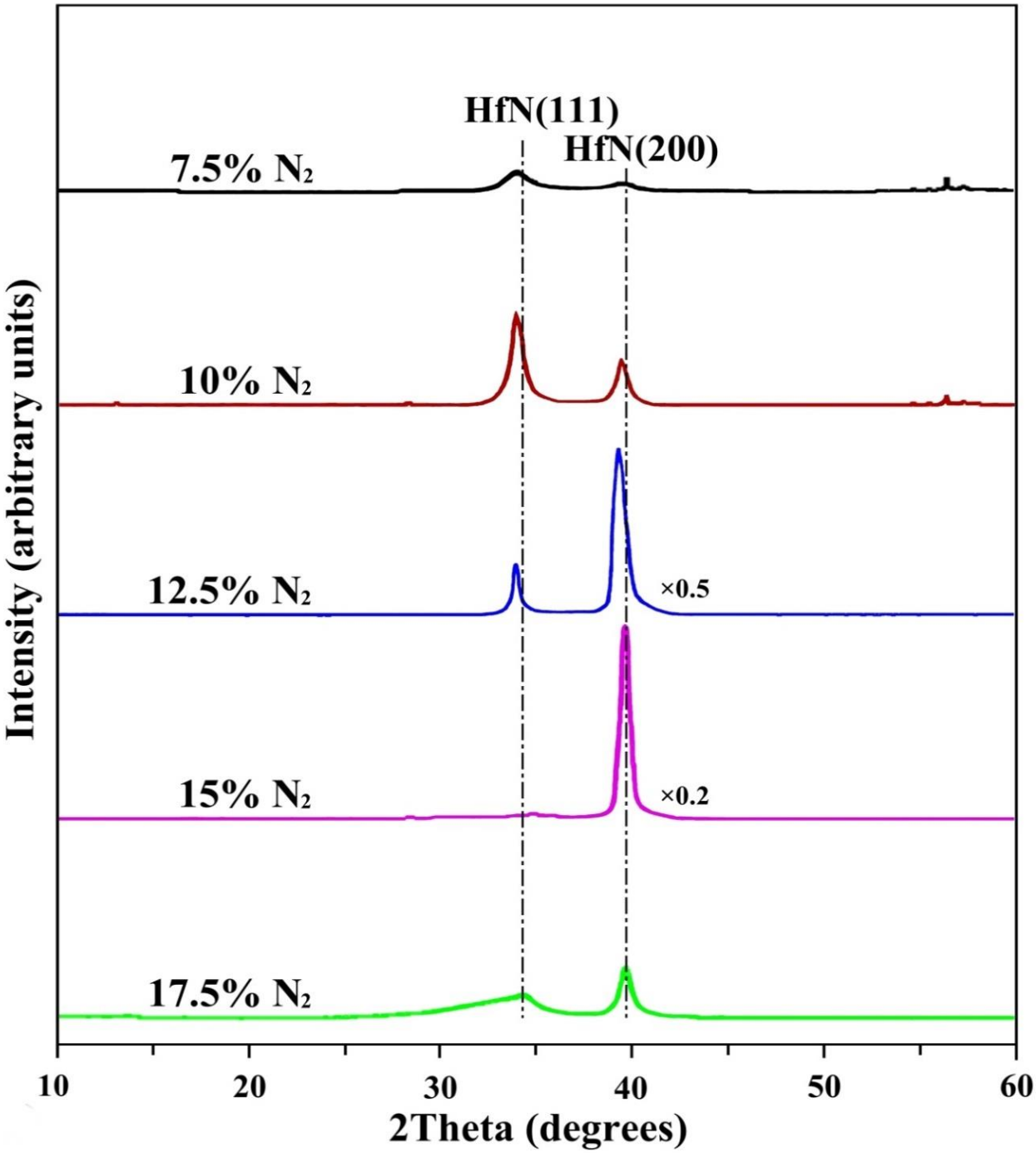

Fig. 4.4.2. XRD patterns of the Hf-Si-N coatings deposited with different nitrogen fraction.

Taking an overview of all the coatings, the mainly present crystal phase is the face-centered cubic hafnium nitride. The XRD pattern of Hf-Si-N deposited in 7.5%N shows two broad diffraction peaks at 2θ-angle of 33.96° and 39.45°, corresponding to the lattice spacing of 2.64 Å and 2.28 Å. These two peaks can be identified as the (111) and (200) of stoichiometric HfN (a= 4.525 Å) with face centered cubic structure (Card No. 33-0592 in Ref. [74]). The peaks are shifted to lower angles compared to the peak position of 34.303° and 39.818° with lattice spacing of 2.61 Å and 2.26 Å according to the standard PDF card of bulk HfN. Slightly higher lattice parameters compared to the bulk samples have been reported commonly for nitride coatings. This is due to the fact that the mobility of dislocations is low in nitrides at temperatures below 1000 °C which may result in the stress generation in coatings [127]. The peak shifting in this coating probably due to two reasons: a) Considering the nitrogen fraction in the gas mixture is low and the deposition rate of Hf is high at the same time, some hafnium atoms may incorporate into the lattice which cause the expansion of the lattice; b) The high compressive stress (~4.2 GPa) existed in the coating which related to the high energy delivered to the coatings by Ar atoms reflected from the sputtered target [66,128].

The XRD pattern of Hf-Si-N deposited in 10%N shows two peaks at 2θ positions of 33.98° and 39.48°, corresponding of lattice spacing of 2.64 Å and 2.28 Å, respectively. These peaks can also be identified as the (111) and (200) of the fcc HfN. These peaks exhibit slight shift to lower angles, too. It can be observed that the intensity of the two peaks in the coating is much stronger than those peaks in the former coating, and (111) is the preferred orientation.

The XRD spectrum of the coating deposited in 12.5% nitrogen in the gas mixture shows two sharp peaks which can be as the (111) and (200) of the fcc HfN. The intensity of the (111) and (200) peaks is further increased compared with the peaks in the coating deposited in 10% nitrogen in the gas mixture. An obvious increment in the preferred (200) orientation along with the concomitant attenuation in (111) texture is clearly observed.

The XRD spectrum of the coating deposited in 15% nitrogen in the atmosphere shows only one sharp peak with tremendously increased intensity. This peak is located at a 2θ position of 39.67°, corresponding to a lattice spacing of 2.27 Å which can be identified as the (200) of fcc HfN. The (111) peak observed in the previous coatings is invisible in this coating. This result indicates that this coating

exhibits a strong preferential orientation with only the (200) of HfN parallel to the coating surface. This (200) peaks is shifted slightly left compared to the peak position of 39.818° with lattice spacing of 2.26 Å. With the increase of silicon content in the coating, smaller sized Si may bond with N which result in the diffraction peak shift right. The - 0.15° peak shift should contribute from both the compressive stress (-2.3 GPa) and the lattice contraction caused by the formation of a substitution solid solution by replacing Hf atoms with Si atoms.

A further increasing of nitrogen fraction up to 17.5% results in a significant decrease in the intensity of the HfN (200) diffraction peak. A very broad HfN (111) peak with is also observed. The shoulder presents on the left of the (111) peak probably due to the amorphous silicon nitride formed with the increasing content of silicon and nitrogen. The crystal orientation is still remained along the (200) plane. These (111) and (200) peaks are located exactly on the 2θ position of standard fcc HfN should also contribute from both the compressive stress (-1.1 GPa) and the increase of silicon content in the coating.

The total energy in the coating can be calculated as the summation of the strain energy and surface energy. The evolution in the preferred orientation can be concluded as the consequence of the competition between the strain energy and surface energy. HfN exhibits similar structure to NaCl which has been demonstrated that the (200) plane has the lowest surface energy and the (111) plane exhibits lower strain energy than the (200) plane. The coatings deposited with nitrogen fraction of 7.5% and 10% all exhibit relative high residual stress, the (111) preferred orientation were resulted from the high energy of bombarding particles that delivered to the coatings, in which strain energy is dominant. With the increasing of nitrogen fraction, the energy delivered to the coatings reduce which leading to the surface atoms are arranged into the (200) plane with the lowest surface energy. The (200) preferred orientation suggests that the strain energy was small and the growth process was surface energy dominated [129-132].

4.4.3 HRTEM Studies

In order to understand the effect of nitrogen content on the microstructure of the Hf-Si-N coatings, systematically TEM studies were conducted. The five Hf-Si-N coatings deposited in different nitrogen fraction of 7.5%, 10%, 12.5%, 15% and 17.5% in the gas mixture are recognized as F1, F2, F3, F4 and

F5. The coating thickness measured from the cross-section TEM images is about 1.0 μm, 880 nm, 1.0 μm, 900 nm and 700 nm for F1 to F5 respectively.

Fig. 4.4.3 shows a comparison among the bright-filed TEM image taken from plan-view TEM foils of Hf-Si-N coatings deposited with different nitrogen fraction in the gas mixture. Fig. 4.4.3(a) is the bright-field TEM image of F1 which presents an inhomogeneous morphology with dark grain structures with the size less than 10 nm.

With the increasing of nitrogen fraction in the gas mixture, the size of the grains increase. As shown in Fig. 4.4.3(b) of F2 which presents grains distributed on the plan-view coating with the size about 10 - 20 nm. Fig. 4.4.3(c) shows the plan-view morphology of F3 which exhibits much bigger grains about 20 - 50 nm separated by very clear grain boundaries. A further increasing the nitrogen fraction in the gas mixture up to 15% results in a gradually decreasing grain size. Fig. 4.4.3(d) is taken from F4 which presents grains with clear boundaries but with smaller size about 15 - 40 nm compared with that in F3. Fig. 4.4.3(e) presents morphology of F5 which shows small grains with relative uniform size around 10 nm separated by thicker boundaries. Fig. 4.4.3(f) presents the SAED of F2 which shows a diffraction ring pattern. No strong texture structure was formed in this coating. The lattice spacing of the inner four rings 1, 2, 3, 4 is about 2.62 Å, 2.27 Å, 1.61 Å and 1.38 Å, respectively, corresponding to the (111), (200), (220) and (311) plane of the fcc HfN structure. The lattice spacing measured from the SAED is little larger than that of bulk HfN may due to the incorporation of hafnium atoms since most of the stress in the coating has been released after TEM sample preparation. This result is in consistent with the result obtained from the XRD analysis. Fig. 4.4.3(g) shows the electron diffraction pattern of F4 which is also diffraction ring pattern. Except the very diffused most inner ring 1, the ring 2, 3, 4 is about 2.25 Å, 1.59 Å and 1.36 Å, respectively, corresponding to the (200), (220) and (311) plane of the fcc HfN structure. The lattice spacing is a little bit smaller than the standard HfN may due to the increase of silicon content leading to the formation of a substitution solid solution. Fig. 4.4.3(h) shows the electron diffraction ring of F5. The lattice spacing of the inner four rings 1, 2, 3, 4 is about 2.59 Å, 2.24 Å, 1.58 Å and 1.34 Å, respectively, corresponding to the (111), (200), (220) and (311) plane of the fcc HfN structure.

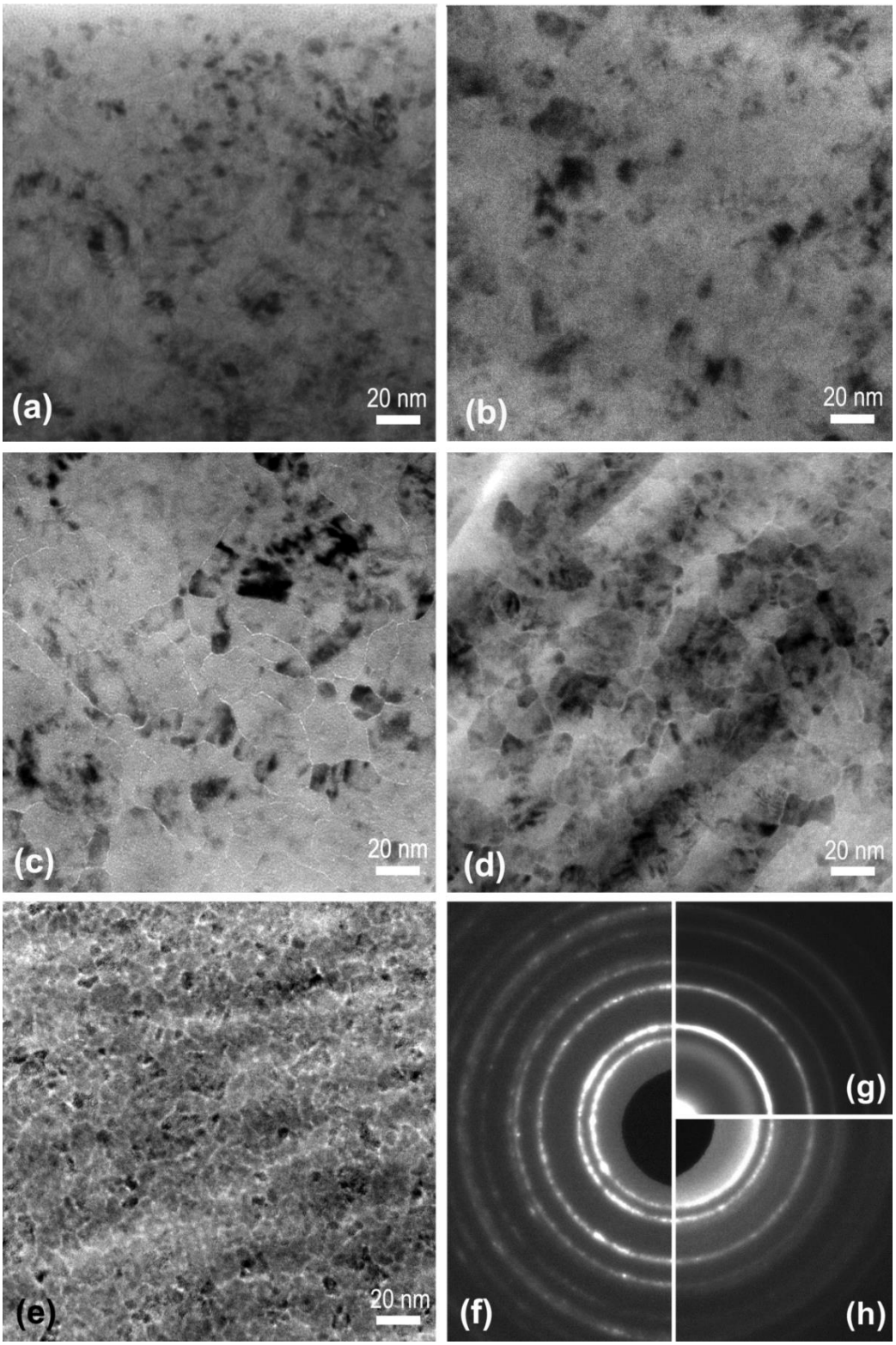

Fig. 4.4.3. Bright-field TEM image of Hf-Si-N coating deposited with nitrogen fraction of (a) 7.5% (b) 10% (c) 12.5% (d) 15% (e) 17.5% in the gas mixture and partial SAED pattern of coating deposited with (f) 10% (g) 15% (h) 17.5% in the gas mixture taken from plan-view TEM foil.

The diffraction ring which correspond to the (111) plane is broad and the inner part of it is diffused, this is also consistent with the shoulder present on the left of the (111) peak in XRD probably due to the presence of an amorphous phase of silicon nitride as both the silicon content and nitrogen content were further increased in the coating.

A comparison of boundary structure among the coatings deposited with different nitrogen fraction in the gas mixture is shown by the plan-view HRTEM images in Fig. 4.4.4. Fig. 4.4.4(a) is a plan-view HRTEM image of F1 which presenting small grains with varied size from 5 – 10 nm are inter-connected with adjacent grains directly without very clear boundaries. Fig. 4.4.4(b) is taken from F2 which shows grains with the size about 10 – 20 nm oriented in different directions are separated with continuous and thin boundaries. Fig. 4.4.4 (c) is an HRTEM image of F3 exhibits an individual grain with a size about 25 nm being isolated from other adjacent grains by very clear boundaries around it. The size of grains in this coating is varied from 20 to 50 nm, which reaches maximum among all these five deposited coatings. With further increase the nitrogen fraction in the gas mixture, the size of grains gradually reduces. As the morphology of F4 shown in Fig. 4.4.4(d), smaller grains compared with those in F3 are separated by amorphous boundaries with the thickness about 0.5 nm. Nano crystalline domain structures separated by thicker amorphous boundaries are observed in F5, as shown in Fig. 4.4.4(e). The nano-domains have a typical size about 8 nm and the thickness of the boundaries is more than 1 nm.

Fig. 4.4.5(a) is a cross-section bright field TEM image of the coating deposited with nitrogen fraction of 7.5% (F1) shows the small columns with the lateral size less than 10 nm. Fig. 4.4.5(f) is a SAED pattern obtained from the cross-section TEM foil of F1 presents a diffraction ring pattern without obvious preferred orientation. The lattice spacing of the inner rings 1, 2, 3 and 4 is about 2.62 Å,2.28Å, 1.61 Å and 1.38 Å, corresponding to the (111), (200), (220) and (311) plane of the fcc HfN structure, respectively. This result is same as the SAED analysis from the plan-view foil which further demonstrated the incorporation of hafnium atoms into the mainly present HfN phase. Fig. 4.4.5(b) is a cross-section bright field TEM image of the coating deposited with nitrogen fraction of 10% (F2) shows columnar structure but with larger width compared to F1. The SAED pattern taken from this coating as shown in Fig 4.4.5(g) shows the similar feather as observed in Fig. 4.4.5(f).

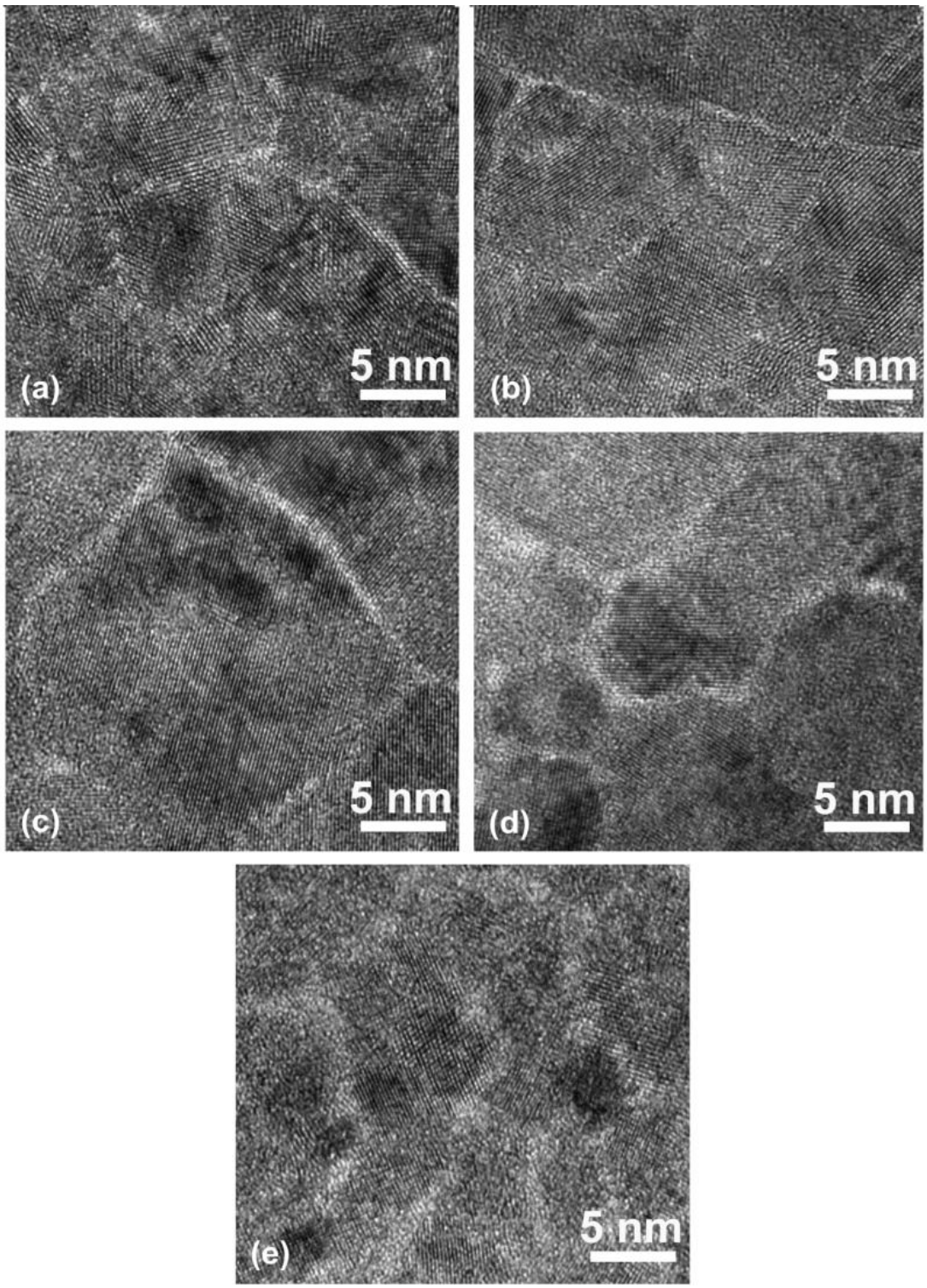

Fig. 4.4.4. Plan-view HRTEM image showing the boundary structure of Hf-Si-N coating deposited with nitrogen fraction of (a) 7.5% (b) 10%(c) 12.5%(d) 15%(e) 17.5% in the gas mixture.

Fig. 4.4.5(c) is a cross-section bright field TEM image of the coating deposited with nitrogen fraction of 12.5% (F3) shows the presence of columnar structures. The lateral size of the columnar structures varies from ~20 nm to ~50 nm. This result is match with the grain size analysis in the plan-view TEM analysis which shows the cross-section view of the columnar structures. Fig. 4.4.5(h) is a SAED pattern taken from the cross- section TEM foil of F3 appears as diffraction rings. The measured lattice spacing of the four inner rings is 2.62 Å, 2.26 Å, 1.60 Å and 1.37 Å which can be identified as the (111), (200), (220) and (311) of the fcc HfN, respectively. The intensity of diffraction spots on the (200) diffraction ring parallel to the coating growth direction is stronger compared to the other diffraction spots indicates that this coating is slightly (200) textured.

Fig. 4.4.5(d) is a cross-section bright filed TEM image of the coating deposited with nitrogen fraction of 15% (F4) which presents very clear multilayer structure with columnar structures grown on it. The inset in Fig. 4.4.5(d) is a nano electron diffraction pattern taken from the multilayer. The analysis of the nano electron diffraction shows the d-spacing between each monolayer is about 4 nm.

Similar multilayer structure with smaller thickness and columnar structures of smaller lateral size is also observed from the cross-section bright field TEM image of F5 as shown in Fig. 4.4.5(e). Multilayer structures are only observed from the coating deposited with the nitrogen fraction of 15% and 17.5%. Fig. 4.4.5(i) is a SAED pattern taken from a cross-section TEM foil of F4 presents a well-defined array of diffraction arcs. The inner three groups of diffraction arcs are located on the diffraction rings of (111), (200) and (220), respectively. The inhomogeneous intensity distribution of the diffraction arcs indicates the formation of strong textured structure.

Further studies show this diffraction pattern consists of diffraction spots from two pairs of diffraction patterns. It can be concluded that the set of (2n 0 0) (n=±1, ±2, ±3…) diffraction spots are shared by two diffraction patterns in zone axis of $[01\bar{1}]$ and [010] resulting in the strongly enhanced diffraction intensity. This set of spots are periodically distributed along with the coating growth direction, such as (200) and $(\bar{2}00)$, this is consistent with the strong preferred (200) diffraction shown in XRD analysis.

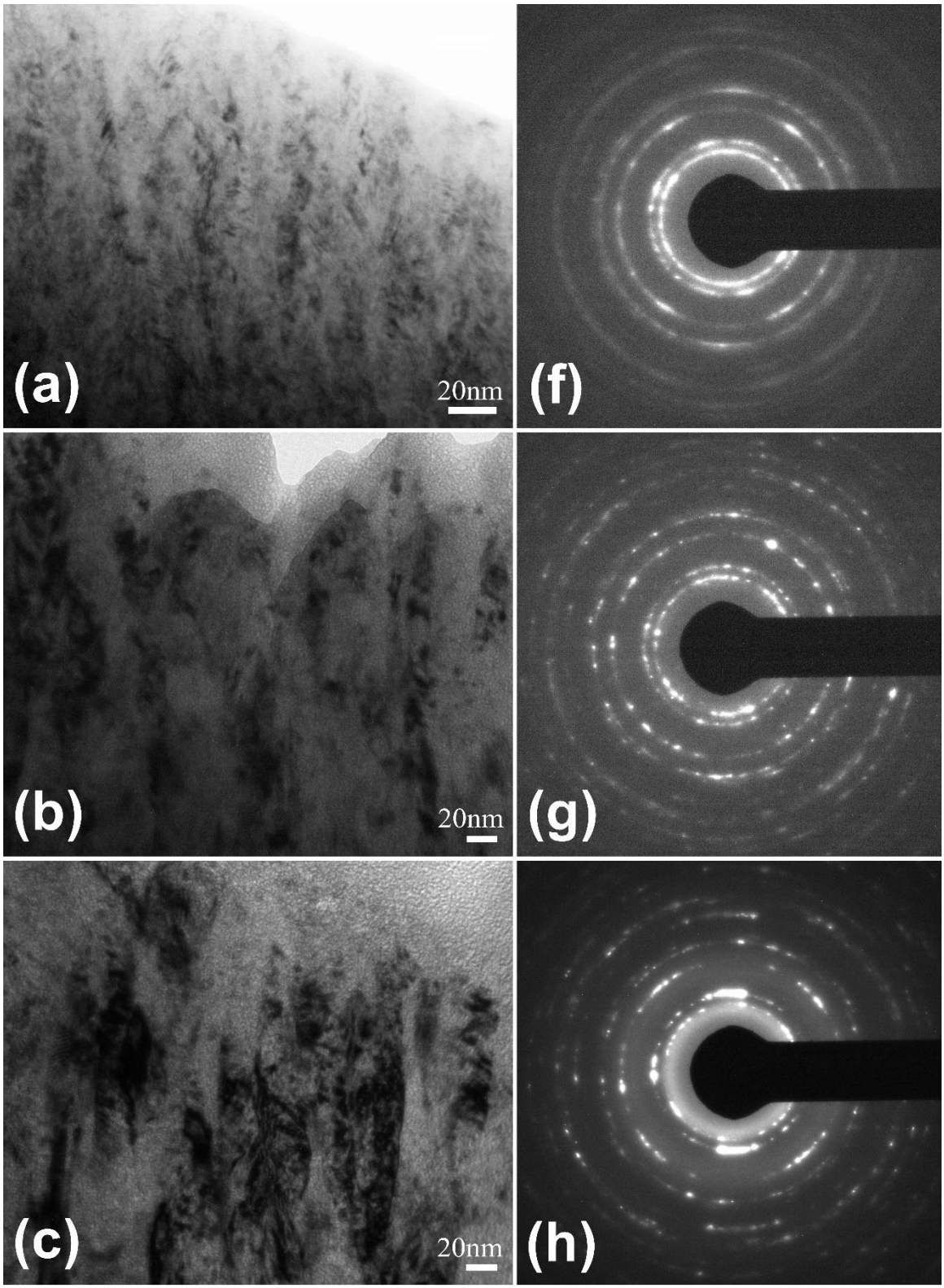

Fig. 4.4.5. Bright-filed TEM image and SAED pattern of Hf-Si-N coating deposited with nitrogen fraction of 7.5% (a, f), 10% (b, g) and 12.5% (c, h) taken from cross-section TEM foils.

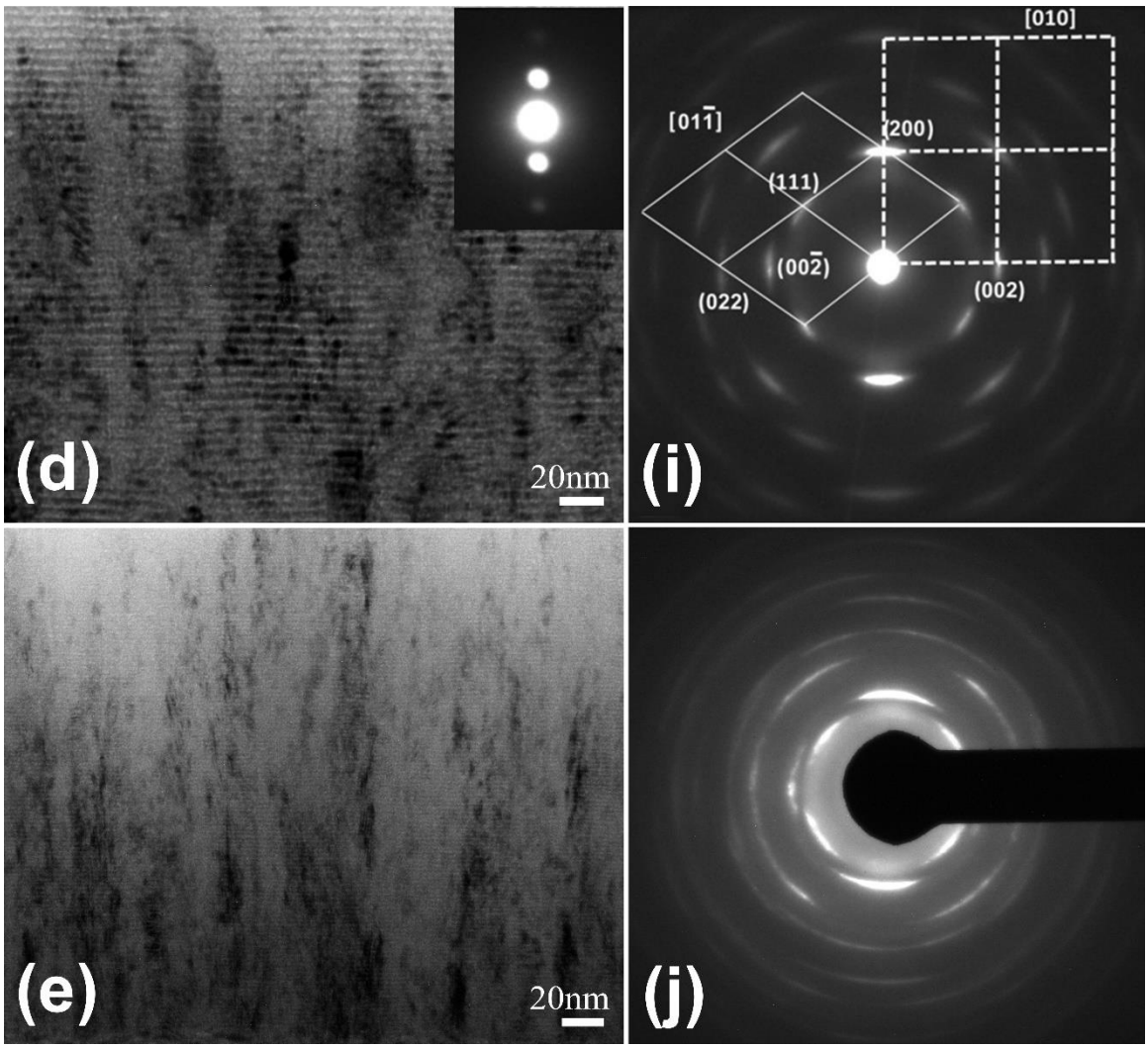

Fig. 4.4.5. Bright-filed TEM image and SAED pattern of Hf-Si-N coating deposited with nitrogen fraction of 15% (d, i), 17.5% (e, j) taken from cross-section TEM foils.

Fig. 4.4.5(j) is a SAED pattern obtained from a cross-section TEM foil of F5 shows diffraction arcs indicating the nanocrystalline structure. The inner diffraction arcs are located on the diffraction rings with lattice spacing of 2.58 Å, 2.24Å, 1.59 Å and 1.35 Å, respectively which can be identified as the (111), (200), (220) and (311) diffractions of the fcc HfN. The reduced lattice constant may due to the incorporation of silicon atoms bonding with nitrogen instead of hafnium to form the substitution solution. The strong intensity of the (200) diffraction arcs present along the coating growth direction obviously indicates the nanocrystals in the coating exhibit a (200) preferred orientation.

Fig. 4.4.6(a) is a cross-section bright field TEM image of the F4. Columnar structures with width of ~20 - 40 nm formed on the multilayers were observed from this coating. The long axis of the columnar structures is aligned with the coating growth direction. Fig. 4.4.6(b) is a dark-field TEM image obtained using the (200) diffraction spot in Fig. 4.4.5(i) showing white columnar structures. The white regions are corresponding to the crystalline exhibits (200) plane parallel to the coating surface, and the white regions dominate most of the dark filed image indicates that this coating exhibits a (200) preferred orientation.

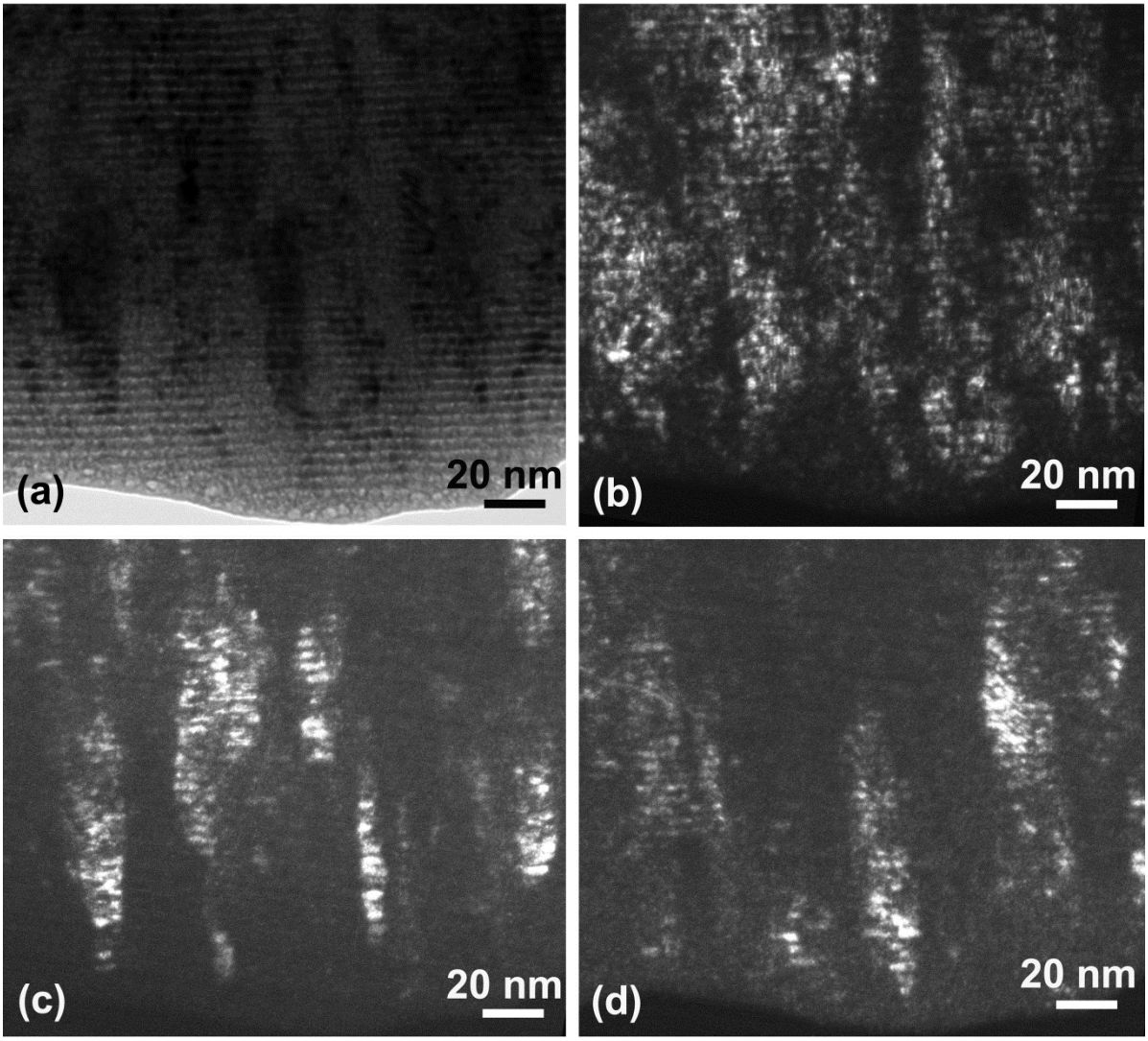

Fig. 4.4.6. (a)Bright-field TEM image, Dark-field TEM image acquired using (b) the HfN-(200) reflection (c) the HfN-(002) reflection(d) the HfN-(111) reflection in Fig. 4.4.5.(i) of the coating deposited with nitrogen fraction of 15% in a cross-section TEM foil.

Fig. 4.4.6(c) is a dark-field TEM image obtained using the (002) diffraction spot from zone axis of [010] in Fig. 4.4.5(d) which also presents white columnar structures but less than that in Fig. 4.4.6(b). The white contrast regions represent the areas exhibit the (002) fringes. Fig. 4.4.6(d) is a dark-field TEM image obtained using the (111) diffraction spot from zone axis of $[01\bar{1}]$ in Fig. 4.4.5(i) which presents some white columnar structures having the (111) planes. As discussed in Fig. 4.4.5(i) the diffraction pattern taken from the coating consisting two set of diffraction patterns shares the (200) diffraction spots, these three dark-field image obtained using three diffraction spots (200), (002) and (111) should be complementary to each other. It can be observed that the white contrast regions in Fig. 4.4.6(b), (c) and (d) are located at different areas, and the white contrast regions will occupy almost the whole dark field image if combine these three dark-field images together.

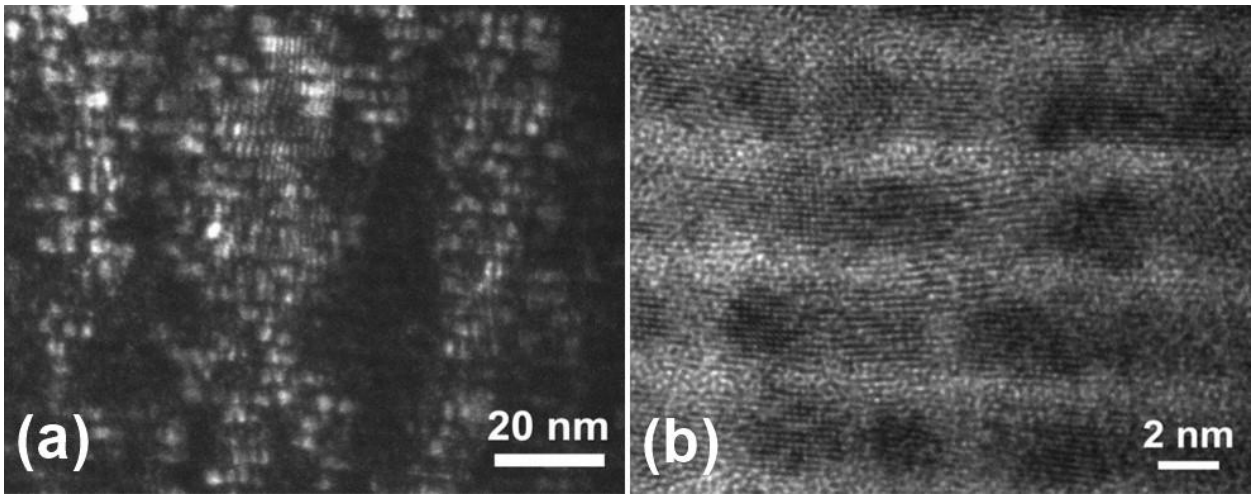

Fig. 4.4.7. (a) Dark-filed TEM image obtained using the HfN-(200) reflection showing small domains on multilayer (b) HRTEM image showing the domain structure on multilayer of the coating deposited with nitrogen fraction of 15% in a cross-section TEM foil.

Fig. 4.4.7(a) is a dark-filed cross-section TEM image of F4 obtained using the HfN (200) reflection in Fig. 4.4.5(d) showing the columnar structures on the multilayers. The columnar are composed of small domains separated by thin boundaries and the columnar consisting the (200) planes grows in the same direction as the coating grows. Fig. 4.4.7 (b) is a HRTEM image of F4 presenting clear layered structure at a period of 4 nm with rough interface between the adjacent layers. The dark layers are crystalline and composed of domains with size about ~ 2 to 5 nm distributed in different orientations. Most of the domains in the columnar possess the (200) direction which are the white contrast domains

in Fig. 4.4.7(a). The bright layers and the thin boundaries between each isolated domains are amorphous which appears as dark lines in Fig. 4.4.7(a).

4.4.4 Mechanical Properties and Residual Stress Measurements

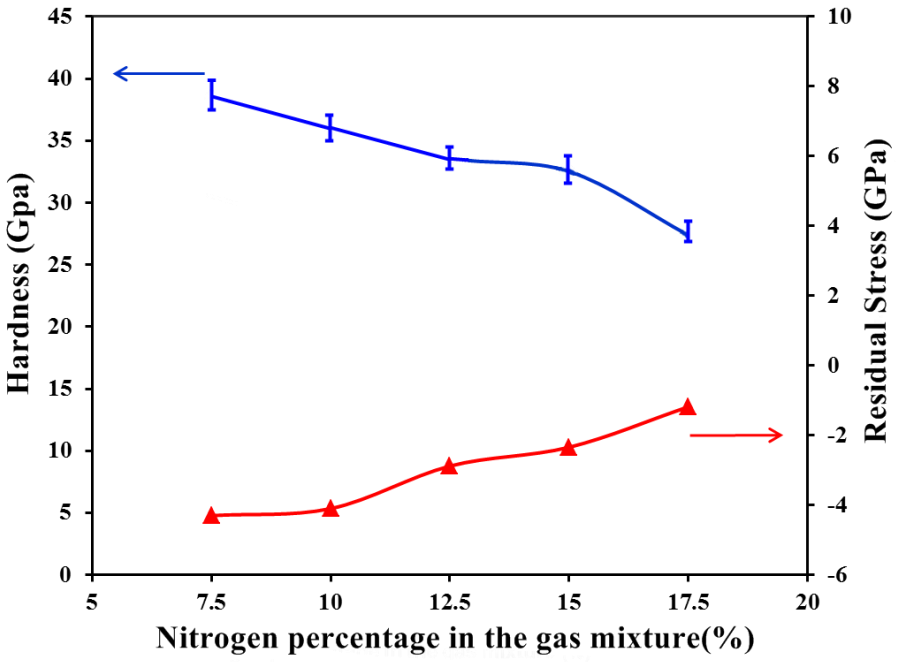

Fig. 4.4.8. Hardness and residual stress of the Hf-Si-N coatings deposited with different nitrogen fraction in the N_2/Ar gas mixture.

Nano-indentation instrument and optical profilometer were used to observe the change in hardness, Young's modulus and residual stress of coatings with the variation of nitrogen fraction in the Ar/ N_2 gas mixture. Fig. 4.4.8 presents the hardness and the residual stress of the Hf-Si-N coatings with nitrogen fraction of 7.5% (F1), 10% (F2), 12.5% (F3), 15% (F4) and 17.5% (F5). The mean hardness for F1, F2, F3, F4 and F5 was 38.5, 35.9, 33.6, 32.5 and 27.4 GPa, respectively. The coating deposited with 7.5% nitrogen in the gas mixture exhibits the highest hardness of 38.5 GPa at a high compressive stress of 4.2 GPa. As the nitrogen fraction increased to 10%, the compressive stress decreased slightly to 4 GPa. With further increase of nitrogen fraction in the atmosphere, the compressive stress in the coatings significantly decreased. The compressive stress of coating deposited with 17.5% nitrogen in the gas mixture is 1.1 GPa.

4.4.5 Summary

Reactive magnetron sputtering was used to fabricate five Hf-Si-N coatings in different Ar/N_2 gas mixture with nitrogen fraction of 7.5%, 10%, 12.5%, 15% and 17.5%. The coatings were studied by XPS, XRD, HRTEM combined with electron diffraction pattern and nano-indentation. The coating deposited in the nitrogen fraction of 7.5% possessing the highest hardness and compressive stress, showing fcc HfN nano-columnar structures (with some excess hafnium atoms incorporated) with width of 5 - 10 nm. No amorphous boundaries were observed between the nano-columnar structures. With the nitrogen fraction in the gas mixture increase to 10%, the lateral size of the HfN nano-columnar structures increased to 10 - 20 nm, and very thin amorphous boundaries were formed. This coating exhibits a slightly (111) texture. Further increase of nitrogen fraction to 12.5% in the gas mixture during deposition results in the lateral size of HfN nano-columnar structures increased to 20 - 50 nm. The thickness of amorphous boundaries increases due to the increase amount of silicon present in the coating. The preferred orientation of this coating has changed to (200) from (111) in the coating deposited in nitrogen fraction of 10%. Coating deposited with 15% nitrogen presents nano-columnar with width of 15 - 40 nm grow on multilayer structures. Most of the nano-columnar structures are oriented with (200) parallel to the coating surface. The multilayer present in the coating showing periodic 4 nm-bilayers composed of crystalline layer and amorphous layer. Nano domains with size of 2 - 5 nm are distributed on the crystalline layers and separated by amorphous boundaries. Coating deposited with 17.5% nitrogen presents similar multilayer structures with the coating deposited with 15% nitrogen. The columnar in this coating shows uniform lateral size about 10 nm and surrounded by more than 1 nm thick amorphous boundaries. Increase of nitrogen content by varying the nitrogen fraction in the N_2/Ar gas mixture results in the change in the grain size and the rearrangement of the crystal orientation in the coating. Increase of silicon content results in the increasing volume of amorphous boundaries and in favor of the formation of multilayer structures.

Chapter 5

MICROSTRUCTURE EFFECTS ON COATINGS WITH OUTSTANDING OXIDATION RESISTANCE

5.1 Introduction

At high temperatures and oxidation environments, many coatings deteriorate quickly due to their thermal instability and chemical degradation. For example, TiSiN, TiCN and SiC based coatings are commonly inefficient or fail due to material degradation at high temperatures [133-135]. During the past decade, high performance advanced ceramics which potentially can serve as high temperature application materials have generated a lot of attention. At the beginning, the attempts to synthesize the superhard crystalline β-C_3N_4 (Predicted to be harder than diamond) have resulted in the development of several different kinds of carbon nitride (CN_x) compounds. Although most of CN_x acquired are amorphous and substoichiometric in nitrogen, these kind of films still possess very useful mechanical properties, such as high hardness, high elastic recovery, good adhesion to substrate and low friction coefficient and wear [136-137]. The polymer-derived ceramic ---- silicon carbon nitride (SiCN) materials have aroused great interests due to their special features compared to those of crystalline Si_3N_4 and SiC mixtures. These materials exhibit specific physical and mechanical properties such as high hardness, wide band gap, strong optical emission and high chemical and thermal stability [137-138]. Moreover, the SiCN ceramics have been reported to remain mechanically stable at both ultra-high temperatures exceeding 1500 °C as well as in corrosive environments [139]. The incorporation of B and N into the SiC coatings can obviously improve the thermal behavior of the coatings which allows them to remain amorphous up to 1800 °C in inert atmospheres [140]. It has also been reported that the addition of a proper amount of B into the Si-C-N system could dramatically increase the thermal stability compared with the Si-B-C ceramics [141-144]. Studies showed that the new quaternary Si-B-C-N system is a good candidate for harsh environment applications due to their outstanding properties, especially high hardness, extraordinary high temperature stability and oxidation resistance. The combination of these properties is very important for many potential applications in coating technologies, high temperature microelectronics and optoelectronics.

Various fabrication techniques were used to prepare Si-B-C-N materials. A lot of early efforts to prepare the Si-B-C-N coatings have been mainly focused on the thermolysis of polymeric precursors at elevated temperatures and also with chemical vapor deposition [145-148]. However, both methods show certain disadvantages, such as the high fabrication temperatures, large amount of hydrogen content remains and also the degradation of material properties [149, 150]. Recently, magnetron sputtering has been proven to be an alternative method to prepare Si-B-C-N coatings due to the low deposition temperature, high deposition rate, free of hydrogen content and uniform deposition for large substrate size and complicated geometries [94-98].

With the knowledge gained from our previous study of magnetron sputtered Hf-B-Si-C system, and considering the important role of nitrogen on the high thermal stability performance of the Si-B-C-N system, nitrogen was incorporated into the Hf-B-Si-C system with the expectation of extending the oxidation resistance of Hf-B-Si-C coatings. Recently, hard and optically transparent Hf-B-Si-C-N coatings with superior high-temperature oxidation resistance have been fabricated using reactive pulsed dc magnetron co-sputtering. The coating with the elemental composition of $Hf_7B_{23}Si_{17}C_4N_{45}$ was found to exhibit the highest oxidation behavior in air (up to 1600 °C). This coating exhibits a hardness of 19 GPa, a Young's modulus of 173 GPa, an elastic recovery of 72%, a residual stress of -0.8 GPa and a high electrical resistivity (higher than 10^8 Ωm). Beside these properties, this coating exhibits high quality, defect free surface and is very well attached to the Si or SiC [73].

In this chapter, two coating systems Si-B-C-N and Hf-B-Si-C-N that all exhibit excellent oxidation behavior are investigated. Thermogravimetric oxidation analysis, the evolution of the microstructure as a function of coatings' exposure to high temperatures are presented below. The motivation of this research was to understand the mechanism of the high temperature oxidation resistance of the coatings which can be applied in model system of coating exhibiting high temperature oxidation resistance in the future.

5.2 Si-B-C-N Coatings

5.2.1 XPS Studies

In a collaborative effort with Professor Vlček's research group from Czech Republic, three representative Si-B-C-N coatings were selected and studied in order to obtain a better understanding about the processing conditions, microstructure evolution and mechanism of oxidation resistance at high temperature. The coatings studied in this work: as deposited Si-B-C-N coating (F1), coating annealed to 1400 °C in He (F2) and coating annealed to 1700 °C in air (F3). The as-deposited coating (F1) presents a composition of $Si_{30-32}B_{10-12}C_{2-4}N_{49-51}$ with low contamination level (H+O+Ar< 4 at.%).

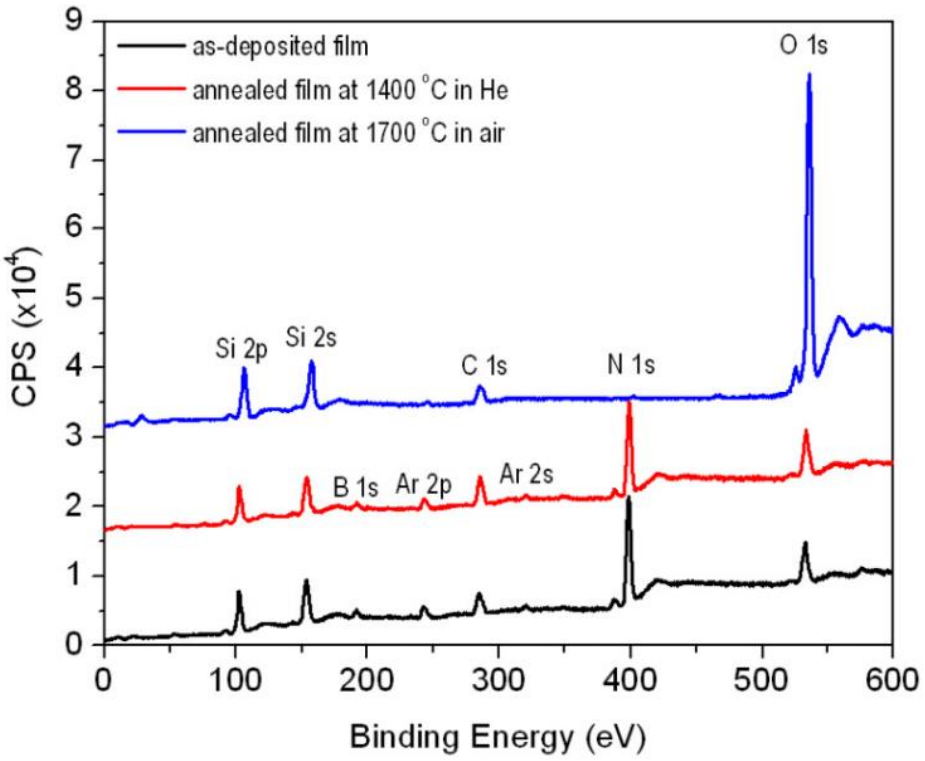

Fig. 5.2.1. XPS survey spectra of the coatings: As-deposited Si-B-C-N, annealed to 1400 °C in He and annealed to 1700 °C in air.

Fig. 5.2.1 shows general XPS survey spectra of the as-deposited Si-B-C-N coating (F1), a coating annealed at 1400 °C in He (F2) and a coating annealed at 1700 °C in air (F3). The composition of the three coatings is summarized in Table 5.2.1. It should be noted that the XPS spectra were obtained after surface cleaning by Ar ion sputtering. The spectra of both F1 and F2 exhibit mainly the

presence of Si, B, C, O, N, and Ar peaks, O and most of the C are from the contaminations. The spectrum of F2 is almost the same as that of F1. This result indicates the treatment of annealing the coatings to 1400 °C in He doesn't show significant change in the chemical composition of the Si-B-C-N coating. The XPS survey spectrum of F3 presents mainly the element of Si and O and absence of B and N peaks. Compared with the spectra of F1 and F2, the intensity of the O 1s peak in the spectrum of F3 is tremendously increased which indicates that the increasing of the O content in F3 resulting from the oxidation of the coating through the loss of the B and N in the coating. Furthermore, the Si 2p peak in the spectrum of F3 was shifted to a higher binding energy position at 103.5 eV compared to those in the F1 and F2 around 101.0 eV by 2.5 eV. The shifting of this peak further confirms the oxidation of Si in the coating F3.

Table 5.2.1. Composition of the F1, F2 and F3 coatings obtained using XPS.

	F1 (at%)	F2 (at%)	F3 (at%)
O 1s	10.1	12.6	55.9
C 1s	15.3	19.0	12.0
N 1s	32.6	29.5	1.0
Ar 2p	2.3	2.2	0.2
Si 2p	29.9	28.6	30.9
B 1s	9.8	8.1	0

The binding energy of the N 1s peak was around 397.5 eV which suggesting the coating consist a mixture of silicon nitrides (397.3 eV) and boron nitrides (398.1 eV). This results was consistent with the observation that the binding energy of Si 2p and B 1s peaks which showing the chemical state of these elements as nitrides. It can be concluded that the excess N in the amorphous coatings favors the bonding of N with Si and B which may because that the Si-Si bonds become unstable when close to the melting point of Si at 1414 °C.

5.2.2 HRTEM Studies

In order to get a better understanding of the microstructure difference of the Si-B-C-N coatings annealed at different temperatures and ambiances, we studied the microstructure of the coatings in details using TEM. Fig. 5.2.2(a) shows a cross-section TEM of the as-deposited Si-B-C-N coating on the SiC substrate with inserted typical SAED pattern of the coating. The thickness of the coating is 2051 nm from TEM measurement, and the coating shows homogenous and uniform amorphous structure are observed over the entire coating. The SAED pattern taken from the coating also confirms the coating exhibits amorphous structure.

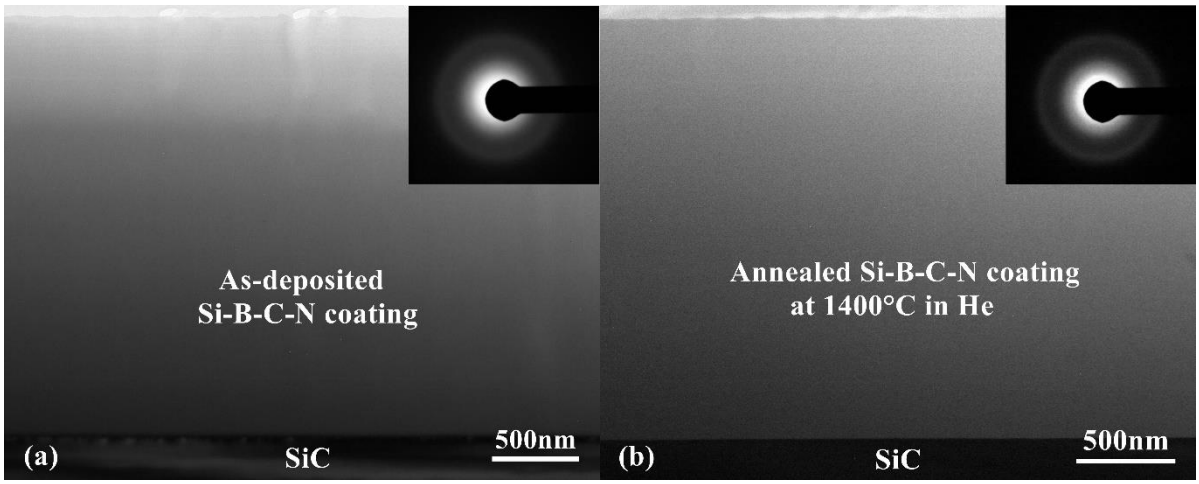

Fig. 5.2.2. Cross-section TEM image and SAED pattern (inserted) of (a) as-deposited coating and (b) coating annealed to 1400°C in He.

Fig. 5.2.2(b) is a cross-section TEM of the Si-B-C-N coating annealed to 1400 °C in He with inserted typical SAED pattern of the coating. The annealed coating has a thickness about 2140 nm, and exhibiting a similar structure to the as-deposited Si-B-C-N coating. Electron diffraction analysis shows that the coating annealed at 1400 °C in He also has an amorphous structure.

Fig. 5.2.3 shows a cross-section HRTEM image of the as-deposited coating. Very typical amorphous structure was observed from the high resolution TEM image. The HRTEM image of the coating annealed to 1400 °C in He shows the same feature as this coating. These results demonstrate that the treatment of annealing Si-B-C-N coatings to 1400 °C in He has no effect on the coatings' microstructure.

Fig. 5.2.4 shows a cross-section TEM image of the Si-B-C-N coating annealed to 1700 °C in air. From the figure, the formation of a three-layered structure can be clearly observed.

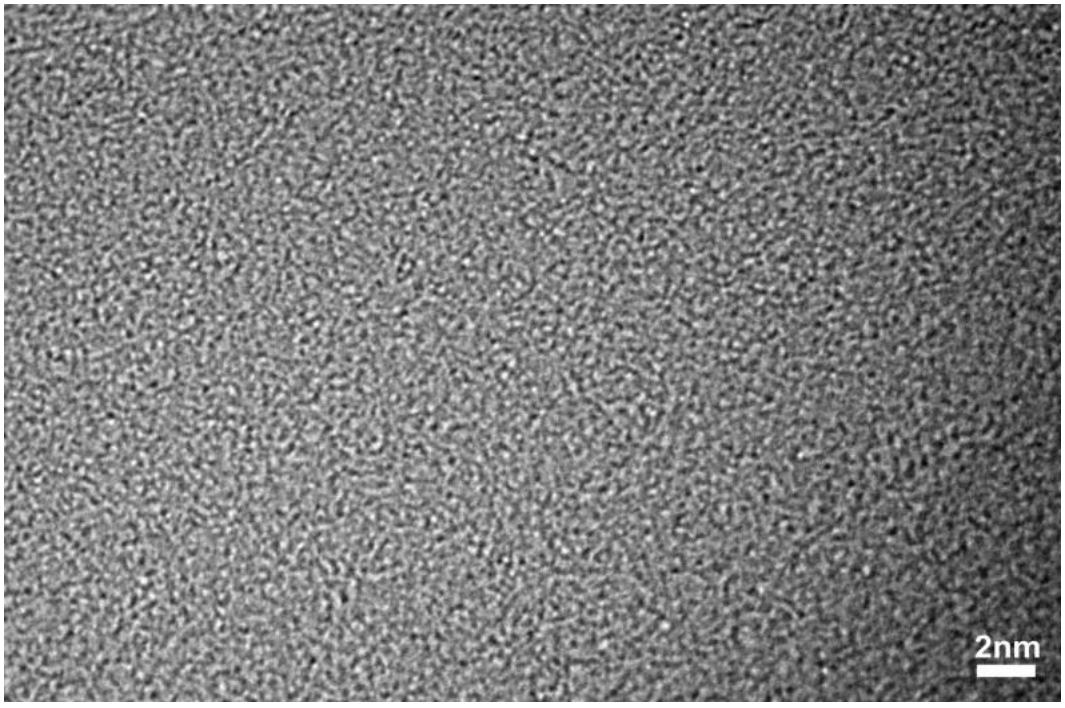

Fig. 5.2.3. Cross-section HRTEM image of the as-deposited coating shows amorphous structure.

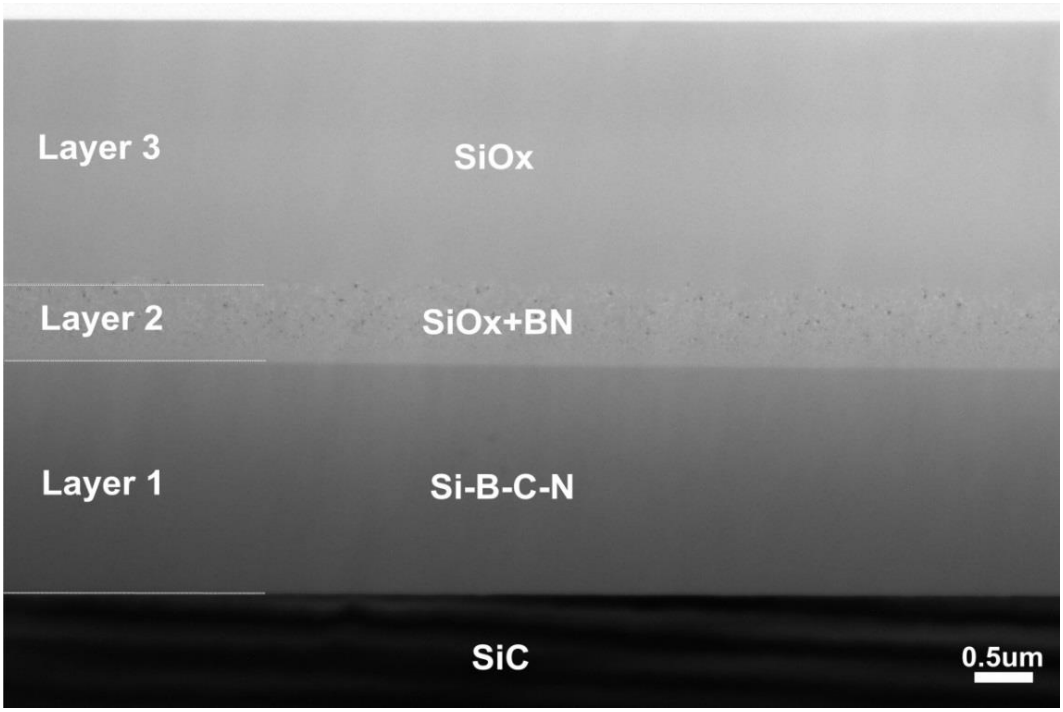

Fig. 5.2.4. Cross-section TEM image of the Si-B-C-N coating annealed to 1700 °C exhibits a three layered structure.

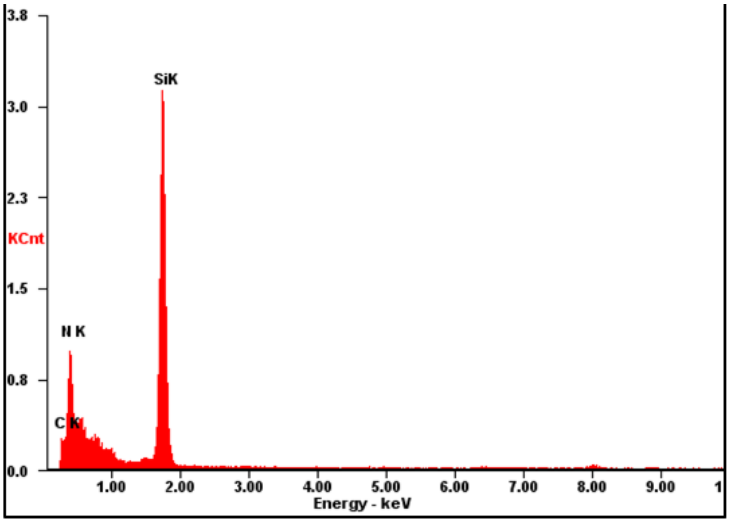

Elem	Weight %	Atomic %
C K	08.00	12.30
N K	41.00	54.10
SiK	51.00	33.60

Fig. 5.2.5. (a) EDS spectrum and the composition analysis results from the base layer in Fig. 5.2.4.

To further analyze the composition of the three different layers, we used EDS to detect the exhibited elements. Fig. 5.2.5 (a) is an EDS spectrum from the bottom layer of the coating where near the SiC substrate. The spectrum exhibits the element of C, N and Si (B cannot be detected from the EDS).

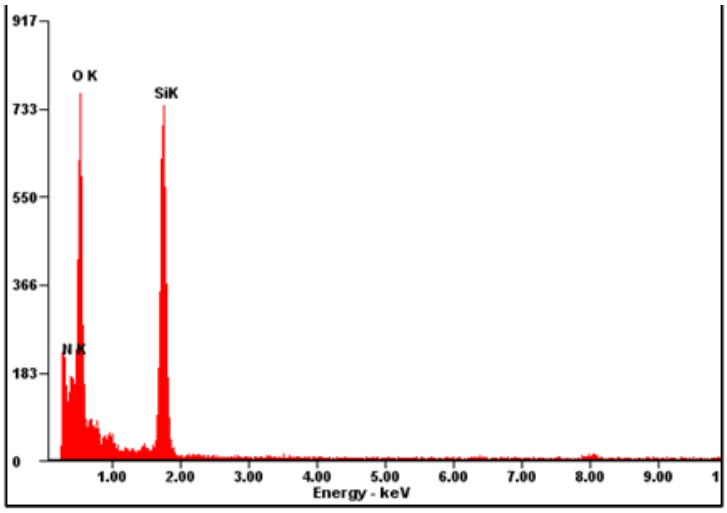

Elem	Weight %	Atomic %
N K	20.20	25.90
O K	48.10	53.90
SiK	31.60	20.20

Fig. 5.2.5. (b) EDS spectrum and the composition analysis results from the transition layer in Fig. 5.2.4.

This result is similar to the EDS results obtained from the as-deposited coating (not shown here), and the atomic ratio of Si to N from the EDS nearly the same with the as-deposited coating. This

indicates that the bottom layer of the coating annealed at 1700 °C in air has almost the same chemical composition as the as–deposited coating.

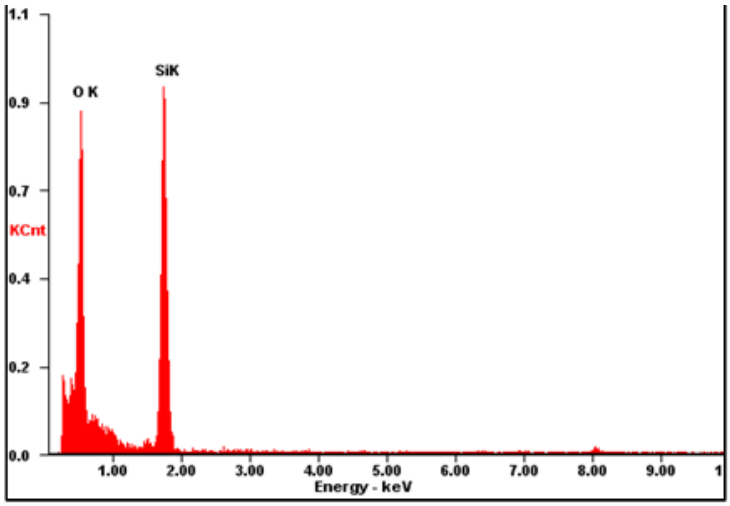

Elem	Weight %	Atomic %
O K	60.60	73.00
SiK	39.40	27.00

Fig. 5.2.5. (c) EDS spectrum and the composition analysis results from the matrix area in the transition layer in Fig. 5.2.4.

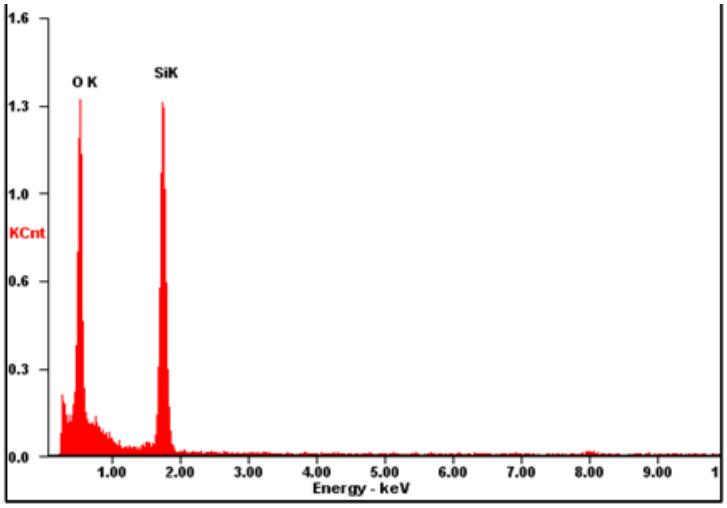

Elem	Weight %	Atomic %
O K	61.00	73.30
SiK	39.00	26.70

Fig. 5.2.5. (d) EDS spectrum and the composition analysis results from the top layer in Fig. 5.2.4.

We named the layer between the base layer and top layer as the transition layer. The EDS spectrum of the transition layer shows the presence of N, O and Si, and the elemental composition is shown in the chart. From the TEM image, we can see the transition layer consist of nano particles dispersed in the matrix. The EDS spectrum from the matrix area (without particle) in the transition layer exhibits the element of O and Si, as shown in Fig. 5.2.5 (c). Fig. 5.2.5 (d) is an EDS spectrum from the top layer of the coating showing only Si and O. N was not observed in this spectrum. The ratio of Si to

O from the matrix in the transition layer is nearly the same with that in the top layer. The TEM analysis shows that both the top layer and base layer exhibit amorphous structure.

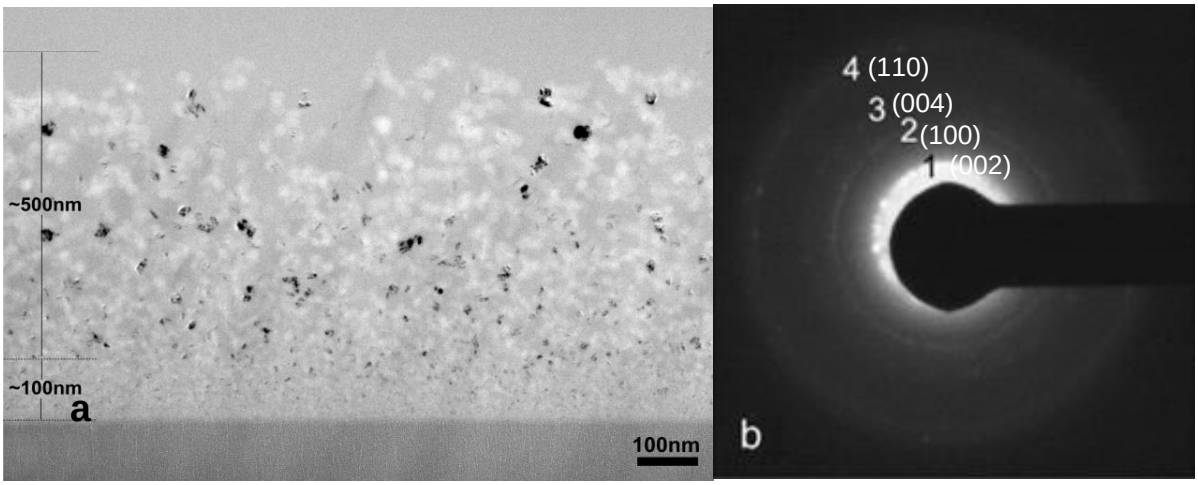

Fig. 5.2.6. (a) Enlarged cross-section TEM image of the transition layer in the Si-B-C-N coating annealed to 1700 °C. (b) SAED of the transition layer.

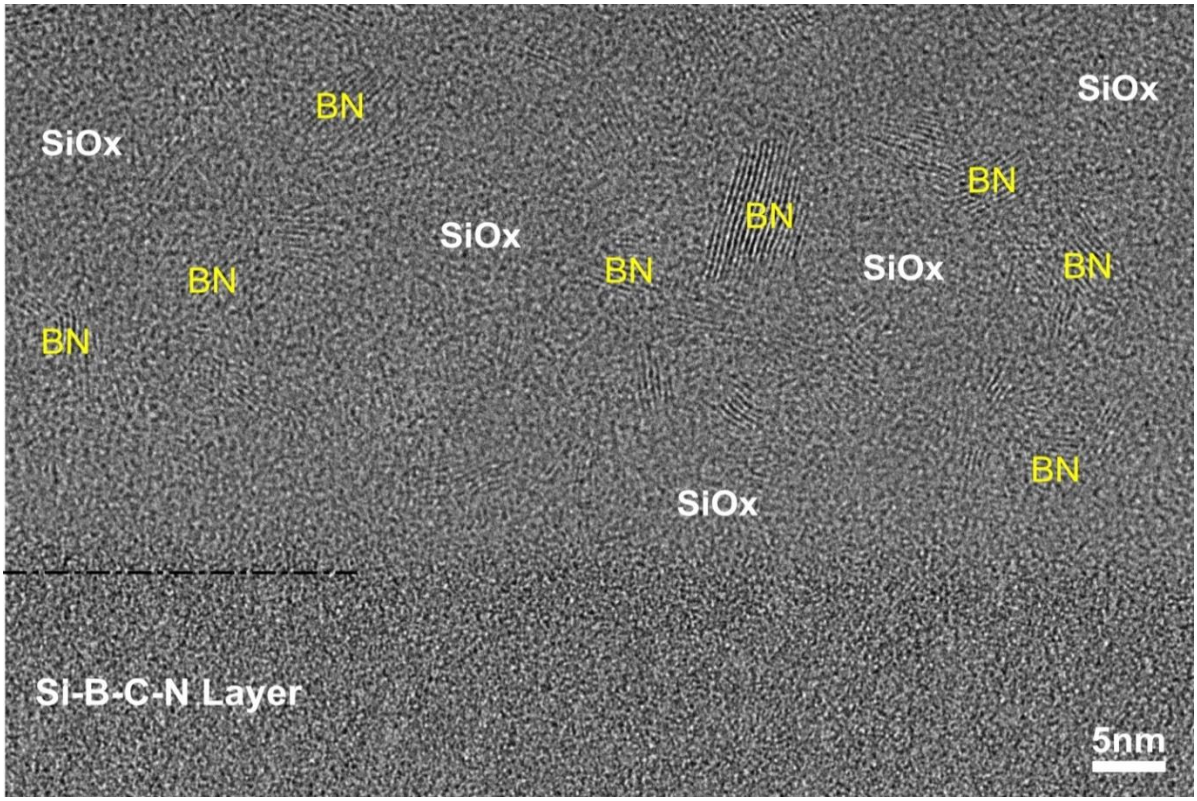

Fig. 5.2.7. Cross-section HRTEM image of Si-B-C-N coating annealed to 1700 °C showing the interface between the base layer and transition layer.

Fig. 5.2.6 (a) is an enlarged cross-section TEM image of the transition layer in the Si-B-C-N coating annealed at 1700 °C in air as the transition layer shown in Fig. 5.2.4. Nanocrystals with a

gradient size along the coating thickness can be observed. The size of the nanocrystals increase from the bottom to the top of the transition layer. A close observation of the transition layer shows that the transition layer can be divided into two sublayers: 1) a sublayer layer (close to the interface between the bottom Si-B-C-N layer and transition layer) with a high density of small nanocrystals exhibit the size of several nanometers, and the thickness is around 100 nm; 2) a sublayer with relative lower density of biggner nanocrystals with the size of 10s nanometers, and the thickness of this subslayer is around 500 nm. Fig.5.2.6 (b) is a SAED pattern taken from a region in Fig.5.2.6 (a). The diffraction ring from 1 to 4 have the lattice spacing of 3.33 Å, 2.16 Å, 1.66 Å and 1.25 Å. The nanocrystals can be identified as the hexagonal BN structure with the lattice parameter a=2.50 Å and c=6.66 Å.

Fig. 5.2.7 is a HRTEM image showing the interface between the base layer and transition layer. The transition layer region which close to the interface shows a high density of small BN nanocrystals (The size is around 2 - 5 nm). The amorphous area around the BN particles is the SiOx matrix.

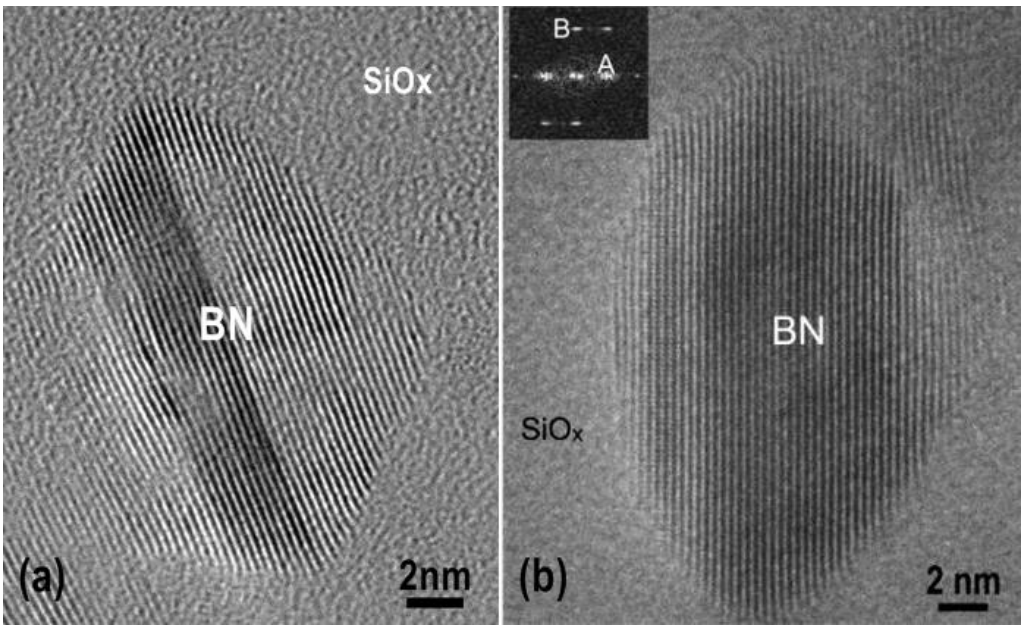

Fig. 5.2.8. (a) and (b) Nanocrystal from the top of the transition layer. Inset in (d) is an FFT of the nanoparticle.

Fig. 5.2.8 (a) and (b) are two HRTEM images obtained from the top of the transition layer presenting a nanocrystal which can be indentified as boron nitride particle with a size of about 20 nm. The inset in 5.1.8(b) is the fast fourier transformation (FFT) of the nanocrystal present in the image and can be indexed as the [1 0 0] zone diffraction of the hexagonal BN. The marked spot A and B in the

FFT can be index as (002) and (010) diffraction plane, respectively. The FFT provides further evidence for the formation of hexagonal boron nitride nanocrystalline in this annealed Si-B-C-N coating. It can be found in both the figure (a) & (b) that the BN nanocrystals are embedded in an amorphous structure. The EDS spectra taken from the amorphous area around the particles present only the element of Si and O which indicates the formation of SiOx amorphous structure surrounding the BN particles.

Fig. 5.2.9 shows the chemical composition variation of the element C, N, O and Si with respect to the depth in the middle layer of Si-B-C-N coating annealed to 1700 °C. It can be seen that the content of C and Si don't vary much with the thickness changes in the coating, i.e., the C and Si content at the bottom part is nearly the same as that on the top part of the middle layer. The content of the O gradually increases with the thickness, whereas that of N gradually decreases with the thickness.

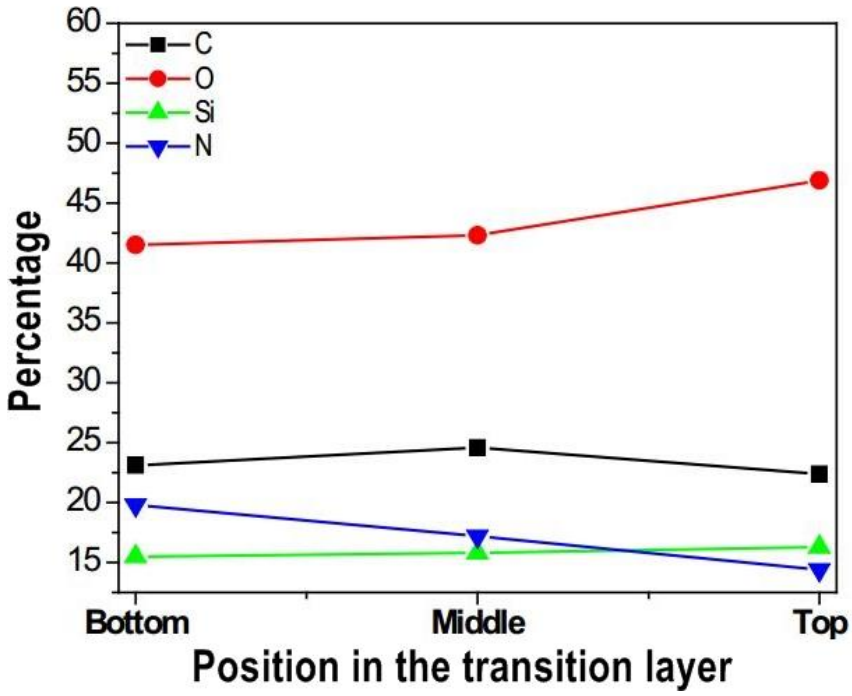

Fig. 5.2.9. Composition variation with respect to the depth in the middle layer of Si-B-C-N coating annealed to 1700 °C.

Fig. 5.2.10 (a) shows a plan-view bright field TEM of the Si-B-C-N coating annealed at 1700 °C in air which presenting BN nanocrystalline distribution in the coating plane over a large area. This plan-view TEM sample was obtained by removing the top layer and the bottom layer (including SiC substrate) using ion milling. The measurement from the TEM image shows the size of the BN nanocrystals varies

from 14 to 21 nm. The lattice spacing of the lattice planes in region ***X*** and ***Y*** in Fig. 5.2.10(b) are 2.06 Å, and can be identified as the (101) planes of the hexagonal boron nitride, while those lattice spacing in area ***u*** and ***v*** are around 3.33 Å which correspond to the (002) planes of BN. The lattice planes in area ***X*** and ***u*** are twisted with respect to ***Y*** and ***v***, respectively.

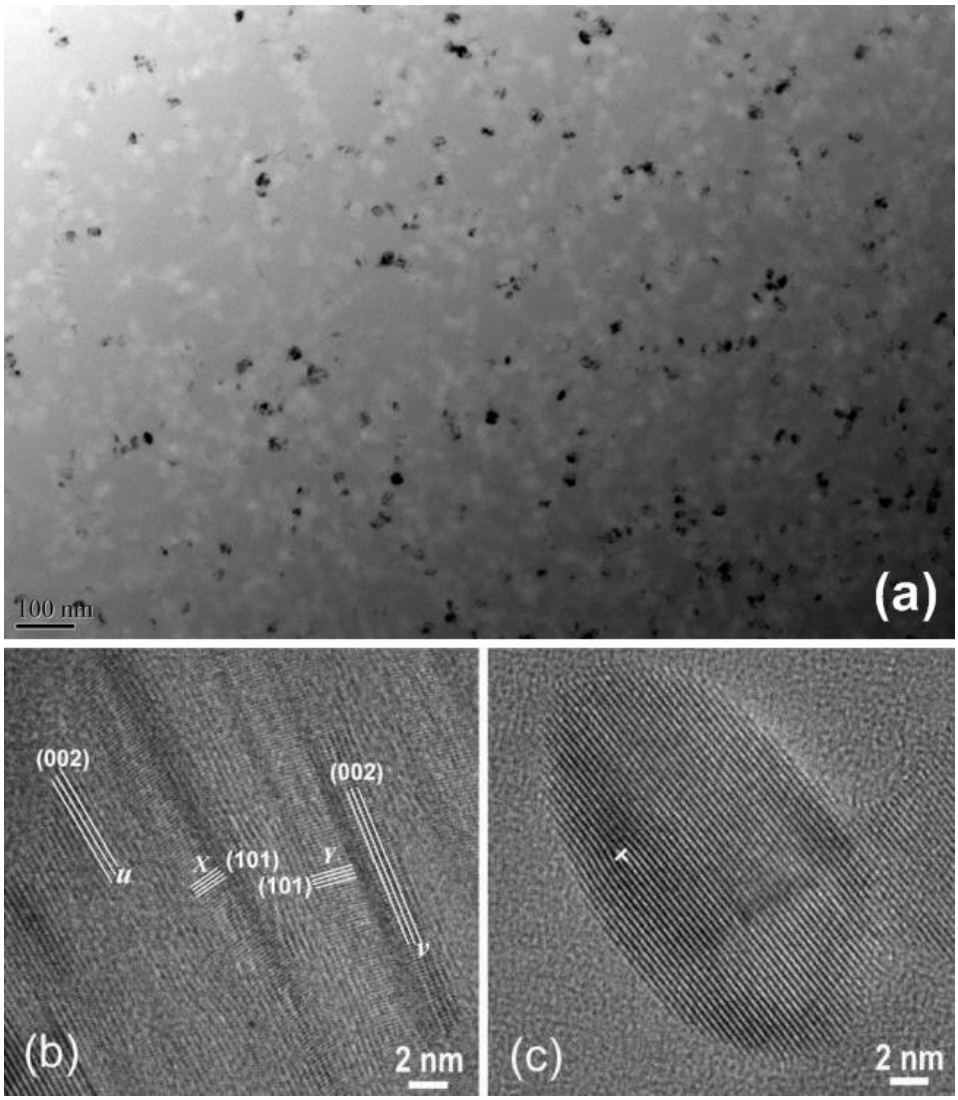

Fig. 5.2.10. (a) Plan-view TEM image of the transition layer of coating annealed to 1700°C in air and (b) HRTEM image of a winkled BN nanocrystal and (c) single BN nanoparticle with edge dislocation in this layer.

This result indicated that the BN nanocrystalline in the transition layer of coating annealed to 1700 °C are highly deformed or exhibit defect structures. This conclusion is further supported by Fig. 5.2.10(c) which is a HRTEM of an individual isolated BN nano particle with a size of about 13 nm. An edge dislocation has clearly observed in this BN nano particle. Comparing the cross-section TEM

image 5.2.8 (a)&(b), and plan-view TEM image 5.2.10(c), the BN particles formed in the transition layer all exhibit an oval rounded shape. The nanoparticles exhibit structure defect and are compressed along the c axis. The final presenting shape of the BN particles should be the result of a compromise between the local stresses and the surface energy.

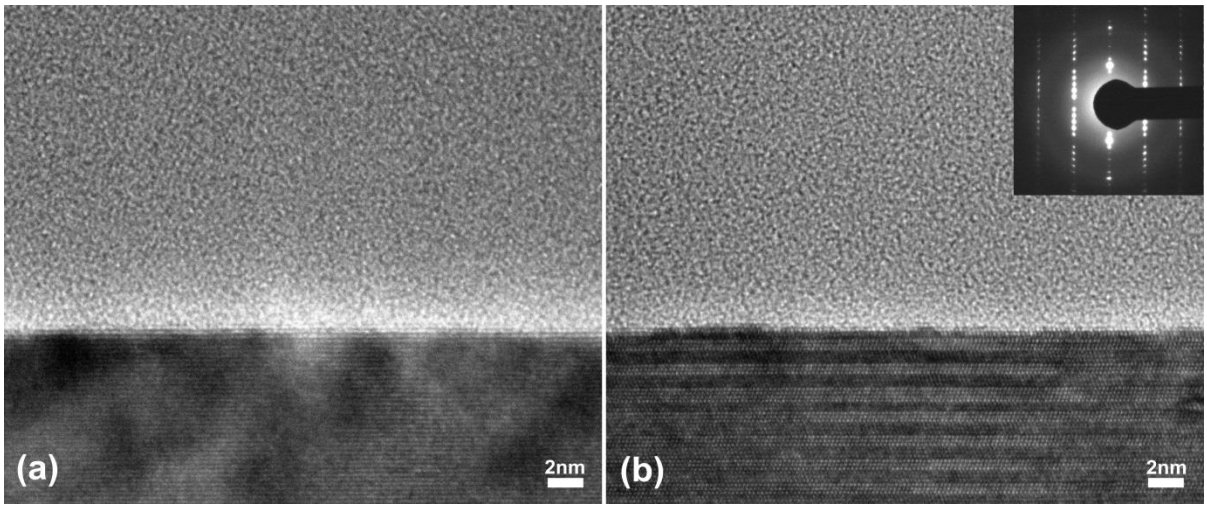

Fig. 5.2.11. Cross-section HRTEM image of the interface between (a) as deposit Si-B-C-N coating and SiC (b) Si-B-C-N coating annealed to 1400°C in He and SiC substrate. Inset in (b) is a SAED of the coating/ substrate interface area.

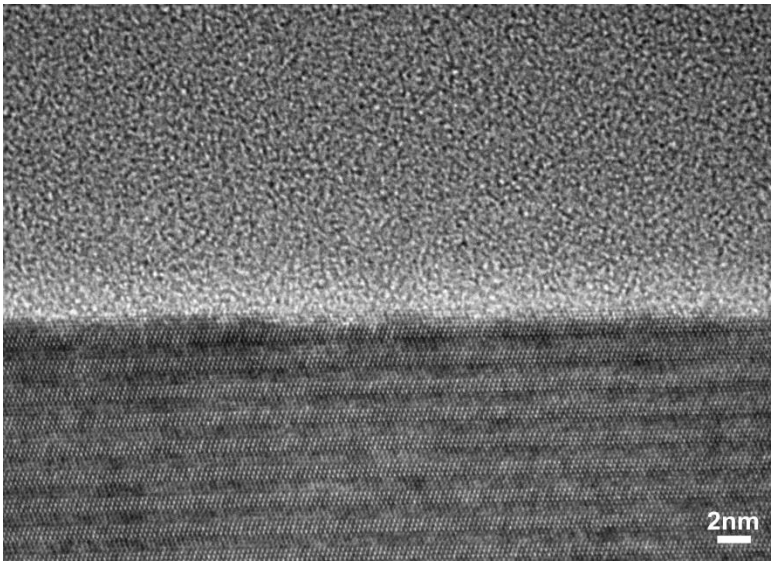

Fig. 5.2.12. Cross-section HRTEM image of the interface between Si-B-C-N coating annealed to 1700°C in air and SiC substrate.

Fig. 5.2.11 (a) is a cross-section HRTEM of the interface between the as deposit Si-B-C-N coating and SiC substrate, and (b) is a cross-section HRTEM of the interface between the Si-B-C-N coating annealed to 1400 °C and SiC substrate. Very sharp and atomically flat interface can be clearly

observed from these two coatings at the same time. This indicates that annealing the Si-B-C-N coating to 1400 °C in He does have any effects on the interface structure between the Si-B-C-N coating and SiC substrate. The inset in (b) is a SAED pattern taken from the interface area which over both the coating and the substrate. The sharp diffraction spots represent the diffraction from the single crystal SiC while the diffused rings represent the diffraction from amorphous Si-B-C-N coating.

Fig. 5.2.12 is a cross-section HRTEM image of the interface between the Si-B-C-N coating annealed to 1700 °C and SiC substrate. It can be observed that the crystal structure of the SiC at the interface was not as sharp as the interface of the two coatings we discussed above. It seems like the top SiC monolayers are degraded due to the diffusion between the coating and substrate, leading to the formation of a rough interface between the coating and SiC substrate.

5.2.3 Nano-indentation Testing

Nano-indentation experiments were performed to study the effect of the annealing on the hardness and Young's modulus of the coatings. A Berkovich diamond tip was used in the nano-indentation tests, and a fused quartz (hardness of 9.25 GPa, modulus of 69.6 GPa) was used as the standard sample to calibrate the apparatus. The indention curves are obtained by plotting the applied force vs the tip displacement. An indenting force of 5000 μN and same loading function were used for test of all of the three Si-B-C-N coatings. The whole procedure was following a three segment load function: 1) The applied force is linearly increased from zero to the maximum value in 5 s; 2) Holding at the maximum force value for 2 s; 3) Linearly decreased from the maximum value to zero in 5 s. To minimize the experimental error, the average hardness and modulus values were determined by performing 3×5 array indents with 2 μm ×2 μm distance for each coating.

Figs. 5.2.13 (a) – (c) show the image of an indentation area on the as deposit Si-B-C-N coating, coating annealed to 1400 °C in He and coating annealed to 1700 °C in air respectively. It can be clearly observed that the indentation area in as deposit coating is larger than that in coating annealed to 1400 °C in He but smaller than that in coating annealed to 1700 °C in He. The indentation area can reflect the hardness of material when the test parameters are the same. The larger the indentation area is, the softer the material is. This indicates that the as-deposited Si-B-C-N coating is softer than the coating annealed at 1400 °C in He, but harder than the coating annealed at 1700 °C in air. Fig. 5.2.13 (d)

presents a typical Force vs. Displacement curve of the three coatings. The mean hardness for as deposit Si-B-C-N coating, coating annealed to 1400 °C in He and coating annealed to 1700 °C in air is 19.51, 22.07 and 9.81 GPa, respectively. The mean modulus is 204.88, 210.81 and 76.50 GPa, respectively.

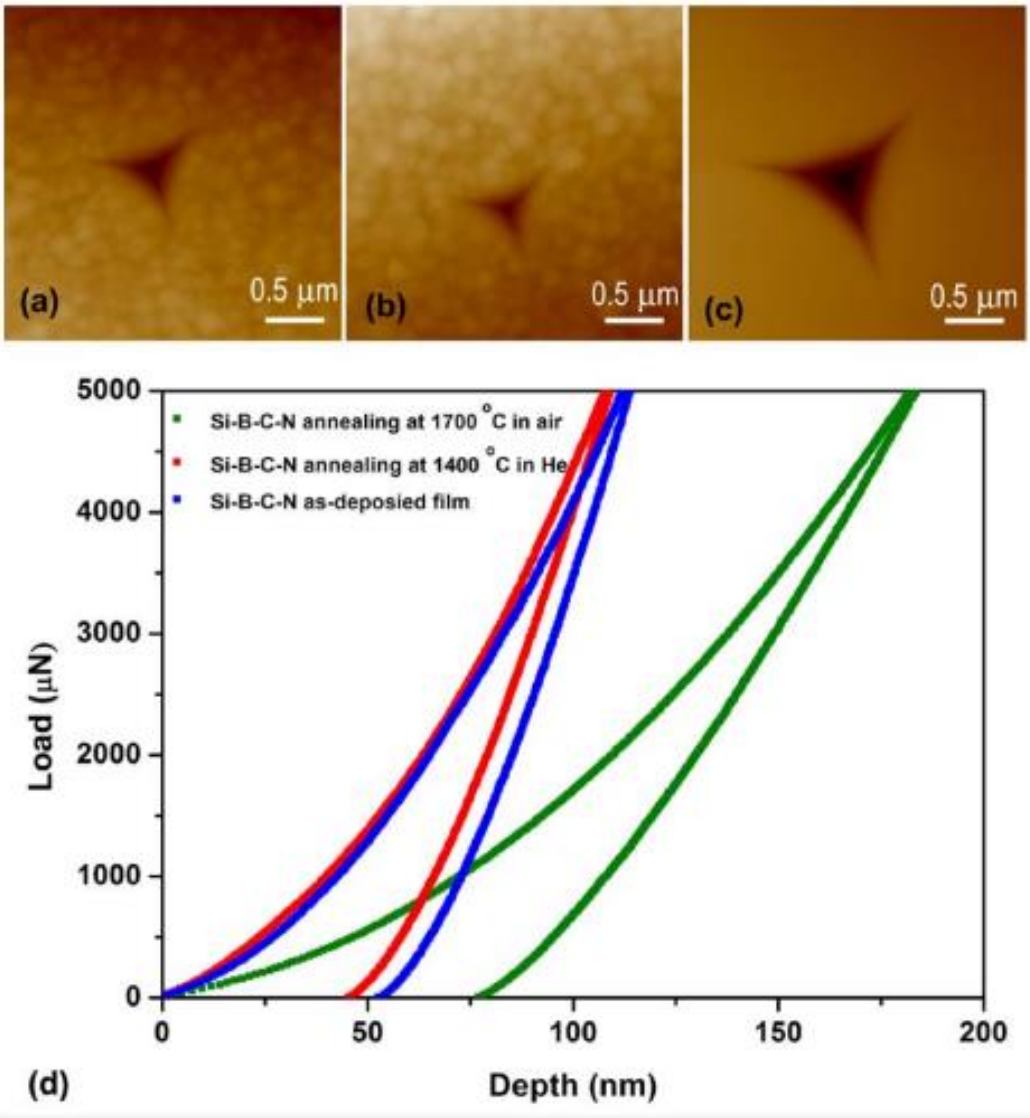

Fig. 5.2.13. Image of an indentation area on the (a) as deposit Si-B-C-N coating, (b) Si-B-C-N coating annealed to 1400 °C in He, (c) Si-B-C-N coating annealed to 1700 °C in air and (d) Force vs. Displacement curves for the three coatings.

Taking the XPS results into consideration, the hardening of the annealed coating at 1400 °C in He could possibly be due to the further promoting bonding of Si, B and C with N and densification of the coating by removing of the structure defects and/or release of the stress in the coating at high

temperature. It has been noticed that the thickness of the coating annealed at 1400 °C in He increased about 50 nm which is about 4.4% compared to the as-deposited coating. It is possible that that the He atoms were diffused into the coating during the annealing causing the increase of the thickness and densification of the coating which makes coating harder.

The decrease of the hardness and modulus of the Si-B-C-N coating annealed to 1700 °C in air may be due to the formation of the SiO_x layer on the coating surface. Considering the EDS result from the different oxidation layer in TEM analysis, spectra of the BN crystalline show presence of N (B cannot be detected) and no N was observed in the surrounding amorphous areas indicating that the crystalline are N rich nano particles (determined as the BN particle from the SAED and HRTEM analysis). The transition layer of the coating can be divided into two sublayers. At the bottom of the transition layer, smaller nanoparticles (~ 5 nm) were formed where has been detected presenting less content of oxygen and higher nitrogen than that in the top of the transition layer where larger nano particles (~ 20 nm) were formed. This indicates that the size of the nanoparticles should be related to the oxygen and nitrogen content. On the top layer of this coating, no B and N were observed based on both XPS and EDS studies and indicating complete dissolve of B and N, and only the SiO_x amorphous structure was formed in this layer.

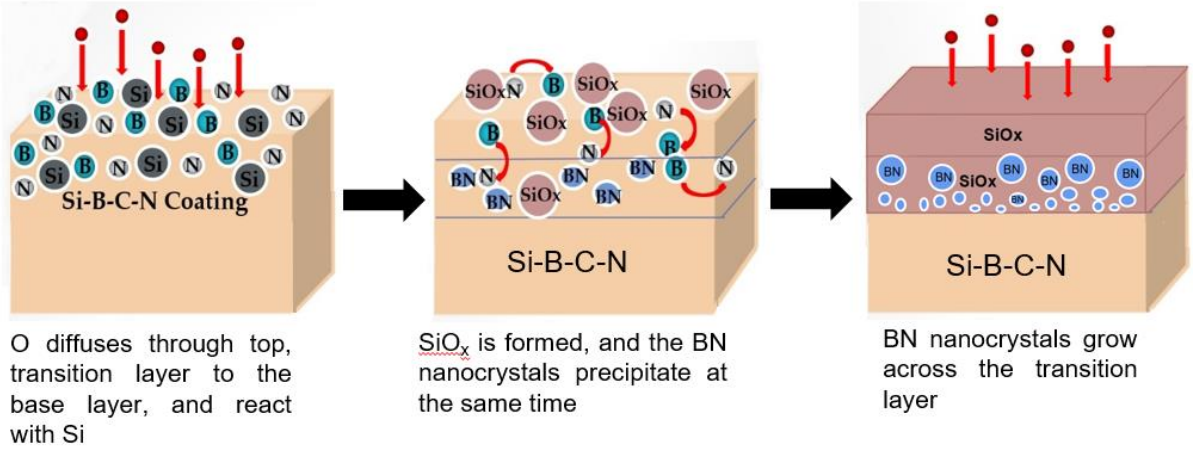

Fig. 5.2.14. Schematic showing the possible mechanism for the high temperature resistance of Si-B-C-N coating.

5.2.4 Oxidation Mechanism

The high temperature oxidation mechanism of the coating is not clear yet. Based on the present results, one possible process of oxidation reaction could be described in the following (shown in Fig. 5.2.14): (1) During the annealing in air, oxygen atoms diffuse into the coating and react with Si atoms to form SiO_x nuclei; (2) With the growth of SiO_x, Si atoms migrate from the surrounding regions where will accordingly become Si poor area, hexagonal boron nitride nuclei starts to form in the Si poor area and grow with continuous loss of Si; (3) With the continuation of the annealing and possibly the increase of temperature, boron nitride crystalline at top layer start to dissolve by the loss of B and N. This provides a reasonable explanation for the microstructure that we observed.

Molecular dynamics simulation for the thermal properties of the Si-B-C-N coatings has been carried out by our collaborators at the University of Minnesota.

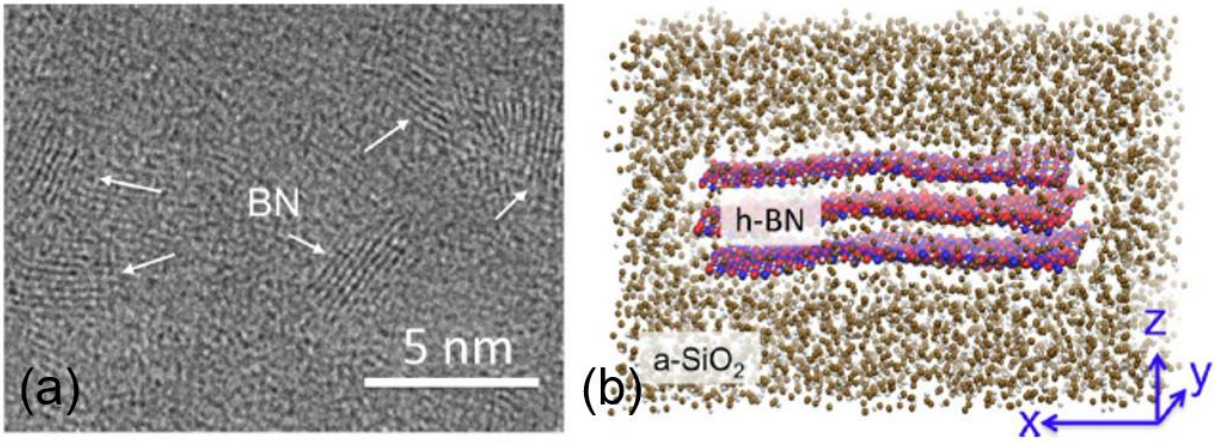

Fig. 5.2.15. (a) HRTEM image showing h-BN nanoparticles embedded in silica, located on top of Si-B-C-N coating material and (b) MD simulation supercell of an h-BN nanoparticle embedded in silica. Adapted after reference [161].

It was found that the presence of three atomic layers of h-BN is important as it introduces significant thermal anisotropy. Based on the thermal anisotropy revealed, the simulation confirms that incorporation of h-BN nanoparticles in silica could establish thermal barriers and heat spreading path in front of the amorphous base layer [161]. The effect may enhance the already high temperature oxidation resistance exhibited by the Si-B-C-N coatings.

5.2.5 Summary

In summary, the as-deposited Si-B-C-N coating with a chemical composition of $Si_{30-32}B_{10-12}C_{2-4}N_{49-51,}$ exhibits an amorphous structure. Annealing the coating to 1400 °C in He has no effect on the

coating's structure or composition. This coating was found to possess a higher hardness compared to the as-deposited coating more than likely due to the promoting bonding of Si, B and C with N and densification of the coating by removing defects. The coating annealed to 1700 °C in air exhibits a three-layered structure: 1) an original, unaffected bottom Si-B-C-N layer with amorphous structure; 2) a transition layer consisting of BN nanocrystals dispersed in amorphous SiO_x matrix (the BN nanocrystals in the transition layer grow along the normal of the coating direction.); and 3) a top layer of amorphous SiO_x depleted in B and N. The formation of this kind of structure involves the oxygen diffusion through the top layer to the base layer, reacting with Si to form the SiO_x and the precipitation, growth of the BN nanocrystals and final oxidation of the BN at the top layer. The high oxidation resistance of Si-B-C-N coating may be attributed to three main reasons: 1) The Si-N bonds in the amorphous structure that prevent the reaction of Si with O; 2) The nucleation of the large amount of BN in front of the base Si-B-C-N layer prevents the further oxygen diffusion to the bottom; 3) a compressive stress field may formed in front of the interface between the base layer and the transition layer because of the precipitation of BN nanocrystals. The presence of the BN nanoparticles can act as a barrier to O diffusion.

5.3 Hf-B-Si-C-N Coatings

In this part, a systematic and detailed microstructural analysis of the as deposited $Hf_7B_{23}Si_{17}C_4N_{45}$ coating and the annealed coatings up to various temperatures from 1100 °C to 1500 °C was conducted using HRTEM and SAED. In addition, the coatings were also characterized using AFM, XRD and nano-indentation measurements. The motivation for this research was to understand the behavior of the high temperature oxidation resistance of coating at by studying its microstructure evolution as a function of its exposure to high temperatures.

5.3.1 XRD Studies

The crystal structures of the as-deposited and annealed $Hf_7B_{23}Si_{17}C_4N_{45}$ coatings were examined by XRD analysis before conducting systematic TEM studies, as shown in Fig. 5.3.1. The XRD spectrum of the as-deposited $Hf_7B_{23}Si_{17}C_4N_{45}$ coating shows no diffraction peaks, indicating the formation of an amorphous like structure. The XRD spectrum of coating annealed up to 1100 °C indicates no change in the amorphous structure. The coating annealed up to 1200 °C shows two broad and low intensity diffraction peaks at 2θ angles of 34.68° and 35.50°, corresponding to lattice spacing of 2.58 Å and 2.53 Å. These peaks were identified to be the (0 2 0) and (2 0 0) of the monoclinic HfO_2 structure (monoclinic-HfO_2, PDF card #: 01-075-6426, ***a***= 5.1187 Å, ***b***=5.1693 Å, ***c***=5.297 Å, ***β***=99.18°, $P2_1/c$) [151] indicates the formation of monoclinic hafnia. With a further increase in the annealing temperature to 1300 °C, the XRD pattern exhibits the same two peaks of (0 2 0) and (2 0 0) of the m-HfO_2 structure, but the intensity of the two peaks are significantly increased.

The coating annealed up to 1400 °C exhibits seven diffraction peaks. Besides the tremendously enhanced two (0 2 0) and (2 0 0) peaks of the m-HfO_2, There are five more peaks appear at the 2θ positions of 17.55° and 28.35°, 30.33°, 31.65° and 54.43°, corresponding to the lattice spacing of 5.05 Å, 3.15 Å, 2.95 Å, 2.83 Å and 1.68 Å, respectively. The former two peaks can be identified as the (1 0 0) and $(\bar{1}\ 1\ 1)$ of the m-HfO_2 structure, while the last two peaks can be identified as the (1 1 1) and (3 0 0) of the m-HfO_2. The lattice spacing of the middle peak (2.95 Å) is equal to that of the (111) of either the orthorhombic HfO_2 (o-HfO_2, PDF # 01-070-2832, ***a***= 5.0073 Å, ***b***=5.2276 Å, ***c***=5.058 Å, Pbcm), or the

cubic HfO_2 (c-HfO_2, ***a***= 5.11 Å, F3m3), and is also very close to that of the (111) of the tetragonal HfO_2 (t-HfO_2, PDF # 07-0342, ***a***= 5.14 Å, ***c***=5.25 Å, $P4_2/nmc$), which is about 2.97 Å [151- 154]. Since it is difficult to distinguish between the o-HfO_2, t-HfO_2 and c-HfO_2 so far, the presence of any of these three structures in the annealed coating is possible. We collectively name this structure as oct-HfO_2.

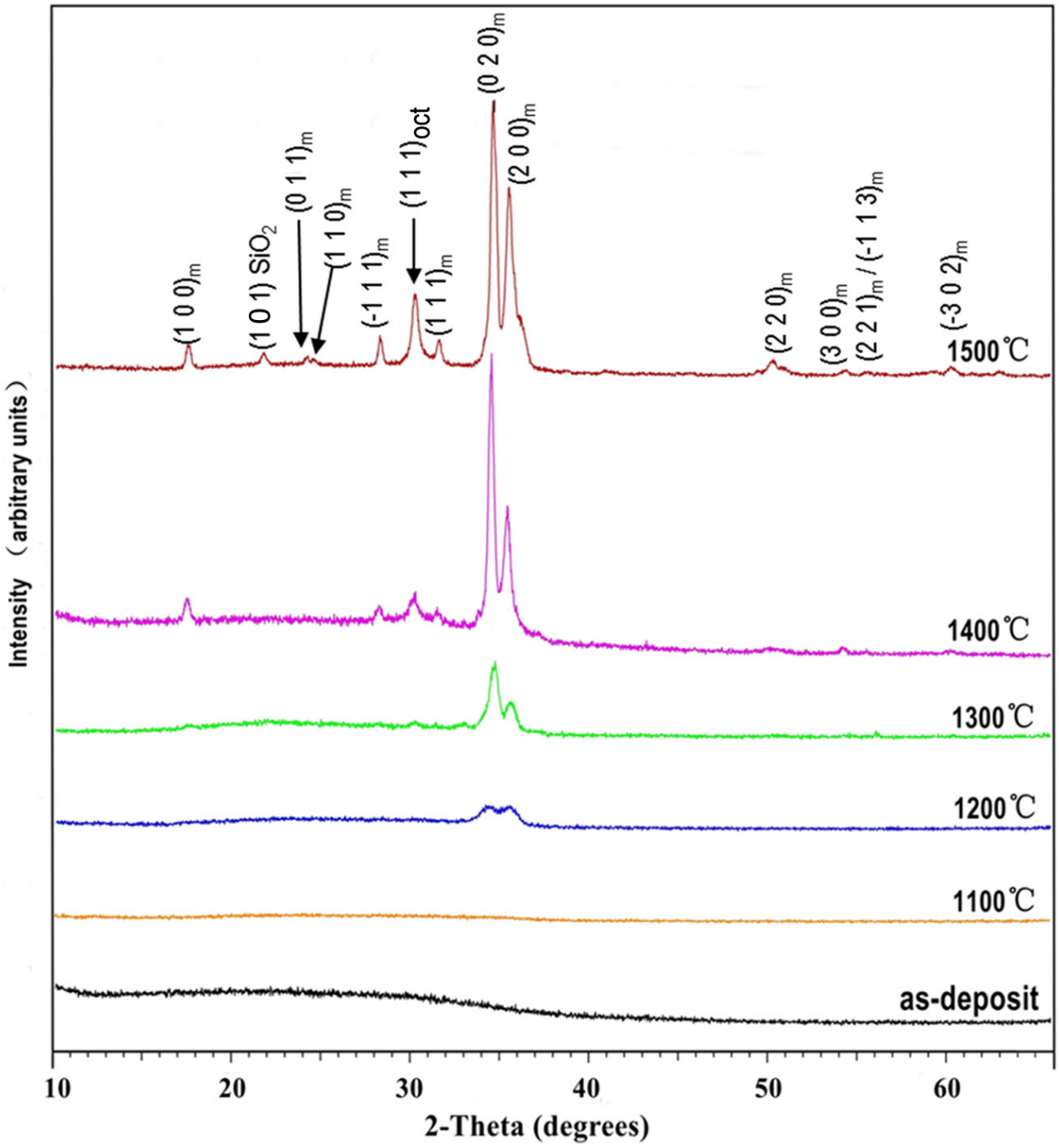

Fig. 5.3.1. XRD patterns of the as-deposited and annealed $Hf_7B_{23}Si_{17}C_4N_{45}$ coatings.

The XRD pattern of the coating annealed up to 1500 °C exhibits all of the peaks present in the coating annealed up to 1400 °C and additional peaks that can be identified as the (0 0 1), (1 1 0), (2 2 0), (2 2 1) or $(\bar{1}\ 1\ 3)$, and $(\bar{3}\ 0\ 2)$ of the m-HfO_2. Furthermore, the peak at a 2θ angle of 21.8° has a lattice spacing of 4.08 Å and is close to the (1 0 1) of cristobalite SiO_2 (tetragonal, PDF #39-1425. ***a***= 4.793 Å, ***c***=6.924 Å, $P4_12_12$) [151].

5.3.2 AFM Studies

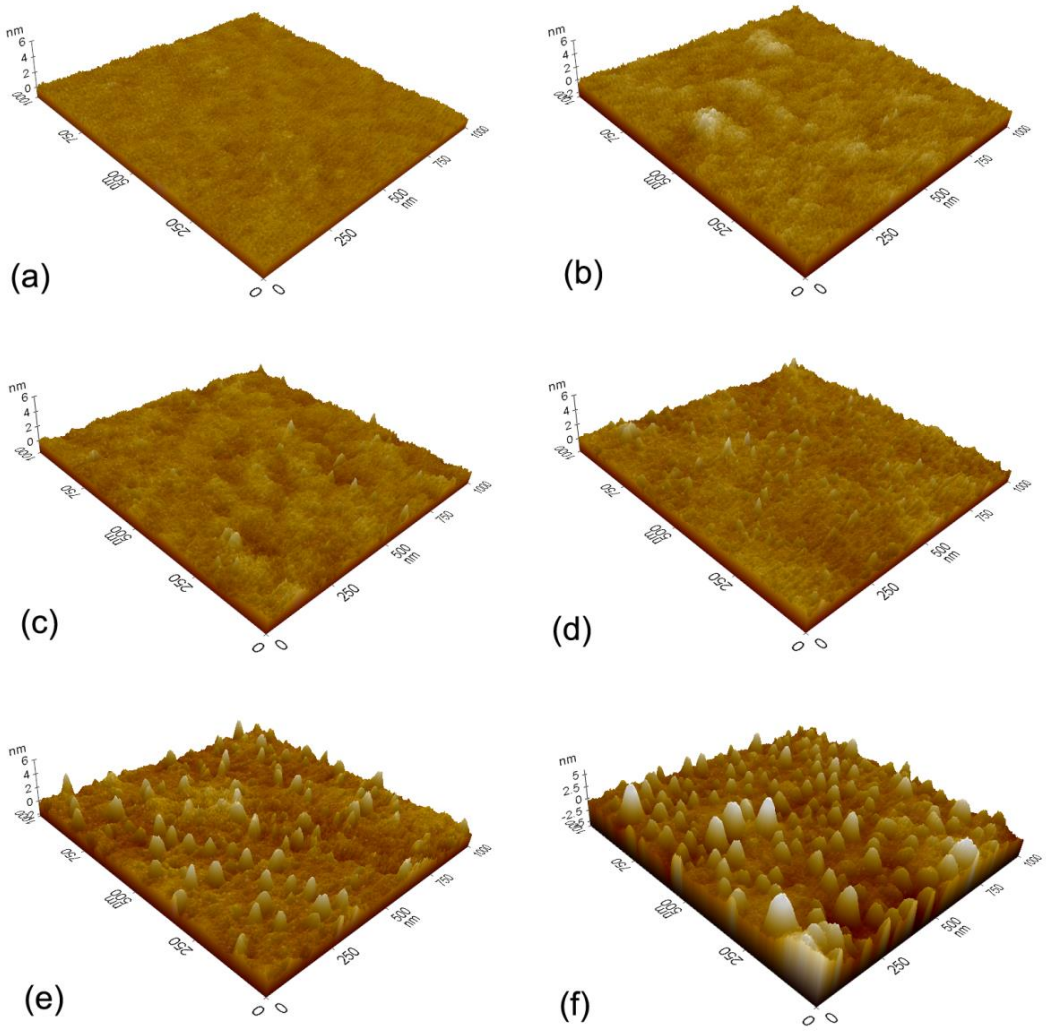

Fig. 5.3.2. Contact AFM 3D images of the (a) as-deposited $Hf_7B_{23}Si_{17}C_4N_{45}$ coating and the annealed coating up to (b) 1100 °C, (c) 1200 °C, (d) 1300 °C, (e) 1400 °C and (f) 1500 °C.

The surface morphology and mean surface roughness (R_a) of the as-deposited and annealed $Hf_7B_{23}Si_{17}C_4N_{45}$ coatings were studied using AFM in the contact mode. The scanning size was 1×1 μm^2.

Figs. 5.3.2(a)-(f) show the three-dimension AFM images showing surface structure evolution of the $Hf_7B_{23}Si_{17}C_4N_{45}$ coatings upon annealing at different temperatures. The as-deposited coating exhibits a very flat and smooth surface structure with R_a = 0.16 nm, as shown in Fig. 5.3.2(a). Annealing the coating up to 1100 °C modified the surface structure slightly and the coating surface appears rougher R_a= 0.3 nm, as shown in Fig. 5.3.2(b). The coating annealed up to 1200 °C exhibits the formation of a few nano islands with the diameter about 14 nm and R_a ≈0.25 nm, as shown in Fig. 5.3.2(c). The coating annealed up to 1300 °C shows more nano islands on the coating surface, as shown in Fig. 5.3.2(d). The size of the nano islands are nearly the same as those in the coating annealed up to 1200 °C. The average roughness of the coating annealed up to 1300 °C is about 0.25 nm, similar to that of the coating annealed up to 1200 °C. With the increasing of the annealing temperature up to 1400 °C, and 1500 °C, the size of nano island increases to ~47 nm and ~53 nm, and R_a increases to 0.40 nm and 0.78 nm, respectively, as shown in Fig. 5.3.2(e) and Fig. 5.3.2(f). These changes are consistent with the crystallization of the coatings by higher annealing temperatures as observed by XRD.

5.3.3 TEM Studies

5.3.3.1 Plan-View Observations

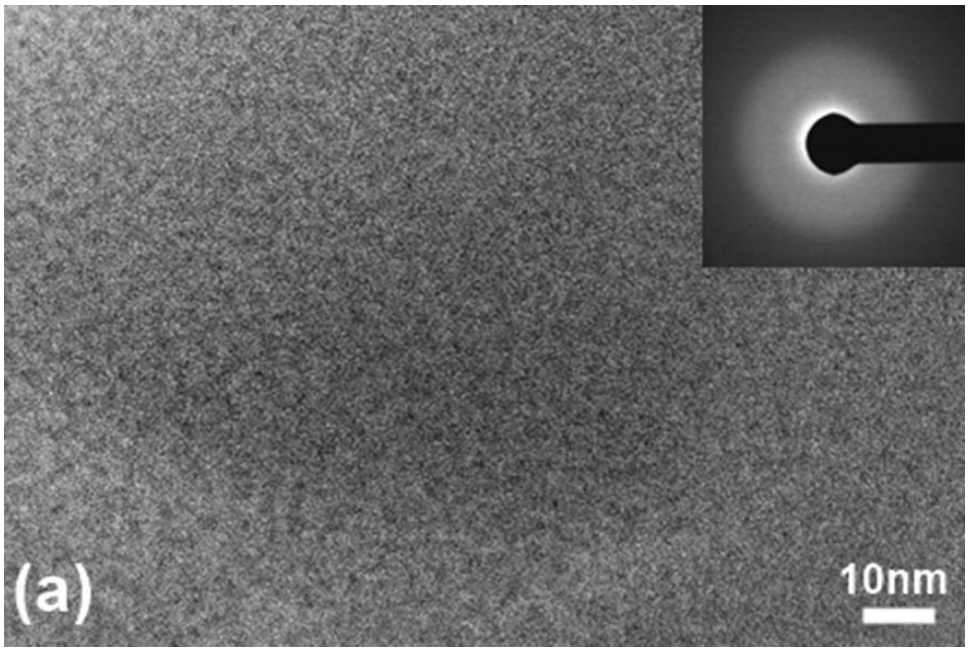

Fig. 5.3.3. (a) Plan-view TEM image and SAED pattern of the as-deposited $Hf_7B_{23}Si_{17}C_4N_{45}$ coating.

The plan-view samples have been prepared from the top surface layer of the annealed coatings where oxidation has taken place. Fig. 5.3.3(a) shows a plan-view TEM image and inset SAED pattern of the as-deposited $Hf_7B_{23}Si_{17}C_4N_{45}$ coating, further confirming its amorphous structure.

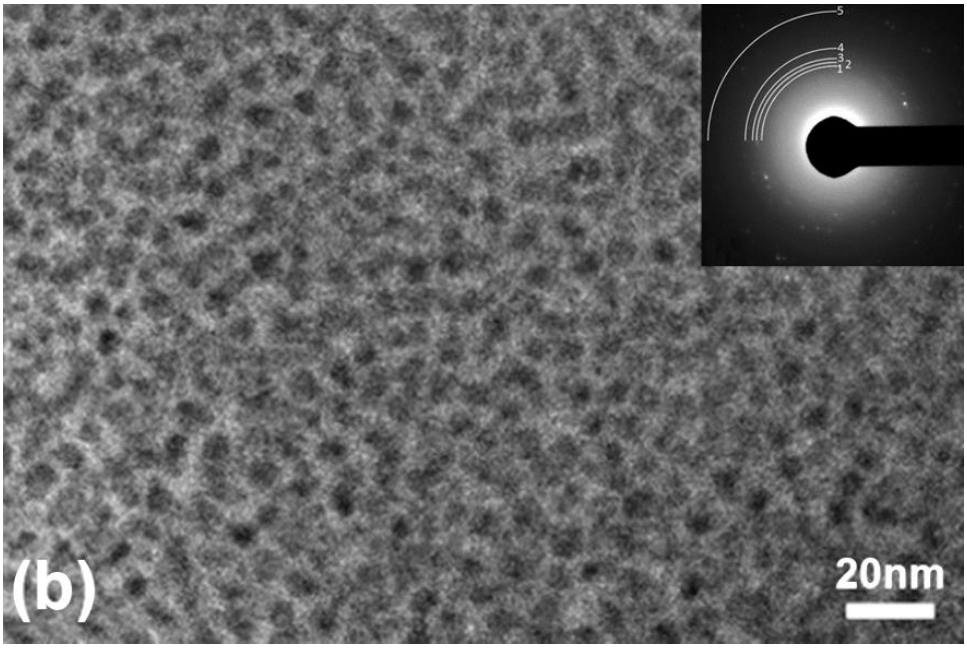

Fig. 5.3.3. (b) Plan-view TEM image and SAED pattern of the $Hf_7B_{23}Si_{17}C_4N_{45}$ coating annealed up to 1100 °C.

Fig. 5.3.3(b) shows the plan-view TEM image of the coating annealed up to 1100 °C, presenting nanoparticles with a size range 3 - 7 nm. The inset SAED pattern presents numerous electron diffraction spots indicating the formation of crystalline. This result is different from the XRD measurement, and the reason will be described later. Taking further analysis, the diffraction spots were found to be nearly located on five diffraction rings 1, 2, 3, 4 and 5 with a lattice spacing of 3.14 Å, 2.94 Å, 2.82 Å, 2.52 Å and 1.81 Å, respectively. The diffraction ring 1, 3 and 4 can be identified as the$(\bar{1}\ 1\ 1)$, (1 1 1) and (2 0 0) of the m-HfO_2. The ring 2 can be possibly identified as the (1 1 1) of oct-HfO_2. The lattice spacing of the ring 5 is equal to that of the (2 2 0) of m-HfO_2, or oct-HfO_2. Electron diffraction study shows that m-HfO_2 and oct-HfO_2 nanocrystalline were nucleated in the $Hf_7B_{23}Si_{17}C_4N_{45}$ coating annealed up to 1100 °C.

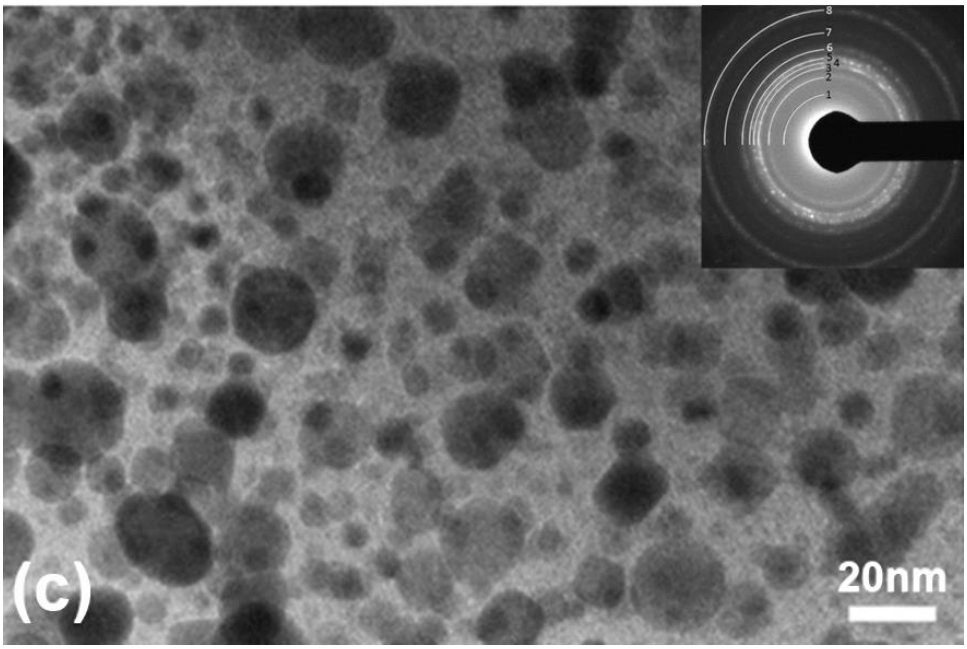

Fig. 5.3.3. (c) Plan-view TEM image and SAED pattern of the $Hf_7B_{23}Si_{17}C_4N_{45}$ coating annealed up to 1200 °C.

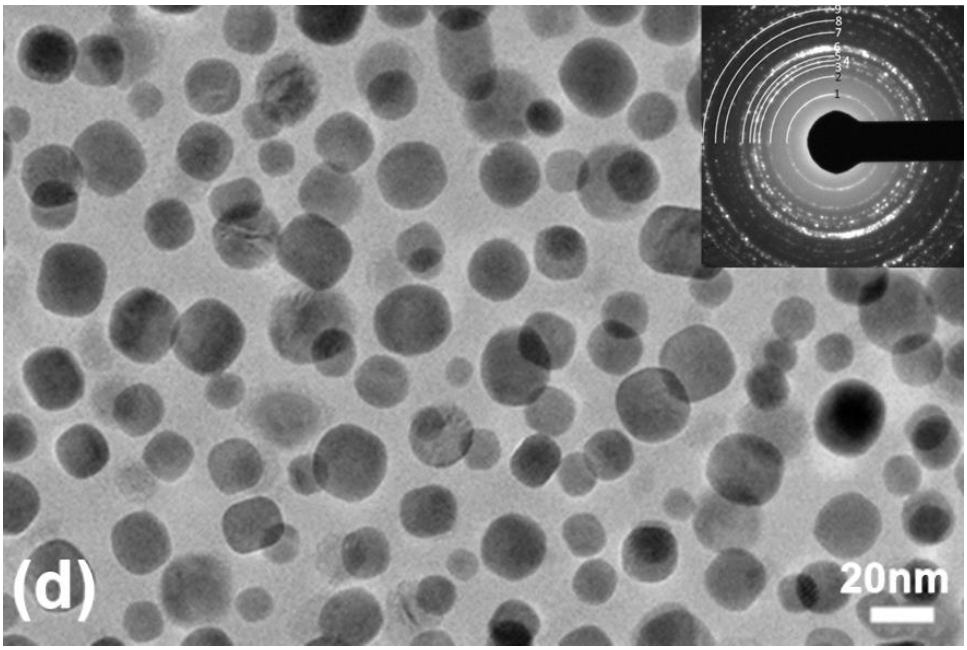

Fig. 5.3.3. (d) Plan-view TEM image and SAED pattern of the $Hf_7B_{23}Si_{17}C_4N_{45}$ coating annealed up to 1300 °C.

Annealing the coating up to 1200 °C resulted in the formation of coarser nanoparticles with a size range from 5 to 20 nm, as shown in Fig. 5.3.3(c). The inset SAED pattern of this coating shows the presence of eight diffraction rings. The corresponding lattice spacing of the diffraction rings 1- 8 is listed in Table 5.3.1. The diffraction ring 1, 2, 3, 5 and 7 can be identified as the (1 0 0), (1 1 0), $(\bar{1}\ 1\ 1)$, (1 1 1)

and $(\bar{2}\ 1\ 1)$ of m-HfO_2. The ring 4 can possibly correspond to the (1 1 1) of oct-HfO_2. The ring 6 is actually a diffraction band with a lattice spacing spanning from ~2.52 Å to ~2.58 Å and is a superposition of (0 2 0) and (2 0 0) of m-HfO_2, (0 0 2) of o-HfO_2, (2 0 0) of t-HfO_2 and (2 0 0) of c-HfO_2. The same situation of the ring 6 applies to ring 8 which is a superposition of (2 2 0) of m-HfO_2 and (2 2 0) oct-HfO_2.

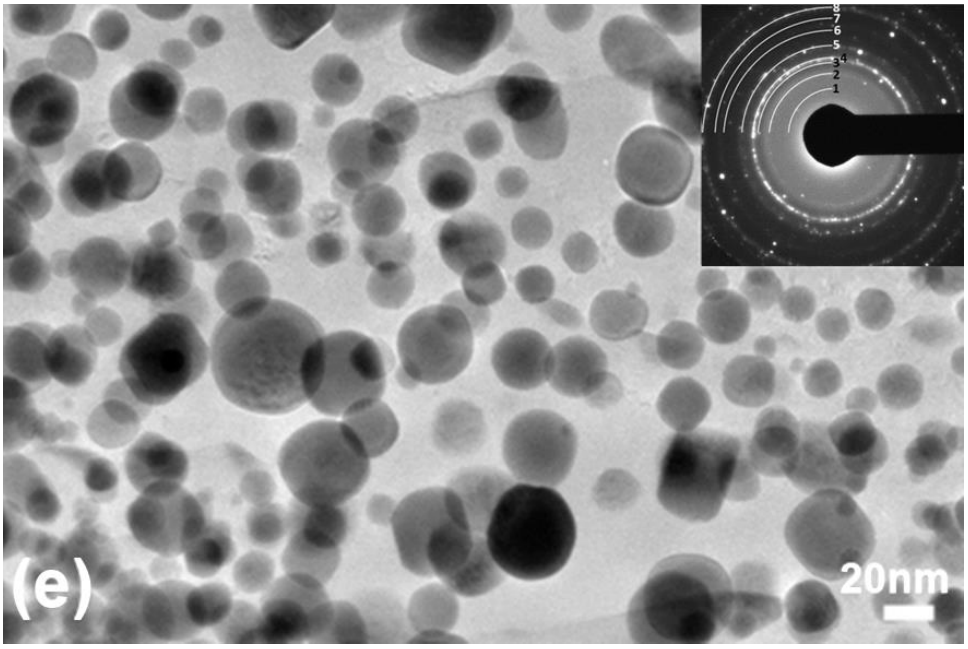

Fig. 5.3.3. (e) Plan-view TEM image and SAED pattern of the $Hf_7B_{23}Si_{17}C_4N_{45}$ coating annealed up to 1400 °C.

Figs. 5.3.3(d), (e) and (f) show images and SAED patterns of the annealed coating up to 1300 °C, 1400 °C and 1500 °C, respectively. It is evident that with the increasing of annealing temperatures, the size of nanoparticles present in the coatings increases. The nanoparticle size in the coatings annealed up to 1300 °C, 1400 °C and 1500 °C ranged from ~9 - 30 nm, ~10 - 52 nm, and ~20 - 55 nm, respectively. The lattice spacing of all diffraction rings is listed in Table 5.3.1. Electron diffraction studies show that the nanoparticles formed in the coatings annealed up to different temperatures exhibit a crystal structure of m-HfO_2 and oct-HfO_2.

HRTEM studies were conducted on the coatings annealed up to different temperatures to get a better understanding of the structure development during the high temperature exposure. Figure 5.3.4 shows representative HRTEM images from the as-deposited and three selected coatings annealed up to 1100 °C, 1300 °C and 1500 °C.

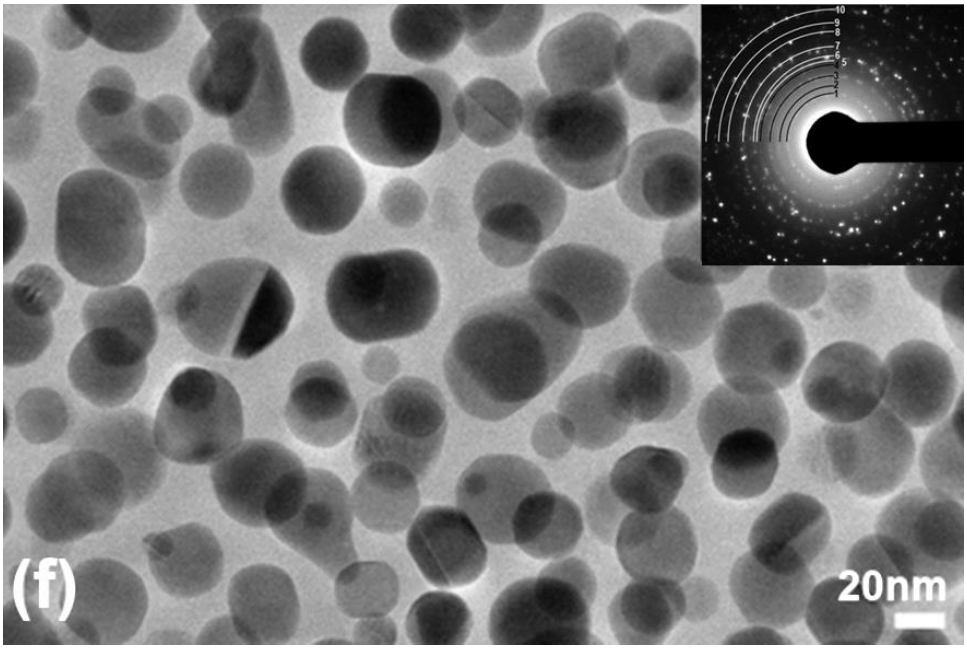

Fig. 5.3.3. (f) Plan-view TEM image and SAED pattern of the $Hf_7B_{23}Si_{17}C_4N_{45}$ coating annealed up to 1500 °C.

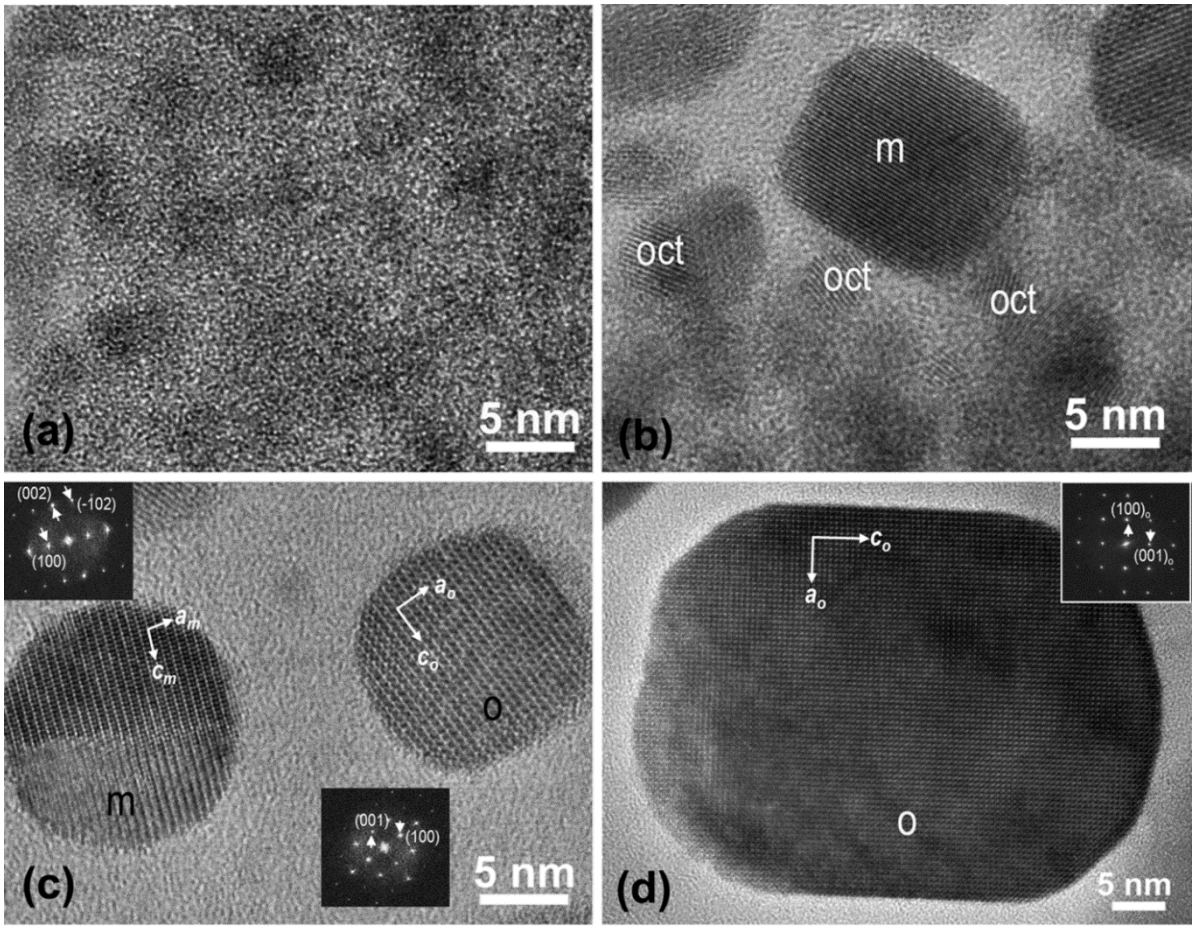

Fig. 5.3.4. Plan-view HRTEM image for (a) as-deposited $Hf_7B_{23}Si_{17}C_4N_{45}$ coating and the coating annealed up to (b) 1100 °C, (c) 1300 °C and (d) 1500 °C.

Table 5.3.1. List of the *d*-spacing of the m-HfO_2, o-HfO_2, and the measured values from the SAED pattern of the coating annealed up to 1100 °C, 1200 °C, 1300 °C, 1400 °C and 1500 °C.

d(Å)	m-HfO_2	o-HfO_2	1100 °C		1200 °C		1300 °C		1400 °C		1500 °C	
	H k l	H k l	Diff.	d(Å)	Diff.	d(Å)	Diff.	d(Å)	Diff.	d(Å)	Diff.	d(Å)
5.051	1 0 0				1	5.05	1	5.05	1	5.05	1	5.05
4.080											2	4.08
3.677	0 1 1											
3.612	1 1 0	1 1 0			2	3.62	2	3.62	2	3.62	3	3.62
3.146	-1 1 1		1	3.14	3	3.14	3	3.14	3	3.14	4	3.15
2.941		1 1 1	2	2.94	4	2.94	4	2.94	4	2.95	5	2.95
2.825	1 1 1		3	2.82	5	2.83	5	2.82			6	2.83
2.584	0 2 0				6	~2.52-2.58	6	~2.52 -2.58	5	~2.52-2.58	7	~2.53-2.58
2.529		0 0 2										
2.527	2 0 0		4	2.52								
2.270	2 1 0								6	2.28		
2.201	-2 1 1				7	2.20						
2.165	-1 2 1						7	2.16			8	2.16
2.052	1 2 1								7	2.05		
1.981	2 1 1						8	1.97			9	1.98
1.811					8	1.81	9	1.81	8	1.80	10	1.81
1.808		2 2 0	5	1.81								
1.807	2 2 0											
1.683	3 0 0											
1.651	2 2 1											
1.645	-1 1 3											
1.646		1 3 0										
1.532	-3 0 2											

Fig. 5.3.4(a) shows a plan-view HRTEM image of the as-deposited $Hf_7B_{23}Si_{17}C_4N_{45}$ coating presenting an amorphous structure. There are some dark, cluster-like regions which may be correspond to Hf-rich areas. Fig. 5.3.4(b) is a plan-view HRTEM image taken from the coating annealed up to 1100 °C exhibiting the presence of nanocrystalline particles. The big nanoparticle marked by “m” shows

lattice fringes with a d-spacing of 2.49 Å and can be identified as the $(\bar{1}\ 0\ 2)$ of the m-HfO_2. However, the small nanoparticles marked by “oct” exhibiting fringes with a d-spacing of 2.95 Å which is still difficult to identify the exact structure. These fringes are identified as the (1 1 1) of oct-HfO_2. Fig. 5.3.4(c) is a plan-view HRTEM image taken from the coating annealed up to 1300 °C showing presence of two well-formed sing crystal nanoparticles with the size about 13 nm. The analysis of corresponding Fast Fourier Transformation (FFT) from single particle indicates that these two particles belong to two different structures. One particle is monoclinic HfO_2 and the other one is orthorhombic. Fig. 5.3.4(d) is a plan-view HRTEM image taken from the $Hf_7B_{23}Si_{17}C_4N_{45}$ coating annealed up to 1500 °C showing presence of an elongated nanoparticle (~37 nm wide, 50 nm long) and its FFT. This particle exhibits an o-HfO_2 structure and is oriented with the [010] parallel to the electron beam. The above results provide enough information to confirm the oct-HfO_2 can be identified as the orthorhombic HfO_2.

5.3.3.2 Cross-section Observations

The microstructure evolution of all $Hf_7B_{23}Si_{17}C_4N_{45}$ coatings as a function of the annealing temperature was studied by cross-section TEM.

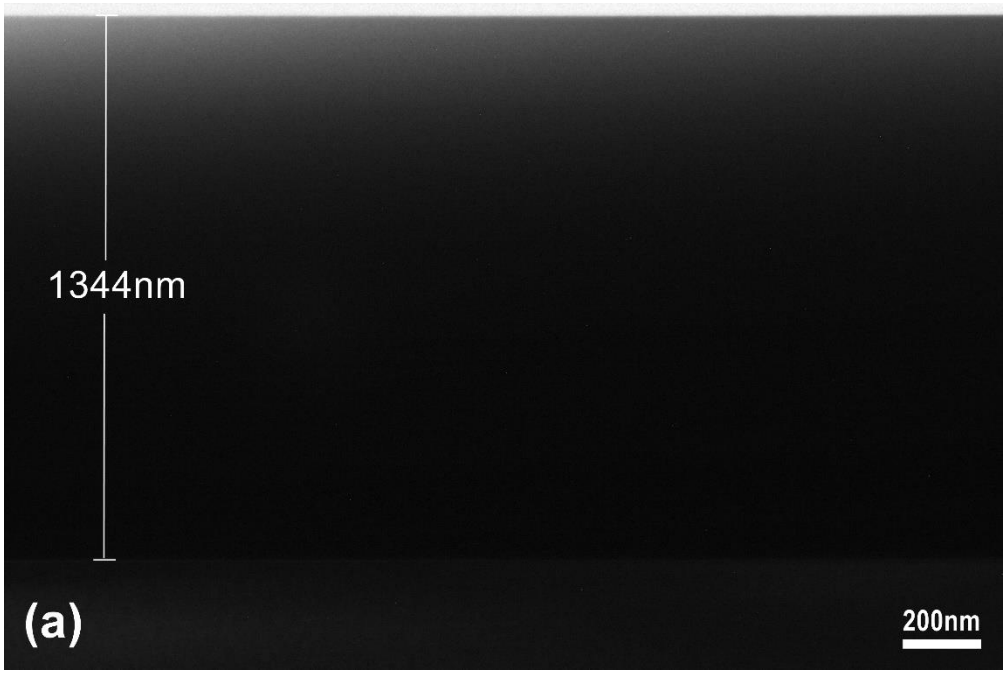

Fig. 5.3.5. (a) Cross-section TEM image for as-deposited $Hf_7B_{23}Si_{17}C_4N_{45}$ coating.

Fig. 5.3.5 (a) shows a cross-section bright-field TEM image of the as-deposited $Hf_7B_{23}Si_{17}C_4N_{45}$ coating presenting the whole coating with thickness of 1344 nm. The HRTEM image of this coating

confirms its amorphous structure (not shown here). The observations from the annealed coatings showed that all coatings developed a top oxidized layer that was composed of two sublayers: 1) *SL-I* next to the interface between the original coating and oxidized layer; 2) *SL-II* at the oxidized layer surface. The morphology of all annealed coatings are illustrated in Figs.5.3.5 (b)-(f).

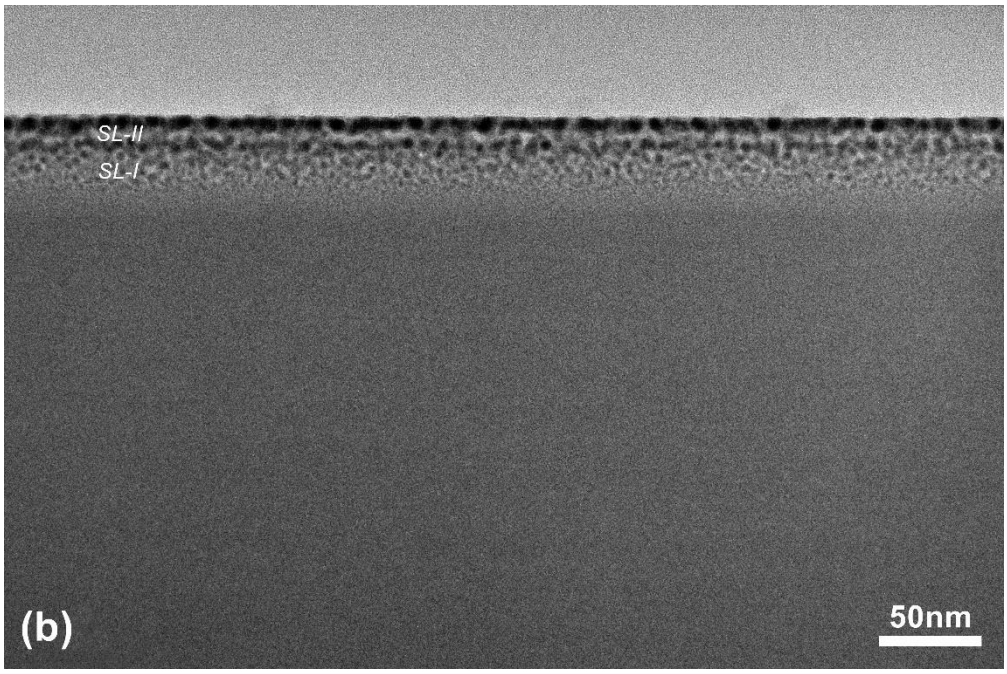

Fig. 5.3.5. (b) Cross-section TEM image for $Hf_7B_{23}Si_{17}C_4N_{45}$ coating annealed up to 1100 °C.

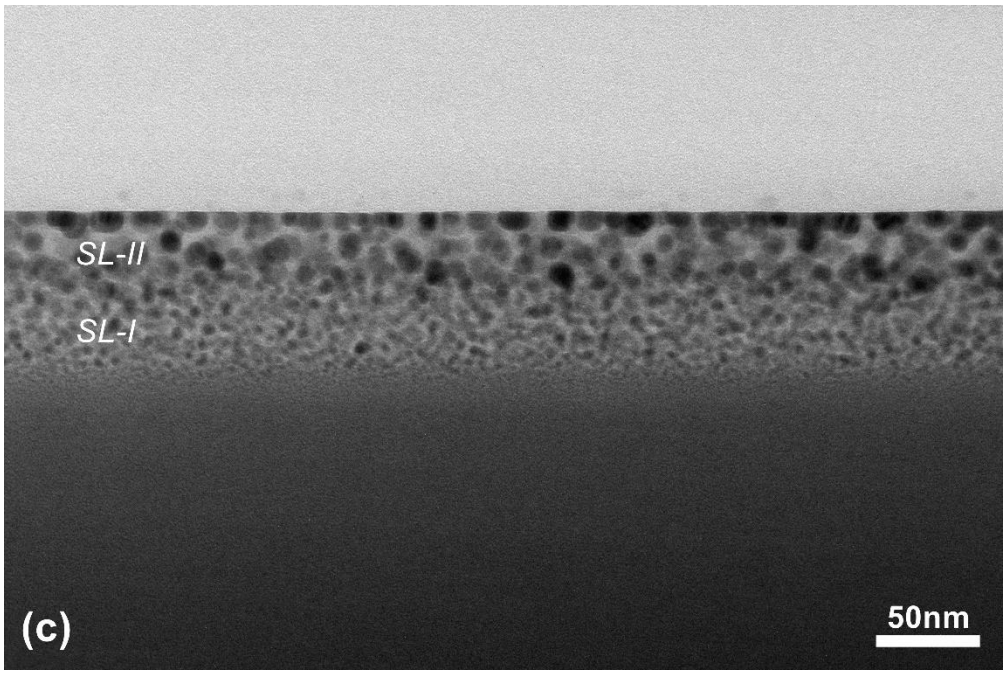

Fig. 5.3.5. (c) Cross-section TEM image for $Hf_7B_{23}Si_{17}C_4N_{45}$ coating annealed up to 1200 °C.

It can be clearly seen that the thickness of the entire oxidized layer and the size of the particles varied with the annealing temperature. The thickness of the two sublayers and the particle size in each sublayer for each annealing temperature are presented in Table 5.3.2.

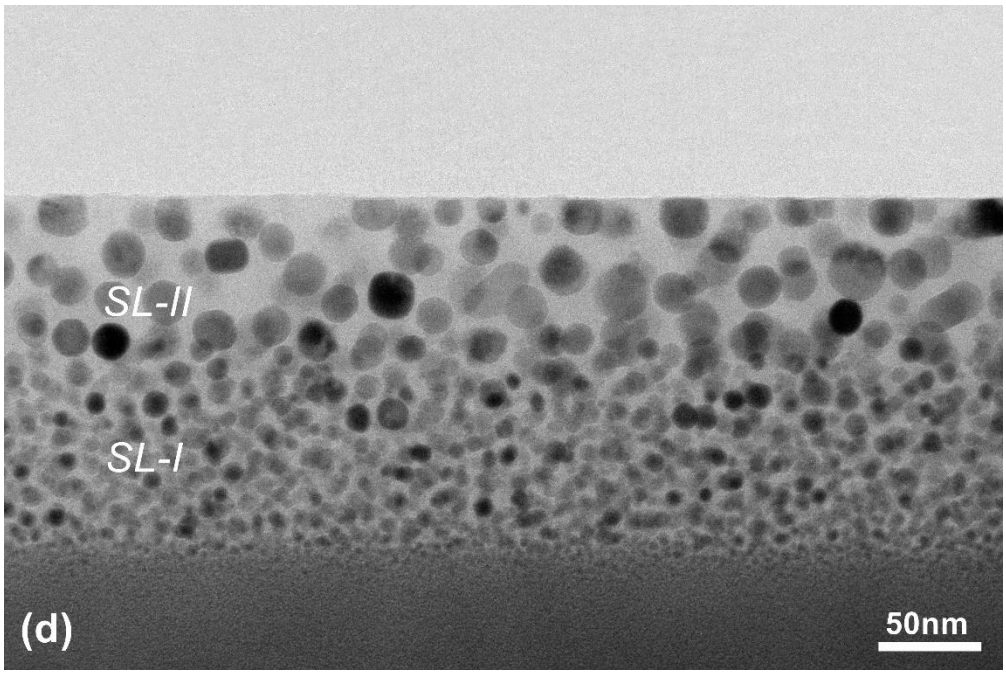

Fig. 5.3.5. (d) Cross-section TEM image for $Hf_7B_{23}Si_{17}C_4N_{45}$ coating annealed up to 1300 °C.

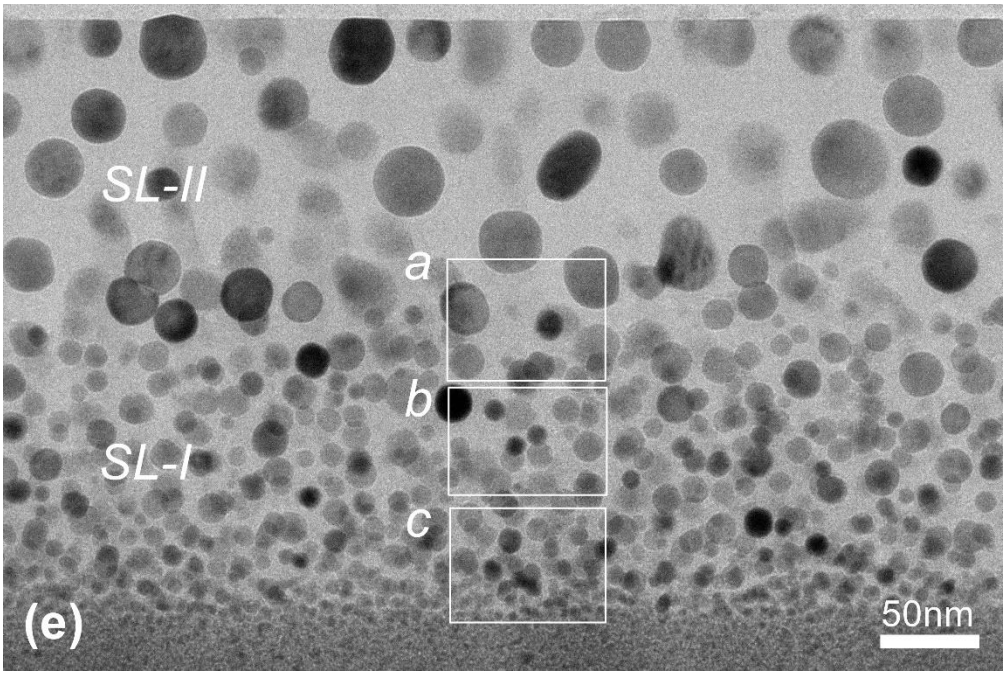

Fig. 5.3.5. (e) Cross-section TEM image for $Hf_7B_{23}Si_{17}C_4N_{45}$ coating annealed up to 1400 °C.

Further analysis of oxidized layer showed that the two sublayers were composed of HfO_2 nanoparticles embedded in an amorphous SiO_x matrix in all coatings. It can be clearly seen that *SL-I* is composed of a dense population of small particles and *SL-II* close to the surface consists of coarser but dispersed particles. As O diffuses and reacts with the coating, HfO_2 nuclei develop at the interface with the original coating and particle growth occurs as the surface is approached.

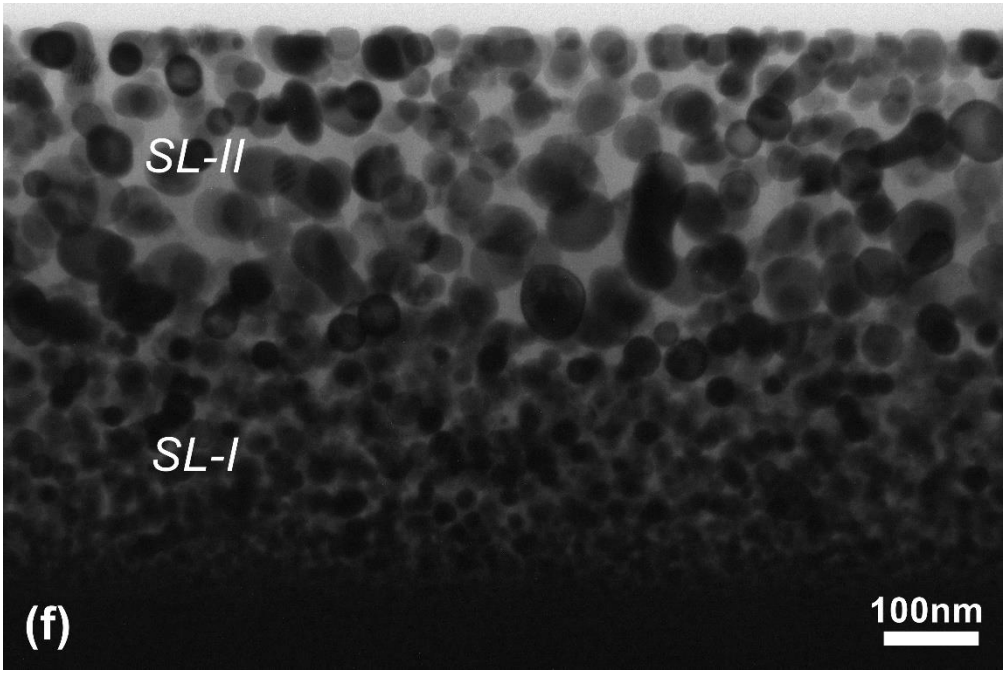

Fig. 5.3.5. (f) Cross-section TEM image for $Hf_7B_{23}Si_{17}C_4N_{45}$ coating annealed up to 1500 °C.

Table 5.3.2. List of the total coating thickness and oxide layer thickness measured by TEM, activation energy for diffusion (*Q*) of the as-deposited and annealed coatings.

Sample	Total thickness (nm)	Oxide layer thickness (nm)	Sublayer *SL-I* Thickness/ Particle size (nm)	Sublayer *SL-II* Thickness/ Particle size (nm)	*Q* (eV)
As-deposited	1344	0			
1100 °C	1352	45	23/4	22/9	3.30
1200 °C	1385	89	45/6	44/15	3.38
1300 °C	1395	190	90/10	90/23	3.42
1400 °C	1310	300	152/15	148/31	3.52
1500 °C	1410	544	275/23	270/47	3.56

It is evident that a very thin oxidized layer (45 nm) developed in the coating annealed up to 1100 ºC with small size nanoparticles (~4 - 9 nm). This layer may be too thin to be detected in XRD and may account for the absence of the XRD signal in Fig. 5.3.1. An interesting observation can be made in Figs. 5.3.5(c)-(e) for the coatings annealed up to 1200 °C, 1300 °C and 1400 °C. The nanoparticles at the top surface were cut abruptly exposing an atomically flat surface, while such phenomena were not observed in the coatings annealed up to 1100 °C and 1500 °C. These results are consistent with the AFM observations that the coating annealed up to 1200 °C is smoother that the coatings annealed up to 1100 °C and 1500 °C exhibited a much rougher surface than the coating annealed up to 1400 °C.

A cross-section HRTEM image taken from the top region near the surface of the oxidized layer in the coating annealed up to 1100 °C is shown in Fig. 5.3.6(a). The nanoparticles are identified to have either m-HfO_2 or o-HfO_2 structure as determined by the spacing of the lattice fringes. The nanoparticles with lattice fringes corresponding to the (111) of o-HfO_2 are marked by “o” in Fig. 5.3.6(a). The lattice fringes in nanoparticles marked by “m_1” and “m_2” have a spacing of ~3.15 Å and ~2.82 Å, corresponding to the $(\bar{1}\,1\,1)$ and (111) of m-HfO_2, respectively. The nanoparticles in Fig. 5.3.6(a) have a size range from 5 nm to 8 nm and the particles at the surface exhibit a round shape without significant distortion in the morphology, resulting in a relative rough surface structure.

A cross-section HRTEM image taken from the surface region of the oxidized layer in the coating annealed up to 1200 °C is shown in Fig. 5.3.6(b). The lattice fringes in the nanoparticle marked by “m” have a spacing of 2.62 Å, corresponding to the (002) of m-HfO_2. The HfO_2 nanoparticle marked by “o” has an orthorhombic structure oriented with its (100) parallel to the coating surface and the $[0\,1\,\bar{1}]$ parallel to the electron beam. The nanoparticles in Fig. 5.3.6(b) have a size range from 8 nm to 15 nm and the prominent parts beyond the surface were cut exposing an atomically flat surface.

A similar cross-section image taken from the surface region of the coating annealed up to 1400 °C is shown in Fig. 5.3.6(c) presenting three m-HfO_2 nanoparticles with a size of ~20 nm. The nanoparticles m_a and m_c are oriented with the (010) parallel to the coating surface and their prominent part beyond the surface was terminated along the (010) atomic surface. A similar appearance of the nanoparticles at the surface was exhibited in the coating that was annealed up to 1300 °C.

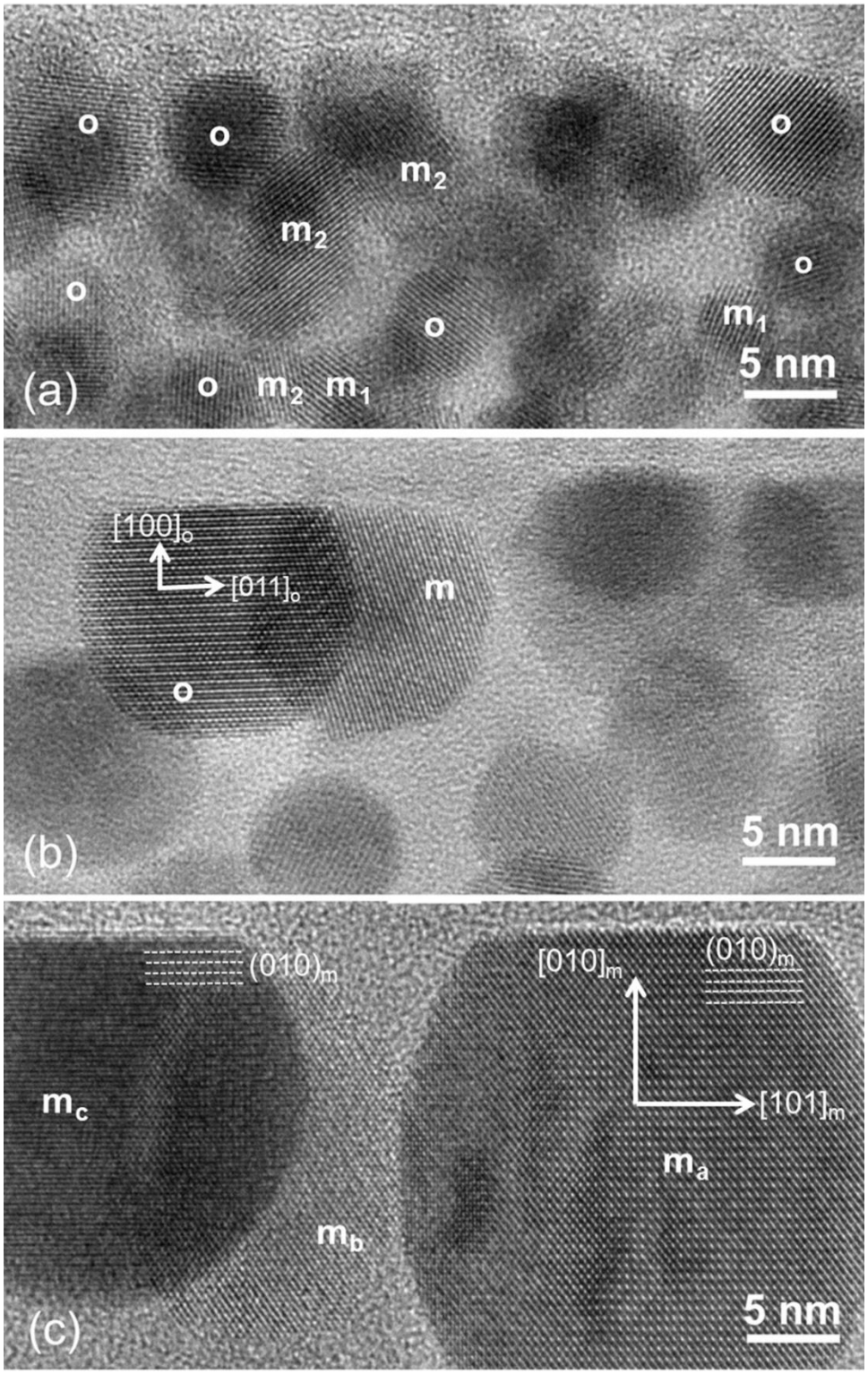

Fig. 5.3.6. Cross-section HRTEM image taken from the top region (surface) of the annealed $Hf_7B_{23}Si_{17}C_4N_{45}$ coatings up to (a) 1100 °C, (b) 1200 °C and (c) 1400 °C.

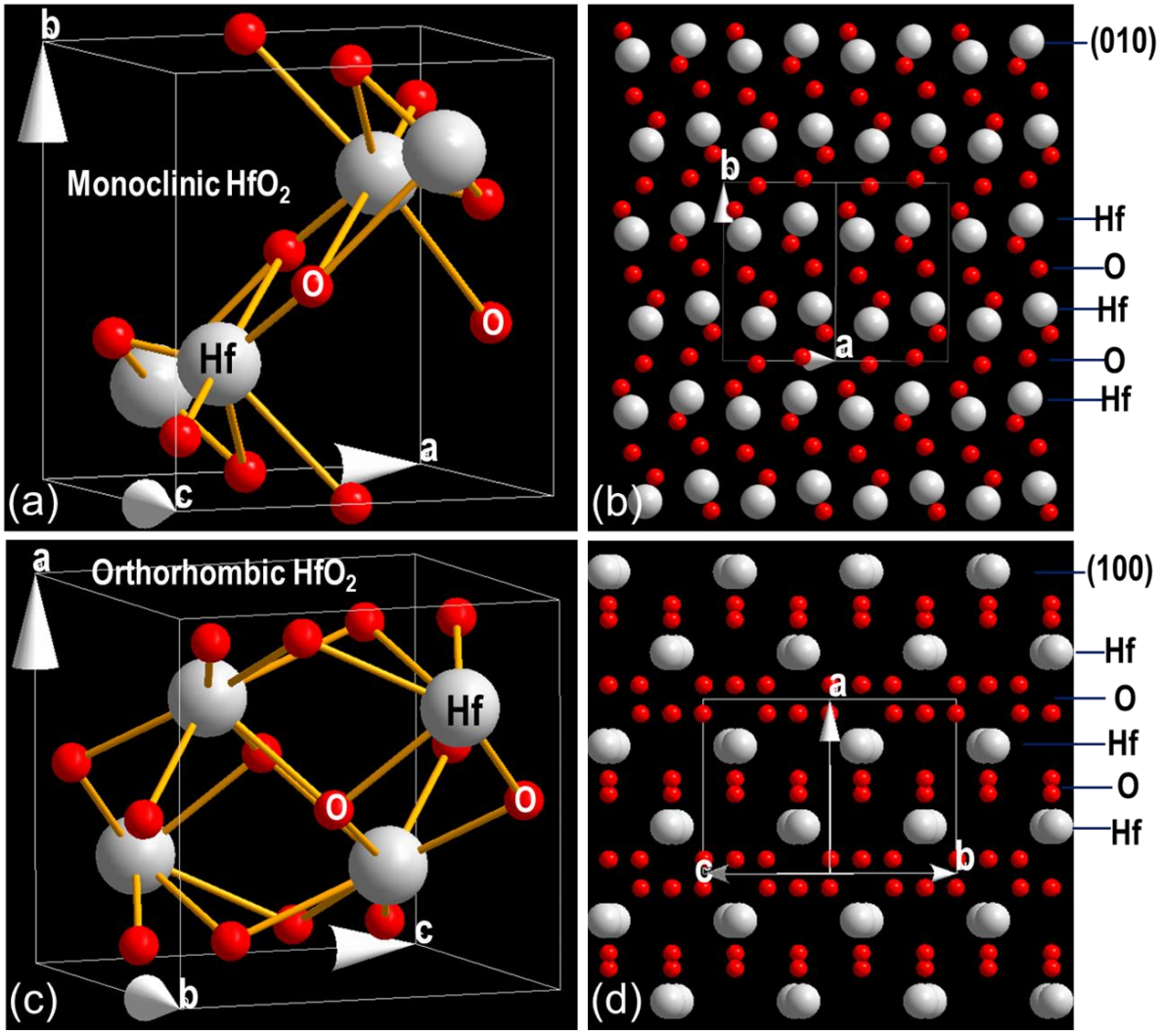

Fig. 5.3.7. Schematic drawing of (a) unit cell of monoclinic HfO_2, (b) a projection of m-HfO_2 along the $[10\bar{1}]$ direction, (c) unit cell of orthorhombic HfO_2 and (d) a projection of o-HfO_2 along the [011] direction.

The atomic cuts of the nanoparticles at the surface along the $(010)_m$ and $(100)_o$ more than likely are associated with the characteristics of these crystallographic structures and the growth process. As schematically illustrated in Figs. 5.3.7(a) and (b), the m-HfO_2 can be considered as a layered structure formed by packing (010) Hf and O layers along the [010] direction. Similarly, the o-HfO_2 can also be considered as a layered structure formed by packing (100) Hf and O layers along the [100] direction, Figs. 5.3.7(c) and (d). The exposure of these O-rich atomic planes can more than likely be attributed to their low surface energy. This morphology is not observed in the coating annealed up to 1100 °C may due to the reason that the oxidized layer is very thin and nanoparticle formation is controlled by

nucleation kinetics. This morphology is not observed in the coating annealed up to 1500 °C may due to the fast growth of the oxide (oxide layer thickness 545 nm). The fast growing overcomes surface energy considerations causing the nanoparticles to extend out of the surface.

5.3.3.3 Coating/Oxidized Layer Interface

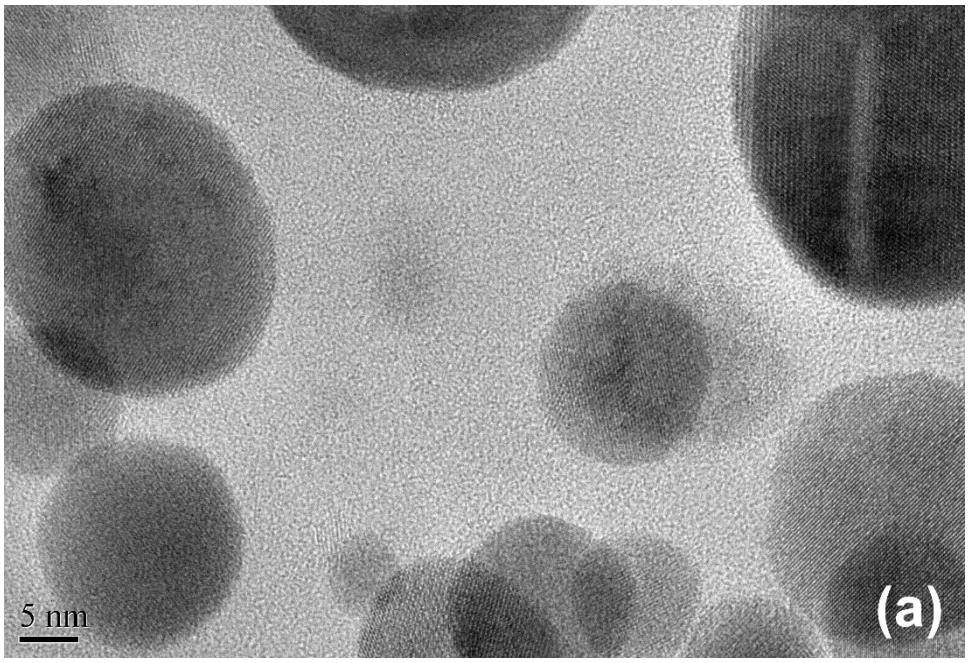

Fig. 5.3.8. (a)Cross-section HRTEM images taken from area ***a*** in the oxidized layer in the annealed $Hf_7B_{23}Si_{17}C_4N_{45}$ coating up to 1400 °C in Fig. 5.3.5(e).

Figs. 5.3.8 (a)-(c) shows cross-section HRTEM images taken from areas at different depths within the oxidized layer of the $Hf_7B_{23}Si_{17}C_4N_{45}$ coating annealed up to 1400 °C. Fig. 5.3.8(a) was taken from the area ***a*** in Fig. 5.3.5(e) within the sublayer *SL-II* which consists of large but dispersed HfO_2 nanoparticles with a size ranging from ~10 to 30 nm. The nanoparticles in Fig. 5.3.8(a) and in the rest of the *SL-II* sublayer were found to be embedded in an amorphous SiO_x matrix.

Fig. 5.3.8(b) was taken from the area ***b*** in Fig. 5.3.5(e) within the sublayer *SL-I* where the HfO_2 nanoparticles have a size ranging from ~10 to 15 nm. The boundary regions between nanoparticles and the matrix are no longer pure amorphous. Lattice fringes with a spacing of ~3.4 Å were observed in several boundary areas (pointed by arrows). This result indicates possible formation of the quartz SiO_2 nanocrystalline structure in the boundary areas. In fact, the formation of quartz is consistent with theoretical predictions of the Hf-Si-O ternary phase diagram [155].

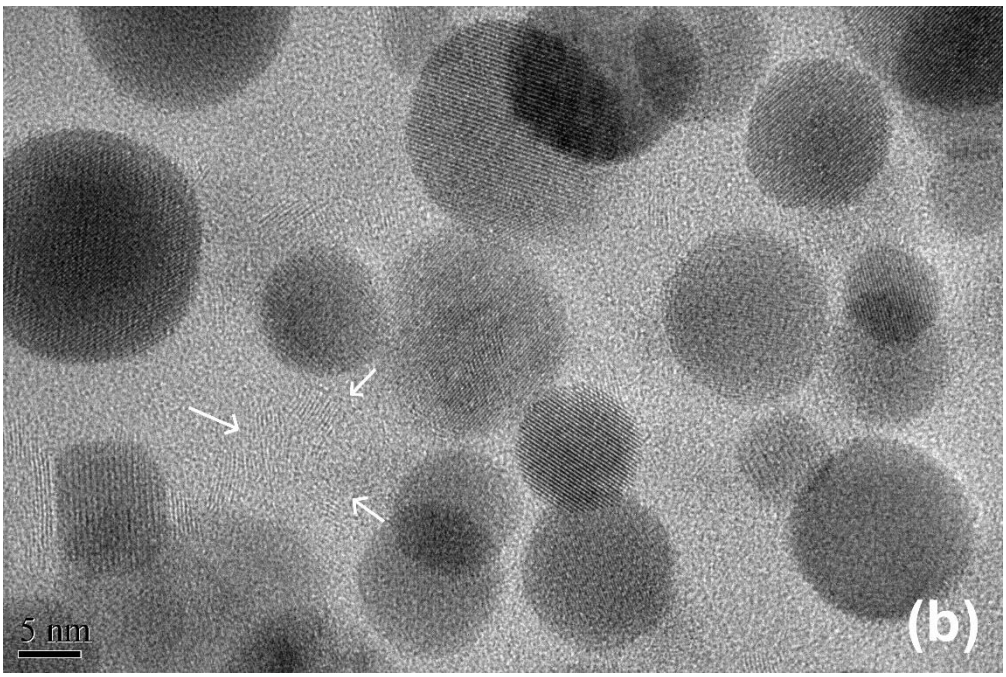

Fig. 5.3.8. (b)Cross-section HRTEM images taken from area ***b*** in the oxidized layer in the annealed $Hf_7B_{23}Si_{17}C_4N_{45}$ coating up to 1400 °C in Fig. 5.3.5(e).

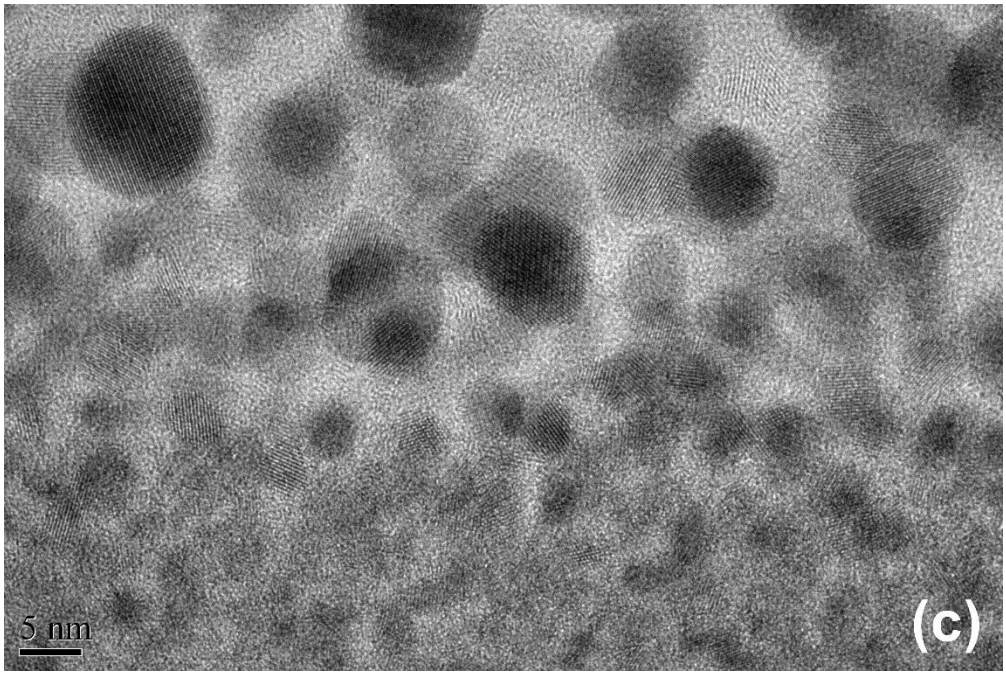

Fig. 5.3.8. (c)Cross-section HRTEM images taken from area ***c*** in the oxidized layer in the annealed $Hf_7B_{23}Si_{17}C_4N_{45}$ coating up to 1400 °C in Fig. 5.3.5(e).

Fig.5.3.8(c) was taken from the interface region between the oxidized layer (*SL-I*) and the continuous homogenous $Hf_7B_{23}Si_{17}C_4N_{45}$ layer in Fig. 5.3.5(e), showing details of the structure across the interface. It was observed that nucleation of fine crystalline nanoparticles 2 - 3 nm took place in the

$Hf_7B_{23}Si_{17}C_4N_{45}$ coating at the interface with the oxidized sublayer *SL-I*. It was also observed that nucleation of these nanoparticles occurred while the $Hf_7B_{23}Si_{17}C_4N_{45}$ coating still maintained an amorphous structure.

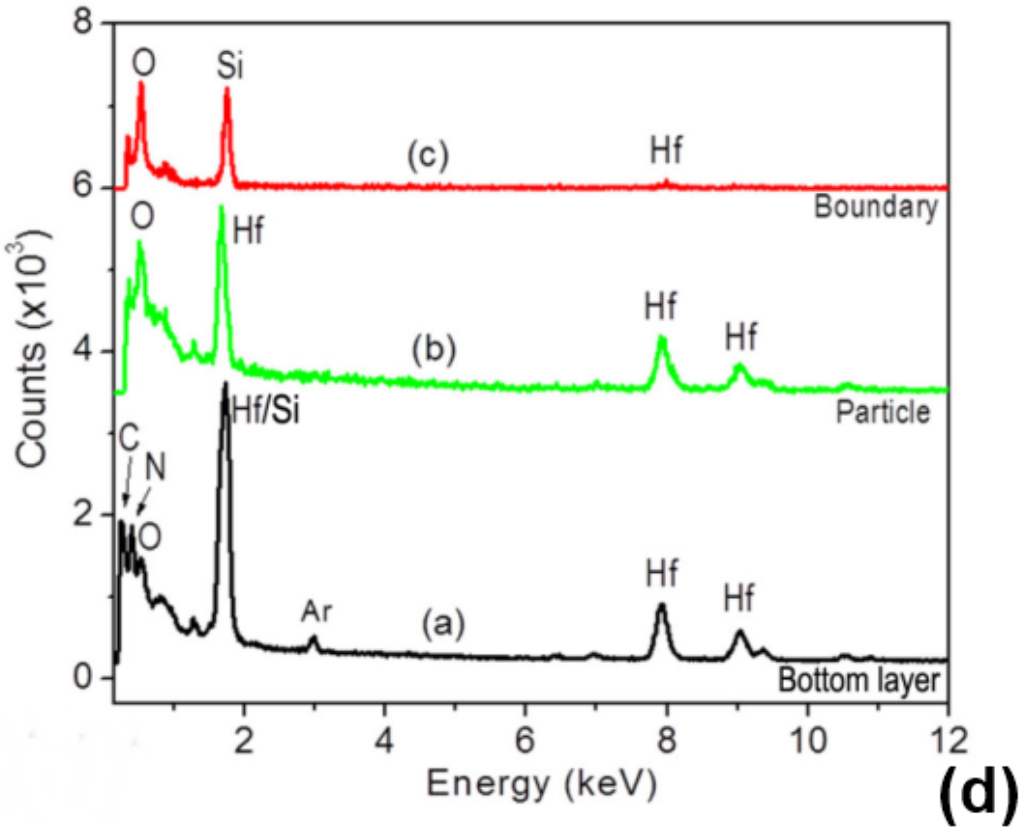

Fig. 5.3.8. (d) EDS spectra taken from an area (marked by arrow heads) within the boundaries (red curve) and a HfO_2 nanoparticle (green curve) in Fig. 5.3.8. (b), and from the bottom layer in Fig. 5.3.8. (c).

Fig. 5.3.8(d) presents three EDS spectra taken from different locations within the coating area in a cross-section TEM foil of the $Hf_7B_{23}Si_{17}C_4N_{45}$ coating annealed up to 1400 °C. The red spectrum was from the marked area by the arrow heads within the boundary region mainly showing presence of O and Si. This result, in addition to the lattice fringes presented in the HRTEM image in Fig. 5.3.8(b), provides further evidence for the formation of the quartz SiO_2 crystalline within the boundaries. The green spectrum was from a spherical nanoparticle in Fig. 5.3.8(b) and showed only presence of O and Hf confirming the formation of HfO_2. The black spectrum was taken from the area under the oxide layer of the coating annealed up to 1400 °C and exhibits presence of Hf, Si, C, N, O and Ar. It should be pointed out that boron is more than likely present but cannot be detected by EDS. EDS spectra taken

from the as-deposited coating and the bottom layer of all annealed coatings up to 1000 °C, 1200 °C, 1300 °C, 1400 °C and 1500 °C show the same spectra as the bottom spectrum shown in Fig. 5.3.8(d). This indicates that the bottom layers in all annealed coatings are chemically stable even up to 1500 °C.

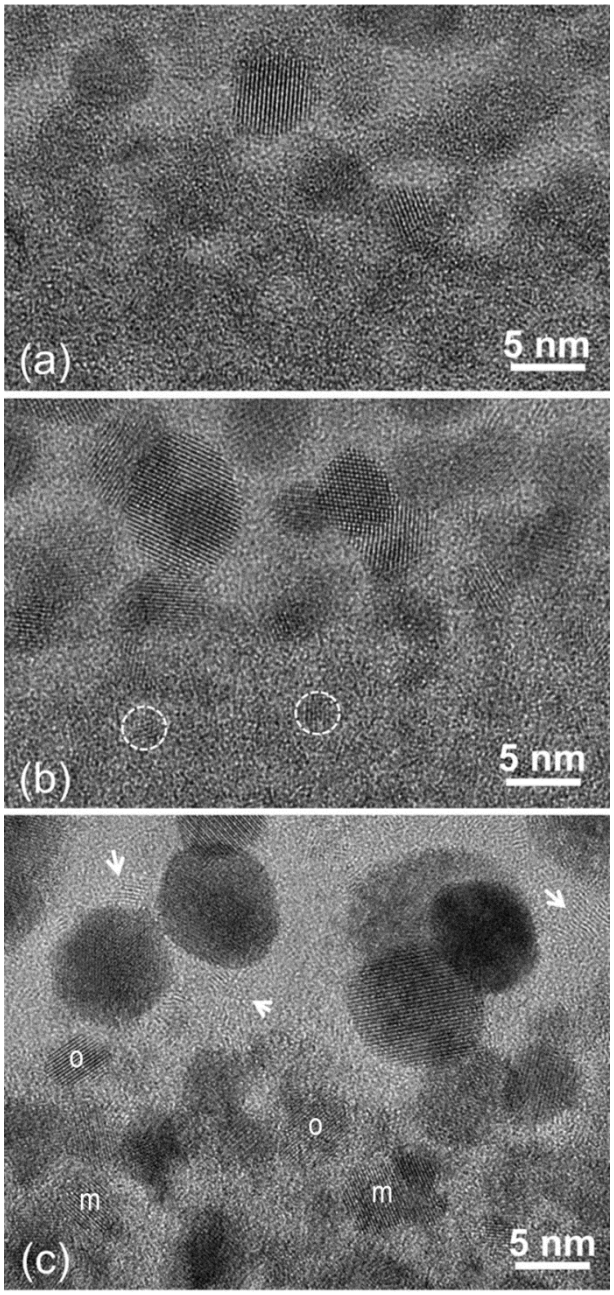

Fig. 5.3.9. Cross-section HRTEM images taken from the interface area between the oxidized layer and the continuous homogenous layer in the $Hf_7B_{23}Si_{17}C_4N_{45}$ coatings annealed up to (a) 1200 °C, (b) 1300 °C and (c) 1500 °C.

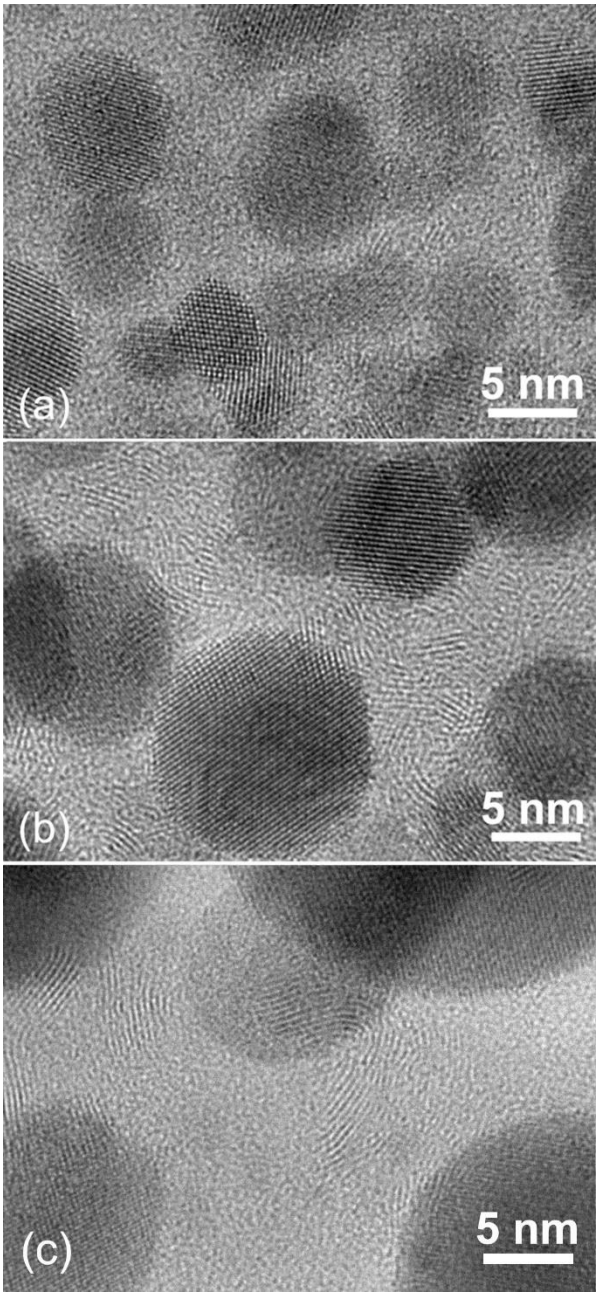

Fig. 5.3.10. Cross-section HRTEM images taken from the oxidized *SL-I* layer in the $Hf_7B_{23}Si_{17}C_4N_{45}$ coatings annealed up to (a) 1300 °C, (b) 1400 °C and (c) 1500 °C.

Figs. 5.3.9(a), (b) and (c) are cross-section HRTEM images taken from the interface area between the oxidized layer (*SL-I*) and the continuous homogenous layer in the coatings annealed up to 1200 °C, 1300 °C and 1500 °C. The nanoparticles in the aforementioned *SL-I* oxidized layer side have a size of ~3-6 nm, ~4-9 nm and ~8-11 nm, respectively. The continuous homogenous layer in Fig. 5.3.9(a) presents an amorphous structure, while that in Fig. 5.3.9(b) shows evidence of crystalline nuclei (marked by circles) formation and that in Fig. 5.3.9(c) presents well developed nanoparticles (~ 5 nm) embedded in the amorphous coating structure. The lattice fringes in the nanoparticles marked by "o" in the continuous homogenous layer, Fig. 5.3.9(c), have a spacing of 2.94 Å corresponding to the (111) of the o-HfO_2, where those marked by "m" have a spacing of ~2.82 Å corresponding to the (111) m-HfO_2. This suggests that as O diffuses through the oxidized layer and reaches the coating/oxidized layer interface, reacts preferentially with Hf atoms in the amorphous structure and nucleates HfO_2 nanoparticles while leaving the rest of the structure as amorphous. This is also supported by the EDS results from the interface presented in Fig. 5.3.8(d). An interesting observation is the significant difference in the size of HfO_2 nuclei in the interface of the continuous layer (~5 nm) and the adjacent HfO_2 particles in the *SL-I* (8-11 nm), Fig. 5.3.9(c). This size difference can be attributed to the kinetics of the oxidation process. As O reaches the interface and reacts preferentially with Hf leaves the rest of the elements in the coating in their original state. Additional O should diffuse to oxidize the Si and develop a SiO_x matrix but in the meantime, the HfO_2 nuclei grow and enter the *SL-I* sublayer. The significant particle size difference can also attest to the oxidation resistance of the coating. It indicates that a significant time interval elapses for the O to diffuse to the interface and oxidize the Si atoms to form an amorphous SiO_x matrix. The preferential oxidation of the Hf atoms in the $Hf_7B_{23}Si_{17}C_4N_{45}$ coating is also supported by considering the lower free energy of oxide formation for Hf compared to Si.

Observations in Fig. 5.3.9(c) also show lattice fringes with a spacing of ~3.4 Å, close to the lattice spacing of the (101) of high quartz SiO_2, that are present in the boundary areas (pointed by arrows). Such fringes can be barely seen in Fig. 5.3.9(b) and they were absent in Fig. 5.3.9(a). This result indicates that the nucleation of quartz SiO_2 starts in the coating annealed up to 1300 °C, and fully develops in the boundary areas in the coatings annealed up to 1400 °C and 1500 °C.

The evolution of the quartz SiO_2 formation in the boundary areas over the annealed temperatures has been investigated in more detail by using cross-section HRTEM to study the oxidized *SL-I* layer in the $Hf_7B_{23}Si_{17}C_4N_{45}$ coatings annealed up to 1300 °C, 1400 °C and 1500 °C. Fig. 5.3.10(a) is a cross-section HRTEM image taken from the *SL-I* layer in the coating annealed up to 1300 °C. The boundaries basically show an amorphous structure except very few regions with formation of SiO_2 nuclei (~1 nm in size). Fig. 5.3.10(b) exhibits a cross-section HRTEM image taken from the *SL-I* layer of the coating annealed up to 1400 °C. High density clusters with a size of ~2 nm and (101) lattice fringes of quartz were observed in the boundary regions. Fig. 5.3.10(c) shows a cross-section HRTEM image taken from the *SL-I* layer in the coating annealed up to 1500 °C. The size of clusters with the (101) lattice fringes of quartz in the boundary regions was increased to ~10 nm. It should be pointed out that the lattice of the (101) of quartz in the boundaries appeared as bended or curved fringes instead of straight lines in all HRTEM images observed. This phenomenon is similar to the lattice fringes of carbon nanotubes or carbon onions. High quartz SiO_2 is a hexagonal structure, the diffraction peak of the (1 0 1) exhibits the highest intensity, while the second strongest diffraction peak of the (1 0 0) only possesses 20% intensity compared to that of the (1 0 1). The high quartz structures were formed in the boundary regions between the nanoparticles, because of the curved or bended lattice planes in addition to the insignificant amount of this structure, the occurrence of such a structure is very difficult to be detected using XRD, even by SAED.

5.3.4 Oxidation Mechanism

A diffusion analysis was conducted, in an effort to obtain an insight of the activation energy for oxygen diffusion (*Q*) in the particular coating. In a diffusion controlled isothermal process, the thickness of the oxide layer *x* is given by:

$$x = \sqrt{Dt} \tag{1}$$

where *D* is the diffusivity of oxygen in the oxide $D = D_o e^{-\frac{Q}{kT}}$, D_o the pre-exponential constant, *k* the Boltzmann's constant, *T* the annealing temperature and *t* the annealing time. The present annealing is not isothermal so the temperature and thus, the diffusivity *D* is a function of time and Eq. 1 becomes

$$x = \int_0^t \frac{1}{2}\sqrt{\frac{D(t)}{t}}dt \quad (2)$$

It should be noted that experimental and theoretical activation energies in the range of Q=0.043-2.5 eV have been reported in the literature for oxygen diffusion in SiO_2 [156-157]. One of the reasons for the reported wide range in Q more than likely relates to the differences in the defect structure of the particular SiO_2. Mikkelsen was able to obtain a single Q=2.44 eV and D_o = 7x10^{-2} cm^{2}s^{-1} for the entire oxidation range of Si between 700-1240 ˚C [158]. In an effort to assess the oxidation resistance of the present $Hf_7B_{23}Si_{17}C_4N_{45}$ coating, we solved Eq. 2 numerically by considering the aforementioned D_o value and the experimentally observed x values listed in Table 5.3.2. In view of the present heating (10 °C /min) and cooling (30 °C /min) rates, the oxide thickness was determined as the sum of all x values resulting from 6 s and 2 s resident time at each degree of the annealing temperature during heating and cooling, respectively. The results produced an average value of Q=3.44 eV.

Considering the Q values obtained for the five annealing temperatures (Table 5.3.2), it is evident that Q increases at higher annealing temperatures. This particular increase in Q can be attributed to the increase of the thickness of the *SL-I* sublayer and formation of high density quartz (2.65 g/cm^3) at higher temperatures. It should be noted that a high density of HfO_2 nanoparticles exists in *SL-I* that form by oxidation of Hf in the amorphous coating. The HfO_2 particles keep growing up until they reach the *SL-I/SL-II* interface up to which point all Hf has been oxidized. In the *SL-II* layer particle growth stops and existing particles coarsen via coalescence in a SiO_x matrix. This means that oxygen is not consumed in sublayer *SL-II* but just diffuses through. In *SL-I* however, the oxygen is gradually consumed as it reacts with Hf and Si growing the HfO_2 nanoparticles and forming the SiO_x matrix thus, creating a much smaller O concentration gradient compared to *SL-II*. Thus, sublayer *SL-I* is expected to act as a much stronger barrier to oxygen diffusion. On the other hand, quartz was nucleated at around 1300 ˚C and was well formed at 1400 ˚C and 1500 ˚C. In fact, room temperature values for quartz as low as D= 10^{-25} cm^{2}s^{-1} have been reported that support this finding [159, 160]. Thus, above 1300 ˚C, the formation of quartz seems to act as an effective diffusion barrier compared to amorphous SiO_x. Thus, above 1300 ˚C higher activation energies are expected.

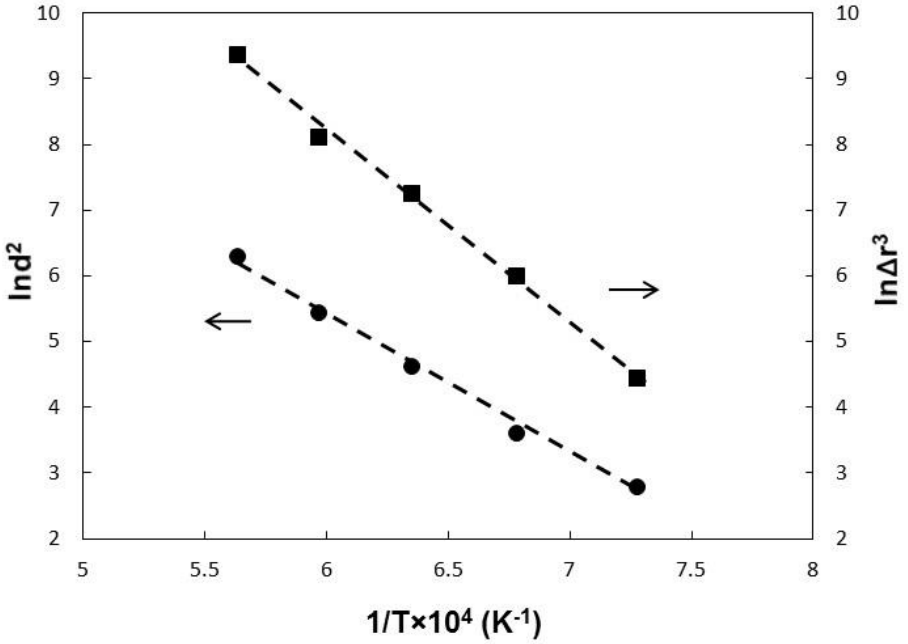

Fig. 5.3.11. Variation of *lnd²* and *lnΔx³* vs *1/T* for the annealed coatings.

It is clear from the above discussion that the present oxidation process is influenced by the formation of the two distinct sublayers *SL-I* and *SL-II*. As noted earlier, *SL-I* involved nucleation and growth of high density of HfO_2 nanoparticles that presumably result in oxidization of all available Hf in that region of the coating. On the other hand, sublayer *SL-II* involved coarsening of the existing particles that were produced in *SL-I*. These processes can be described by a growth process in *SL-I* and a coarsening process in *SL-II*. Thus, in *SL-I* the HfO_2 particle size *d* can be described by a similar expression as Eq. 1 that produces a linear relationship between *lnd²* and *1/T*

$$\ln d^2 = -\frac{Q}{k}\frac{1}{T} + \ln t + \ln D_0 \qquad (3)$$

Similarly, the coarsening of the existing particles is expected to follow an Ostwald's ripening process as

$$\Delta r^3 = r^3 - r_o^3 = D\gamma C_e t \qquad (4)$$

where *r* and r_o are the final and the initial mean radius of the nanoparticles, γ the interfacial energy and C_e the equilibrium solubility of the particles. Eq. 4 then becomes

$$\ln \Delta r^3 = -\frac{Q}{k}\frac{1}{T} + \ln \gamma + \ln C_e + \ln t + \ln D_0 \qquad (5)$$

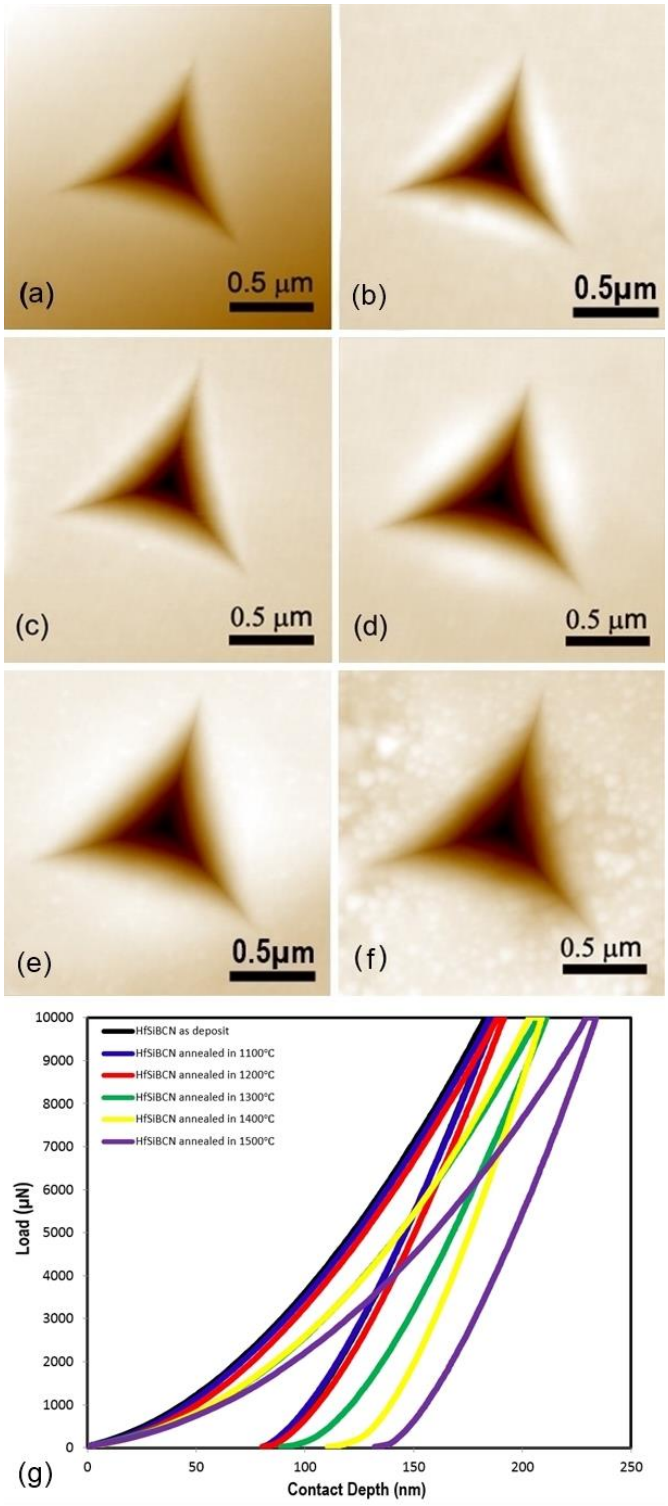

Fig. 5.3.12. Indentation images of the (a) as-deposited $Hf_7B_{23}Si_{17}C_4N_{45}$ coating and the coating annealed up to (b) 1100 °C, (c) 1200 °C, (d) 1300 °C, (e) 1400 °C and (f) 1500 °C. Force vs. Displacement curves for the as-deposited $Hf_7B_{23}Si_{17}C_4N_{45}$ coating and the five annealed coatings (g).

Fig. 5.3.11 presents the variation of lnd^2 and $ln\Delta r^3$ as a function of 1/T. The results clearly suggest a growth and an Ostwald ripening process in sublayers *SL-I* and *SL-II*, respectively.

As noted earlier, the defect structure and integrity of the oxidized layer that forms can play a major role as a barrier for O diffusion. Nano-indentation experiments were conducted to assess the integrity of the oxidized layer formed during the annealing process. Fig. 5.3.12 (g) shows typical Force vs. Displacement curves for the six coatings. The hardness values, effective modulus and penetration depths are listed in Table 5.3.3. Figs. 5.3.12(a) - (f) show typical images of the indentations on the as-deposited coating, and the annealed coating up to 1100 °C, 1200 °C, 1300 °C, 1400 °C, and 1500 °C, respectively. The as-deposited $Hf_7B_{23}Si_{17}C_4N_{45}$ coating exhibited a hardness of 16.7 GPa. The hardness of the coating annealed up to 1100 °C is similar to that of the original coating due to the low thickness of the oxidized layer and probably the presence of the HfO_2 nanoparticles (~3-7 nm) embedded in the amorphous structure. It is apparent that as the

annealing temperature increased, *H* decreased due the higher contribution from the oxidized layer. Looking into the penetration depth, the oxidized layer accounts for a significant portion of it (annealing up to 1200 ˚C and 1300 ˚C) and eventually, the entire penetration is within the oxidized layer (annealing up to 1400 ˚C and 1500 ˚C). However, considering that the hardness values for SiO_2 range from 4.5-9.5 GPa, it is clear that the present results suggest that the oxidized layer formed during annealing has high density and integrity. This is further supported by the images in Figs. 5.3.12(a-f). All annealed coatings exhibited dense structures without any visible defect and/or crack formation next to the indentations.

Table 5.3.3. List of hardness (*H*), effective modulus (E^*) and contact depth measured by nano-indentation using a Berkovich tip of the as-deposited and annealed coatings.

Sample	Hardness (GPa)	Effective Modulus (GPa)	Contact Depth (nm)
As-deposited	16.7	153.5	131
1100 °C	16.7	150.2	131
1200 °C	15.8	149.9	135
1300 °C	13.0	128.1	152
1400 °C	11.5	144.6	164
1500 °C	9.6	124.1	182

In view of the present observations, the high-temperature oxidation mechanism of the present $Hf_7B_{23}Si_{17}C_4N_{45}$ coating shows some similarities with that of Si-B-C-N coating [161] but also some system specific differences. The present mechanism can be described as follows: (i) O diffuses through the *SL-II* sublayer and reaches the *SL-II*/*SL-I* interface; (ii) in the SL-I sublayer, some O reaches the interface with the original coating and reacts preferentially with Hf nucleating a dense population of HfO_2 while the remaining O is consumed across the thickness of the sublayer by growing the nucleated HfO_2 particles and oxidizing the rest of the elements in the coating forming the SiO_x-based matrix; (iii) the high population density of the HfO_2 nanoparticles along with the precipitation of high density nano quartz SiO_2 within the *SL-I* sublayer in front of the base layer can provide an additional diffusion barrier

for O; (iv) formation of nano sized HfO_2 can also reduce heat transfer to the interface in view of its low thermal conductivity (0.49 - 0.95 $Wm^{-1}K^{-1}$) [162]; (v) the heat transfer process and O diffusion from the surface to the interface can also be adversely affected by the presence of the coarse HfO_2 nanoparticles dispersed in the SiO_x amorphous matrix in the *SL-II* sublayer. Thus, the obtained Q=3.44 eV represents the activation energy for the entire oxidation process and characterizes the high temperature oxidation resistance of the $Hf_7B_{23}Si_{17}C_4N_{45}$ coating.

5.3.5 Summary

All annealed coatings were found to exhibit a two-layered structure composed of the inner as-deposited amorphous layer followed by a nanocomposite oxidized surface layer. The nanocomposite layer consists of HfO_2 nanoparticles with either a monoclinic or an orthorhombic structure in an amorphous SiO_x matrix and exhibits two sublayers. The bottom sublayer involves a dense population of small (up to several nm) HfO_2 nanoparticles close to the interface that follow a nucleation and growth process. The surface sublayer exhibits large (up to several tens nm) but dispersed HfO_2 nanoparticles that coarsen via Ostwald ripening. The oxidation mechanism involves preferential reaction of diffused oxygen with Hf in the as-deposited coating resulting in the nucleation of a high density of HfO_2 nanoparticles at the coating/oxidized layer interface. Also, the gradual growth of the HfO_2 nanoparticles and formation of an amorphous SiO_x matrix along with precipitation of quartz SiO_2 forming an effective oxygen diffusion barrier. The average activation energy for the oxidation process was found to be 3.44 eV that is significantly higher than that for diffusion in dense SiO_2 attesting to the high oxidation resistance of the present coating.

Chapter 6

SUMMARY OF ALL INVESTIGATED COATINGS

Table 6.1. Summary of coatings that have been studied.

Coating	Microstructure	Hardness (GPa)	Stability	Other Properties
$Zr_{61}B_{27}C_6N_3(0\%N_2)$	FCC B-rich Zr(B,C,N) nano-columnar (lateral size ~ 20 nm-60 nm) surrounded by amorphous structure.	13.5		High-quality defect-free; High electrical conductivity; Low compressive stresses; High thermal stability.
$Zr_{41}B_{30}C_8N_{20}(5\%N_2)$	FCC nano-needles (length ~40 nm and width ~10 nm) that composed of ZrN and/or Zr(B,C,N) nano-domains semi-coherently joined by Zr-N monolayer interfaces.	37	Oxidation resistance in air up to 550 °C.	
$Zr_{26}B_{26}C_6N_{42}(10\%N_2)$	Refined crystalline ZrN nano-needle structures (~2 nm) embedded in an amorphous structure.	17.2	Oxidation resistance increases with the increases of amorphous structure, up to 700 °C ($Zr_{19}B_{24}C_3N_{52}$-50%N_2).	
$Zr_{24}B_{19}C_6N_{49}(15\%N_2)$	Amorphous-like structure	14.8		
$Hf_{27}B_{57}C_8(0\%Si)$	Nano-columnar structure of h-HfB_2 (length ~50-60 nm, width of ~5-10 nm), no amorphous boundaries between columnar structures.	37.1	Oxidation resistance in air up to 600 °C.	Smooth, defect-free; High thermal conductivity; High electrical conductivity; Low compressive stresses.
$Hf_{23}B_{55}Si_2C_{11}(1\%Si)$	Nano-columnar structure of h-HfB_2 (length ~ 20- 30 nm, width < 5 nm), surrounded by ~1 nm thick amorphous boundaries.	34.1	Oxidation resistance in air up to 640 °C.	
$Hf_{22}B_{54}Si_9C_9(7.5\%Si)$	Refined nano-needles (wide ~2-3 nm) being composed of randomly oriented multi-nanocrystalline.	30.9	Oxidation resistance in air up to 700 °C.	
$Hf_{21}B_{28}Si_{35}C_7(30\%Si)$	Nanocomposite structure of HfB_2 nano-crystalline (~1-2 nm) embedded in an amorphous matrix.	16.0	Oxidation resistance in air up to 800 °C.	
Hf-Si-N(7.5%N_2)	FCC HfN nano-columnar structures with width of 5-10 nm, no amorphous boundaries.	38		High-quality defect-free; Smooth surface.
Hf-Si-N(10%N_2)	FCC HfN nano-columnar structures with lateral size 10-20 nm, very thin amorphous boundaries.	35.9		
Hf-Si-N(12.5%N_2)	FCC HfN nano-columnar structures with lateral size 20-50 nm with changed preferred crystal orientation to (200), more amorphous boundaries.	33.6		
Hf-Si-N(15%N_2)	FCC nano columnar with lateral size of 15~40 nm grown on multilayer structures. Nano domains with size of 2-5 nm on crystalline layers separated by amorphous boundaries.	32.5		
Hf-Si-N(17.5%N_2)	FCC nano columnar about 10 nm surrounded by more than 1 nm thick amorphous boundaries.	27.4		
$Si_{30-32}B_{10-12}C_{2-4}N_{49-51}$	Amorphous	19.5	Oxidation resistance in air up to 1500 °C, Thermal stability in inert gas up to1700 °C.	Low internal stress; Low thermal conductivity; Optically transparent.
$Hf_7B_{23}Si_{17}C_4N_{45}$	Amorphous	19	Oxidation resistance in air up to 1700 °C.	High thermal stability.

6.1 Summary of Coatings with Enhanced Hardness

Three transition metal based nanocomposite coating systems Zr-B-C-N, Hf-B-Si-C and Hf-Si-N fabricated with magnetron sputtering were studied with the goal of getting better understanding of the microstructure effects on hardness.

High quality defect-free Zr-B-C-N coatings with high hardness, low internal stress, high electrical conductivity and thermal stability were studied. A slight change in the nitrogen content in the plasma was found to cause tremendous differences in the hardness, oxidation resistance and electrical resistivity of the coatings. With the varied amount of the nitrogen in the coatings, the structure also varied from nanocolumnar ($Zr_{61}B_{27}C_6N_3$) to an entirely amorphous-like structure ($Zr_{24}B_{19}C_6N_{49}$).

A new nanostructure resulting in hardness enhancement has been discovered from the $Zr_{41}B_{30}C_8N_{20}$ coating which possesses the highest hardness (37 GPa), modulus (317 GPa) and electrical conductivity (electrical resistivity of 1.7×10^{-6} Ωm). The nanostructure exhibits the following features as: grains composed of sub nano-domains with same orientation separated by semi-coherent monolayer boundaries. The monolayer boundaries have characteristics similar to the anti-phase boundaries but with around 30% displacement in the adjacent domains (over 50% displacement in the typical anti-phase boundaries). The hardness enhancement occurred in this kind of structure may be due to many reasons. Movement of dislocations may be effectively reduced due to the stress field generated around the semi-coherent monolayer interface. Sliding of nano-domains along this kind of grain boundary may also be significantly reduced. The well aligned crystal orientation of the adjacent sub-nano-domains separated by the semi-coherent interface and the strong bonding between atoms at the interface may also have some effects on hardness.

Studies from the Zr-B-C-N coatings also indicate that increasing the nitrogen content in the coating will not only result in decrease in the grain size but also increase in volume of amorphous phase between grains. This means that decrease in grain size is always accompanied by increase of amorphous phase surrounding the grains. This fact indicates that it may be difficult to control grain size and volume of amorphous phase between grains simultaneously when selected elements are incorporated into the coatings.

The hard and multifunctional Hf-B-Si-C coatings with high thermal conductivity and electrical conductivity were studied by microstructure analysis. The incorporation of Si into the coating resulted in the microstructural refinement and eventual formation of amorphous structure. The Si-free $Hf_{27}B_{57}C_8$ coating possesses the highest hardness and highest compressive stress, consisting of hexagonal HfB_2 nano-columnar structures with preferred orientation of the (001) tilted ~30° away from the coating surface. No amorphous boundaries were formed.

The $Hf_{23}B_{55}Si_2C_{11}$ coating with slight incorporation of Si (2 at%) possesses a similar high hardness but with over 60% reduces compressive stress. This coating consists smaller nano-columnar structures (~ 20 - 30 nm long and < 5 nm wide), surrounded by ~1 nm thick amorphous boundaries. The plan-view HRTEM image of this coating clearly shows nanocrystalline domains with a typical size of about 5 nm are separated by amorphous boundaries with thickness ~1 nm. Nearly all the nano domains are well aligned with the same crystal orientation. This structure is very similar to one of the suggested structures that result in hardness enhancement. The hardness of this coating may be further increased if the thickness of the amorphous boundaries can be further reduced to 1 - 2 monolayer thick. The stress relaxation in this coating may be explained by the realignment of the crystallographic orientation of the nano-columns and the decrease in the size of columns.

The $Hf_{22}B_{54}Si_9C_9$ coating consists of refined randomly oriented nano-needles (~2 - 3 nm wide). The $Hf_{21}B_{28}Si_{35}C_7$ coating consists of a nanocomposite structure of HfB_2 nanocrystalline (1 - 2 nm) embedded in an amorphous matrix. The results indicate that increasing Si will result in increased volume fraction of the amorphous boundaries, refined microstructure and modified orientation of the HfB_2 crystal structures, which will significantly reduce compressive stress.

A series of Hf-Si-N coatings was fabricated using reactive magnetron sputtering in different gas mixture. The hardness, residual stress, addition of silicon content and several preferred crystallographic orientations were investigated in details. The Hf-Si-N coating exhibits highest hardness when there is no amorphous boundaries formed and the lateral size of the HfN nanocolumnar structure is about 5 -10 nm.

Another new nanostructure can result in the hardness enhancement has been discovered from the Hf-Si-N coating deposited with 15% nitrogen in the gas mixture. This coating is composed of nano

columns with lateral size of 15~40 nm growing on multilayer structures. The columnar structures in this coating are composed of nano-domains (~2 - 5 nm) with the same crystallographic orientation separated by thin amorphous boundaries. This structure is very similar to the structure in Fig. 2.2 (b), can be described as columnar nanostructure composed of the grains assembled in nanocolumns surrounded by tissue phase. However, the nano columnar structures observed in this coating are more special since all columnar structures are growing on multilayer. Therefore, this coating could be strengthened in two ways. The hardness of coating is determined by the resistance to dislocation formation and motion, sliding of grain boundaries and bonding distortion. In this new nanostructure, dislocations need to glide across layers and within individual layers, the nucleation and gliding of dislocations is inhibited by the small dimension across the columns and the boundary sliding between domains can be inhibited by the high cohesive strength of the tissue phases. The hardness of the Hf-Si-N coating deposited with 15% nitrogen in the gas mixture will be further improved if the size of the columns and the thickness of the amorphous boundaries can be slightly reduced. These results indicate that increase of nitrogen content in the Hf-Si-N coating resulted in the variation in grain size and alteration in the crystal orientation. The increasing amount of silicon content in this coating resulted in the reducing of compressive stress, increasing volume of amorphous boundaries and may be in favor of the formation of multilayer structures.

6.2 Summary of Coatings with Outstanding Oxidation Resistance

Amorphous Si-B-C-N coatings exhibit extraordinary oxidation resistance and many other unique combination of properties which make them ideal candidates for the applications in protective coatings, microelectronics. The Si-B-C-N coating can remain amorphous when annealed to 1700 °C in inert gas. Such high temperature oxidation resistance is attributed to the formation of an outer amorphous SiO_2 layer and an inner nano composite layer of finely distributed h-BN nano crystals embedded in an amorphous SiO_2 matrix. The molecular dynamics simulation from the other research group also confirms that incorporation of h-BN nanoparticles in silica could establish thermal barriers and heat spreading path in front of the amorphous base layer [161].

Hard and optically transparent $Hf_7Si_{17}B_{23}C_4N_{45}$ coating with superior high-temperature oxidation resistance also exhibits other desirable properties such as low residual stress, high corrosion resistance

and high electrical conductivity. The Hf-Si-B-C-N coating has a superior high-temperature oxidation resistance in air due to the formation of an oxide barrier on the surface above 1000 °C. The oxide layer has a nanocomposite structure consisting of HfO_2 nanocrystalline surrounded by a SiO_2-based amorphous matrix.

It can be concluded that the barrier layer formed during annealing of amorphous coatings can ensure a very good protection of the substrate against oxidation from external atmosphere. The annealed Hf-B-Si-C-N coatings are composed of HfO_2 grains embedded in the amorphous SiO_x matrix. However, this kind of protection only works under the following conditions: (1) the nanocrystalline grains are dispersed in amorphous matrix; (2) the grains are well separated to ensure no direct contact between the atmosphere and substrate through the grain boundaries. This suggests that protection will be limited by the complete crystallization of coatings. During the annealing, the amorphous structure gradually converts to nanocrystalline and then to crystalline structure with the increasing of annealing T. This indicates the oxidation resistance of the protective coating is limited by the thermal stability of its amorphous structure. The oxidation resistance of amorphous coating will increase when thermal stability of its amorphous structure increases. In order to increase oxidation resistance temperature, the selection of correct element composition to build the amorphous structure with high crystallization temperature is very important.

6.3 Discussion Based on All Coatings

The $Zr_{41}B_{30}C_8N_{20}$ coating exhibits the high hardness (37 GPa) and modulus (317 GPa). However, the oxidation resistance of this coating in air is only up to 550 °C. The amorphous-like $Zr_{24}B_{19}C_6N_{49}$ coating exhibits low hardness of 14.8 GPa. However, the oxidation resistance of $Zr_{24}B_{19}C_6N_{49}$ coating can be increased to 700 °C due to the increased amount of amorphous structure.

The silicon free $Hf_{27}B_{57}C_8$ coating exhibits the highest hardness among all Hf-B-Si-C coatings up to 37 GPa. However, this coating starts to be oxidized around 600 °C. With the increasing of silicon content, the hardness of Hf-B-Si-C coatings decrease and the oxidation temperature increased. The $Hf_{21}B_{28}Si_{35}C_7$ coating (30% Si in the target erosion area) exhibits the lowest hardness about 16 GPa. However, the oxidation resistance of this coating is up to 800 °C. The hardness of the $Hf_{22}B_{54}Si_9C_9$

coating (7.5% Si in the target erosion area) is about 31 GPa which is relative good hardness. The oxidation resistance of this coating has been improved to 700 °C.

Based on the above results, it can be concluded that the designing of nanostructure is very important for the hardness enhancement and the other unique properties of nanocomposite coatings. However, oxidation resistance of all the coatings with enhanced hardness is relatively low and is not sufficient for many applications. When the operation temperature of coatings overpasses a critical temperature, nanostructure of nanocomposite coatings will be destroyed and the unique properties will no longer exist. Therefore, it is very important to improve the thermal stability of hard coatings. The Si-B-C-N coatings exhibit ultrahigh thermal stability up to 1400 °C in He. It has been found that the role of nitrogen in ultrahigh thermal stability of Si-B-C-N coatings is very important. The thermal stability of coatings will be limited if there are too many Si-Si bonds present in coatings since the Si-Si bonds become unstable when close to the melting point of Si (1414 °C). Excess of nitrogen in amorphous coatings favors the local bonding of N with Si, B and C while suppressing the formation of Si-Si bonds. A sufficient high value of nitrogen in the Si-B-C-N coating is needed to achieve its high stability at elevated temperatures.

The studies from coatings with outstanding oxidation resistance show that the Si-B-C-N coating exhibits low hardness less than 20 GPa but high oxidation resistance up to 1600 °C in air. The Hf-Si-B-C-N exhibits low hardness around 17 GPa but high oxidation resistance up to 1600 °C in air. Amorphous coatings exhibit relatively low hardness, however, they are usually more thermally stable and can ensure good protection of substrate against oxidation.

The silicon content is an important factor to control the hardness and oxidation resistance. In the coatings with enhanced hardness, the silicon content determines the continuity of the amorphous phase. If silicon content is too low, there will be no amorphous boundaries or the nanocrystalline grains will not be fully surrounded by amorphous boundaries. Therefore, the oxidation resistance of the coating will be very low. Incorporation of a proper amount of silicon into the coating, the size of grains will be reduced and the grains will be fully surrounded by a thin layer of amorphous phase. The thin amorphous boundaries can reduce the sliding of grain boundaries which result in the hardness enhancement. The amorphous boundaries can also act as an efficient diffusion barrier which result in the improvement of

oxidation resistance. Further increasing of amorphous phase results in decreasing of hardness and increasing of oxidation resistance. Besides, the compressive stress induced during deposition can be released by adding silicon since silicon forms longer and more flexible bonds than boron and carbon. Increasing of silicon content also results in refining of the microstructure and realignment of the crystallographic orientation. In amorphous coatings, the silicon can react with oxygen first to form the stable SiO_x matrix which acts as an oxygen diffusion barrier to hinder further oxidation of coating. With the increasing amount of amorphous phase, the oxidation resistance of coatings increases at the expense of hardness. This indicates that a compromise between the oxidation resistance and hardness can be reached by introducing proper amount of amorphous phase.

The nanocomposite coatings composed of small amount of nanograins embedded in amorphous matrix have the potential to protect the substrate against oxidation. These nanocomposite coatings can be formed by the post-deposition nanocrystallization of amorphous material. With the correct selection of elements forming the nanocomposites, the two phases existing in the amorphous material should exhibit different crystallization temperatures. When the annealing temperature is between the two crystallization temperatures, one phase will start to crystalize and the other phase will remain amorphous. In this way, good protection of substrate against oxidation will be ensured since nanograins are not in a mutual contact which removes direct connection with the external atmosphere. The hardness may not be comparable to the enhanced hardness of nanocomposite coatings with special nanostructure, but should be higher than amorphous coatings.

Chapter 7

CONCLUSIONS

A better understanding of the effects of microstructure on the hardness and oxidation resistance of coatings was obtained from two groups of new generation ceramic coatings. Two new nanostructures that can result in the hardness enhancement have been discovered from the microstructure studies of nanocomposite coatings with enhanced hardness. These two structures are: 1) Grains composed of sub nano-domains with same orientation separated by semi-coherent monolayer boundaries. 2) The columnar structures, grow on multilayers, consist a bundle of small subdomains separated by thin boundaries. Besides these discoveries, the realignment of crystallographic orientation of the nano columnar structures and the formation of proper thin amorphous boundaries between the columnar structures will also result in enhancement of hardness and reduction of compressive stress. The coatings exhibit high hardness in this research all contain grains with size around 10 nm, indicating that controlling grain size during the formation of coatings is very important to achieve high hardness. The decrease in grain size is always accompanied by the increase of amorphous phase in the coatings. Increasing amorphous phase will result in softening of coatings. However, the formation of amorphous structure will result in improvement of oxidation resistance due to the absence of continuous connection between the coating surface and the substrate through grain boundaries.

During the annealing of Si-B-C-N coating in air, oxygen atoms diffuse into the coating and react with silicon atoms to form the SiO_x and the hexagonal BN nanocrystals precipitate at the same time. The high oxidation resistance of the Si-B-C-N coating should be attributed to the presence of the BN in front of the base layer interface which act as a barrier to the O diffusion. Similarly, during the annealing of the Hf-B-Si-C-N coatings, an effective oxygen diffusion barrier was formed by the precipitation of HfO_2 nanoparticles with a dense amount of SiO_x matrix and SiO_2 forming in front of the base layer interface. Therefore, the barrier layer, which consists of nanograins dispersed in amorphous matrix formed at the surface of amorphous coating, is very important for protecting the substrate against oxidation.

The hardness enhancement of coatings is based on nanostructure while the oxidation resistance enhancement is based on the suppression of crystallization. Based on the knowledge gained from microstructure studies, it is very difficult to produce coatings that exhibit enhanced hardness and extraordinary oxidation resistance simultaneously. However, a compromise between the oxidation resistance and hardness can be reached if nanocomposite coatings are composed of small amount of nanograins embedded in amorphous matrix. With small amount of well separated nanograins dispersed in the amorphous matrix, the hardness of this kind of nanocomposite coatings is expected to be higher than amorphous coatings. At the same time, good protection of substrate against oxidation can be ensured since there is no direct contact between the substrate and the external atmosphere.

REFERENCES

[1] J. Musil (2012) Hard nanocomposite coatings: Thermal stability, oxidation resistance and toughness, Surf. Coat. Technol. 207: 50-65.

[2] S. Veprek, S. Reiprich (1995) A concept for the design of novel superhard coatings, Thin Solid Films 268: 64-71.

[3] S. Veprek, M. Haussmann, S. Reiprich, L. Shizhi, J. Dian (1996) Novel thermodynamically stable and oxidation resistant superhard coating materials, Surf. Coat. Technol. 86-87: 394-401.

[4] A.D. Pogrebnjak, V.M. Beresnev (2012) Hard Nanocomposite Coatings, Their Structure and Properties, http:// dx.doi.org/10.5772/50567.

[5] A.D. Pogrebnjak, A.P. Shpak, N.A. Azarenkov, V.M. Beresnev (2009) Structures and properties of hard and superhard nanocomposite coatings, Russ. Acad. Sci. 52(1): 29-54.

[6] C. Subramanian, K.N. Strafford (1993) Review of multicomponent and multilayer coatings for tribological applications, Wear 165: 85-95.

[7] D. Mcintyre, J.E. Greene, G. Hakansson, J.E. Sundgren, W.D. Munz (1990) Oxidation of metastable single phase polycrystalline $Ti_{0.5}Al_{0.5}N$ films: Kinetics and mechanisms, J. Appl. Phys. 67: 1542-1553.

[8] F. Vaz, L. Rebouta, M. Andritschky, M.F. Silva, J.C. Soares (1997) Thermal oxidation of $Ti_{1-x}Al_xN$ coatings in air, J. Eur. Ceram. Soc. 17: 1971-1977.

[9] P.H. Mayrhofer, A. Hörling, L. Karlsson, J. Sjölen, T. Larsson, C. Mitterer, L. Hultman (2003) Self-organized nanostructures in the Ti-Al-N system, Appl. Phys. Lett. 83: 2049-2051.

[10] S. PalDev, S.C. Deevi (2003) Single layer and multilayer wear resistant coatings of (Ti,Al) N: a review, Mater. Sci. Eng. A 342: 58-79.

[11] A. Horling, L. Hultman, M. Oden, J. Sjolen, L. Karlsson (2005) Mechanical properties and machining performance of $Ti_{1-x}Al_xN$-coated cutting tools, Surf. Coat. Technol. 191: 384-392.

[12] S.J. Bull, A.M. Jones (1996) Multilayer coatings for improved performance, Surf. Coat. Technol. 78: 173-184.

[13] U. Helmersson, S. Todorova, S.A. Barnett, J.E. Sundgren, L.C. Markert, J.E. Greene (1987) Growth of single-crystal TiN/VN strained-layer superlattices with extremely high mechanical hardness, J. Appl. Phys. 62: 481-484.

[14] M. Shinn, L. Hultman (1992) Growth, structure and microhardness of epitaxial TiN/NbN superlattices, J. Mater. Res. 7(4): 901-911.

[15] A. Gregor, V. Podgursky, E. Adoberg and P. Kulu (2006) Hard coatings manufacturing technology used in tooling, 5th International DAAAM Baltic Conference, Tallinn, Estonia.

[16] https://www.pvd-coatings.co.uk/theory/pvd-coatings-2/.

[17] J. Musil (2000) Hard and super-hard nanocomposite coatings, Surf. Coat. Technol. 125: 322-330.

[18] J. Musil, P. Baroch, P. Zeman (2008) Hard nanocomposite coatings: Present Status and Trends, Plasma Surface Engineering Research and its Practical Applications: 1-33.

[19] H. Holleck (1986) Material selection for hard coatings, J. Vac. Sci. Technol. A 4(6): 2661-2669.

[20] M. Shinn, S.A. Barnett (1994) Effect of superlattice layer elastic moduli on hardness. Appl. Phys. Lett. 64(1): 61-63.

[21] H. Söderberg, M. Oden, J.M. Molina, L. Hultman (2005) Nanostructure formation during deposition of TiN/ SiN_x nanomultilayer films by reactive dual magnetron sputtering. J. Appl. Phys. 97, 114327: 1-8.

[22] L. Lin, J.J. Moore, W.C. Moerbe, M. Pinkas, B. Mishra, G.L. Doll, W.D. Sproul (2010) Structure and properties of selected (Cr-Al-N, TiC-C, Cr-B-N) nanostructured tribological coatings. Int. Journal of Refractory Metals & Hard Materials 28: 2-14.

[23] P.H. Mayrhofer, C. Mitterer, J.G. Wen, J.E. Greene, I. Petrov (2005) Self-organized nanocolumnar structure in superhard TiB_2 thin film. Appl. Phys. Lett. 86, 131909: 1-3.

[24] S. Veprek, S. Reiprich, L. Shizhi (1995) Superhard nanocrystalline composite materials: The TiN/Si_3N_4 system. Appl. Phys. Lett. 66(20): 2640-2642.

[25] S. Veprek (1999) The search for novel, superhard materials. J. Vac. Sci. Technol., A 17(5): 2401-2420.

[26] A.M. Torres-Huerta, M.A. Dominguez-Crespo, A. Alanis-Valdelamar, E. Onofre-Bustamante, M.L. Escudero-Rincón, M.C. María-Lorenza, J.A. Lois-Correa (2015) Role of Preparation Method on the Microstructure and Mechanical Properties of PPy/Ni Organic–Inorganic Hybrid Bilayer Coatings on Carbon Steel. Metall. Mater. Trans. A (46): 1741-1755.

[27] G. Erkens (2007) New approaches to plasma enhanced sputtering of advanced hard coatings, Surf. Coat. Technol. 201: 4806-4812.

[28] M. Tului, G. Marino, T. Valente (2006) Plasma spray deposition of ultra-high temperature ceramics, Surf. Coat. Technol. 201: 2103-2108.

[29] D.R. Clarke, M. Oechsner, N.P. Padture (2012) Thermal-barrier coatings for more efficient gas-turbine engines, MRS Bulletin, 37: 891-898.

[30] D.R. Clarke and S.R. Phillpot (2005) Thermal barrier coating materials, Mater. Today 8(6): 22-29.

[31] J. Musil, J. Vlček, P. Zeman (2008) Hard amorphous nanocomposite coatings with oxidation resistance above 1000 °C, Adv. Appl. Ceram. 107(3): 148-154.

[32] J. Musil, P. Zeman (2007) Hard a-Si_3N_4/ MeN_x nanocomposite coatings with high thermal stability and high oxidation resistance, Solid State Phenom 127: 31-36.

[33] M.M. Opeka, I.G. Talmy, E.J. Wuchina, J.A. Zaykoski, S.J. Causey (1999) Mechanical, thermal, and oxidation properties of refractory hafnium and zirconium compounds. J. Eur. Ceram. Soc. 19: 2405-2414.

[34] R. Hauert, J. Patscheider (2000) From alloying to nanocomposites- Improved performance of hard coatings, Adv. Eng. Mater. 2(5): 247-259.

[35] D. Zhong, E. Sutter, J.J. Moore, G.G. Mustoe, E.A. Levashov, J. Disam (2001) Mechanical properties of Ti-B-C-N coatings deposited by magnetron sputtering. Thin Solid Films 398: 320-325.

[36] S. Shimada, M. Takahashi, J. Tsujino, I. Yamazaki, K. Tsuda (2007) Deposition and wear resistance of Ti-B-N-C coatings on WC- Co cutting tools from alkoxide solutions by thermal plasma CVD. Surf. Coat. Technol. 201: 7194-7200.

[37] J. Lin, B. Mishra, J.J. Moore, M. Pinkas, W.D. Sproul (2008) Structure and properties of Ti-B-C-N nanocomposite coatings synthesized using pulsed closed field unbalanced magnetron sputtering. Surf. Coat. Technol. 203: 588-593.

[38] J. Lin, J.J. Moore, B. Mishra, M. Pinkas and W.D. Sproul (2010) The structure and mechanical and tribological properties of TiBCN nanocomposite coatings. Acta Mater. 58: 1554-1564.

[39] Q.H. Luo, Y.H. Lu (2011) Microstructure and mechanical properties of reactive magnetron sputtered Ti-B-C-N nanocomposite coatings. Appl. Surf. Sci. 258: 1021-1026.

[40] L.E. Toth (1971) Transition metal carbides and nitrides, Academic Press, New York, p188.

[41] P.C. Johnson, H. Randhawa (1987) Zirconium nitride films prepared by cathodic arc plasma deposition process, Surf. Coat. Technol. 33: 53-62.

[42] L.V. Leaven, M.N. Alias, R. Brown (1992) Corrosion behavior of ion plated and implanted films, Surf. Coat. Technol. 53(1): 25-34.

[43] P. Panjan, B. Navinsek, A. Zabkar, V. Marinkovic, D. Mandrino, J. Fiser (1993) Structural analysis of Zr-N and Ti-N films prepared by reactive plasma beam deposition, Thin Solid Films 228: 233-237.

[44] U.K. Wiiala, I.M. Penttinen, A.S. Korhonen (1990) Improved corrosion resistance of physical vapor deposition coated TiN and ZrN. Surf. Coat. Technol. 41: 191-204.

[45] S. Horita, M. Kobayashi, H. Akahori and T. Hata (1994) Material properties of ZrN film on silicon prepared by low-energy ion-assisted deposition. Surf. Coat. Technol. 66: 318-322.

[46] K.T. Rie, A. Gebauer, J. Whole (1995) Studies on the synthesis of hard coatings by plasma-assisted CVD using metallo-organic compounds. Surf. Coat. Technol. 74-75: 362-368.

[47] K.T. Rie, C. Pfohl, S.H. Lee, C.S. Kang (1997) Development of zirconium and boron containing coatings for the application on aluminium diecasting tools by means of MO-PACVD. Surf. Coat. Technol. 97: 232-237.

[48] J.S. You, C.S. Kang, S.H. Lee, C. Pfohl and K.T. Rie (1999) Thermal characteristics of a Zr (B,C,N) coated layer manufactured by the PACVD process. Surf. Coat. Technol. 112: 230-235.

[49] J. Vlcek, P. Steidl, J. Kohout, R. Cerstvy, P. Zeman, S. Proksova and V. Perina (2013) Hard nanocrystalline Zr-B-C-N films with high electrical conductivity prepared by pulsed magnetron sputtering. Surf. Coat. Technol. 215: 186-191.

[50] E. Zapata-Solvas, D.D. Jayaseelan, H.T. Lin, P. Brown, W.E. Lee (2013) Mechanical properties of ZrB_2- and HfB_2- based ultra-high temperature ceramics fabricated by spark plasma sintering, J. Eur. Ceram. Soc. 33: 1373-1386.

[51] S.N. Dub, A.A. Goncharov, S.S. Ponomarev, V.B. Filippov, G.N. Tolmacheva, A.V. Agulov (2011) Mechanical properties of $HfB_{2.7}$ nanocrystalline thin films. J. Superhard Mater. 33: 151-158.

[52] A.A. Goncharov, S.N. Dub, A.V. Agulov (2013) Structure, composition, and physicomechanical characteristics of HfB_2 and Hf-B-N films. Phys. Metals Metallog. 114: 95-101.

[53] M.M. Opeka, I.G. Talmy, J.A. Zaykoski (2004) Mechanical properties of ZrB_2 composites. J. Mater. Sci. 32: 5887-5894.

[54] J.W. Lawson, M.S. Daw, C.W. Bauslicher (2011) Lattice thermal conductivity of ultra-high temperature ceramics ZrB_2 and HfB_2 from atomistic simulations. J. Appl. Phys. 083507: 1-4.

[55] F. Monteverde, A. Bellosi and L. Scatteia (2008) Processing and properties of ultra-high temperature ceramics for space applications, Mater. Sci. Eng. A 485: 415-421.

[56] S.R. Levine, E.J. Opila, M.C. Halbig, J.D. Kiser, M. Singh, J.A. Salem (2002) Evaluation of ultra-high temperature ceramics for aero propulsion use, J. Eur. Ceram. Soc. 22: 2757-2767.

[57] M.M Opeka, I.G. Talmy and J.A. Zaykoski (2004) Oxidation-based materials selection for 2000 °C + hypersonic aero surfaces: Theoretical consideration and historical experience, J. Mater. Sci. 32: 5887-5904.

[58] E. Wychina, M. Opeka, S. Causey, K. Buesking, J. Spain, A. Cull, J. Routbout, F. Guitierrez-Mora (2004) Designing for ultra-high temperature applications: the mechanical and thermal properties of HfB_2, HfC_x, HfN_x and αHf, J. Mater. Sci. 39: 5939-5949.

[59] A.L. Chamberlain, W.G. Fahrenholtz and G.E. Hilmas (2004) High-strength zirconium diboride-based ceramics, J. Amer. Ceram. Soc. 87: 1170-1172.

[60] M. Mallik, K.K. Ray, R. Mitra (2011) Oxidation behavior of hot pressed ZrB_2-SiC and HfB_2-SiC composites, J. Eur. Ceram. Soc. 31: 199-215.

[61] J. Han, P. Hu, X. Zhang, S. Meng, W. Han (2008) Oxidation-resistant ZrB_2-SiC composites at 2200 °C, Compos. Sci. Technol. 68: 799-806.

[62] F. Monteverde, A. Bellosi (2004) Microstructure and properties of an HfB_2-SiC composite for ultra-high temperature applications, Adv. Eng. Mater. 6: 331-336.

[63] E.L. Corral and R.E. Loehman (2008) Ultra-high temperature ceramic coatings for oxidation protection of carbon-carbon composites, J. Amer. Ceram. Soc. 91: 1495-1502.

[64] C.M. Carney, T.A. Parthasarathy, M.K. Cinibulk (2011) Oxidation resistance of hafnium diboride ceramics with additions of silicon carbide and tungsten boride or tungsten carbide, J. Amer. Ceram. Soc. 94: 2600-2607.

[65] C.M. Carney (2009) Oxidation resistance of hafnium diboride-silicon carbide from 1400 to 2000 °C, J. Mater. Sci. 44: 5673-5681.

[66] J. Kohout, J. Vlček, J. Houška, P. Mareš, R. Čerstvý, P. Zeman, M.H. Zhang, J.C. Jiang, E.I. Meletis, Š. Zuzjaková (2014) Hard multifunctional Hf-B-Si-C films prepared by pulsed magnetron sputtering. Surf. Coat. Technol. 257: 301-307.

[67] J. Marschall, Y.K. Chen (2004) Modeling surface oxidation in transient aerothermal heating environments, 42nd AIAA Aerospace sciences meeting and exhibit, Reno, Nevada, 1124-1137.

[68] X. Zhang, P. Hu, J. Han, S. Meng (2008) Ablation behavior of ZrB_2-SiC ultra-high temperature ceramics under simulated atmospheric re-entry condition, Composl. Sci. Technol. 68: 1718-1726.

[69] T.A. Parthasarathy, R.A. Rapp, M. Opeka, R.J. Kerans (2007) A model for the oxidation of ZrB_2, HfB_2 and TiB_2, Acta Mater. 55: 5969-5977.

[70] E. Opila, S. Levine, J. Lorincz (2004) Oxidation of ZrB_2- and HfB_2- bases ultra-high temperature ceramics, J. Mater. Sci. 39: 5969-5977.

[71] S.C. Zhang, G.E. Hilmas, W.G. Fahrenholtz (2008) Improved oxidation resistance of zirconium diboride by tungsten carbide additions, J. Amer. Ceram. Soc. 91: 3530-3535.

[72] P. Hu, X. Zhang, J. Han, X. Luo, S. Du (2010) Effect of various additives on the oxidation behavior of ZrB2-based ultra-high temperature ceramics at 1800 °C, J. Amer. Ceram. Soc. 93: 345-349.

[73] P. Zeman, S. Zuzjakova, P. Mares, R. Cerstvy, M.H. Zhang, J.C. Jiang, E.I. Meletis, J. Vlcek (2016) Superior high-temperature oxidation resistance of magnetron sputtered Hf-B-Si-C-N film, Ceram. Int. 42: 4853-4859.

[74] International Centre for Diffraction Data, PDF-2 Database Sets 1–47, Pennsylvania, U.S.A., 1997.

[75] W.G. Fahrenholtz, G.E. Hilmas (2010) Ultra-high temperature ceramics- An introduction to ultra-high temperature ceramics, AZO Materials.

[76] J. Cotton (2010) Ultra high ceramics, Adv. Mater. Processes June: 26-28.

[77] E. Wuchina, E. Opila, M. Opeka, W. Fahrenholtz and I. Talmy (2007) UHTCs: Ultra-high temperature ceramic materials for extreme environment applications, Electrochem. Soc. Interface Winter: 30-36.

[78] C. Mitterer (1997) Borides in thin coating technology, J. Solid State Chem. 133: 279-291.

[79] R. Wiedemann and H. Oettel (1998) Tempering behavior of TiB_2 coatings, Surface Engineering 14: 299-304.

[80] M. Berger, L. Karlsson, M. Larsson, S. Hogmark (2001) Low stress TiB_2 coating with improved tribological properties, Thin Solid Films 401: 179-186.

[81] W.G. Fahrenholtz, G.E. Hilmas (2007) Refractory diborides of zirconium and hafnium, J. Am. Ceram. Soc. 90: 1347-1364.

[82] S.C. Zhang, G.E. Hilmas, W.G. Fahrenholtz (2008) Pressurelesss sintering of ZrB_2-SiC ceramics, J. Am. Ceram. Soc. 91[1]: 26-32.

[83] S.A. Ghaffari, M.A. Faghihi, F.G. Fard, H. Mandal (2013) Spark plasma sintering of TaC-HfC UHTC via disilicides sintering aids, J. Eur. Ceram. Soc. 33(8): 1479-1484.

[84] A.L. Chamberlain, W.G. Fahrenholtz and G.E. Hilmas (2006) Pressureless sintering of zirconium diboride, J. Am. Ceram. Soc. 89(2): 450-456.

[85] X.H. Zhang, G.E. Hilmas, W.G. Fahrenholtz, D.M. Deason (2007) Hot pressing of tantalum carbide with and without sintering additives, J. Am. Ceram. Soc. 90(2): 393-401.

[86] A. Balbo, D. Sciti (2008) Spark plasma sintering and hot pressing of ZrB2-MoSi2 ultra-high temperature ceramics, Mater. Sci. Eng. A 475(1-2): 108-112.

[87] U. Anselmi-Tamburini, Y. Kodera, M. Gasch, C. Unuvar, Z.A. Munir, M. Ohyanagi, S.M. Johnson (2006) Synthesis and characterization of dense ultra-high temperature thermal protection materials produced by field activation through spark plasma sintering (SPS): I. Hafnium Diboride, J.Mater. Sci. 41(10): 3097-3104.

[88] J.R. Creighton, P. Ho (2001) Introduction to chemical vapor deposition (CVD), 2001 ASM International, Product code: #06682G.

[89] S. Zhang, D. Sun and X.L. Bui, Magnetron sputtered hard and yet tough nanocomposite coatings with case studies: nanocrystalline TiN embedded in Amorphous SiN_X, Nanocomposite thin films and coatings: Processing, properties and performance, Chapter 1: 1- 104.

[90] S. Veprek, A. Niederhofer, K. Moto, T. Bolom, H.D. Mannling, P. Nesladek, G. Dollinger and A. Bergmaier (2000) Composition, nanostructure and origin of the ultra hardness in nc-TiN/ a-Si_3N_4/a- and nc-$TiSi_2$ nanocomposites with H_v=80 to ≥105 GPa, Surf. Coat. Technol. 133-134: 152-159.

[91] S. Veprek, G.J. Maritza, V. Heijman (2006) The formation and role of interfaces in superhard nc-MeN/ a-Si_3N_4 nanocomposites, Surf. Coat. Technol. 201: 6064-6070.

[92] S. Veprek, G.J. Maritza, V. Heijman (2008) Industrial applications of superhard nanocomposite coatings, Surface and Coatings Technology 202: 5063-5073.

[93] C.W. Zou, H.J. Wang, M. Li, Y.F. Yu, C.S. Liu, L.P. Guo, D.J, Fu (2010) Characterization and properties of TiN-containing amorphous Ti-Si-N nanocomposite coatings prepared by arc assisted middle frequency magnetron sputtering, Vacuum 84: 817-822.

[94] K. Lukaszkowicz, J. Sondor, A. Kriz, M. Pancielejko (2010) Structure, mechanical properties and corrosion resistance of nanocomposite coatings deposited by PVD technology onto the $X_6CrNiMoTi_{17-12-2}$ and $X_{40}CrMoV_{5-1}$ steel substrates, J. Mater. Sci. 45: 1629-1637.

[95] R.F. Bunshah, Handbook of deposition technologies for films and coatings: science, technology, and applications. 2nd. Materials science and process technology series.

[96] P.J. Kelly, R.D. Arnell (2000) Magnetron sputtering: a review of recent developments and applications, Vacuum 56: 159-172.

[97] M. Ohring (1991) Chapter 4: Discharges, Plasmas, and Ion-Surface Interactions, Materials Science of Thin Films (Deposition & Structure): 145-148.

[98] S. Swann (1988) Magnetron sputtering, Physics in Technology 19: 67-75.

[99] J.A. Thornton (1974) Influence of apparatus geometry and deposition conditions on the structure and topography of thick sputtered coatings, J. Vac. Sci. Technol. 11(4): 666-670.

[100] J.A. Thornton (1975) Influence of substrate temperature and deposition rate on structure of thick sputtered Cu coatings, J. Vac. Sci. Technol. 12: 830.

[101] J.A. Thornton (1977) High rate thick film growth, Ann. Rev. Mater. Sci. 7: 239-260.

[102] J.A. Thornton (1986) The microstructure of sputter-deposited coatings, J. Vac. Sci. Technol. A4 (6): 3059-3065.

[103] R.F. Zhang, S. Veprek (2006) On the spinodal nature of the phase segregation and formation of stable nanostructure in the Ti-Si-N system. Mater. Sci. Eng. A 424: 128-137.

[104] J. Vlcek, K. Rusnak, V. Hajek (1999) Reactive magnetron sputtering of CN_x films: Ion bombardment effects and process characterization using optical emission spectroscopy, J. Appl. Phys. 86(7): 3646-3654.

[105] J. Vlček, P. Calta, P. Steidl, P. Zeman, R. Čerstvý, J. Houška, J. Kohout (2013) Pulsed reactive magnetron sputtering of high-temperature Si-B-C-N films with high optical transparency. Surf. Coat. Technol. 226: 34-39.

[106] J. Vlček, Š. Potocký, J. Čížek, J. Houška, M. Kormunda, P. Zeman (2005) Reactive magnetron sputtering of hard Si-B-C-N films with a high-temperature oxidation resistance. J. Vac. Sci. Technol. A 23(6): 1513-1522.

[107] M. Braic, M. Balaceanu, A. Vladescu, C.N. Zoita, V. Braic (2011) Study of (Zr.Ti) CN, (Zr.Hf) CN and (Zr,Nb)CN films prepared by reactive magnetron sputtering, Thin Solid Films 519: 4092-4096.

[108] M.P. Gispert, A.P. Serro, R. Colaco, E. Pires, B. Saramago (2007) Wear of ceramic coated metal-on-metal bearings used for hip replacement, Wear 263: 1060-1065.

[109] M. Balaceanu, T. Petreus, V. Braic, C.N. Zoita, A. Vlasdescu, C.E. Cotrutz and M. Braic (2010) Characterization of Zr-based hard coatings for medical implant applications, Surf. Coat. Technol. 204: 2046-2050.

[110] P.C. Johnson, H. Randhawa (1987) Zirconium nitride films prepared by cathodic arc plasma deposition process, Surf. Coat. Technol. 33: 53-62.

[111] P. Panjan, B. Navinsek, A. Zabkar, D. Mandrino, J. Fiser (1993) Structure analysis of ZrN and TiN coatings prepared by reactive plasma beam deposition, Thin Solid Films 228: 233-237.

[112] E. Kelesoglu, C. Mitterer, M.K. Kazmanli, M. Urgen (1999) Microstructure and properties of nitride and diboride hard coatings deposited under intense mild- energy ion bombardment, Surf. Coat. Technol. 116-119: 133-140.

[113] V. Braic, M. Braic, M. Balacenu, A. Vladescu, C.N. Zoita, I. Titorencu, V. Jinga (2011) (Zr,Ti) CN coatings as potential candidates for biomedical applications, Surf. Coat. Technol. 206: 604-609.

[114] S. Jayaraman, J.E. Gerbi, Y. Yang, D.Y. Kim, A. Chatterjee, P. Bellon, G.S. Girolami, J.P. Chevalier, J.R. Abelson (2006) HfB_2 and Hf-B-N hard coatings by chemical vapor deposition, Surf. Coat. Technol. 200: 6629-6633.

[115] H.T. Johnson-Steigelman, A.V. Brinck, S.S. Parihar, P.F. Lyman (2004) Hafnium silicide formation on Si(001), Phys. Rev. B69 235322:1-25.

[116] I. Mizushima, M. Watanabe, A. Murakoshi, M. Hotta, M. Kashiwagi, M. Yoshiki (1993) Hole generation by icosahedral B_{12} in high-dose boron as-implanted silicon, Appl. Phys. Lett. 63: 373-375.

[117] C. Vincent, H. Vincent, H. Mourichoux, J. Bouix (1992) Characterization by XPS and SEM of reactive chemical vapor deposited boron carbide on carbon fiber, J. Mater. Sci. 27: 1892-1900.

[118] B.O. Johansson, J.E. Sundgren, U. Helmersson, M.K. Hibbs (1984) Structure of reactively magnetron sputtered Hf-N films, App. Phys. Lett. 44(7): 670-672.

[119] S. Shinkai and K. Sasaki (1999) Influence of sputtering parameters on the formation process of high-quality and low resistivity HfN thin film, Jpn. J. Appl. Phys. 38: 2097-2102.

[120] E. Bruninx, A.F.P.M. Eenbergen, P.V. Werf, J. Haisma (1986) X-ray photoelectron spectroscopy of hafnium nitride, J. Mater. Sci. 21: 541-546.

[121] S. Veprek, S. Reiprich, L. Shizhi (1995) Superhard nanocrystalline composite materials: The TiN/Si_3N_4 system, Appl. Phys. Lett. 66(20): 2640-2642.

[122] J.D. Bressan, R. Hesse, E.M. Silva (2001) Abrasive wear behavior of high speed steel and hard metal coated with TiAlN and TiCN, Wear, 250: 561-568.

[123] S.H. Kim, J.W. Jang, S.S. Kang, K.H. Kim (2002) Synthesis and mechanical evaluation of nanocomposite coating layer of nc-TiN/a-Si_3N_4 on SKD 11 steel by sputtering, J. Mater. Proc. Technol. 130-131: 283-288.

[124] A. Arranz, C. Palacio (2000) Tantalum nitride formation by low-energy (0.5-5keV) nitrogen implantation, Surf. Interface Anal. 29: 653-658.

[125] A. Arranz (2004) Synthesis of hafnium nitride films by 0.5-5keV nitrogen implantation of metallic Hf: an X-ray photoelectron spectroscopy and factor analysis study, Surf. Sci. 563: 1-12.

[126] I. Bertoti (2002) Characterization of nitride coatings by XPS, Surf. Coat. Technol. 151-152: 194-203.

[127] B.O. Johansson, U. Helmersson, M.K. Hibbs, J.E. Sundgren (1985) Reactively magnetron sputtered Hf-N films. I. composition and structure, J. Appl. Phys. 58(8): 3104-3111.

[128] C.A. Davis (1993) A simple model for the formation of compressive stress in thin films by ion bombardment, Thin Solid Films, 226(1): 30-34.

[129] U.C. Oh and J.H. Je (1993) Effects of strain energy on the preferred orientation of TiN thin films, J. Appl. Phys. 74(3): 1692-1696.

[130] C.V. Thompson (2000) Structure evolution during processing of polycrystalline films, Annu. Rev. Mater. Sci, 30: 159-190.

[131] S. Consiglio, W. Zeng, N. Berliner and E.T. Eisenbraun (2008) Plasma-assisted atomic layer deposition of conductive hafnium nitride using tetrakis (ethylmethylamio) hafnium for CMOS gate electrode applications, J. Electrochem. Soc. 155(3): 196-201.

[132] J. Pelleg, L.Z. Zevin, S. Lungo (1991) Reactive-sputter- deposited TiN films on glass substrates, Thin Solid Films, 197: 117-128.

[133] Y.H. Cheng, T. Browne, B. Heckerman, P. Gannon, J.C. Jiang, E.I. Meletis, C. Bowman, V. Gorokhovsky (2009) Influence of Si content on the structure and internal stress of the nanocomposite TiSiN coatings deposited by large area filtered arc deposition, J. Phys. D: Appl. Phys. 42, ID 125415.

[134] Y.H. Cheng, T. Browne, B. Heckerman, E.I. Meletis (2011) Influence of the C content on the mechanical and tribological properties of the TiCN coatings deposited by LAFAD technique, Surf. Coat. Technol. 205 (16): 4024-4029.

[135] X. Yang, L. Ying, H.F. Cai and F. Cao (2015) The degradation behavior of SiC coated PIP-C/ SiC composites in thermal cycling environment, Composites Part B 79: 204-208.

[136] J. Clzek, J. Vlcek, S. Potocky, J. Houska, Z. Soukup, J. Kalas, P. Jedrzejowski, J.E. Klemberg-Sapieha, L. Martinu (2008) Mechanical and optical properties of quaternary Si-B-C-N films prepared by reactive magnetron sputtering, Thin Solid Films 516: 7286-7293.

[137] L.C. Chen, K.H. Chen, S.L. Wei, P.D. Kichambare, J.J. Wu, T.R. Lu, C.T. Kuo (1999) Crystalline SiCN: a hard material rivals to cubic BN, Thin Solid Films 355-356: 112-116.

[138] B.P. Swain, N.M. Hwang (2008) Study of structural and electronic environments of hydrogenated amorphous silicon carbonitride (a-SiCN:H) films deposited by hot wire chemical vapor deposition, Appl. Surf. Sci. 254: 5319-5322.

[139] R. Riedel, G. Passing, H. Schonfelder, R.J. Brookz (1992)Synthesis of dense silicon-based ceramics at low temperature, Nature 355: 714-716.

[140] P. Baldus, M. Jansen, D. Sporn (1999) Ceramic fibers for matrix composites in high temperature engine applications, Science (285): 699-703.

[141] A. Muller, P. Gerstel, M. Weinman, J. Bill, F. Aldinger (2001) Correlation of boron content and high temperature stability in Si-B-C-N ceramics II, J. Eur. Ceram. Soc. 21: 2171-2177.

[142] P.A. Ramakrishnan, Y.T. Wang, D. Balzar, L.A. Haluschka, R. Riedel, A.M. Hermann (2001) Silicoboron–carbonitride ceramics: A class of high temperature dopable electronic materials. Appl. Phys. Lett. 78: 3076-3078.

[143] A.M. Hermann, Y.T. Wang, P.A. Ramakrishnan, D. Balzar, L.A.C. Haluschka and R. Riedel (2001) Structure and electronic properties of Si-(B)- C-N ceramics, J. Am. Ceram. Soc. 84: 2260-2264.

[144] J. Houska, J. Vlcek, S. Hreben, M.M.M. Bilek, D.R. Mckenzie (2006) Effect of B and the Si/C ratio on high-temperature stability of Si-B-C-N materials, Europhys. Lett. 76(3): 512-518.

[145] P. Gerstel, A. Müller, J. Bill and F. Aldinger (2003) Synthesis and High-Temperature Behavior of Si/B/C/N Precursor-Derived Ceramics without “Free Carbon”, Chem. Mater. (15): 4980-4986.

[146] P.A. Ramakrishnan, Y.T. Wang, D. Balzar, L.A. Haluschka, R. Riedel, A.M. Hermann (2001) Silicoboron–carbonitride ceramics: A class of high-temperature, dopable electronic materials, Appl. Phys. Lett. (78): 3076-3078.

[147] M.A. Rooke, P.M.A. Sherwood (1997) Surface studies of potentially oxidation protective Si-B-N-C films for carbon fibers, Chem. Mater. 9(1): 285-296.

[148] D. Hegemann, R. Riedel, C. Oehr (1999) PACVD- derived thin films in the system Si-B-C-N, Chem. Vap. Deposition 5, No.2: 61-65.

[149] M. Weinmann, J. Schuhmacher, H. Kummer, S. Prinz, J. Peng, H.J. Seifert, M. Christ, K. Müller, J. Bill, F. Aldinger (2000) Synthesis and thermal behavior of novel Si-B-C-N ceramic precursors, Chem. Mater. 12(3): 623-632.

[150] H.P. Baldus, M. Jansen (1997) Novel high-performance ceramics—amorphous inorganic networks from molecular precursors, Angewandte Chemie International Edition, 36: 328-343.

[151] Powder Diffraction File™, PDF-2, Release 2009, ICDD, International Centre for Diffraction Data, Newton Square, PA, USA.

[152] G.B. Senft, V.S. Stubican (1983) Phase relations and ordering in the system HfO_2CaO, Mater. Res. Bull. 18: 1163-1170.

[153] J. Wang, H.P. Stevens (1992) Review Hafnia and hafnia-toughened ceramics, J. Mater. Sci. 27: 5397-5430.

[154] C.E. Curtis, L.M. Doney, J.R. Johnson (1954) Some properties of hafnium oxide, hafnium silicate, calcium hafnate, and hafnium carbide, J. Amer. Ceram. Soc. 37: 458-465.

[155] D. Shin, R. Arroyave, Z.K. Liu (2006) Thermodynamic modeling of the Hf-Si-O system, Calphad 30: 375-386.

[156] B.E. Deal, A.S. Grove (1965) General relationship for the thermal oxidation of Silicon, J. Appl. Phys. 36: 3770-3778.

[157] T. Hoshino, M. Hata, S. Neya, Y. Nishioka, T. Watanabe, K. Tatsumura, I. Ohdomari (2003) Diffusion of molecular and atomic oxygen in silicon oxide, Jpn. J. Appl. Phys. 42: 3560-3565.

[158] J.C. Mikkelsen (1982) Diffusivity of oxygen in silicon during steam oxidation, Appl. Phys. Lett. 40: 336-337.

[159] S.C. Elphick, C.M. Graham (1998) The effect of hydrogen on oxygen diffusion in quartz: evidence for fast proton transients, Nature 335: 243-245.

[160] J.J Perez-Bueno, R. Ramirez-Bon, Y.V. Vorobiev, F. Espinosa-Beltran and J. Gonzalez-Hernandez (2000) Oxygen diffusion in silicon oxide films produced by different Methods, Thin Solid Films 379: 57-63.

[161] Y. Ni, J.C. Jiang, E.I. Meletis, T. Dumitrică (2015) Thermal transport across few-layer boron nitride encased by silica, Appl. Phys. Lett. 107:031603.

[162] M.A. Panzer, M. Shandalov, J.A. Rowlette, Y. Oshima, Y.W. Chen, P.C. McIntyre, K.E. Goodson (2009) Thermal properties of ultrathin hafnium oxide gate dielectric films, IEEE Electron Device Lett. 30: 1269-1271.

APPENDIX A

LIST OF JOURNAL PUBLICATIONS

1. **Minghui Zhang**, Jiechao Jiang, Efstathios I. Meletis, Sarka Zuzjakova, Pavel Mares, Microstructure of Hard and Optically Transparent $Hf_7B_{23}Si_{17}C_4N_{45}$ film at High Temperatures (Submitted).
2. Sarka Zuzjakova, Pavel Mares, Radomir Cerstvy, **Minghui Zhang**, Jiechao Jiang, Efstathios I. Meletis. Superior high-temperature oxidation resistance of magnetron sputtered Hf-B-Si-C-N film, Ceramic International, 42(4), 4853-4859 (2016).
3. Nai-Wen Pi, **Minghui Zhang**, Jiechao Jiang, Aleander Belosludtsev, Jaroslav Vlcek, Jiří Houška, Efstathios I. Meletis. Microstructure of hard and optically transparent HfO_2 films prepared by high-power impulse magnetron sputtering with a pulsed oxygen flow control, Thin Solid Films, 619, 239-249 (2016)
4. Yishu Wang, **Minghui Zhang**, Efstathios I. Meletis. On the novel biaxial strain relaxation mechanism in epitaxial composition graded $La_{1-x}Sr_xMnO_3$ thin film synthesized by RF magnetron sputtering, Coatings, 5(4), 802-815 (2015).
5. **Minghui Zhang**, Jiechao Jiang, Pavel Mares, Jiří Houška, Jaroslav Vlček, Efstathios I. Meletis. Effect of the Si content on the microstructure of hard, multifunctional Hf-B-Si-C films prepared by pulsed magnetron sputtering, Applied Surface Science, 357, 1343-1353 (2015).
6. Xiaona Zhu, Xing Xu, Zach Harrell, Ruyan Guo, Amar S. Bhalla, **Minghui Zhang**, Jiechao Jiang, Chonglin Chen, Xiangming Chen, Ferroelectric Domain Structure Evolution in $Ba(Zr_{0.1}Ti_{0.9})O_3/(Ba_{0.75}Ca_{0.25})TiO_3$ Heterostructures, Advances, 5, 65811-65817 (2015).
7. **Minghui Zhang**, Jiechao Jiang, Jiří Houška, Jiří Kohout, Jaroslav Vlček, Efstathios I. Meletis. A study of the microstructure evolution of hard Zr-B-C-N films by high-resolution transmission electron microscopy, Acta Materialia, 77, 212-222 (2014).
8. Jiří Kohout,Jaroslav Vlček,Jiří Houška, Pavel Mareš, Radomír Čerstvý, Peter Zeman**, Minghui Zhang,** Jiechao Jiang, Efstathios I. Meletis. Hard multifunctional Hf-B-Si-C films prepared by pulsed magnetron sputtering, Surface Coating Technology, 257, 301-307 (2014).
9. Q. Zou, M. Liu, G.Q. Wang, H.L. Lu, T.Z. Yang, H.M. Guo, C.R. Ma, X. Xu, **M.H. Zhang,** J.C. Jiang, E. I. Meletis, Y. Lin, H. J. Gao and C.L. Chen, Step Terrace Tuned Anisotropic Transport Properties of Highly Epitaxial $LaBaCo_2O5.5_{s+\delta}$ Thin Film on Vicinal $SrTiO_3$ Substrates, ACS Appl. Mater. Interfaces, 6(9), 6704-6708 (2014)
10. Jie He, **Minghui Zhang**, Jiechao Jiang, Jaroslav Vlček, Petr Zeman, Petr Steidl, and Efstathios I. Meletis. Microstructure Characterization of High-temperature, Oxidation Resistant Si–B–C–N Films, Thin Solid Films, 542, 167-173 (2013).

APPENDIX B

CONFERENCE PUBLICATIONS AND PRESENTATIONS

1. Microstructure Characterization of Hard, Multifunctional Hf-B-Si-C Films, **Minghui Zhang**, Jiechao Jiang, P. Mareš, J. Houska, J. Vlček and Efstathios I. Meletis, 5th International Conference from Nanoparticles and Nanomaterials to Nanodevices and Nanosystems (IC4N), June 26-30, 2016, Poster Presentation, Porto Heli, Greece.
2. Characterization of Nanocomposite, Hard, Multifunctional Zr-B-C-N Coatings, **Minghui Zhang**, Jiechao Jiang, J. Houska, J. Kohout, J. Vlcek and Efstathios I. Meletis, 12th International Conference on Durability of Composite Systems (DURACOSYS), June 12-15, 2016, Poster Presentation, University of Texas at Arlington, Texas, USA.
3. Effects of Silicon Content on the Microstructure and Properties of Hf-B-Si-C Thin Films, **Minghui Zhang**, Jiechao Jiang, Efstathios I. Meletis, J. Kohoutl, J. Vlček and J. Houska, 51st The Texas Society for Microscopy Meeting, February 18-20, 2016, Oral Presentation, Houston, Texas, USA.
4. Effect of Nitrogen Content on the Microstructure and Hardness of Hard Zr-B-C-N Coatings, **Minghui Zhang**, Jiechao Jiang, J. Vlcek, P. Steidl, J. Kohout, R. Cerstvy and Efstathios I. Meletis, 2015 AVS Chapter Conference, August 5, 2015, Poster Presentation, Denton, Texas, USA.
5. The Study of Hf-Si-B-C Thin Films Prepared by Pulsed Magnetron Sputtering, **Minghui Zhang**, Jiechao Jiang, Efstathios I. Meletis, J. Kohoutl, J. Vlček and J. Houska, 50th The Texas Society for Microscopy Meeting, February 19-21, 2015, Poster Presentation, Austin, Texas, USA.
6. Effect of Nitrogen Content on the Microstructure and Hardness of Hard Zr-B-C-N Coatings, **Minghui Zhang**, Jiechao Jiang, J. Vlcek, P. Steidl, J. Kohout, J. Houska and Efstathios I. Meletis, 2014 Microscopy & Microanalysis Meeting, August 3-7, 2014, Oral Presentation, Hartford, CT, USA.
7. High-Resolution Transmission Electron Microscopy of Hard Zr-B-C-N Coatings, **Minghui Zhang**, Jiechao Jiang, J. Vlcek, P. Steidl, J. Kohout, J. Houska and Efstathios I. Meletis, 41st ICMCTF, April 28-May 2, 2014, Oral Presentation, San Diego, CA, USA.
8. High-Resolution Transmission Electron Microscopy and Electron Diffraction of Hard Zr-B-C-N Films, **Minghui Zhang**, Jiechao Jiang, J. Vlcek, P. Steidl, J. Kohout, J. Houska and Efstathios I. Meletis, 2014, Oral Presentation, Arlington, TX, USA.
9. Microstructure Characterization of High-Temperature Oxidation Resistant Si-B-C-N Films, Jie He, **Minghui Zhang**, Jiechao Jiang, Jaroslav Vlček, Petr Zeman, Petr Steidl, and Efstathios I. Meletis, April 18-20, 2013, Oral Presentation, Irving , Texas, USA.

BIOGRAPHICAL INFORMATION

Minghui Zhang completed her Bachelor Degree in Materials Science and Engineering from Beijing University of Chemical Technology in June, 2011. During her undergraduate study, she focused on the inorganic nonmetal material engineering, especially ceramics and composites, and she had over two years of experience as an undergraduate researcher in lab.

At 2011 Fall, Minghui joined the University of Texas at Arlington for the BS to Ph.D. Program, and started research in the Surface and Nano Engineering Laboratory under the supervise of Dr. Efstathios I. Meletis. During her study in UT Arlington, her research is focus on microstructure analysis and mechanism exploration of transition metal-based hard and high temperature oxidation resistant ceramic coatings. Minghui also worked as the Researching Assistant in the Characterization Center of Materials and Biology with the guidance of Dr. Jiechao Jiang. Minghui Zhang has over five years of experience on thin film deposition via Magnetron Sputtering, and she is very experienced on the materials characterization skills and microstructure analysis. She is specialized on SEM, XRD, TEM, analytical TEM, high-resolution TEM, electron diffraction analysis, TEM sample preparation and also other major materials characterization techniques. During her graduate education at University of Texas at Arlington, Minghui received Academic Excellence Award, Best Paper Award, Lockheed Martin Missiles and Fire Control Scholarship and Dissertation Scholarship. She has several journal paper publications from her work and has attended several conference presentations at Texas Society for Microscopy Meeting, Microscopy and Microanalysis Meeting, DURACOSYS, and International Conference on Metallurgical Coatings and Thin Films.